SECONDARY FLOW IN AN ANNULAR CASCADE

OF HIGH TURNING. ANGLE TURBINE BLADES

By

S. H. MOUSTAPHA B.Sc.(Eng.), M.Eng.

A Thesis

Submitted to the School of Graduate Studies

in Partial Fulfilment of the Requirements

for the Degree

Doctor of Philosophy

McMaster University

March 1978

SECONDARY FLOW IN AN ANNULAR CASCADE

OF HIGH TURNING ANGLE TURBINE BLADES

TO MY FATHER

DOCTOR OF PHILOSOPHY·(1978)   McMASTER UNIVERSITY
(Mechanical Engineering) ·   Hamilton, Ontario

TITLE: Secondary Flow in an Annular Cascade of High
                Turning Angle Turbine Blades

AUTHOR: S. H. Moustapha, B.Sc.   (Cairo University)

                        M.Eng. (McMaster University) ·

SUPERVISOR: Dr. J. H. T. Wade

NUMBER OF PAGES: xvii, 201

ABSTRACT

Approximately half of the aerodynamic losses in a turbomachine blade row are attributed to cascade secondary losses. Looking at the existing literature on secondary flows, there is a lack of detailed experiments carried out on annular cascade of high turning angle turbine blades.

The purpose of this investigation was to construct and carry out detailed experiments on a unique large scale annular cascade of high turning angle turbine blades. Cascade tests, at a Reynolds number based on the blade chord of 3×10^5 to 6×10^5, consisted of inlet and exit flow parameters traverses, blade passage pressure distributions and flow visualization. The results, presented in the form of contours and radial distributions, were analysed and compared with the results of previous investigations.

The tests showed that the flexibility designed into the cascade rig has achieved the purpose of tailoring the inlet flow conditions according to the test requirements. The total pressure loss contours revealed a large single loss region at the middle of the blade passage. The yaw angle contours showed regions of significant flow under-turning and overturning in the main stream. Good agreement was found between the measured cascade secondary loss coefficient and those calculated from the available correlations.

ACKNOWLEDGEMENTS

The author wishes to express his sincere gratitude and indebtedness to his supervisor Dr. J. H. T. Wade. His helpful advice and continuous encouragement were invaluable throughout the course of this investigation.

The author wishes to acknowledge the cooperation of Mr. S. El-Shammaa in the construction of the cascade rig and his useful suggestions at different stages of this work.

Valuable discussions with Dr. J. H. Stannard at the final stages of this research are thankfully acknowledged.

Particular thanks are extended to the men of the McMaster University Engineering Machine Shop.

Thanks also are due to Ms. B. Bedell for typing the manuscript.

The financial support provided by the National Research Council of Canada through grant A1585 is also acknowledged.

Finally, I should like to express my special appreciation to my wife Maha and my daughter Rasha for their love and encouragement during this work.

TABLE OF CONTENTS

LIST OF FIGURES

LIST OF TABLES

NOMENCLATURE

Symbols	Description
a	Speed of sound
C	Blade chord
C_L	Lift coefficient
$C_{L\bar{z}}$	Zweifel lift coefficient (defined in Table 2)
Cp_s	Static pressure loss coefficient
Cp_o	Total pressure loss coefficient
E	Voltage
h	Blade span
H	Shape factor
M	Mach number
N	Blade passage area ratio
P	Static pressure
P_o	Stagnation pressure
r	Radial coordinate
R	Reference radial direction
R_N	Reynolds number
s	Streamline direction
S	Blade pitch
V	Absolute flow velocity
V_a	Axial flow velocity
Y_T	Total blade losses
Y_p	Blade profile losses
Y_s	Blade secondary losses
Y_1^*	Inlet boundary layer losses

$x, y, z,$	Cartesian coordinates (Fig. 2)
u, v, w	Secondary velocities in x, y and directions
Z	Blade loading parameter (Eqn. 28)
α	Flow yaw angle measured with the axial direction
α'	Flow yaw angle measured with the plane of the leading edge, i.e., equal to $(90^\circ - \alpha)$
β	Blade angle with respect to the axial direction
Γ	Circulation
Γ_{ps}	Passage secondary circulation (Eq.9)
Γ_{tf}	Trailing filament circulation (Eq.10)
Γ_{ts}	Trailing shed circulation (Eq.11)
γ	Flow pitch angle
Δ	Increment
δ	Boundary layer thickness at which the absolute velocity is equal to 99% of the free stream velocity
δ^*	Boundary layer displacement thickness
ϵ	Total turning angle
η	Vorticity normal to the streamline
θ	Tangential direction
μ	Fluid viscosity
ξ	Streamwise vorticity
ξ_{ps}	Passage secondary vorticity (Eq.13)
ξ_{tf}	Trailing filament vorticity (Eq.14)
ξ_{ts}	Trailing shed vorticity (Eq.15)
π	Constant = 3.14159

ρ	Fluid density
Σ	Summation
ϕ	Angle between the normal to the Bernoulli surface and the principal normal to the streamlines (Fig. 2)
ψ	Secondary flow stream function
Ω	Vorticity vector
L.E.	Leading edge
T.E.	Trailing edge
B.H.P.	Brake horsepower
c.f.m.	Cubic feet per minute
p.s.i.	Pounds per square inch
r.p.m.	Revolutions per minute
r.m.s.	Root mean square

Subscripts

0	Stagnation
1	Passage inlet
2	Passage exit
a	Axial
i	Inter
o	Outer
m	Mean
s	Static
T	Total

CHAPTER 1

INTRODUCTION

Successful aerodynamic design of a turbomachine
depends mainly on the accurate estimation of the losses
and on the understanding of the different parameters
influencing them. Losses in a turbomachine can broadly
be divided into three main groups. The first group is the
profile losses associated with the skin friction over the
blade surfaces. The second group is the annulus losses
due to the skin friction on the inner and outer walls of
the annulus. The third group is the secondary losses
resulting from the interaction between the blade ends and
the boundary layer on the annulus walls. This last group
can be further subdivided into four areas of importance:

1.   Cascade secondary losses due to the effect of
     turning the annulus boundary layer.

2.   Corner losses as a result of the flow in the corner
     formed by the blades and the annular walls.

3.   Clearance losses caused by the fluid flow through
     the clearance between the tip of the rotating blade
     rows and the annular walls.

4.   Mainstream secondary losses due to the vortices
     trailing from the blades.

An attempt has been made in Fig. 1 to show these losses
in a pictorial fashion.

Approximately half of the aerodynamic losses in a
turbomachine blade row are attributed to the secondary
losses and in particular to "cascade secondary losses".
Thus to further improve the performance of turbomachines,
especially considering the trend towards using high turning
angle turbine blades of low aspect ratio, it is necessary
that the cause, mechanism, and effects of cascade secondary
flow be thoroughly understood. The effects of secondary
flow on turbomachine·performance are mainly in the associated
vortices which cause dissipation of energy and tend to
promote separation in the corner between the blades and the
annulus walls. Also circulatory flows within the passage
cause the fluid to leave the blade rows at angles other than
the design angle and therefore cause downstream blade rows
to operate off the design point..

Over the past two decades a significant amount of
theoretical and experimental studies has been made to
investigate the secondary flow phenomena. Several theoreti-
cal models, empirical formulae and correlations have been
proposed for the calculation of the secondary flow losses
in turbine cascades. However, the difficulty in using
any of these existing models and correlations is a lack of
detailed cascade data that can serve as an experimental
reference for the evaluation of any assumptions used in

Cascade Secondary Vortices

Trailing Vortices

Direction of Rotation

Corner Flow Losses

Annulus Losses

Main Flow Direction

Tip Clearance Losses

Profile Losses
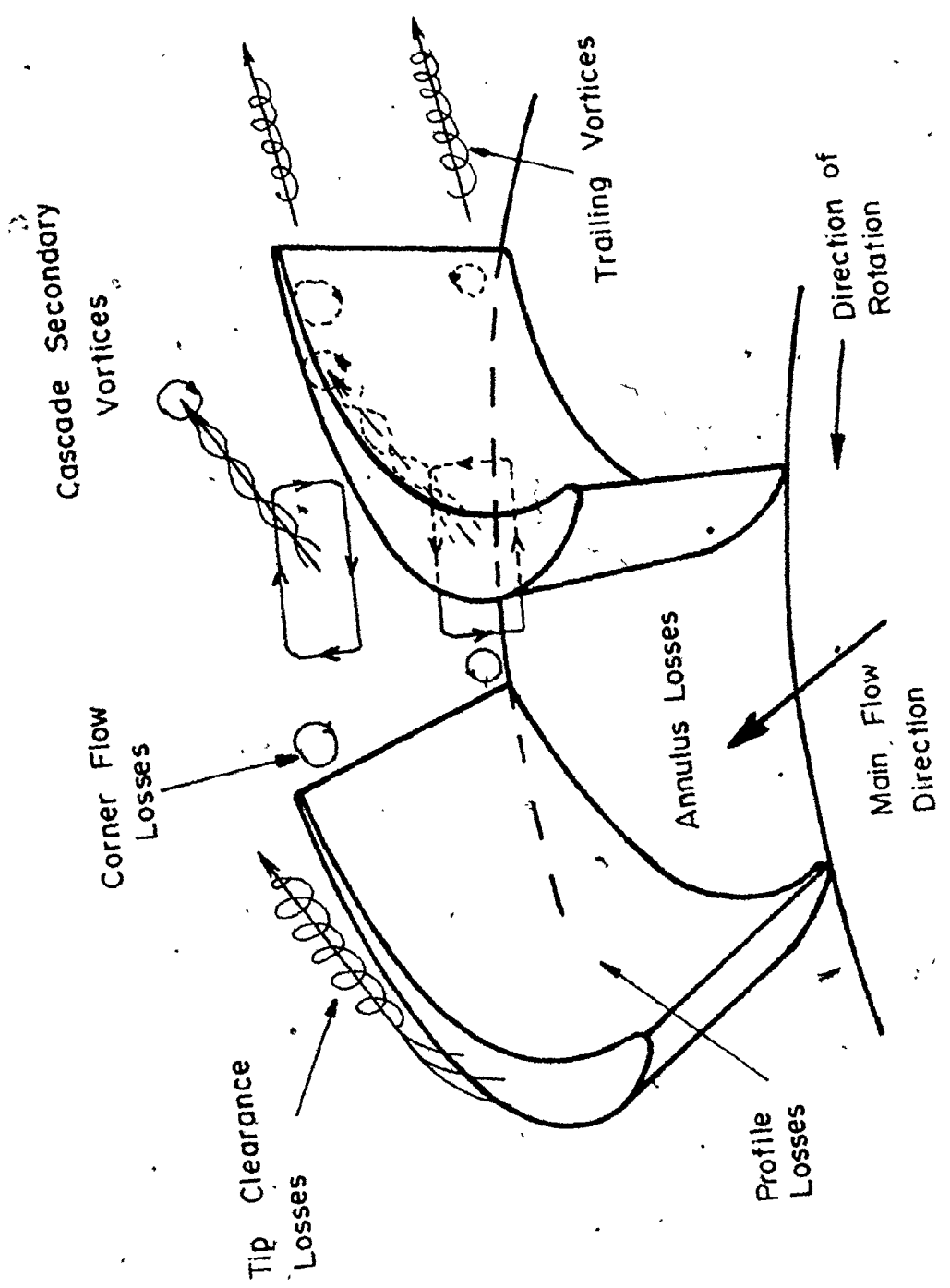
Fig. 1 The Losses Occurring in a Turbomachine Passage.

their derivation, and for the computation of the aero-
dynamic losses predicted by the correlations.

Turbine research at McMaster University was initiated
in 1971 by the design of a series of high turning angle
turbine blade profiles ($\sim130^{\circ}$) by Malhotra [37]. One of these
blade shapes was tested by Stannard [38] over a range of
pressure ratios in a rectilinear blow-down wind tunnel. In
1973, Myachin [36] designed a large scale (7.5:1 with respect
to blade dimensions in the rectilinear cascade) annular
cascade rig, and proposed several studies to be conducted for
the investigation of the secondary flow phenomenon in high
turning angle cascades. In 1975, the author with the
cooperation of El Shammaa* started the design simplifications
and construction of the annular cascade rig.

It is the purpose of this study to carry out detailed
experiments on the annular cascade rig and to present, discuss
and analyze the experimental results with the hope of provid-
ing a better understanding of the flow field within a high
turning angle turbine passage.

To establish in which directions a contribution could
best be made, the present study began with a review of the
current knowledge concerning secondary flows in turbomachinery.
This review, which is given in Chapter 2, covered the basic
secondary flow equations, the inviscid techniques for pre-
dicting streamwise vorticity, the methods in use for comput-
ing secondary losses and finally the available experimental

_____

* Ph.D student, Dept. of Mech. Eng., McMaster Univ., Hamilton,
Ontario, Canada.

measurements in turbine cascades.

The experimental apparatus and instrumentation are
described in Chapters 3 and 4. The annular cascade rig
consisted mainly of an inlet section, a test section and an
exit section connected to a fan. For the test section a
modern design of turbine blades was used having a turning
angle of $128°30'$, a span of 190.5 mm and an axial chord of
188.5 mm. The exhaust fan permitted test section inlet
velocity up to 47m/s, which provided realistic blade chord
Reynolds numbers in the range of 3×10^5 to 6×10^5.

In Chapter 5, a brief outline of the preliminary
experiments has been given, together with the scope of the
tests performed on the rig. The experimental work started
with an inlet flow study which is described in Chapter 6.
The objective of this investigation was to measure the
inlet flow conditions and make the necessary adjustments
to produce uniform flow angle and velocity at the inlet
to the cascade.

In Chapter 7, the blade passage pressure distribu-
tion is presented and compared with the two-dimensional
potential flow distribution. The exit flow parameters were
measured for different inlet speeds and the results given
in Chapter 8 in the form of loss contours and flow angle
changes. Qualitative information is also presented in the
form of photographs showing particle deposits on the blade
and annular surfaces as a result of smoke filament flow
visualization studies.

CHAPTER 2

REVIEW OF THE LITERATURE

Cascade secondary flow results from the imbalance between the pressure gradients imposed by the main stream on the boundary layer fluid, and the centrifugal force of the low velocity boundary layer fluid. Thus the low momentum boundary layer fluid turns through a larger angle than the free stream fluid. A component of vorticity is therefore produced in the streamwise direction, resulting in both radial and tangential perturbations of velocity at the exit from the blade rows which are proportional to the magnitude of the entry vorticity and the turning angle.

Over the past two decades a significant amount of material has been accumulated both in theory and experiment into the investigation of secondary flow in turbomachines. Several excellent reviews have been made including those by Lakshminarayana [1]*, Hawthorne [2], Dunham [3] and Horlock [4]. In this chapter the secondary flow basic equations will be presented, followed by the present state of the theoretical and experimental studies with special emphasis on turbine cascade tests.

---

* Numbers in brackets designate references.

2.1   Secondary Flow Equations

Squire and Winter [5] established the basis for
the current theoretical approach to secondary flow in a
turbomachine. They pointed out that although the non-
uniformity that causes the secondary flow is created by
viscous effects, the secondary flow itself can be considered
inviscid. They solved the equations of motion for steady,
inviscid and incompressible flow to obtain an expression
for the streamwise component of vorticity (Fig. 2) at the
exit of the cascade, in the form:

$$\xi_2 = - 2n_1 \epsilon \tag{1}$$

This expression is only valid for small turning angles (up
to 90°), constant area flow and high aspect ratios. Squire
and Winter also defined a secondary flow stream function,

$$\frac{\partial^2 \psi}{\partial y^2} + \frac{\partial^2 \psi}{\partial z^2} = - \xi_2 \tag{2}$$

The radial and tangential components of the velocity
perturbation at the cascade exit can be found by differ-
entiating the stream function,

$$v = \frac{\partial \psi}{\partial z} ; \quad w = \frac{\partial \psi}{\partial y} \tag{3}$$

Hawthorne [6] derived a more general expression
for the change in streamwise vorticity along a streamline
in steady, inviscid and incompressible flow in the absence
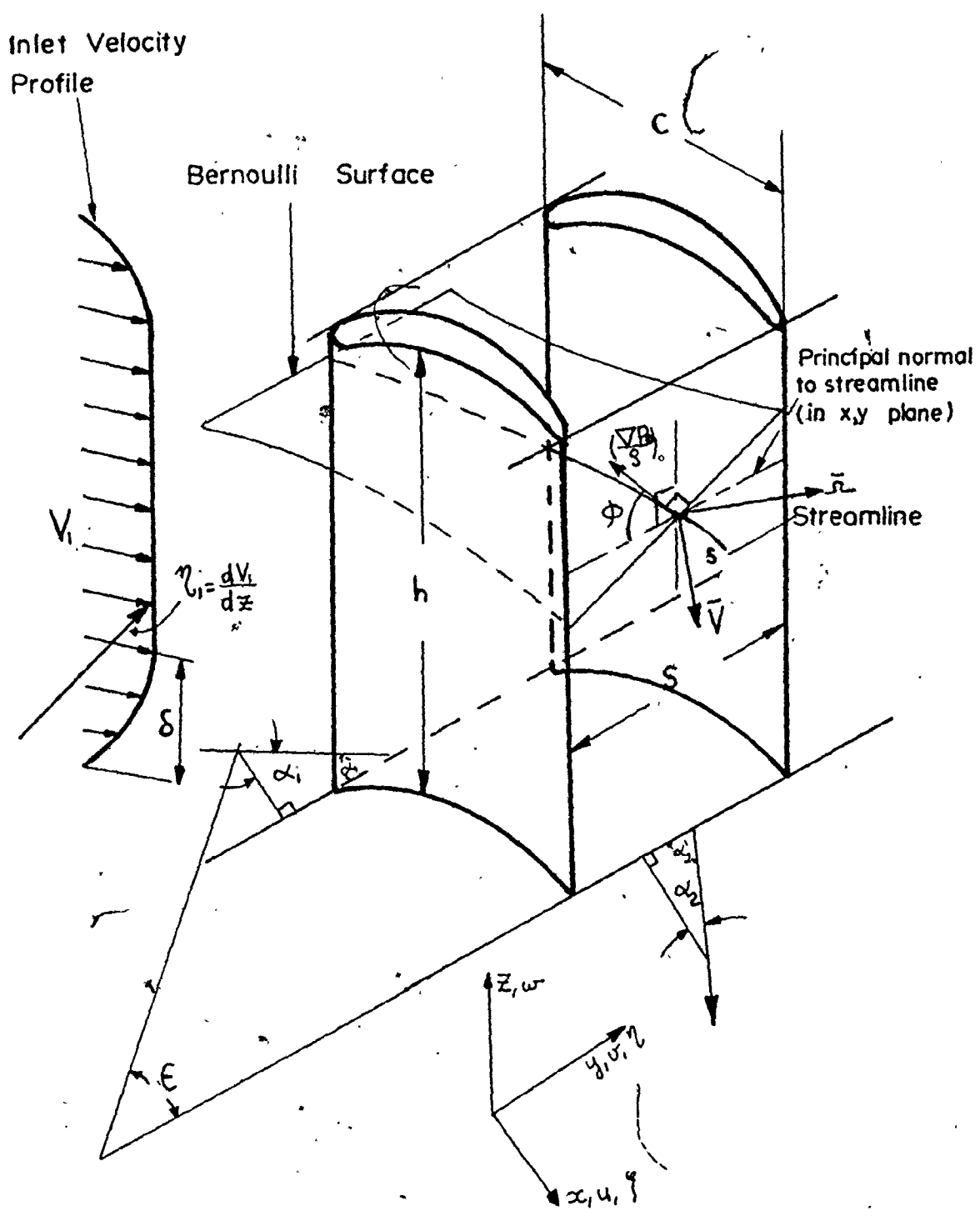
Fig. 2 Definition of Flow and Passage Parameters.

body forces,

$$\left(\frac{\xi}{V}\right)_2 - \left(\frac{\xi}{V}\right)_1 = -2 \int_1^2 \left| grad\ \left(\frac{P_o}{\rho}\right) \right| \frac{\sin\ \phi}{V^2}\ d\epsilon \qquad (4)$$

Hawthorne pointed out that it is possible to solve for secondary vorticity if (a) the secondary flow occurs in planes which are normal to the average direction of flow, (b) the secondary vorticity is normal to these planes, (c) the secondary flow may be treated as a two-dimensional plane flow superimposed on the main flow, and (d) the behaviour of the Bernoulli surfaces and streamlines is known. The first three assumptions can be met only in cascades of low turning angle.

Preston [7] obtained the results of the Squire and Winter analysis [5] and of Hawthorne's analysis [6] by a relatively simple method in which he made use of Kelvin's theorem in the form "For an inviscid fluid the circulation in a circuit moving with the fluid remains constant".

By treating the secondary flow as a three-dimensional perturbation of a quasi two-dimensional flow approaching a bend, Hawthorne [8] was able to show another method of obtaining the components of vorticity as defined in Equation (4). Morris [9] extended Hawthorne's [6] analysis and showed that secondary vorticity can be generated not only through the action of a non-uniform flow field on curved streamlines; but also whenever the flow kinetics are such

that the vector curl $(\bar{V} \times \bar{\Omega})$ has a component in the streamwise direction.

Another approximate expression for the streamwise vorticity developed in a cascade has been given by Loos [10], which takes into account the excessive turning of the flow in the wall boundary layer and is perhaps the most useful relation to the turbomachinery designer. By assuming the axial velocity to be unchanged Loos derived the following expression:

$$\xi_2 - \xi_1 = \frac{\eta_1}{\cos\alpha_1 \cos\alpha_2} [\alpha_2 - \alpha_1 + \frac{\sin 2\alpha_2 - \sin 2\alpha_1}{2}] \quad (5)$$

He also modified Squire and Winter's formula for diverging or converging cascade flow as follows:

$$\xi_2 = - \frac{(N - 1/N)}{\ln N} \eta_1 \epsilon \quad (6)$$

where N is the blade passage area ratio.

Ehrich [11] developed a theory for predicting the secondary flow in a cascade of twisted blades and obtained the following expression for the secondary stream function,

$$\nabla^2 \psi = 2\epsilon \left(\frac{dV}{dy}\right) + V \left(\frac{d\epsilon}{dy}\right) \quad (7)$$

Louis [12] has provided an interesting development of the basic equations (1 to 4) to allow for the effect of viscosity.

The secondary vorticity equations presented so far,

describe the secondary flow developed in the channel between the blades, but it is not the only vorticity that exists in the downstream flow. Hawthorne [13], and Hawthorne and Armstrong [14] provided further expressions for the vorticity components downstream of a cascade in the following form:

(i)   Due to cascade secondary flow, "the cascade secondary vorticity" of circulation

$$\Gamma_{ps} = \frac{dV}{dz} \left(-V\oint\frac{ds}{V} + \frac{S}{2}\frac{\sin2\alpha_2 - \sin2\alpha_1}{\cos\alpha_1}\right) \qquad (9)$$

(ii)   Due to stretching of the vortex filament, initially perpendicular to the entry stream, "the trailing filament vortices of circulation",

$$\Gamma_{tf} = \frac{dV}{dz} V \oint \frac{ds}{V} \qquad (10)$$

(iii)   Due to change of circulation along the blade span, "trailing shed vortices of circulation",

$$\Gamma_{ts} = - S\cos\alpha_1 \frac{dV}{dz} (\tan\alpha_2 - \tan\alpha_1) \qquad (11)$$

The arithmetical summation of these circulations has some physical significance in that it is theoretically possible to calculate the vorticity knowing the circulation and hence solve the stream function equation to obtain the change in the outlet flow angle.

2.2 Theoretical Investigations

Approximate solutions for the secondary vorticity
fields have been classified by Hawthorne [15]. The two
parameters of importance are the magnitude of the entry
shear and the deflection of the flow. Thus four kinds of
flow can be considered depending on the relative magnitude
of these two parameters. Of particular interest is the
small shear, large deflection flow case in which a primary
irrotational flow contorts the Bernoulli surfaces and the
vortex filaments found in the approaching shear flow. The
vortex filaments are stretched and twisted by the primary
flow thus inducing the secondary flow. This type of flow
is referred to as the "secondary flow approximation" and is
the one most commonly used to describe secondary flows in
turbomachines.

Hawthorne [16], basing his analysis on the secondary
flow approximation solved Equation (2) for a plane cascade
by using a rapidly convergent series. Expressions for
the change in average outlet angle α_2 for low turning
cascades were presented.

Although the secondary flow approximation has given
a real insight into the behaviour of the flow in cascades,
the approximation loses validity for cascades accepting a
steep inlet velocity profile, for example, in regions close
to the wall. Thus the distortion of the Bernoulli surface,
spanwise flows and the effects of viscosity should be taken

into account. Lakshminarayana and Horlock [17] showed that
for moderate turning angles in which the inlet vorticity
is unchanged through the cascade, the Bernoulli distor-
tion (ϕ) due to an incremental flow turning ($\Delta\epsilon$) is given
by the expression:

$$\phi = \frac{\pi}{2} - \frac{\eta_1 (\Delta\epsilon)^2 C}{2 \epsilon V} \qquad (11)$$

By substituting Equation (11) into Equation (4) and
assuming that the stagnation pressure varied only in the
spanwise direction they obtained the following expression:

$$\left(\frac{\xi}{V}\right)_2 - \left(\frac{\xi}{V}\right)_1 = -2 \int_0^\epsilon \frac{\eta_1}{V} \cos\left(\frac{\eta_1 (\Delta\epsilon) C}{2 \epsilon V}\right) d\epsilon \qquad (12)$$

In Ref. [17], the spanwise displacement of the flow and the
viscous effect were taken into consideration, but the
analysis was restricted to compressor cascades which
involved low turning angles.

Recently Bardon, Moffatt and Randall [18] estimated
the secondary flow effects on gas outlet angles in
rectilinear cascades with moderate turning angles (less
than 60°). They used the equations given in Ref. [6] and
[17] and by means of a finite-difference stepwise pro-
cedure they solved the equations for vorticity, stream
function, secondary velocities and exit angle change. They
presented several correlations for assessing the spanwise

variation of the gas exit angle.

Hawthorne and Armstrong [19] developed an analysis for predicting the angle change in moderate turning cascades taking into consideration the displacement effect after the cascade trailing edge.

Came [20] and Marsh [21], presented two simple derivations for the components of vorticity defined by Hawthorne [14]. An expression was obtained for the difference in the time taken for fluid particles to travel over the blade pressure and suction surfaces, and which was used to define the three components of vorticity for one blade pitch and for unit blade span in the form:

$$\frac{\xi_{ps}}{\eta_1} = \frac{\cos^2\alpha_m}{\cos\alpha_1} (\tan\alpha_1 - \tan\alpha_2) + \frac{1}{2} \frac{\sin2\alpha_1 - \sin2\alpha_2}{\cos\alpha_1} \qquad (13)$$

$$\frac{\xi_{tf}}{\eta_1} = - \frac{\cos^2\alpha_m}{\cos\alpha_1} (\tan\alpha_1 - \tan\alpha_2) \qquad (14)$$

$$\frac{\xi_{ts}}{\eta_1} = \cos\alpha_1 (\tan\alpha_1 - \tan\alpha_2) \qquad (15)$$

Analysis of secondary flow in an annular cascade has also been carried out by Hawthorne and Novak [2] and Dixon [22] for axial inlet flow but with variation of the outlet flow angle α_2 along the span (now taken as r). They resolve the secondary vorticity ξ_2 into tangential and axial components, the former ($\xi_2 \sin\alpha_2$) causing a radial gradient of axial velocity and the latter leading to an

equation for a Stokes stream function describing the radial (r) and tangential (θ) velocities in the trailing edge plane of the form:

$$\nabla^2 \psi = - \xi_2 \cos \alpha_2 \qquad (16)$$

The three-dimensional boundary-layer theory has been applied to the problem of secondary flow in several papers. Loos [23], Herzig and Hansen [24] studied the incompressible three-dimensional laminar boundary layer over a flat plate for curved free streamlines in the plane of the plate. Loos solved the equations for a specific case where the free streamlines had a parabolic shape. Herzig and Hansen extended the analysis to obtain exact solutions for general streamline paths, removing the previous restriction of small turning, by simply represent-ing the blade contour with an approximate polynomial. Johnston [25] introduced his well-known triangular plot for three-dimensional turbulent boundary layers generated by secondary flow. He found, based on experimental evidence, that the cross flow in the outer part of the boundary layer may be given by the expression:

$$\left(\frac{v}{V}\right) = - 2 \varepsilon \left(1 - \frac{u}{V}\right) \qquad (17)$$

2.3 Experimental Investigations

There exists a large amount of experimental data relating to secondary flow, but mostly restricted to low

turning angle cascades. Some experiments were specifically aimed at checking the theory; several other results revealed facets of the physical phenomena and the effect of cascade and flow parameters on flow losses.

To verify the theory as presented, Squire and Winter [5] obtained good agreement between Equations (1,2 &3) and their tests conducted on a 94.8° deflection channel. However they concluded that the secondary flow approximation broke down near the wall where the viscous effects become significant. Hawthorne and Armstrong [14] and [19] compared their analysis with experiments performed on turbine blades placed in a rectangular cross-section wind tunnel. Good correlation was found between the measured and calculated outlet angle variation. Lakshminarayana [17] also found good agreement between the calculated outlet angle and tests conducted on an 82° turning angle cascade. Other investigations to verify the secondary flow theory can be found in the review papers [1] and [4].

To put the secondary flow loss correlations in perspective it is perhaps worth mentioning the fact that the prediction of turbine profile losses due to the nominally two-dimensional boundary layers on the blade surfaces, is in itself a challenging problem. The profile losses are of course influenced by many factors which affect the development of the blade boundary layer. These include the large variations in velocity and the resulting pressure gradients

along the blade surface, the highly curved blade surfaces which either tend to suppress the boundary layer turbulence (on the suction surface) or promote it (on the pressure surface), surface roughness, trailing edge thickness, incidence and transition on the blade surface. The first profile losses (and secondary losses) correlations for turbine blading were presented by Ainley and Mathieson [26] for different cascade geometry. Ainley's correlations are still widely used in modern gas turbine design. Baljé and Binsley [27] presented contours of profile losses for different inlet and exit angles at optimum pitch to chord ratios. Recently Denton [28] reviewed seven methods of predicting the profile losses, compared the losses with 79 cascade results and finally concluded that none of them predicted the losses accurately. Neverthless, some progress could be made by obtaining the losses from calculation of the velocity distribution and the boundary layer growth on the blade surfaces and in the wake.

Secondary flow in a cascade may be presented by the local outlet angle change ($\Delta\alpha_2$) and a loss coefficient (ΔP_o). These parameters may be expected to be a function of V_1, δ_1, H_1, C, h, S, ρ, μ, a, ξ_1 and the flow geometry [4]. These independent parameters can be grouped into non-dimensional forms to give:

$$\Delta\alpha_2, \Delta P_o = f\ (\frac{z}{C}, R_N, M, \frac{\delta_1}{C}, H_1, \frac{\xi_1 \delta_1}{V_1}, \frac{h}{C}, \frac{S}{C}, C_L) \qquad (18)$$

Here the lift coefficient (C_L) or the other blade-loading parameter represents the most important effect of flow geometry.

Dunham [3] has found from a survey of experimental data, a correlation showing the effect of aspect ratio (h/C) and lift coefficient (C_L) on ΔP_o. He also presented a tentative expression for the inlet boundary layer effect and derived the following correlation for ΔP_o (average) based on experimental results:

$$\Delta P_o \text{(av)} = \frac{C}{h} \frac{\cos\alpha_2}{\cos\beta_1} \frac{C_L^2}{(S/C)^2} \frac{\cos^2\alpha_2}{\cos^3\alpha_m} (0.0055+0.078\sqrt{\frac{\delta_1^*}{C}}) \qquad (19)$$

The first term in the boundary layer function shown in parenthesis is the downstream wall boundary component and the second term is the vortex core loss component. Dunham concluded however that his correlation for losses has to be verified by experiments on turbine cascades particularly with high turning angles.

Brown [29] investigated the secondary flow phenomena in rectilinear cascades with 132° deflection. He obtained the variation of the exit flow angle from the cascade and pressure loss coefficients as a function of the blade span. The measured secondary losses were ten times smaller than the predicted losses using various correlations. It should be noted that this is the largest deflection (132°) which has been investigated experimentally according to the

literature.

Recently Came [30] presented secondary loss measurements for various inlet boundary layer thickness and inlet angle for a large turbine cascade with a maximum turning angle of 85°. Came presented his measurements in the form of loss contours and spanwise variations as a function of the inlet conditions. He defined the secondary losses as a function of the inlet boundary layer losses and introduced the following correlation,

$$\Delta P_o = (\frac{C_L}{S/C})^2 \frac{\cos^2\alpha_2}{\cos^3\alpha_m} \frac{\cos\alpha_2}{\cos\beta_1} (0.25 \ Y_1^* + 0.009 \ \frac{C}{h}) \qquad (20)$$

where Y_1^* defines the inlet boundary layer losses. Dunham's correlation [19] was also shown to be in good agreement with Came's experimental results.

In order to understand the physical nature of the secondary flow in a cascade, flow visualization studies have been carried out often in conjunction with pressure measurements. Rohlik and others [31] performed experiments on an annular turbine nozzle cascade using three different blade profiles. Detailed data were taken including surveys of total pressure and exit angle in the free stream, wake and boundary layer regions immediately downstream of the cascade. Flow visualization techniques included surface flow studies (by means of hydrogen sulfide and paint traces) and smoke flow studies. They showed clearly how low energy

air originating in the outer wall boundary layer was swept
not merely onto the blade suction surface but all the way
down the trailing edge towards the hub until it was finally
discharged near the inner wall. In these cases, the tip
secondary loss was very small and the hub secondary loss
considerably larger. To what extent the profile loss was
affected was not known. Herzig [32] and Turner [33]
reported similar studies on annular cascades with the aim
of explaining the fundamental aspects of the boundary layer,
flows in turbomachines.

Sjolander [34] performed experiments in an annular
cascade of turbine nozzle guide vanes with two main objectives:
firstly to try to develop a better understanding of the
endwall boundary layer by a combination of flow visualiza-
tion and experimental measurements and secondly to try to
make the measurements sufficiently complete that they could
be used as a test case for endwall boundary layer calculation
schemes. He clearly demonstrated that even in a situation
where the overall pressure gradients are strongly favourable,
local areas of adverse pressure gradient could still result
in boundary layer separations which had a significant influence
on the rest of the flow.

Recently, Langston and others [35] carried out
detailed measurements of the subsonic flow in a large scale
plane turbine cascade ($\epsilon = 110^{\circ}$) to evaluate the three-

dimensional nature of the flow field. Flow visualization
was done on the blade and endwall surfaces, and measurements
were carried out at eight different axial planes through
the cascade. The characteristics of the endwall boundary
layer were presented showing that three-dimensional
separation is an important feature of endwall flow.

2.4 Conclusions

After reviewing the state of the art on secondary
flow, the following conclusions can be drawn:

1. The growth of secondary vorticity in cascades and
   changes in outlet angles due to secondary flow,
   can be calculated reasonably well for weak shear flows
   and moderate deflections (say up to 80°).

2. Although the flow pattern associated with secondary
   losses is understood, the magnitudes of the losses
   are still open to discussion and verification.

3. Annular cascades with high deflection angles should
   be investigated to define the secondary flow para-
   meters in turbine bladings.

4. More attention must be given to the measurement
   and calculation of wall boundary layers in cascades.

5. Finally it is necessary to broaden the applicability
   of the theoretical models so that they can be
   applied to multistage machines.

CHAPTER 3

THE ANNULAR CASCADE RIG

In order to meet many of the flow conditions felt in a full annular cascade with high turning angles, a unique three dimensional testing rig was designed [36] with the aim of carrying out detailed investigations of both free stream and secondary flows. In the basic design of the testing rig the following principles were laid down:

1. The design required an annular model to provide for the maximum conditions of similarity between the model flow and that which takes place in a twisted cylindrical passage i.e., the preservation of the radial flow component.

2. The largest possible model scale to be chosen in order to provide maximum room within the blade passages for detailed investigations of both flow and wall pressure distributions.

3. To provide uniform inlet flow conditions to the test section and to measure the influence of the inlet section on the downstream parameters.

4. To minimize the influence of the outlet section on the upstream conditions.

To achieve these goals, the inlet and exit sections had walls of the specific design shown in Fig. 3. Fig. 4

CAPTIONS FOR FIGURES 3 TO 9

1.   The Bellmouth Entrance

2.   The Turning Cascade

3.   The Plane Cascade

4.   The Inlet Section

5.   The Test Section

6.   The Exit Section

7.   Annular Traversing Segments

8.   The Test Section Leading Edge

9.   The Test Section Trailing Edge

10. The Plenum Chamber

11. Auxiliary Fan Speed Control

12. Barometer

13. Multitube Manometer for Blade Passage
     Pressure Measurements

14. Provision for Inlet Flow Control (Sec. 6.3)

15. Micromanometers for Both Main and Boundary Layer
     Flow Measurements

16. Gas Bottles for the Smoke Probe

17. Chambers for Future Boundary Layer Control

Inlet Midchannel Streamline

4

5

6

Outlet Midchannel Streamline
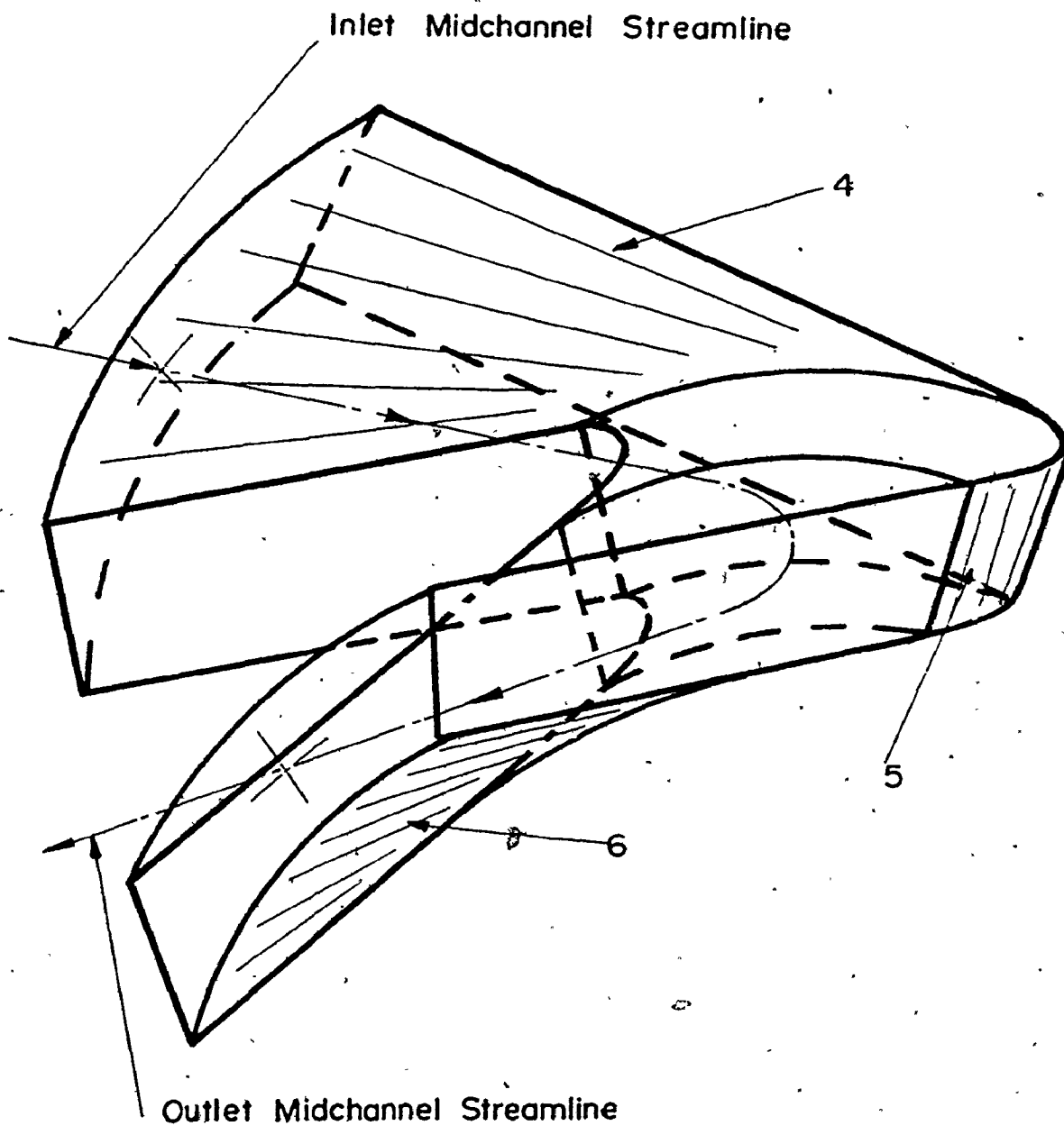
Fig. 3 · The Inlet and Exit Section Walls

Fig. 4 . A Projection in the x,y Plane of the Cross Section View of the Annular Cascade Rig Generated by the Mid Channel Stream Tube.

Note: All dimensions are in millimeters
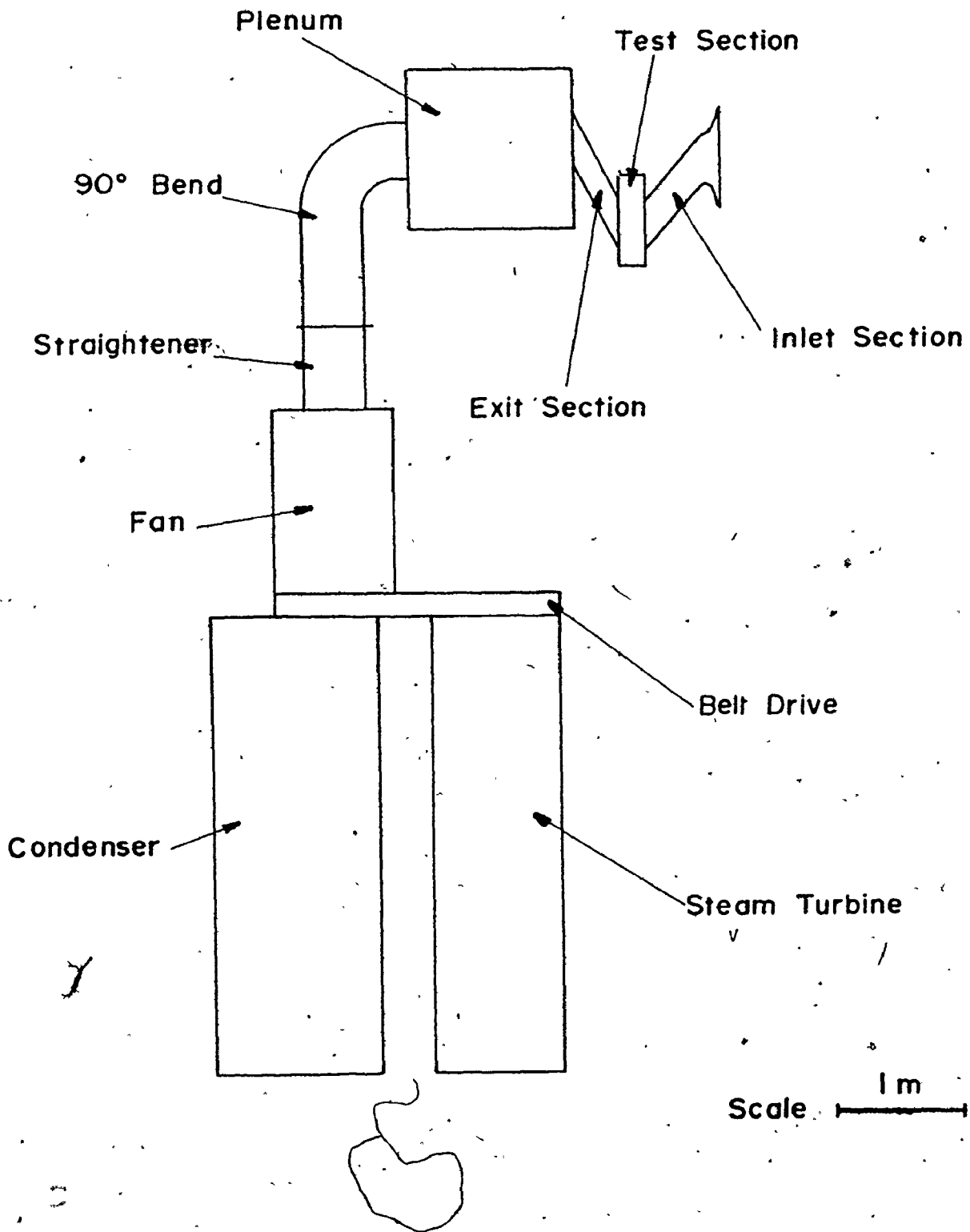
Fig. 5 Test Facility General Layout

Fig. 6. Annular Cascade "B" showing the Instrument Ports
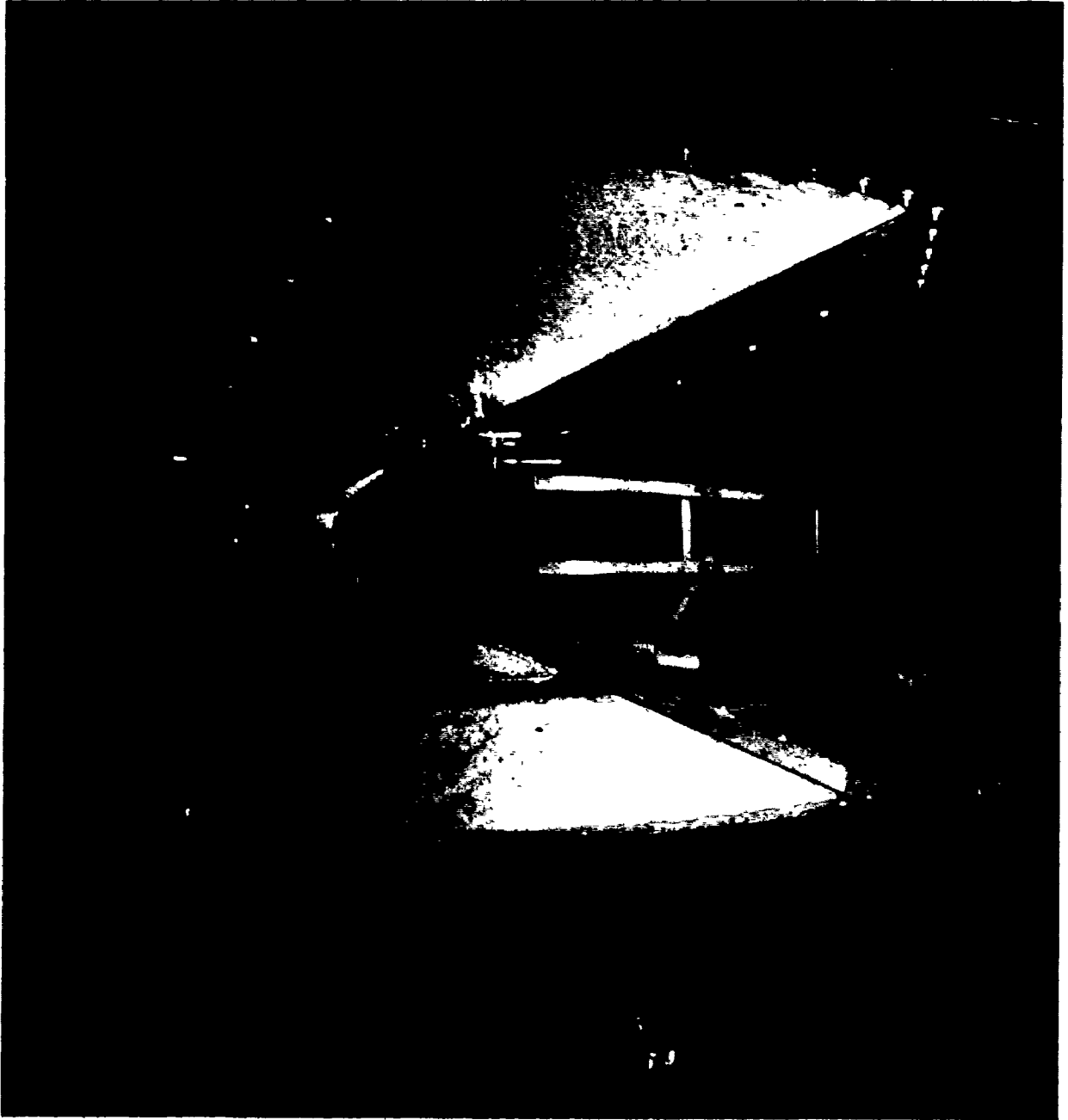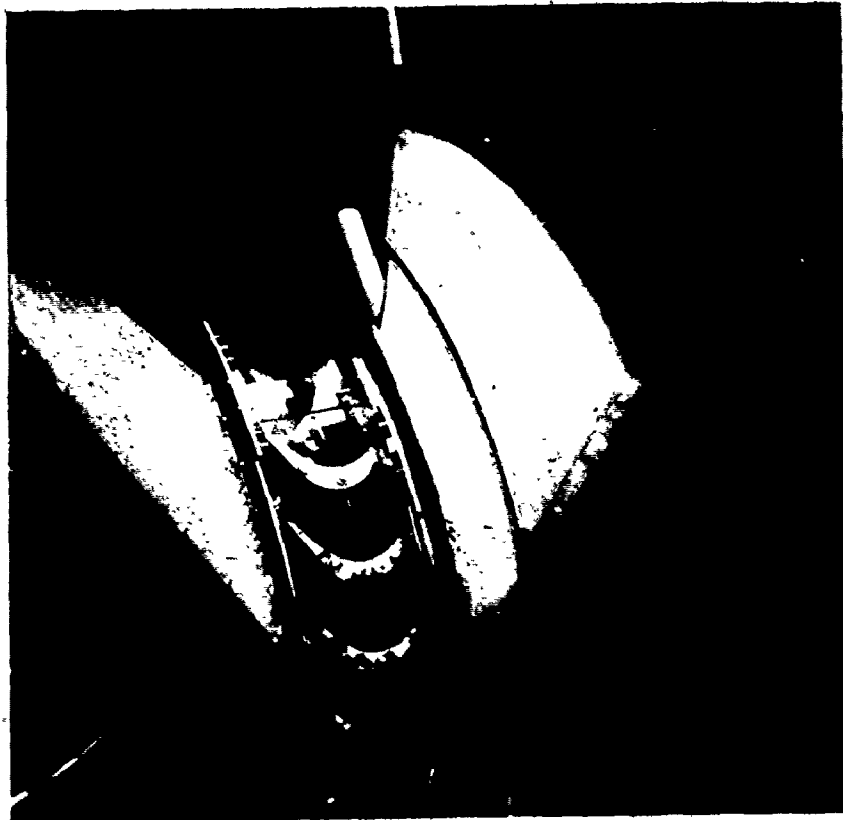
Fig. 8   The Annular Cascade Rig (Top View)

Fig. 9   The Cascade Rig-Showing the Inlet
Traversing Station.

is a cross-sectional view showing the test facility which
consisted of three main parts:

1. An inlet section, including a bellmouth entrance
and space for supplementary cascades, which provided a 64°
inlet air angle.

2. A test section which was composed of a 45° segment
of an annular cascade. The test section housed four blades
circumferentially spaced at 15° with a turning angle of
$128^{\circ}30'$.

3. An outlet section which was connected to an exhauster
fan.

Fig. 5 shows the test rig layout and Fig. 6 to 9 give views
of the rig and the auxiliary equipment. A brief description
of each part will be given in the following sections and
detailed description of the rig can be found in Reference
36 and Appendix A.

3.1 Test Rig Entrance

The inlet of the test rig consisted mainly of a bell-
mouth entrance followed by a turning cascade and finally
a plane cascade.

3.1.1 The Bellmouth Entrance

A bellmouth entrance (Fig. 10) was constructed out
of wood to divert the flow to the inlet section. The bell-
mouth extended over an arc of 53° and had a wall radius of
100 mm.
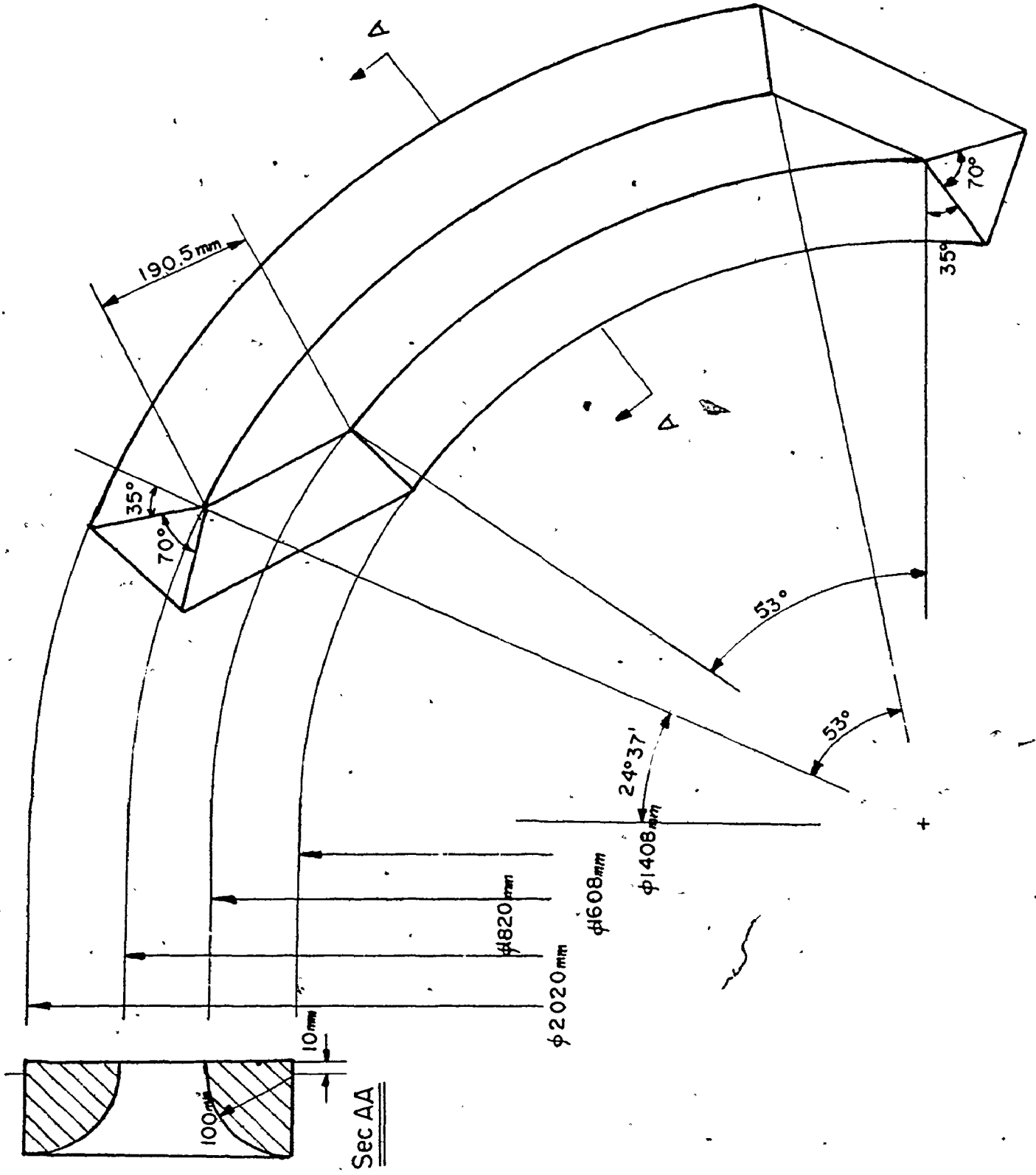
Fig. 10 The Bellmouth Entrance

3.1.2 The Turning Cascade

A turning cascade was designed with the object of
turning the flow from the bellmouth section to an exit
angle of 64°. This was achieved by means of 21 curved
blades equally spaced on a circular arc of 53° (Fig. 11).
The side walls of the turning cascade was manufactured out
of wood by laminating wood sections and then contouring
them to the proper dimensions.

3.1.3 The Plane Cascade

Following the turning cascade a plane cascade was
provided with the main object of ensuring that the streamline
surfaces were planes and inclined at 64° to a plane passing
through the blade leading edge. This was done by intro-
ducing 21 flat blades (Fig. 12). The inner and outer walls
of this cascade were in fact an extension of those of the
inlet section (Fig. 4), but it was decided to make this
part separate for ease of manufacture and to facilitate
installing the blades. Similar to the turning cascade the
outer walls of the plane cascade section were manufactured
out of wood.

For rigidity reasons and to facilitate installation,
it was decided to make the curved and plane blades as one
piece fabricated from 1 mm aluminum sheet. Fig. 13 shows
a typical blade composed of two sections, after being cut
to size and rolled to the proper curvature.
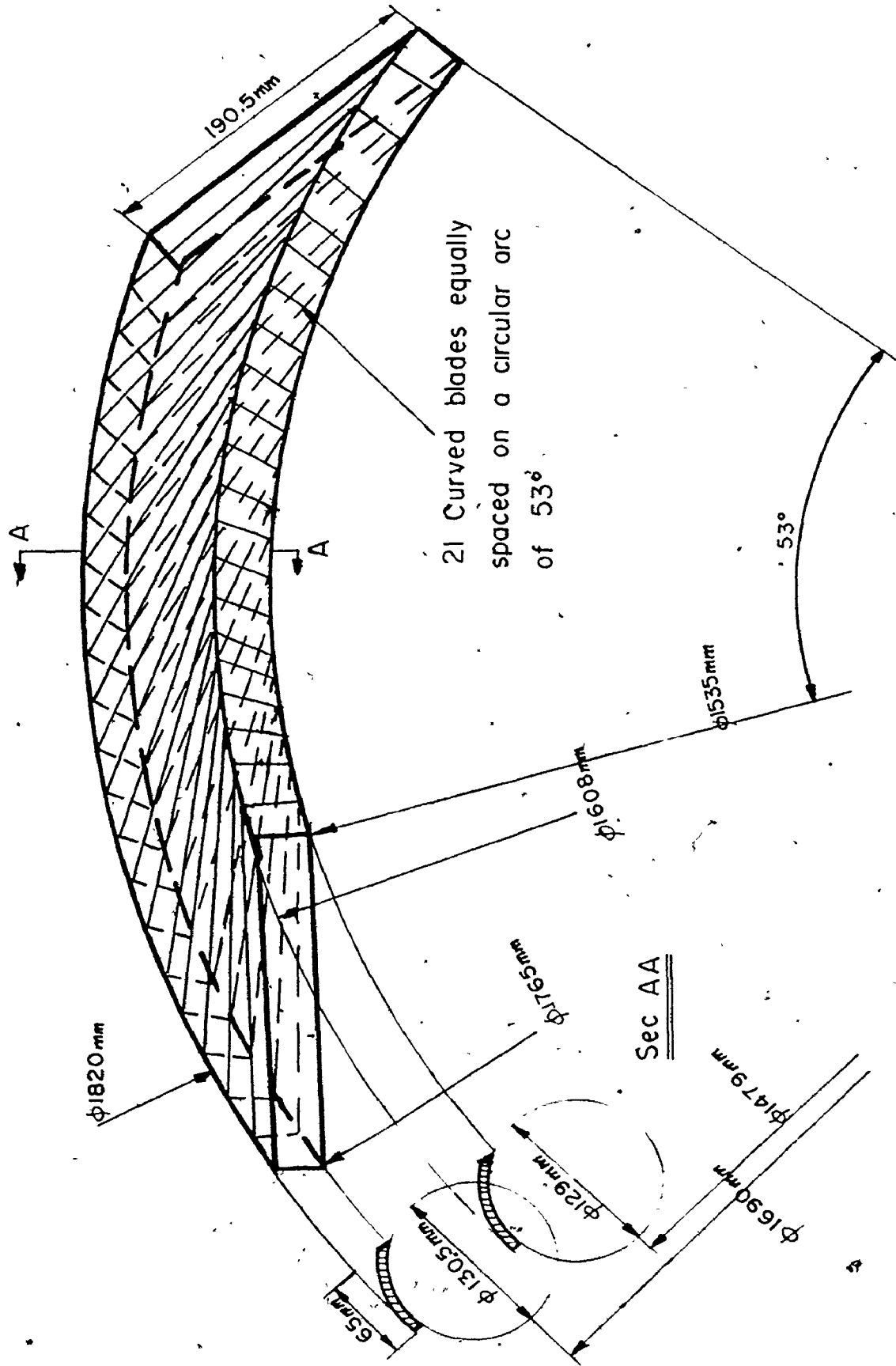
Fig. 11 The Turning Cascade Section

21 Curved blades equally spaced on a circular arc of 53°

190.5mm

A
A

ϕ1535mm

53°

ϕ1608mm

ϕ1820mm

ϕ1765mm

Sec AA

ϕ1479mm

ϕ1690mm

ϕ129 mm

ϕ1305mm

65mm

30mm

29°

68mm

1905 mm

φ1756 mm

21 Plane blades equally
spaced on a circular arc
of 53°

φ1664mm

φ1535mm

φ1430mm

53°
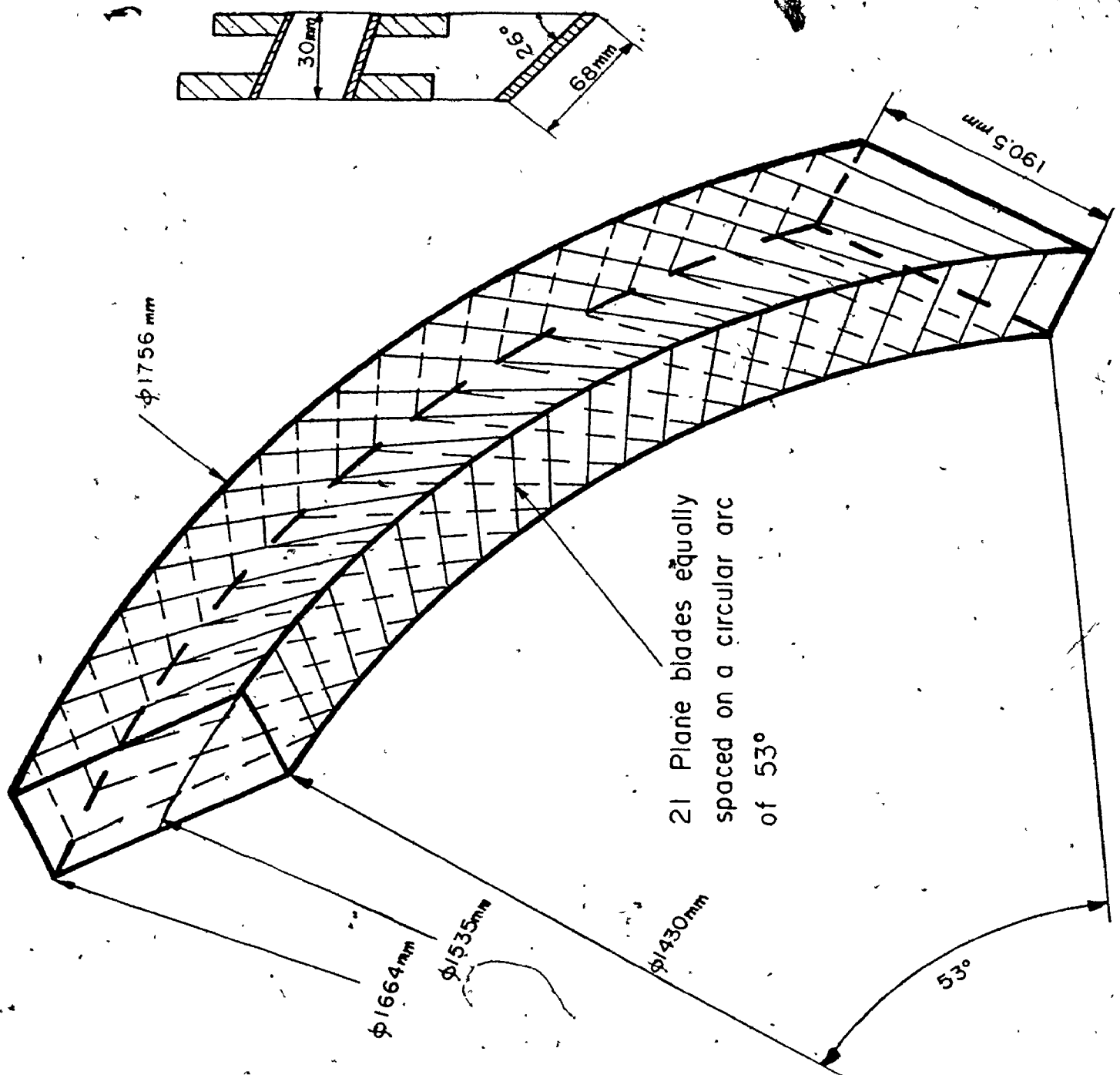
Fig. 1.2 The Plane Cascade Section
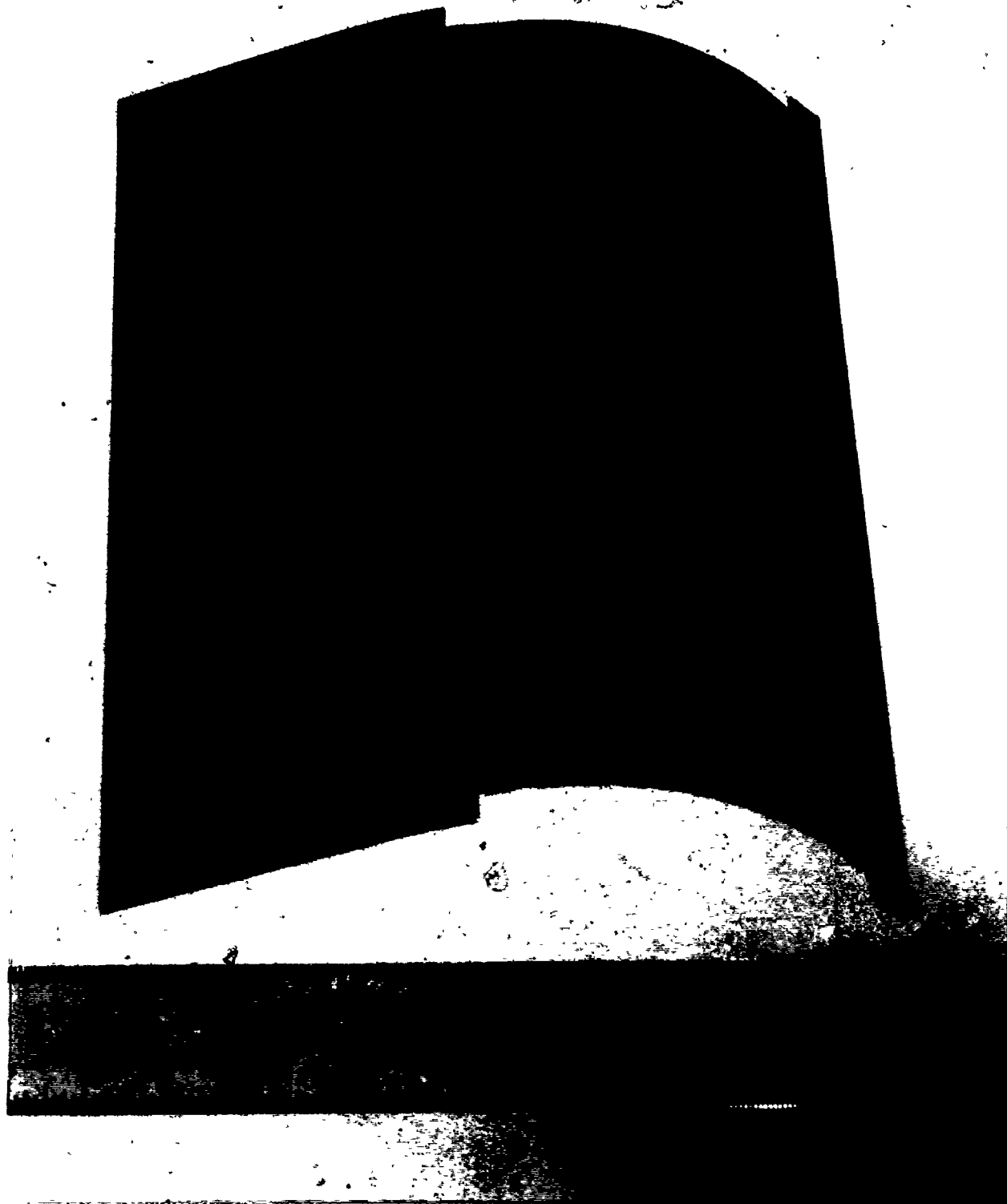
Fig. 13 Test Rig Entrance Blade

3.2   The Inlet Section

The inlet section was designed to produce uniform pressure, velocity and flow angle fields at the entrance of the cascade.   In order to achieve this design the annular boundary walls of the inlet section were generated by the rotation of a rectangle, inclined at 64° to the leading edge plane, through an angle of 53°.   The inlet section circumferential pitch (53°) was made larger than the test section circumferential pitch (45°) in order to reduce the side walls effect on the center blade passage (Fig. 14).   It should be noted that the axial cross sections of the inlet passage were of equal areas.

Due to the complexity of the inlet section geometry, it was decided to manufacture a male mould first and then cover it with F.R.P.*.   The inlet section plug was made out of layers of wood, which were cut oversize at each section of the inlet and stacked on top of each other in a certain fashion so as to represent a step oversize plug. The plug was then finished to the inlet section dimensions by a pattern maker.   The F.R.P. cover (5 mm thick) was then made in three parts: an inner and an outer part to enable one to extract the plug and to facilitate surface finishing, and a 90° sliding annular segment designed to be part of the inner wall and used for inlet flow traversing (see Appendix A for a drawing of the inlet section flange).

---

* Fibre Reinforced Plastic

ϕ1664 mm

r_o

ϕ1430 mm

r_i

Midchannel streamline
surface

ϕ762 mm

53°

Note: r_i & r_o are defined in Appendix A

R

673 mm

ϕ1143 mm
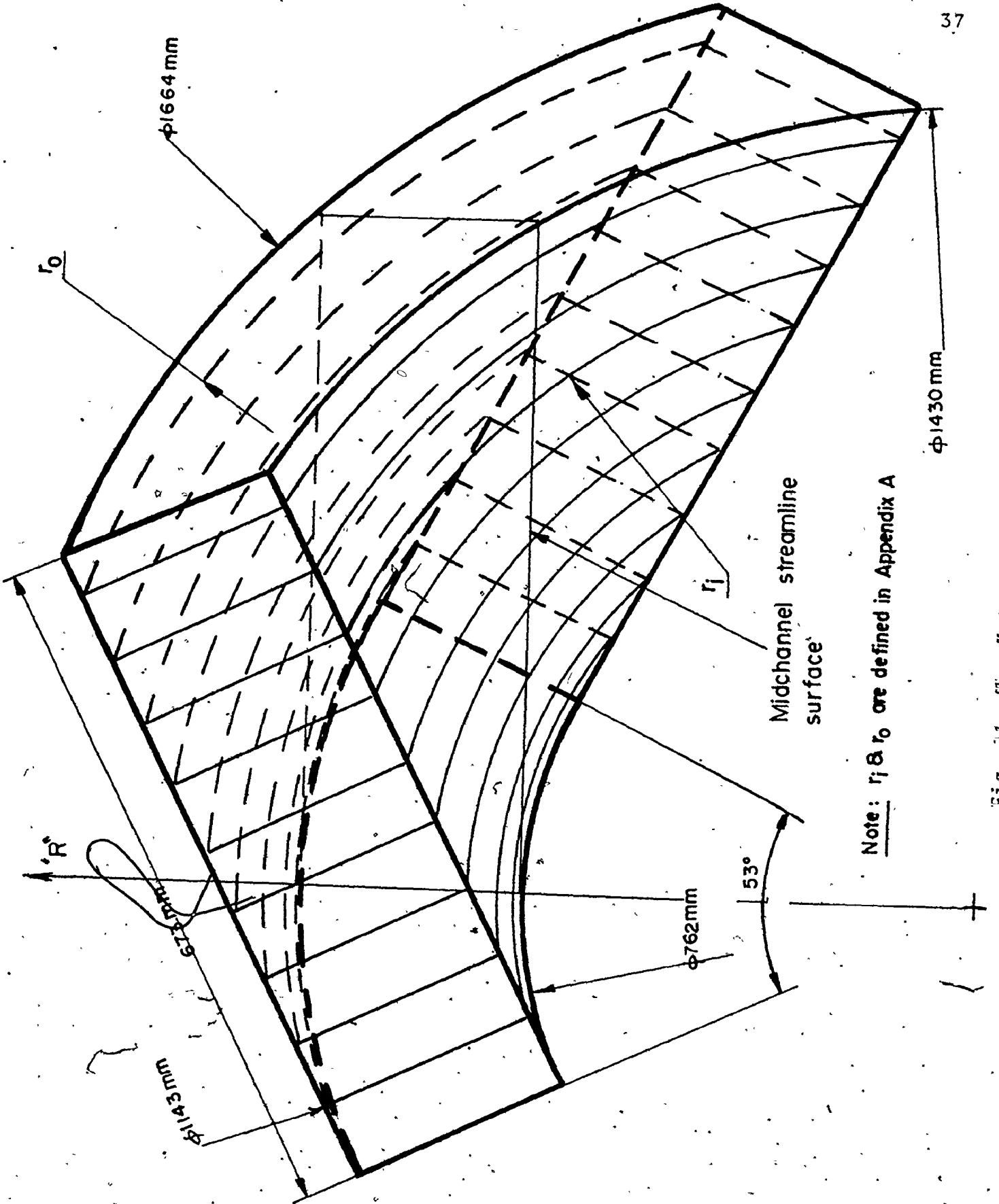
Fig. 2. The Inlet Section

3.3   The Test Section

The cascade test section, as shown in Fig. 15 to
17 was a 45° segment of an annulus with an inner radius
of 381 mm, an outer radius of 571.5 mm and a length of
193.5 mm.   The annular section consisted mainly of three
blade passages (15° each), designed with the object of
providing the proper working conditions in the center blade
passage, within which the measurements were to be made.
The geometrical parameters of the annular cascade section
are given in Table 1.   The test section consisted of the
blades and the annular walls.

3.3.1   The Blades

The profile of the blades selected for testing was
cylindrical and of the "flat-back" type in which the
region of the blade suction surface downstream of the throat
was flat (Fig. 18 and 19).   This blade profile was designed
by Malhotra [37] and used recently by Stannard [38] for
two dimensional testing at high pressure ratios.   Four
blades were manufactured by the Division of Mechanical
Engineering, National Research Council at Ottawa.   Two
blades which constituted the center blade passage were made
out of clear acrylic plastic, and the other two, used as
side walls, were made out of aluminum.   After the blades were
instrumented (Chapter 4), the end walls were contoured
using a numerically controlled milling machine in the

Fig. 15 Overall View of Test Section
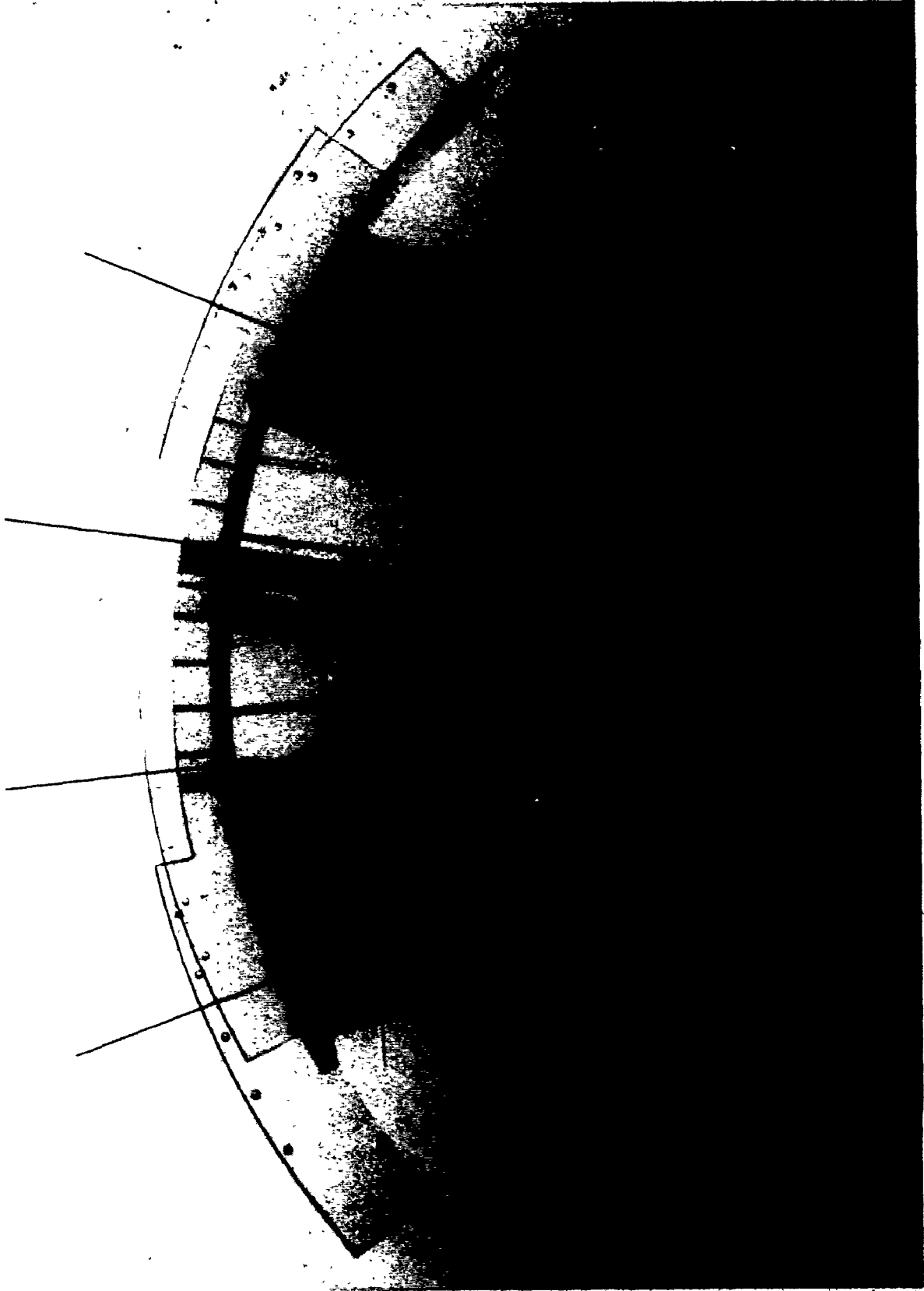
Fig. 16 Test Section Leading Edge
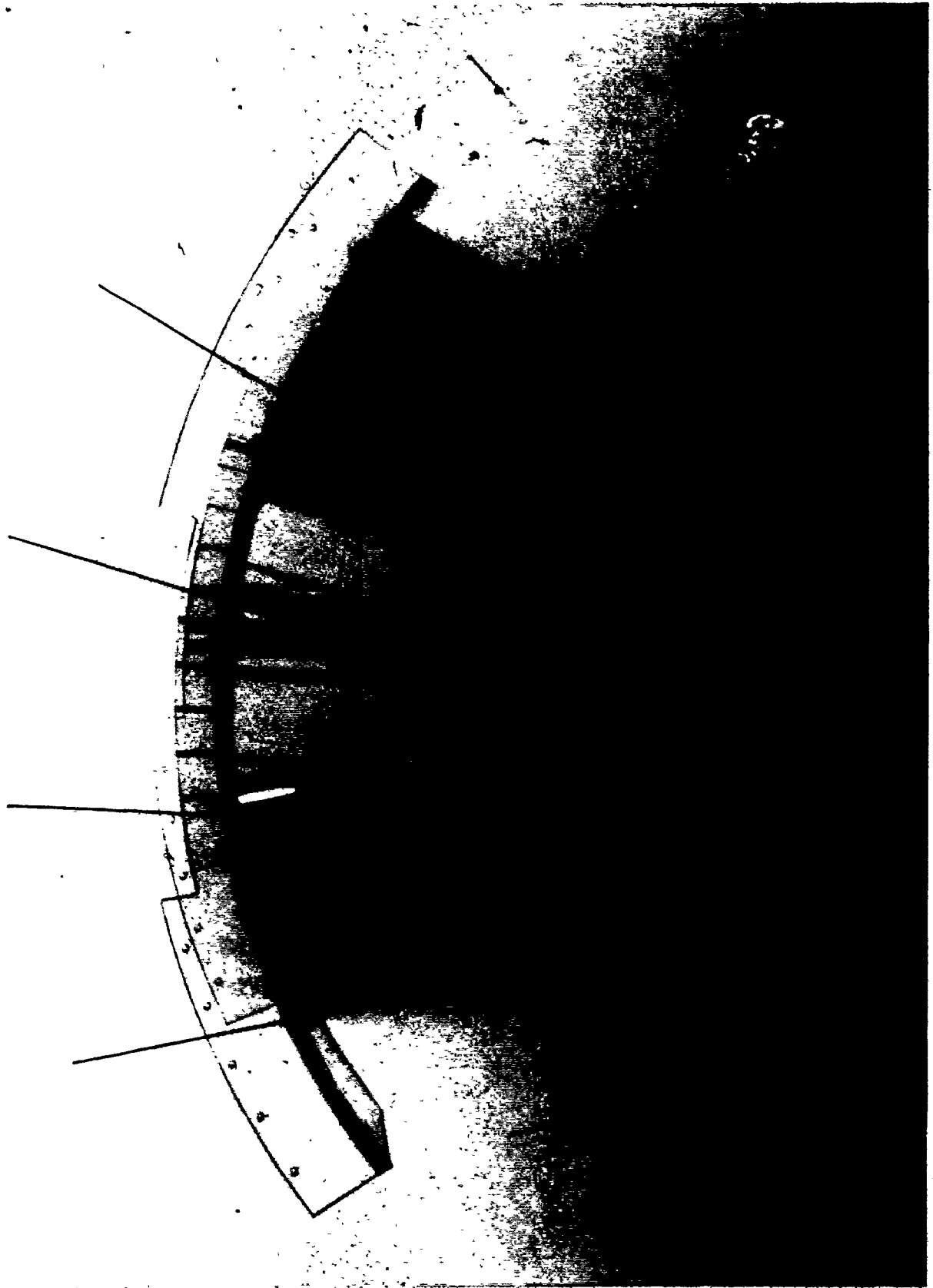
Fig. 17 Test Section Trailing Edge

Table I

Geometrical Parameters
of the Rig

Middle diameter to blade height ratio	5.0
Pitch to chord ratio at the middle diameter	0.66
Blade aspect ratio	1.0
Blade axial chord	188.5 mm
Blade turning angle	$128^{\circ}30'$
Blade inlet angle	64°
Blade exit angle	64.5°
Blade Zweifel lift coefficient	1.0

$$\{C_{LZ} = 2 \cos^2 \alpha_m \frac{S}{C}(\tan \alpha_1 - \tan \alpha_2)\}$$

Suction Surface

166mm

Trailing Edge (T.E.)

25°30'

Pressure Surface

Leading Edge (L.E.)
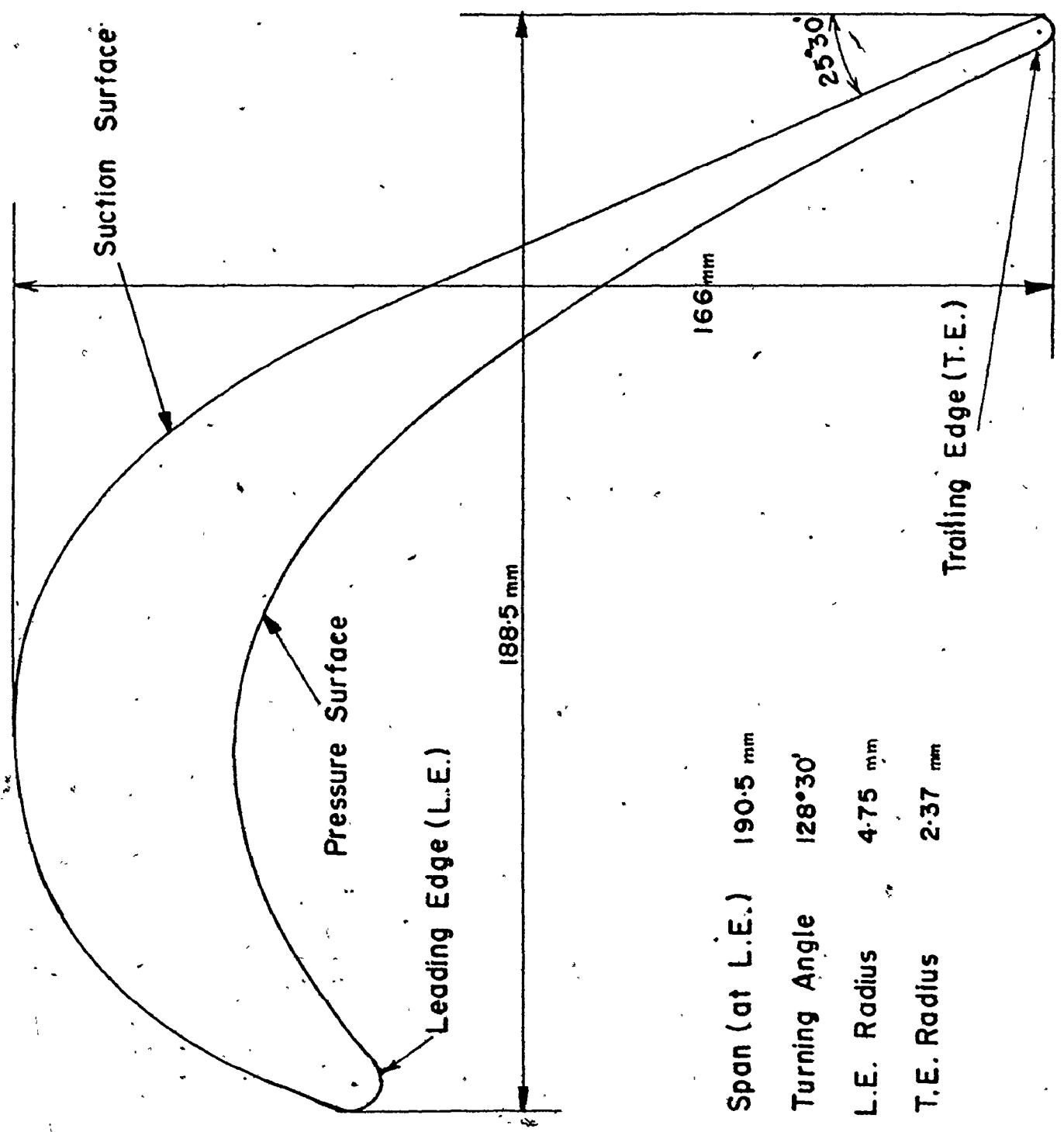
188·5 mm

Span (at L.E.)	190·5 mm
Turning Angle	128°30'
L.E. Radius	4·75 mm
T.E. Radius	2·37 mm

Fig. 18   The Blade Profile
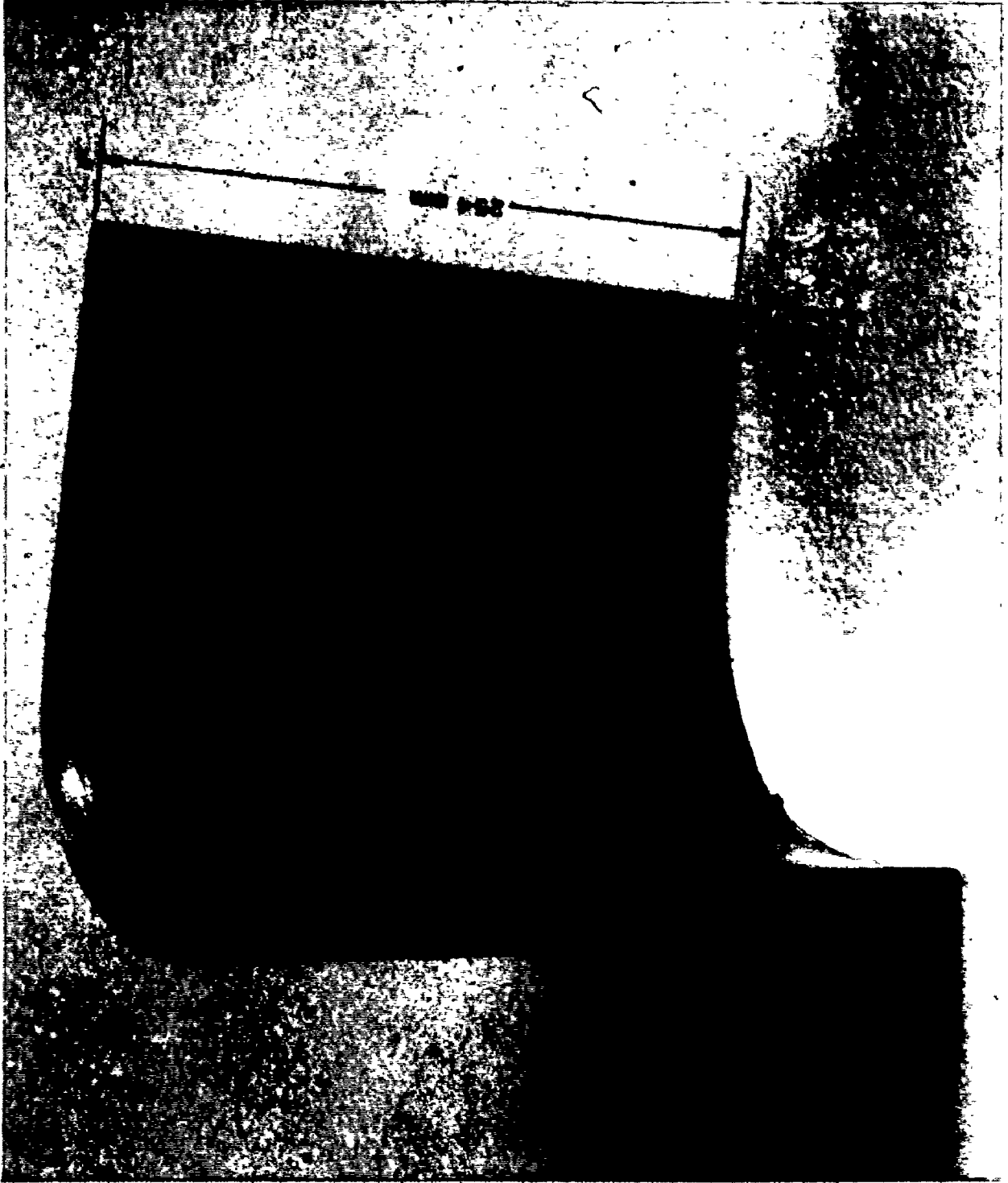
Fig. 19 The Annular Cascade Rig Blade

Canadian Institute of Metalworking at McMaster University.

3.3.2 The Annulus

In order to allow for observation of the flow within the test passage, the annulus walls of the cascade were manufactured from 12 mm clear acrylic plastic. Figs. 20 and 21 show the geometry of the annulus at the leading and trailing edge respectively. The passage center at inlet was chosen as the reference radial direction "R". The positioning of the blades into the annulus was made with the radial directions of the leading edge generatrixes lying in one vertical plane. As a result of this positioning, the trailing edges were tilted about 6.5° from the local radial direction at exit, and had a span of 196.5 mm compared with 190.5 mm at the leading edge.

A computer program was prepared in order to describe the test section geometry, i.e., blade coordinates, blade and wall intersections and passage area at each axial location. The results are given in Appendix B.

3.4 The Exit Section

The exit section was designed to provide a non-gradient stream of potential flow and a constant outlet angle along the radius (64.5°). In order to achieve this design, the exit section walls were formed by the rotation of straight lines inclined at $64^{\circ}30'$ to the trailing edge

Reference radial direction "R"

Radial direction of blades L.E.

Outer flange

Annular tip

1905 mm

15°

ϕ1143 mm

ϕ1270 mm

25°

45°

80°

ϕ635 mm

ϕ762 mm

12

Annular root

Inner flange
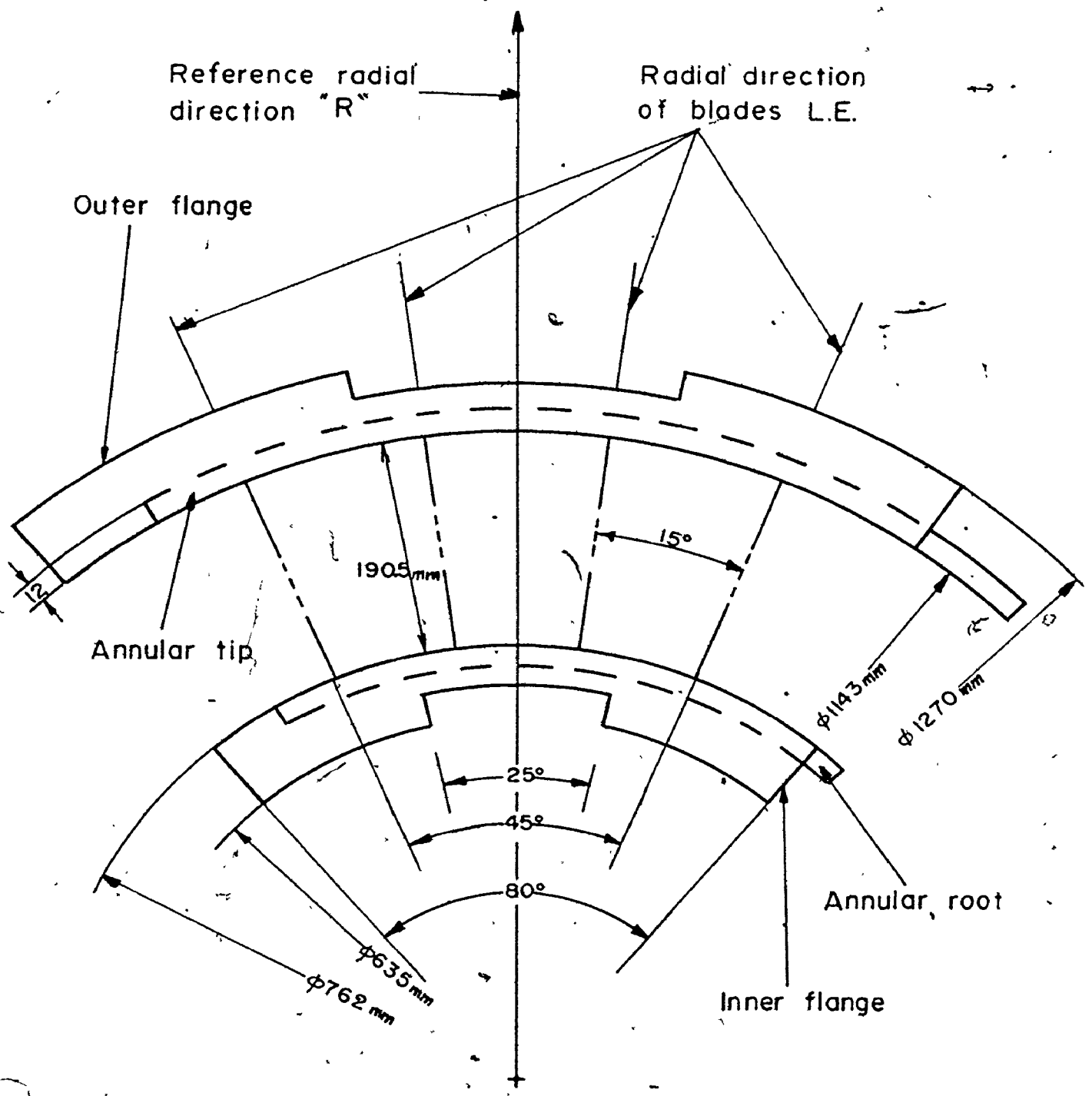
Fig. 20 Test Section Leading Edge Geometry
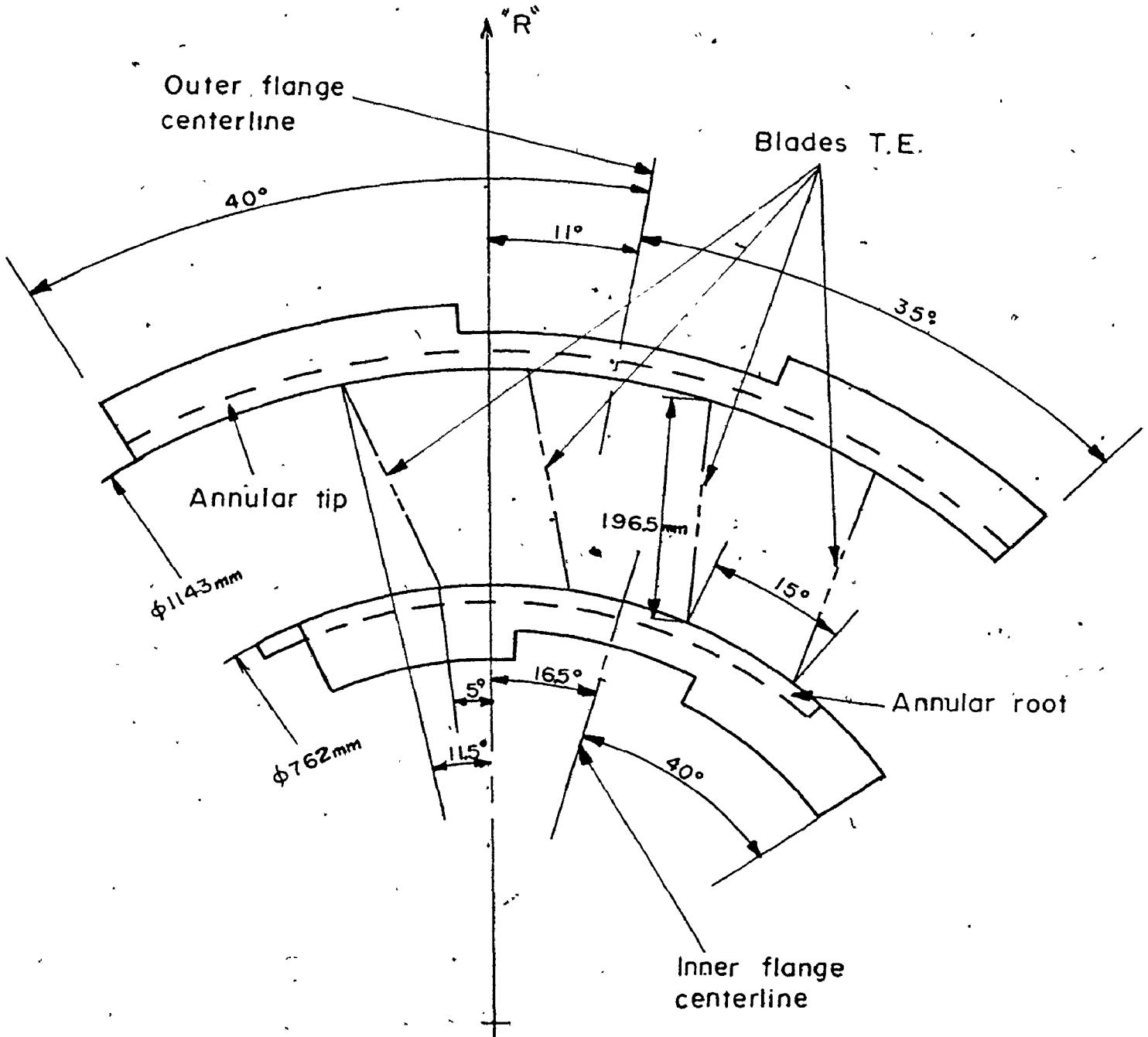
Fig. 21   Test Section Trailing Edge   Geometry

plane (Fig. 22). The length of the exit section was such
as to allow for the attainment of reasonably uniform flow
parameters in the exit plane.

The exit section was manufactured with the same
procedure described for the inlet section, except for the
mould which was manufactured out of high density foam with
the aid of the numerical control machine. However some
difficulties were encountered with the foam construction
method, especially when making the F.R.P. cover. In
order to avoid these difficulties and to reduce time and
cost, it was decided to construct the inlet plug (manufactured
after the exit plug) out of wood by a pattern-maker (Sec.
3.2).

3.5   The Air Supply

Air was supplied by means of a Sheldon XB-19
exhauster fan capable of delivering 10920 c.f.m. of air
against a 6 inch static head of water at 1282 r.p.m. and
18.6 B.H.P. The prime mover was a Greenwood and Batley
steam turbine producing 20 H.P. at its maximum speed of
3000 r.p.m. The steam turbine was selected as the motive
power due to the availability of the power transmission
equipment and as experience had shown that it was capable
of providing a nearly constant fan speed with variations
less than 1% over runs of six hours duration. The fan speed was
controlled by means of a Heenan and Froude water brake dynamometer
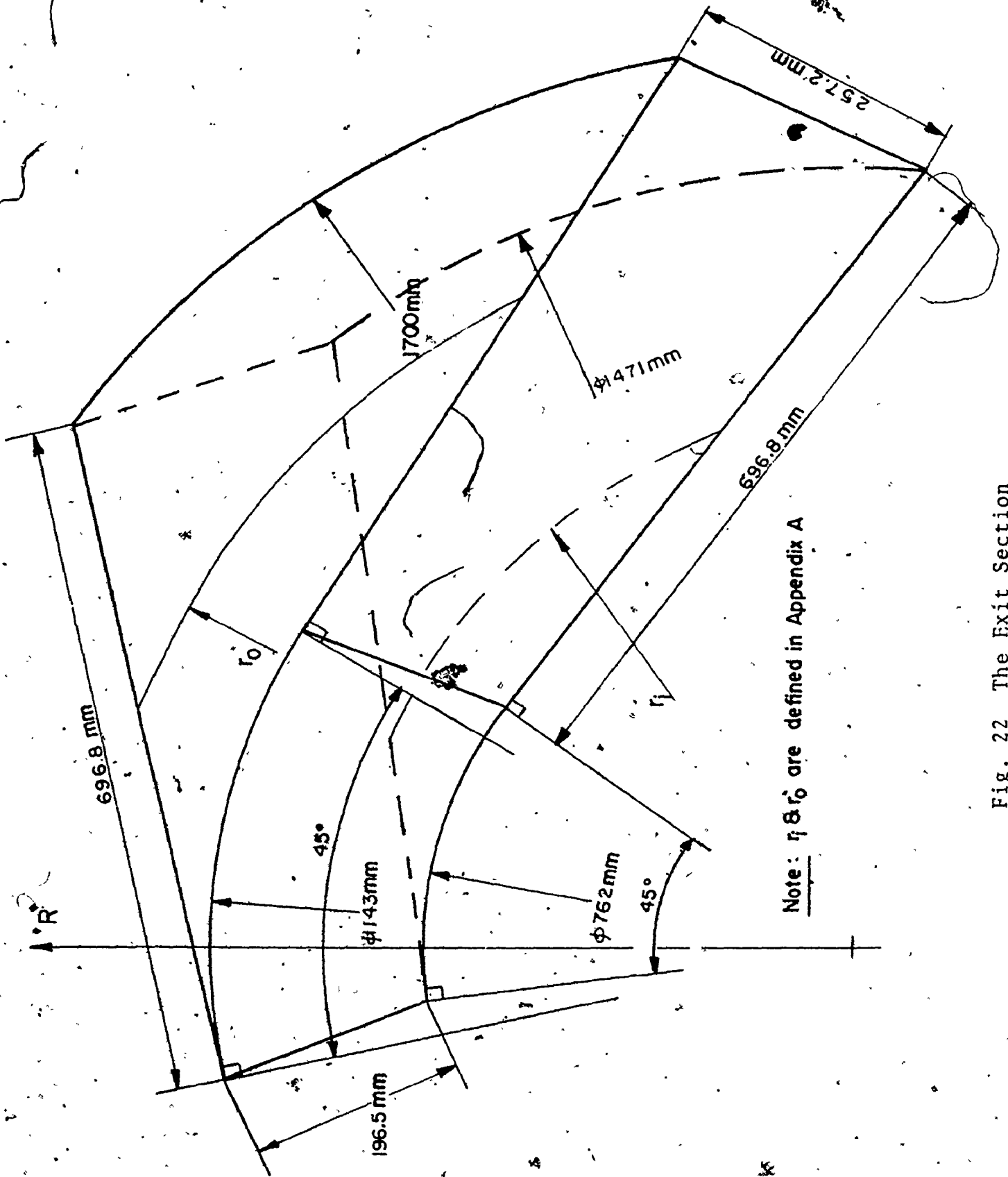
Note: r_i & r_o are defined in Appendix A

Fig. 22 The Exit Section

directly coupled to the turbine. To provide for a more efficient operation of the fan a straightener section with a by-pass control was fitted to the fan inlet. Due to floor space limitations, a sheet metal 90° bend was installed between the straightener and the plenum chamber. The plenum chamber (4x5x4 feet) provided the connection between the bend and the exit section of the test rig. The provision of the exit section of the test rig into the plenum chamber side, was made taking into consideration that it was approximately centered with respect to the circular opening provided for the 90° bend (Fig. 85 Appendix A). In order to isolate the test rig from vibrations, due to the power plant and fan, the exit section was connected to the plenum chamber through rubber joints and metal hold-down strips (Fig.86, Appendix A).

CHAPTER 4

INSTRUMENTATION

In analysing the flow through a blade passage, the primary requirements are to define the static and total pressure fields within the passage and to measure or calculate the flow velocity and direction. Further information which tends to show global effects can often be obtained using flow visualization techniques.

The instrumentation provided for the three dimensional test rig can be divided into the following areas:

1. Instrumentation of the blade passage.

2. Instrumentation for mainflow traverses upstream and downstream of the cascade.

3. Instrumentation for boundary layer traverses upstream and downstream of the cascade.

4. Flow visualization instrumentation.

4.1 Blade Passage Instrumentation

A total of 130 static pressure taps were installed in the blades and annular surfaces forming the center blade passage. Some aspects of the blade passage instrumentation can be seen in Fig. 15. Fig. 23 defines the axial locations of the blades and annular walls static pressure taps.
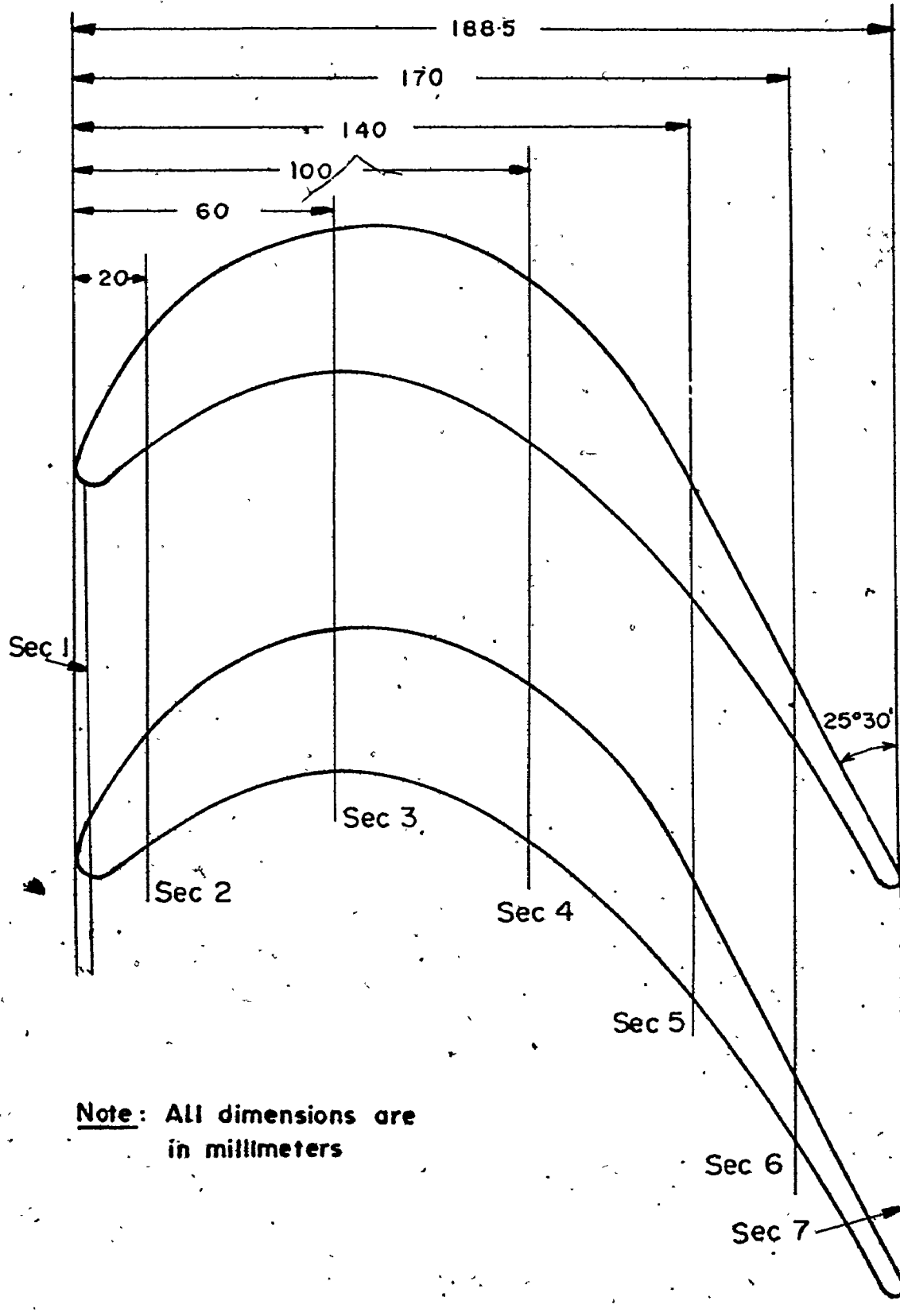
Fig. 23 Test Section Measuring Stations.

4.1.1 Blade Instrumentation

Static taps, 1 mm diameter, were drilled at the
different measuring sections, perpendicular to one blade
pressure surface and the next blade suction surface
respectively according to the radial ordinates given in
Figs. 24 and 25. The first measuring section, positioned
so that the tap was installed on the blade leading edge,
served for measuring the total pressure at the cascade inlet.
The next five sections permitted the measurement of the
pressures over the blade surfaces. The static pressure
taps in sections 1 to 5 were then communicated to the root
or tip surface of the blade through larger holes of 3.7 mm
diameter (Sec. A.A, Fig. 24). Stainless steel tubes
(50 mm long) were press fitted in each of these holes
through corresponding holes drilled in the annular walls.
At section 6, due to the small thickness of the blades,
the pressure taps were communicated with grooves milled into
the back of each blade surface. Hypodermic stainless steel
tubes with a 1 mm diameter hole facing the pressure tap were
bent, as shown in Sec. B.B, Fig. 25, and then cemented in
the grooves. The surface of the blades was then refinished
to its original contour.

4.1.2 Annulus Instrumentation

The angular positions of the static pressure taps
for the annular root and tip surfaces are shown in Fig. 26.
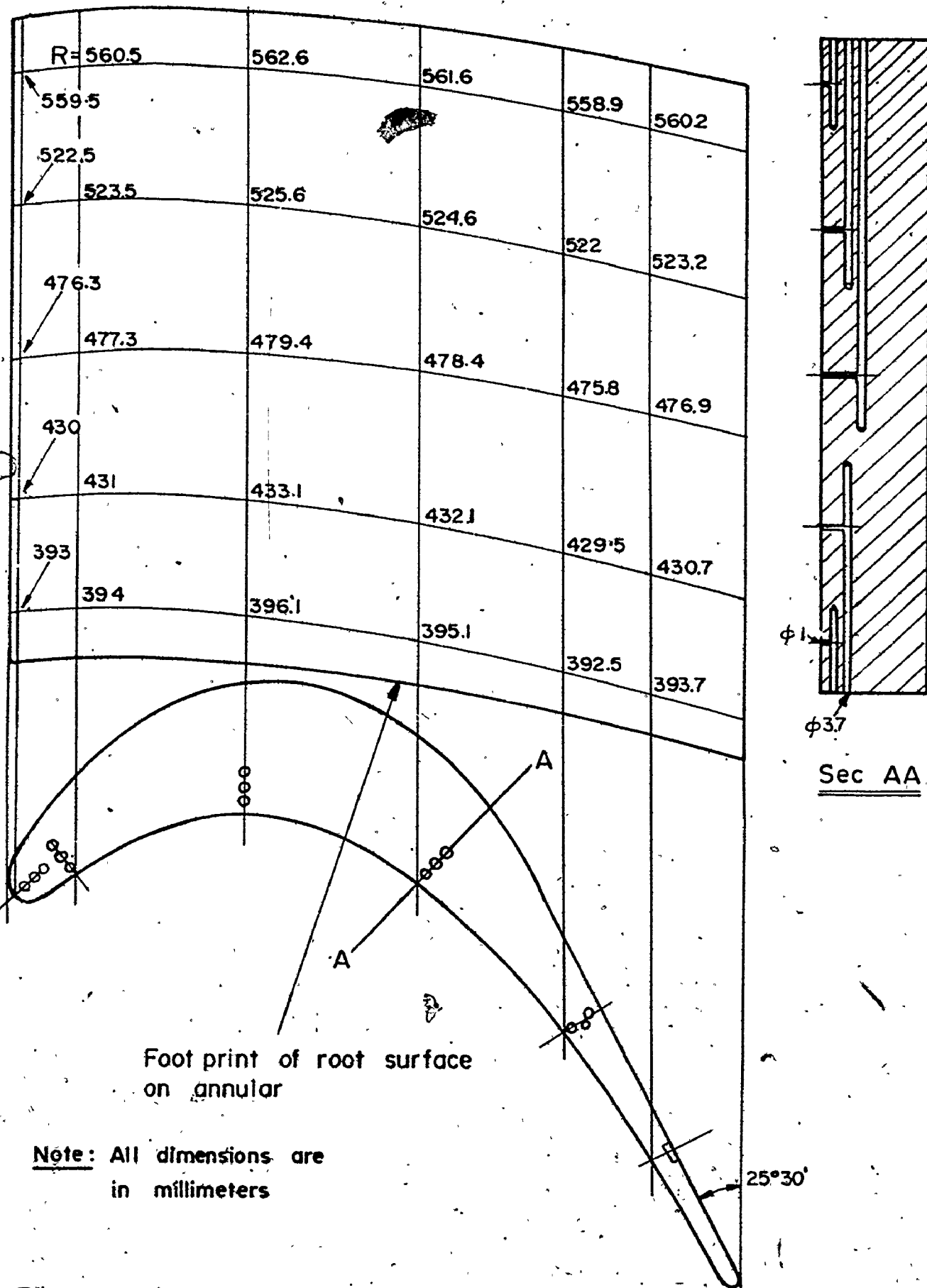
Fig. 24 Blade Pressure Surface Instrumentation

Note: All dimensions are in millimeters

Sec BB
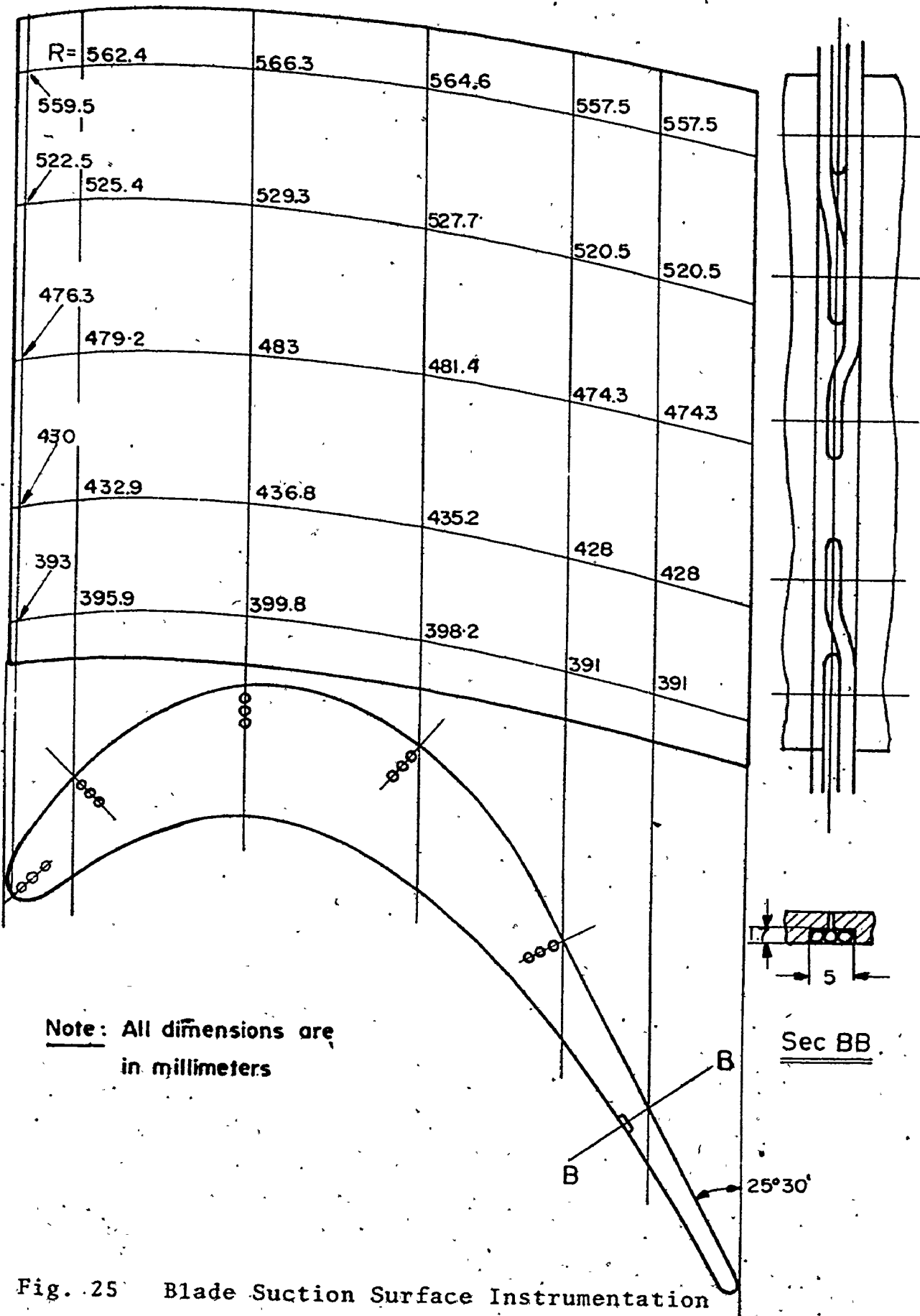
Fig. 25   Blade Suction Surface Instrumentation
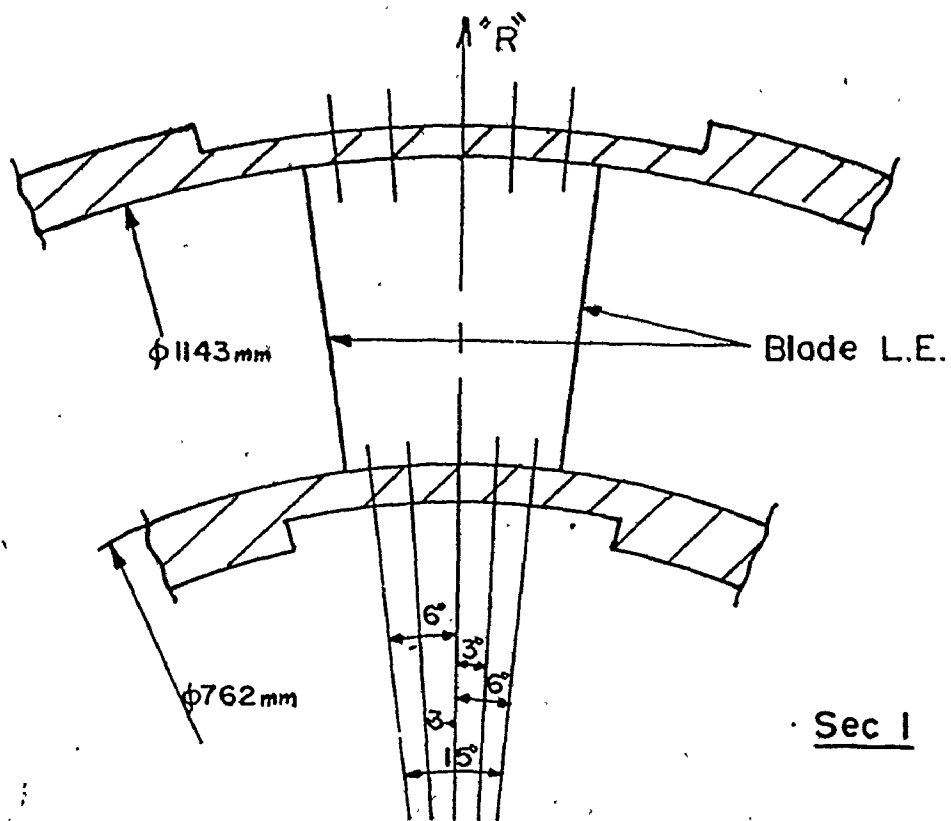
Note: Please refer to Fig. 23 for the axial locations of sections 1 to 7)
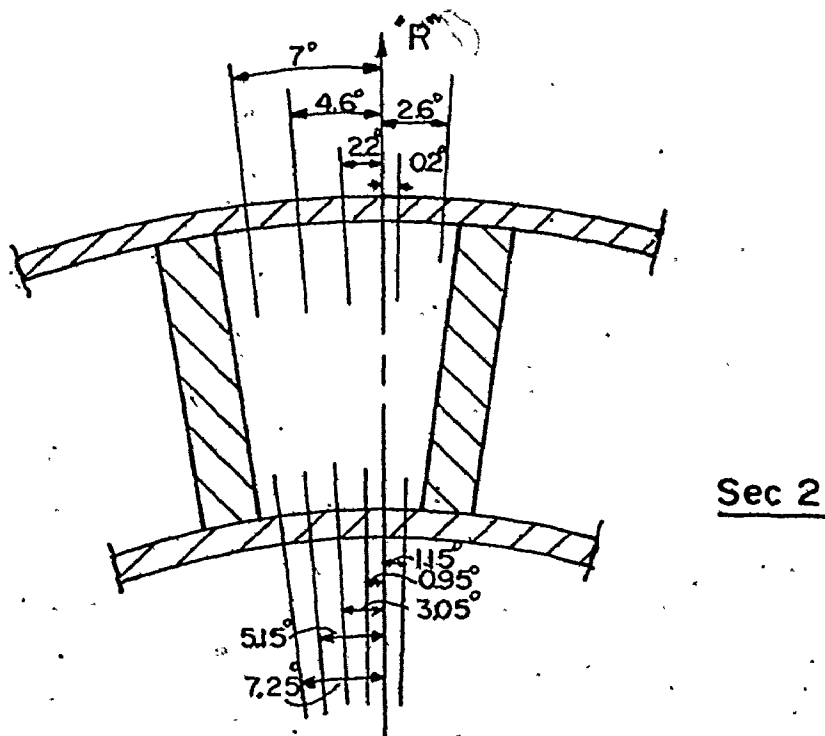
Fig. 26(a) Annular Wall Instrumentation
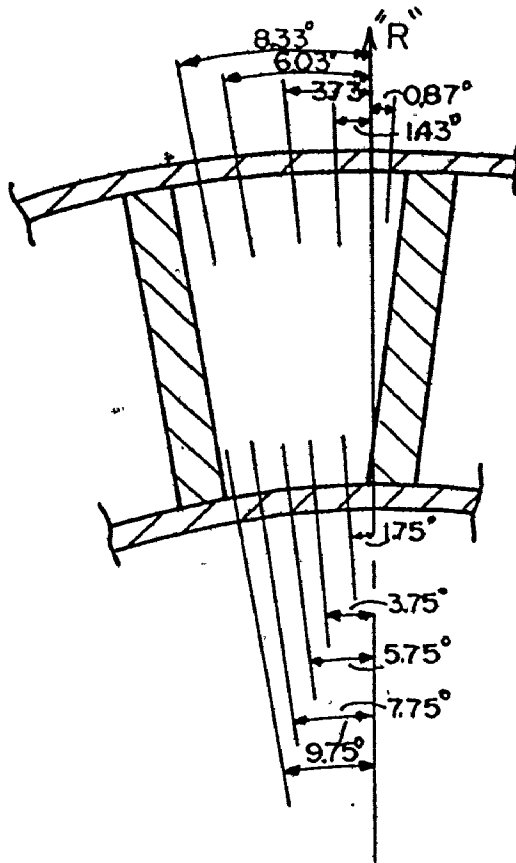
Sec 3

Sec 4

Fig. 26 (b)

Sec 5

Sec 6

R

18.64°
17°
14°
11°
8°
5°
3.64°

φ1143mm

9.34

B

Blade T.E.

10.5°
13.5°
16.5°
19.8°

B

φ762mm

22.5°
24.34°

Sec 7

0.5mm

0.25mm

45°

φ3.17mm

12.7mm

6.4mm

Sec AA

38.1mm

φ0.5mm

15.9mm
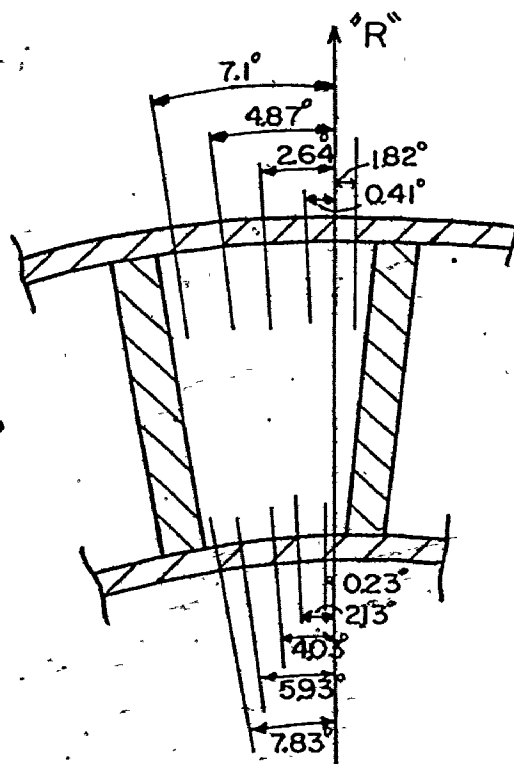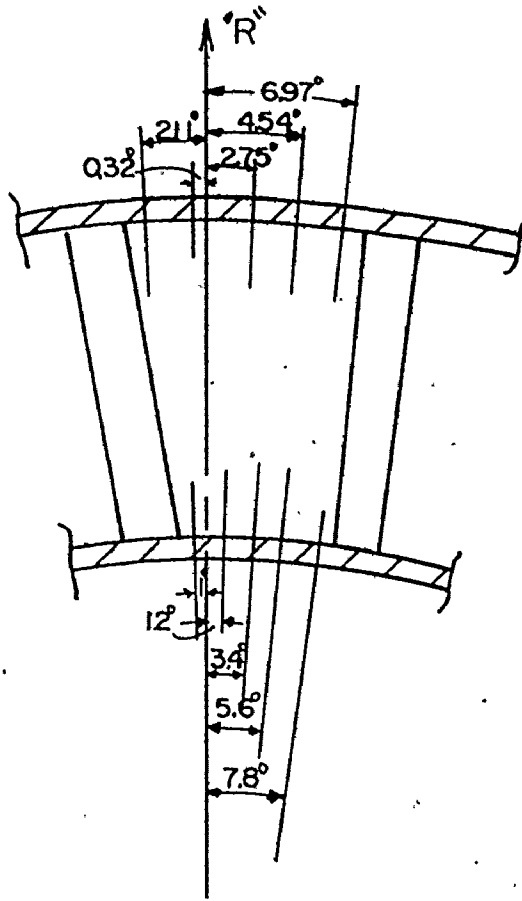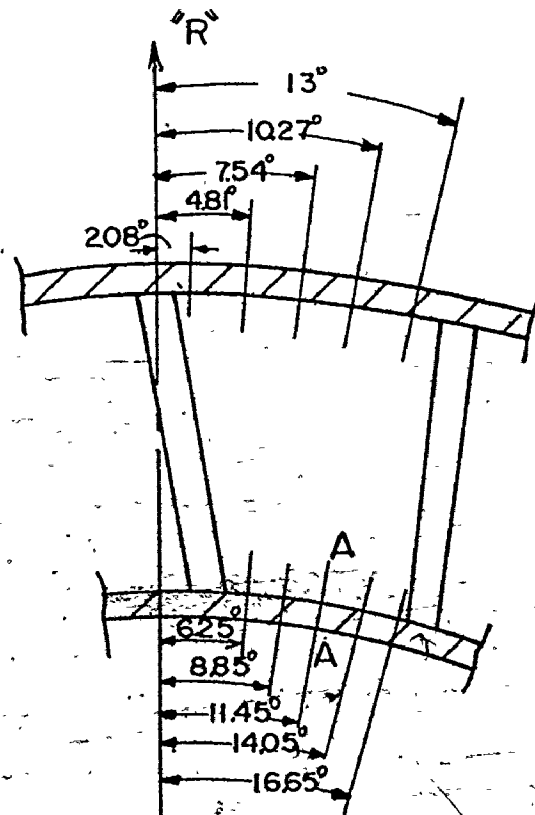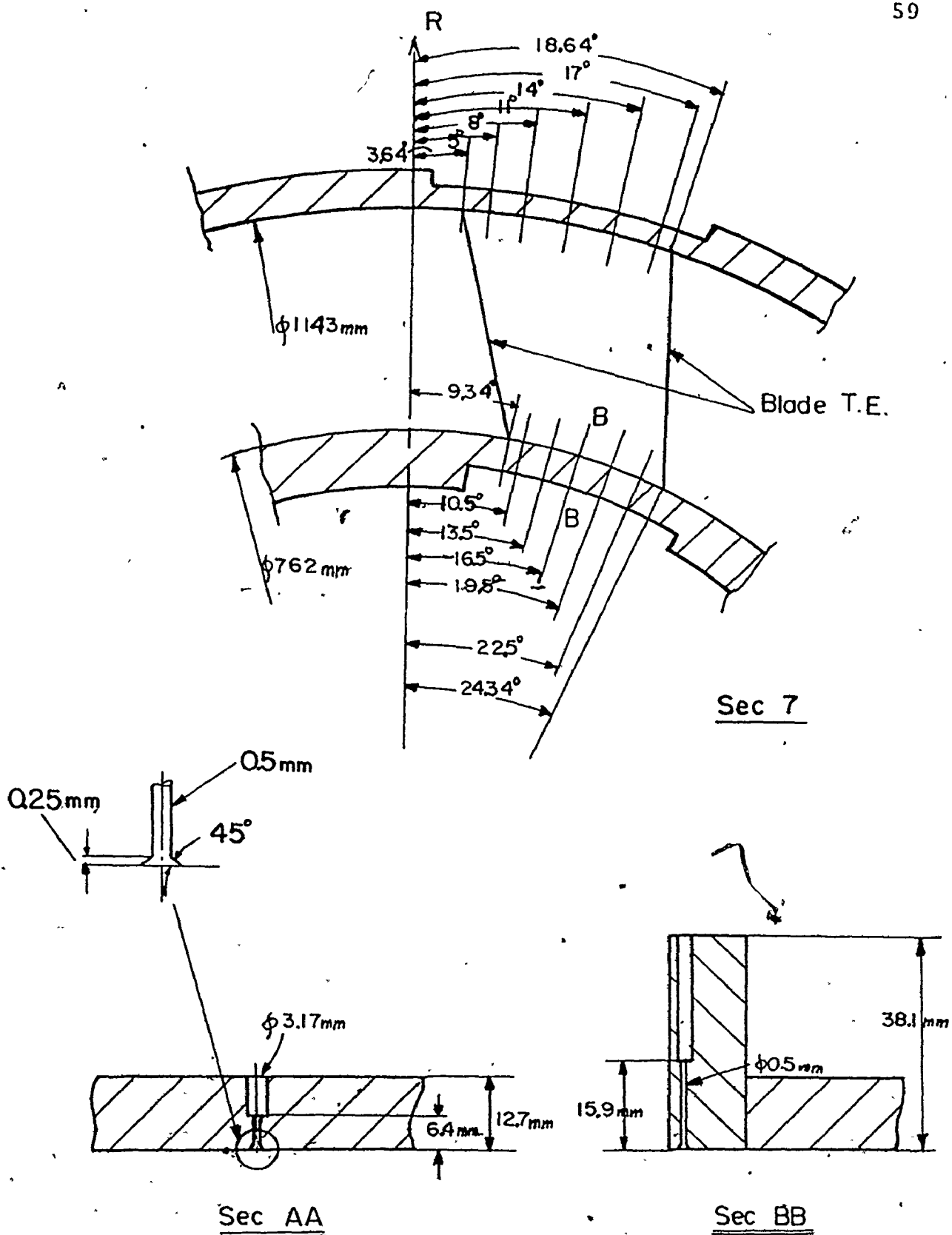
Sec BB

Fig. 26 (d)

All the locations are given with respect to the reference radial direction at the leading edge plane. The pressure taps provided for measuring sections 2 to 6 are shown in Sec. A.A of Fig. 26. Sec. B.B shows the tap installation at the leading and trailing edge plane.

All the stainless steel tubes, projecting through the cascade annular walls, allowed for a simple connection between the static pressure taps and a multitube water manometer*. The manometer capacity was limited to 36 tubes, while as stated previously, a total of 130 readings were necessary to define the pressure distribution within the blade passage. Therefore a scanning board was designed so that one could make the measurements in four stages. These included 35 readings on each of the annular walls and 30 readings on each of the blade surfaces. The steady state condition achieved by the power source permitted the measurement to be carried out in a continuous fashion with a negligible change in the flow conditions.

4.2 Main Flow Instrumentation

The main flow field measurements were made using a United Sensor three dimensional probe. The probe had a prism shaped sensing head with a diameter of 1/8 inch to

---

* Model 10397 T.E.M. Instruments, Crawley, England.
** Model DA-125

facilitate its entry into the test rig. The main body of the probe was made of 1/4' inch stainless steel, tube for added strength and rigidity. The probe, shown in Fig. 27, was designed with five sensing taps. The first was a forward facing hole which measured total pressure accurately to $\pm$ 1/2% over an angular range of $\pm$ 10°. Two lateral pressure taps were used for measuring static pressure and yaw angle, and two pressure taps above and below the center hole were used for the measurement of pitch angle up to $\pm$ 40°. Flow measurements with the three dimensional probe were performed by rotating the probe axis until the pressure indicated by the side holes were equal. The yaw angle was then measured from a suitable reference direction. The center hole, the two pitch holes and one of the yaw hole pressures were then recorded. By means of the calibration curve supplied by the manufacture (Appendix C), the pitch angle, total pressure and static pressures were calculated. It should be noted with reference to the calibration chart that the total pressure reading was insensitive to pitch angle variation up to $\pm$ 30°.

The traversing gear used, shown in Fig. 27, allowed both a linear and a rotation motion. The linear motion with a range of 250mm and an advance of 0.05 inch per revolution was used to traverse the flow radially. A turntable with a 360° travel and an accuracy of $\pm$ 0.2° was used to measure the yaw angle. In order to traverse the main flow upstream and downstream
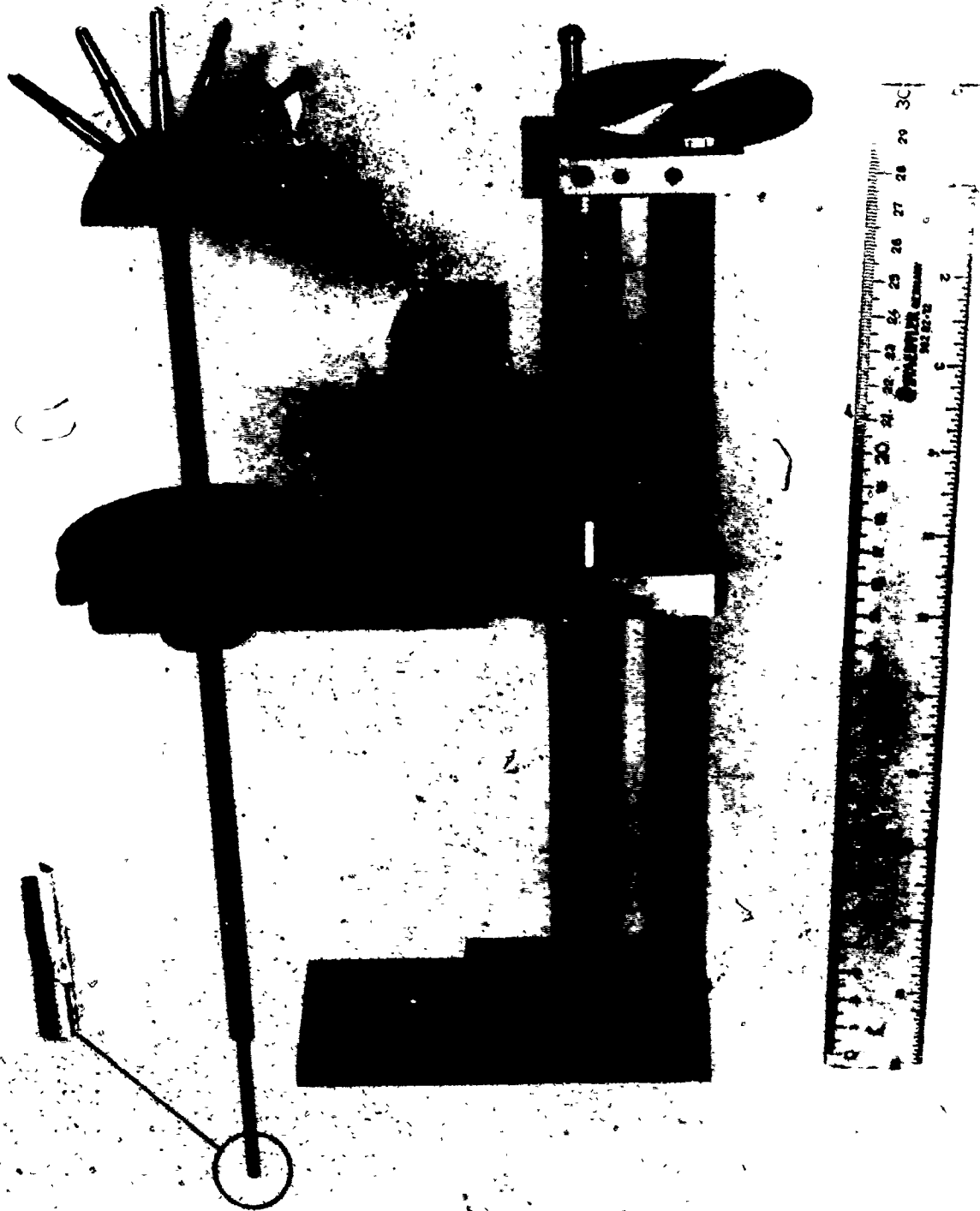
Fig. 27 The Traversing Gear and the Three-Dimensional Probe

of the cascade, the traversing mechanism was mounted on the sliding annular segment in the inlet and exit section flanges (See Figs. 83 and 84, Appendix A). By moving the sliding segment, the flow parameters could be traversed in the circumferential direction up to $\pm$ 25° with a 0.5° increment. Pressure measurements were made by means of three micromanometers having oil as the working fluid (specific gravity 0.826), which could read accurately to .001 inch of oil.

4.3 Boundary Layer Instrumentation

Special boundary layer probes were designed and constructed in order to measure the boundary layer thicknesses on the inner and outer walls, upstream and downstream from the cascade. Fig. 28 shows the probes which were made by sliding small hypodermic stainless steel tubes into each other to obtain the desired reduction in area and shape without sacrificing rigidity. The tip of each probe was flattened and the crank-like design of the probe head was used to reduce stem and support effects on the measurements. Because of the wall effect, boundary layers are far more sensitive in this regard than free stream flows. Pressure taps were drilled in the wall of the inlet section in the same plane as the tip of the probe to measure wall static pressures. The total and static pressures were combined to yield the boundary layer velocity profile. For the exit

Note: All dimensions are in millimeters

0.61

1.35

1.067 O.D.
0.686 I.D.

1.473 O.D.
1.067 I.D.

2.108 O.D.
1.60 I.D.

Boundary Layer Location	L	D	1_1	1_2	1_3
Inner wall	190.5	3.04	9.0	8.0	46.0
Outer wall	304.8	6.40	9.0	8.0	46.0
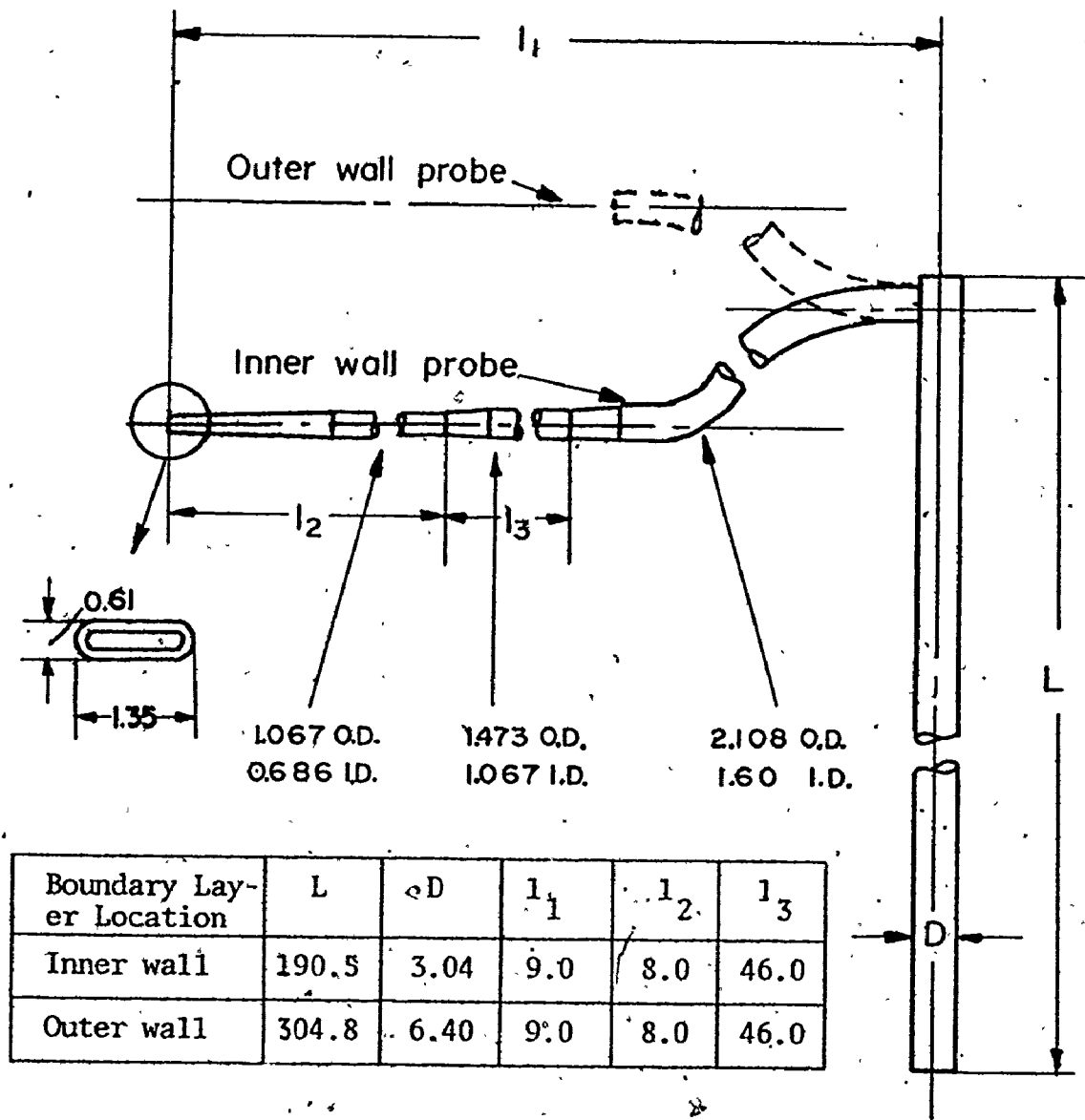
Fig. 28 Boundary Layer Probe

section, static taps in section 7 (Fig. 23) were used
for this purpose. The boundary layer traverses were
made employing the same traversing mechanism and mano-
meter used for the main flow measurements.

4.4   Flow Visualization Instrumentation

The flow visualization was performed by means of
a low speed smoke probe (Fig. 29) designed by the Low
Speed Aerodynamic Laboratory at The National Aeronautical
Establishment in Ottawa (Ref. 39).

The probe was designed so that two jets one of
anhydrous ammonia and the other of sulphur dioxide gas
were emitted from the probe at approximately 90° to each
other. The gas jets mixed in the free air just beyond the
probe tip to produce a dense white cloud of ammonia sulphite
smoke. This smoke generator was easily controlled and
adjusted on or off by needle valves installed in the gas
lines. The probe was installed in the same position
used for mainflow and boundary layer instrumentation at the
cascade inlet. Due to the toxic nature of the produced smoke,
precautions were taken to adequately ventilate the testing
area.
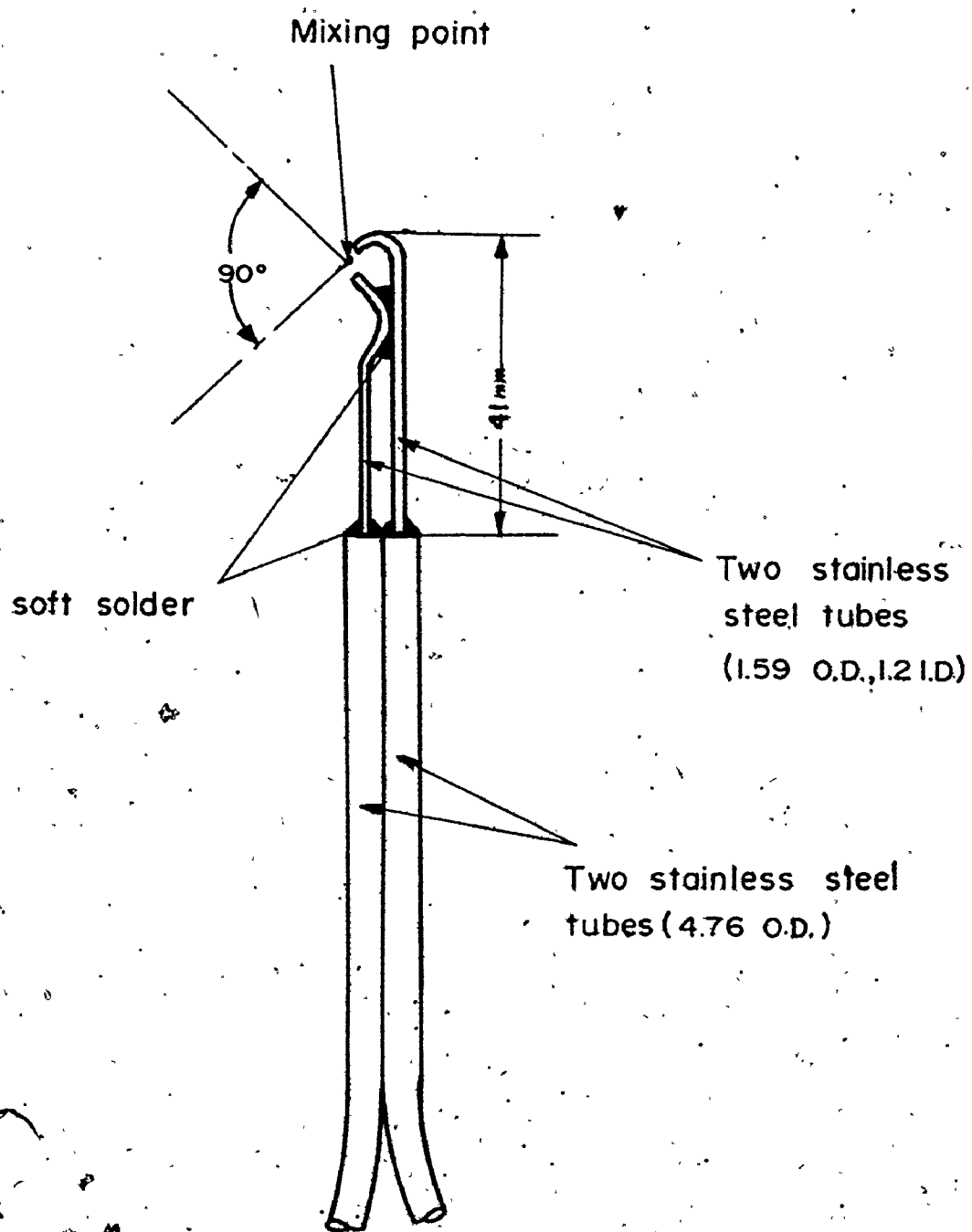
Fig. 29 The Smoke Probe

CHAPTER 5

EXPERIMENTAL PROCEDURE

In this chapter a brief outline of the experimental methods and the scope of the measurements will be given.

5.1 Vibration Tests

The dynamic stability of the annular cascade rig, especially at the test section (made of acrylic plastic), was analysed at different fan speeds. Using a dynamic pick-up coupled to a microphone amplifier and to a Fourier Analyser, it was possible to measure the frequency and amplitude of vibrations at the test section in the x, y and z planes. In the original installation it was found that the amplitude of vibration in the axial direction was about 0.19 mm at a fan speed of 700 r.p.m. The vibrations in the rig appeared to be periodic in nature and to be generated by some flow instability in the system. This flow induced vibration was traced to the 90° bend downstream of the plenum chamber. Further investigation showed that, by allowing some air to flow in the by-pass located at the entrance to the fan, the amplitude of vibrations was reduced by a factor of 5.7 for the same general operating conditions. With this simple adjustment the operation of

the cascade rig was very stable at all available test speeds.

5.2 Cascade Inlet Operating Speeds

With the by-pass in operation, the cascade inlet velocity range was 23 m/s to 47 m/s corresponding to a fan speed range from 600 to 1300 r.p.m. These operating speeds gave a R_N based on the blade chord of 3×10^5 to 6×10^5. It should be noted that, in the technical literature the range of R_N for secondary flow investigations is normally between 10^5 and 10^6. Tests showed that the power source and the fan stability were such that for continuous runs of six hours duration the fan speed did not change more than 1% with a negligible effect on the inlet flow conditions.

5.3 Inlet and Exit Measuring Stations

The inlet and exit flow conditions were obtained at two traverse stations located at a distance of 27:5 mm upstream and downstream of the cascade test section. It should be recalled that in the present test configuration two sliding-annular segments were provided to perform these traverses (see Appendix A). Figs. 30 and 31 defined the measuring stations, the circumferential traversing locations and the footprints of the leading and trailing edge of the blades in the corresponding measuring stations. Standard practice dictated that the inlet measure-
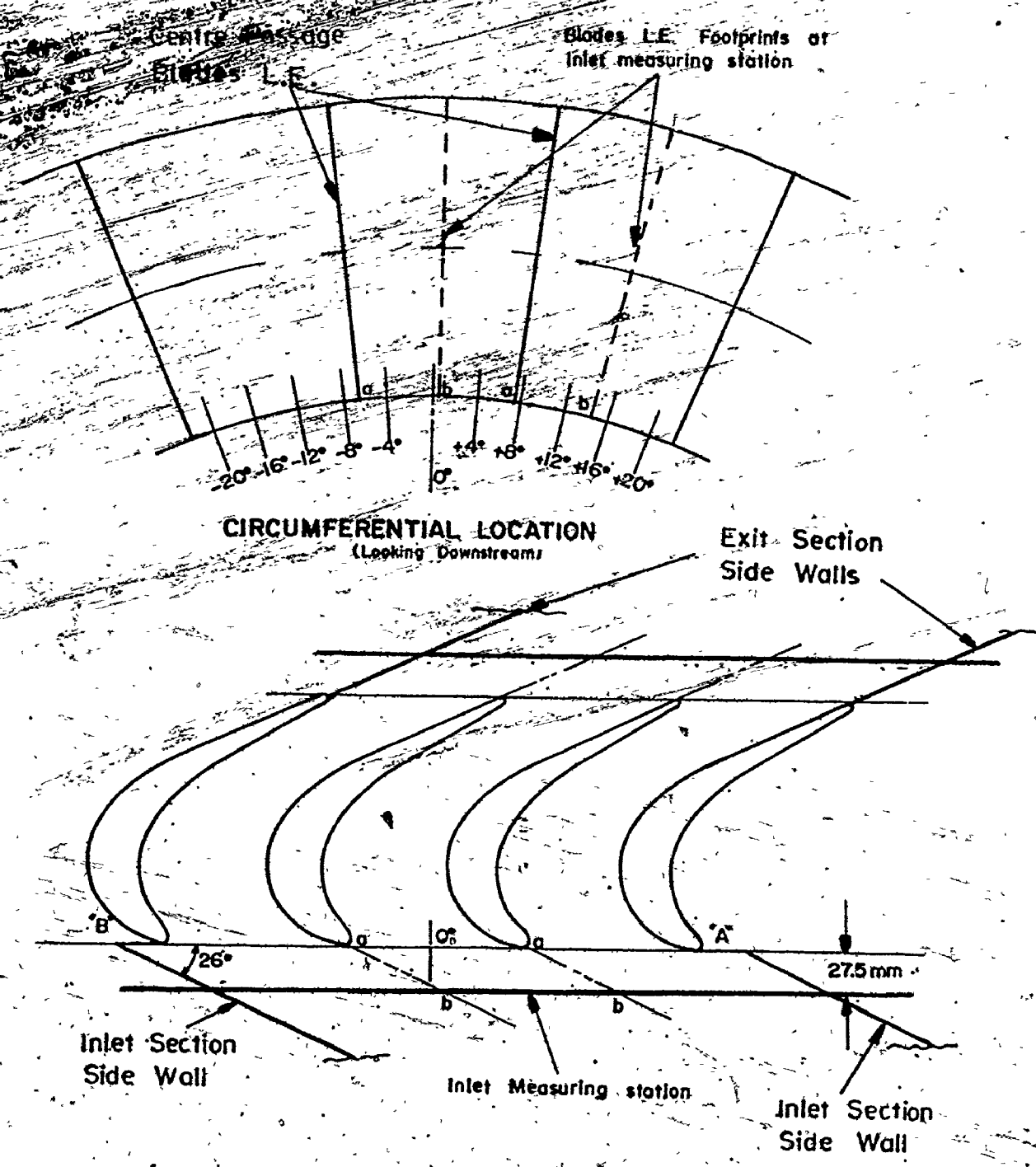
CIRCUMFERENTIAL LOCATION
(Looking Downstream)

Centre Passage
Blades L.E.

Blades L.E. Footprints of
Inlet measuring station

-20° -16° -12° -8° -4° 0° +4° +8° +12° +16° +20°

Exit Section
Side Walls

Inlet Section
Side Wall

Inlet Measuring station

Inlet Section
Side Wall

26°

27.5 mm

Fig. 30 The Inlet Measuring Station

Blades T.E.

Blades T.E." Footprints at Exit Measuring Station

-20° -16° -12° -8° -4° 0° +4° +8° +12° +16° +20°

CIRCUMFERENTIAL LOCATION
(Looking downstream)

25°30'   c   10°   c   d   27.5 mm

Exit Measuring Station
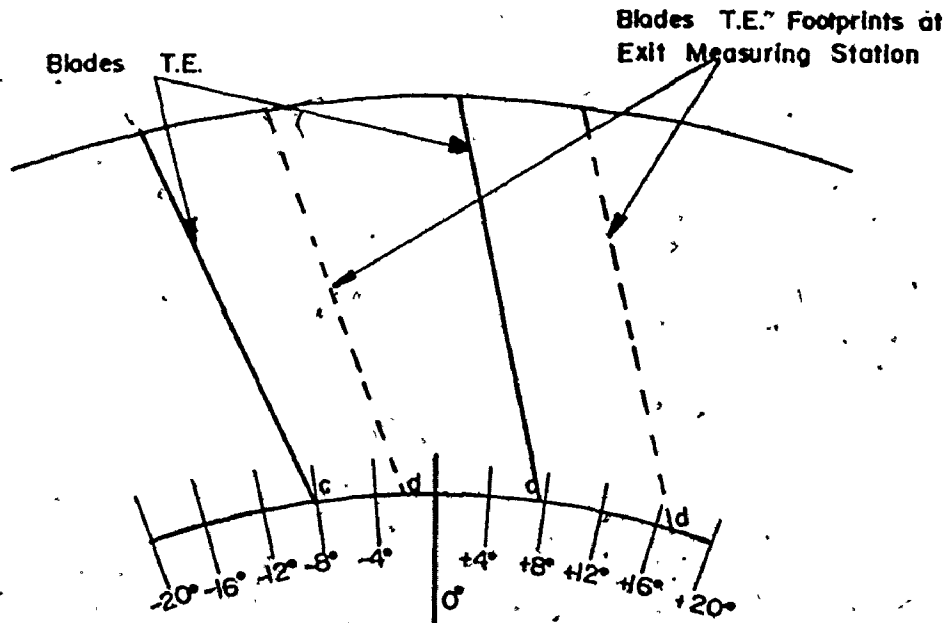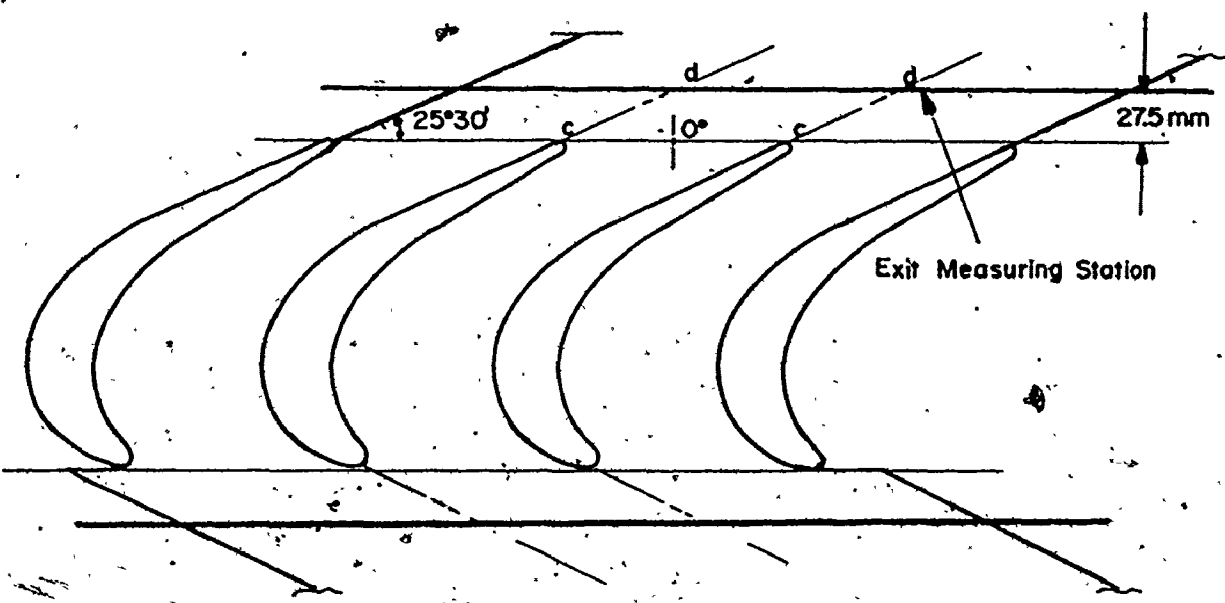
ments should be taken at a distance of at least two leading
edge radii upstream of the cascade (the L.E. radius for
the present cascade was 4.75 mm), or in a region where
the flow was undisturbed by the leading edge effect. The
measuring stations in the present test rig were selected
taking into account the complexity of the geometry of both
the inlet and exit sections. Further intrusion of the
measuring stations into the inlet and exit sections would
have eliminated the possibility of providing a measuring
station which could accurately scan in a radial direction
at a constant circumferential position.

5.4 Scope of the Tests

The annular cascade tests can be summarized as
follows:

(i) For a fan speed of 700 r.p.m., a complete set of
radial and circumferential inlet flow traverses were
obtained in order to define the effect of the leading edge
on flow parameters and to find the optimum inlet conditions
to the center blade passage. This work is described in
Chapter 6.

(ii) The pressure distributions over the center blade
passage which were formed typically of two blades and two
annular surfaces were measured. The results which are given
in Chapter 7 are presented in terms of pressure contours
and pressure variations along both the span and the chord of

the cascade.

(iii) For three different speeds covering the fan operating range, complete inlet and exit main flow, and boundary layer traverses were carried out. The inlet flow parameters were defined and contours of exit total pressure losses and flow angles were derived. The spanwise variations of the exit flow parameters and pressure losses in the cascade were calculated and are presented in Chapter 8.

(iv) The results of flow visualization tests using smoke injected at the inlet measuring station into the cascade are also described in Chapter 8.

CHAPTER 6

DETERMINATION OF THE INLET
FLOW TO THE CASCADE

In any wind tunnel investigation, the quality
of the flow in the working section determines the degree
of confidence which could be placed on the experimental
measurements. This was particularly true in the present
tests since it was known that secondary flow generated by
highly curved turbine blades was very sensitive to inlet
flow conditions. At the entrance to the testing cascade
the inlet flow conditions called for uniform pressure,
velocity and flow angle fields in both the radial and
circumferential directions.

The main objectives of the inlet flow study
presented in this chapter, were twofold:

1.   To determine the optimum inlet conditions utilizing
those experimental measures which have been designed into
the test rig, in order to effect adjustments of the flow
parameters at the inlet section to the cascade.

2.   To define the upstream influence of the blade
leading edges on the circumferential flow field.

Fig. 30 in Chapter 5, defined the inlet measuring
station and the circumferential traversing locations. The
flow yaw angle used in this chapter has been taken to be

the angle between the flow direction and the leading edge plane (i.e., $90^{b}-\alpha$).

The graphical representation of the experimentally measured data in this chapter includes smoothly drawn curves which are considered to represent average values of the parameter at each location.

6.1 Yaw Angle Distribution

With the aid of the three-dimensional probe, traverses were made at different radial and circumferential positions to obtain the yaw angle distribution. In the radial direction the flow angle appeared to vary at most over a range of $\pm 2^{o}$ across the annulus (Fig. 32). In the circumferential direction the yaw angle varied periodically, for all radii as shown in Fig. 33. It could be noticed from this variation that the peaks corresponded to positions traversed across the footprint of the blade leading edges and the valleys coincided with the center of the blade passages. A more complete circumferential traverse of yaw angle is shown in Fig. 34 at midradius. The lower yaw angles measured at a circumferential position of 24° (Point A, Fig. 30) with respect to those measured at a position of -12° (Point B, Fig. 30) were caused by the difference in the geometry of the two side walls.

The leading edge effect on yaw angles was verified by means of a two-dimensional analysis carried out with the
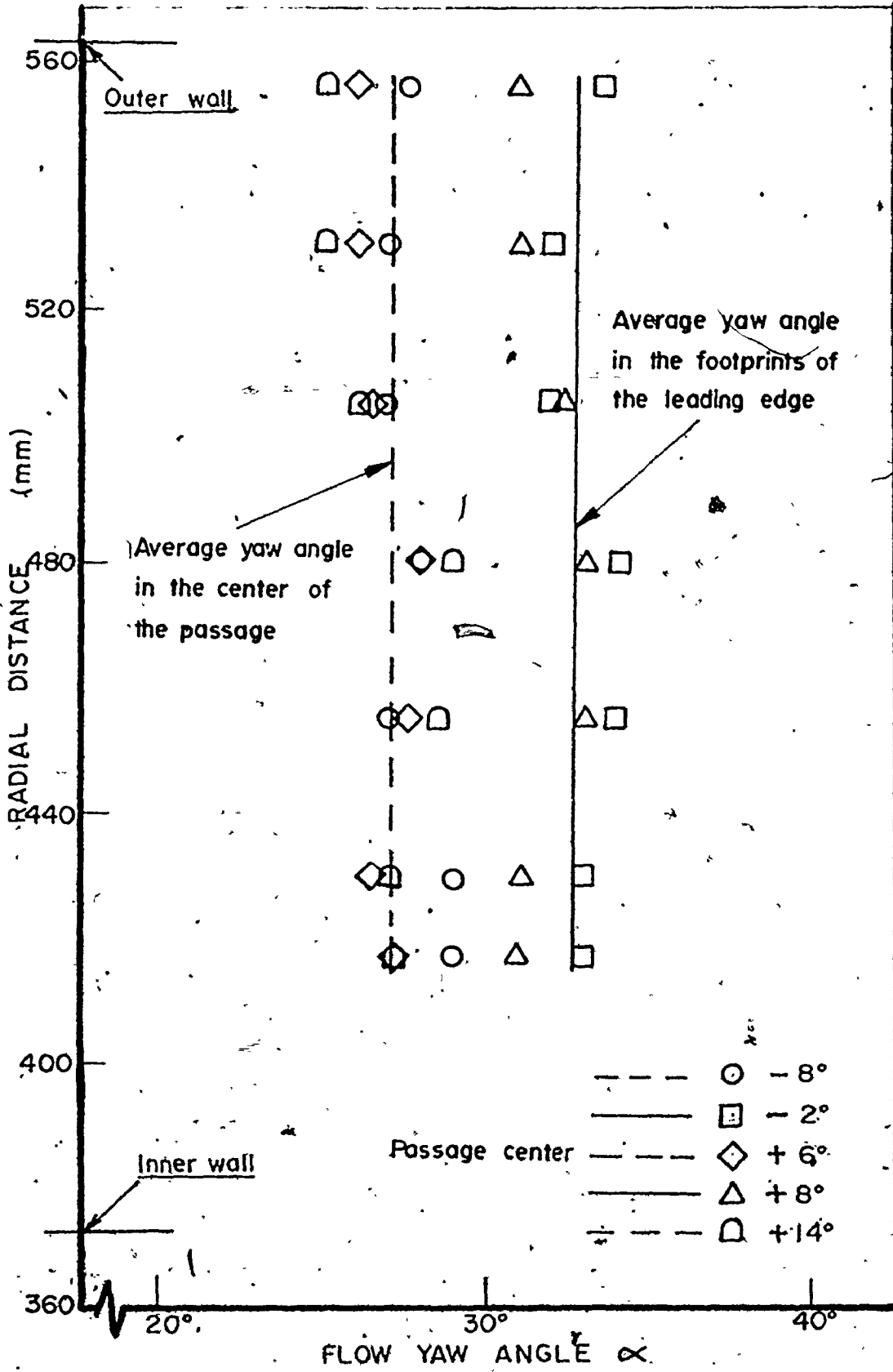
Fig. 32 Radial Distribution of Yaw Angle.
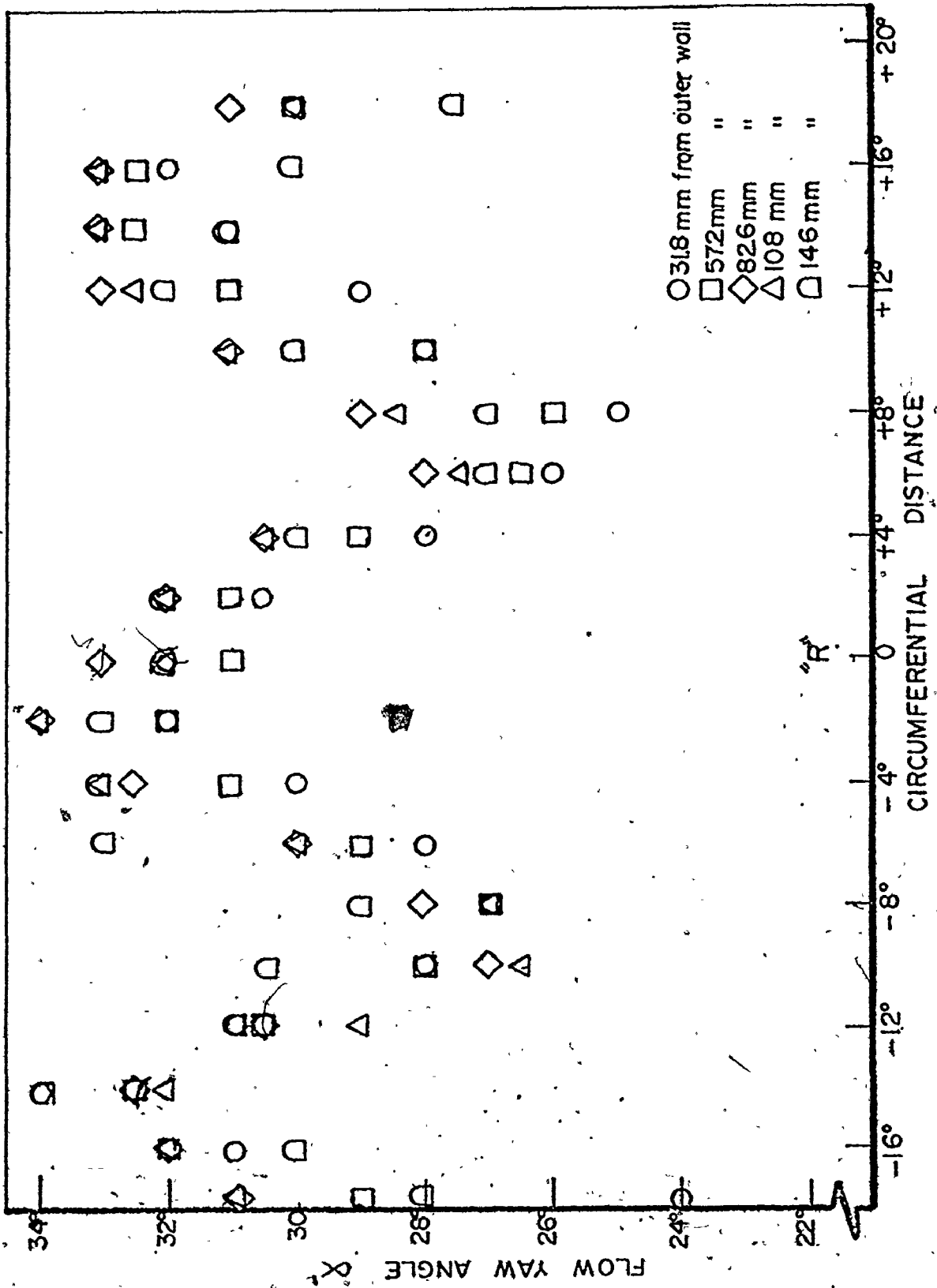
Fig. 33 Circumferential Distribution of Flow Yaw Angle for Different Radii.
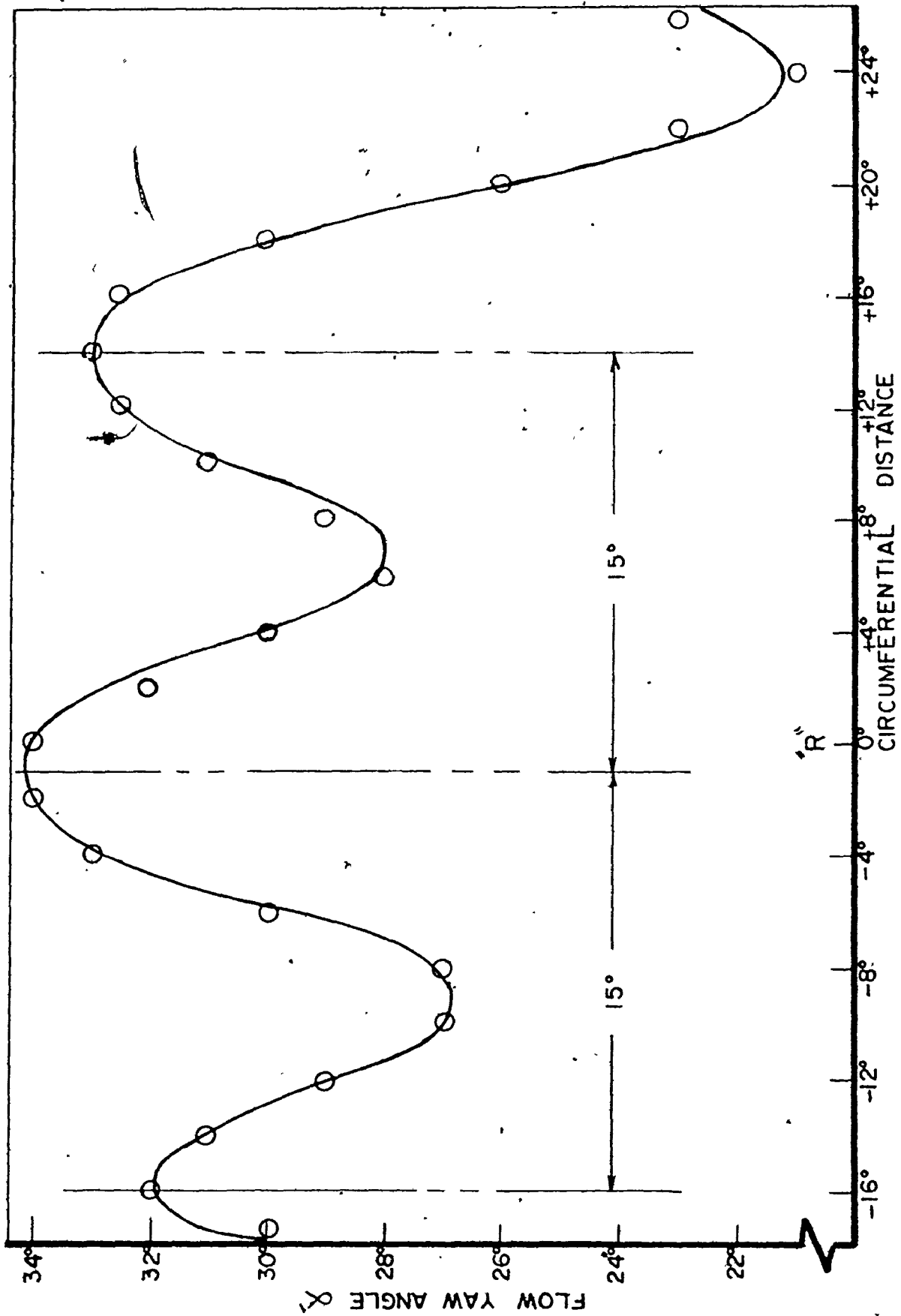
Fig. 34 Circumferential Distribution of Flow Yaw
Angle at Midradius.

aid of a potential field plotter employing carbon coated
paper and silver paint. The equipotentials were drawn at
midradius geometry as shown in Fig. 35 and the flow angles
measured by drawing perpendiculars to the equipotentials
at the inlet measuring station. The potential flow angle
distribution (Fig. 36) agreed quite well with the experi-
mental yaw angle.

6.2   Inlet Velocity Distribution

Figures 37, 38 and 39 show the flow velocity
distribution in the radial and circumferential directions.
In the radial direction a negative velocity gradient was
found from the inner wall to the outer wall (Fig. 37).
The curves in Fig. 37, which indicated typical average values
have not been extended into the wall areas because the
three dimensional probe did not have the same degree of
accuracy when used near the walls of which it was capable when
used in the free stream. Fig. 38 shows the circumferential dis-
tribution of velocity at different radii. The effect of
the leading edge on velocity was to decelerate the flow
in the positions across the footprints of the blade leading
edges, thus giving a cyclic velocity variation similar to
the one obtained for the yaw angles. A more complete
circumferential velocity distribution is given in Fig. 39
at midradius. It can be seen that a circumferential velocity
gradient existed between the two side walls and once again
_____
* to solve Laplace's Equation for 2-D imcompressible flow.
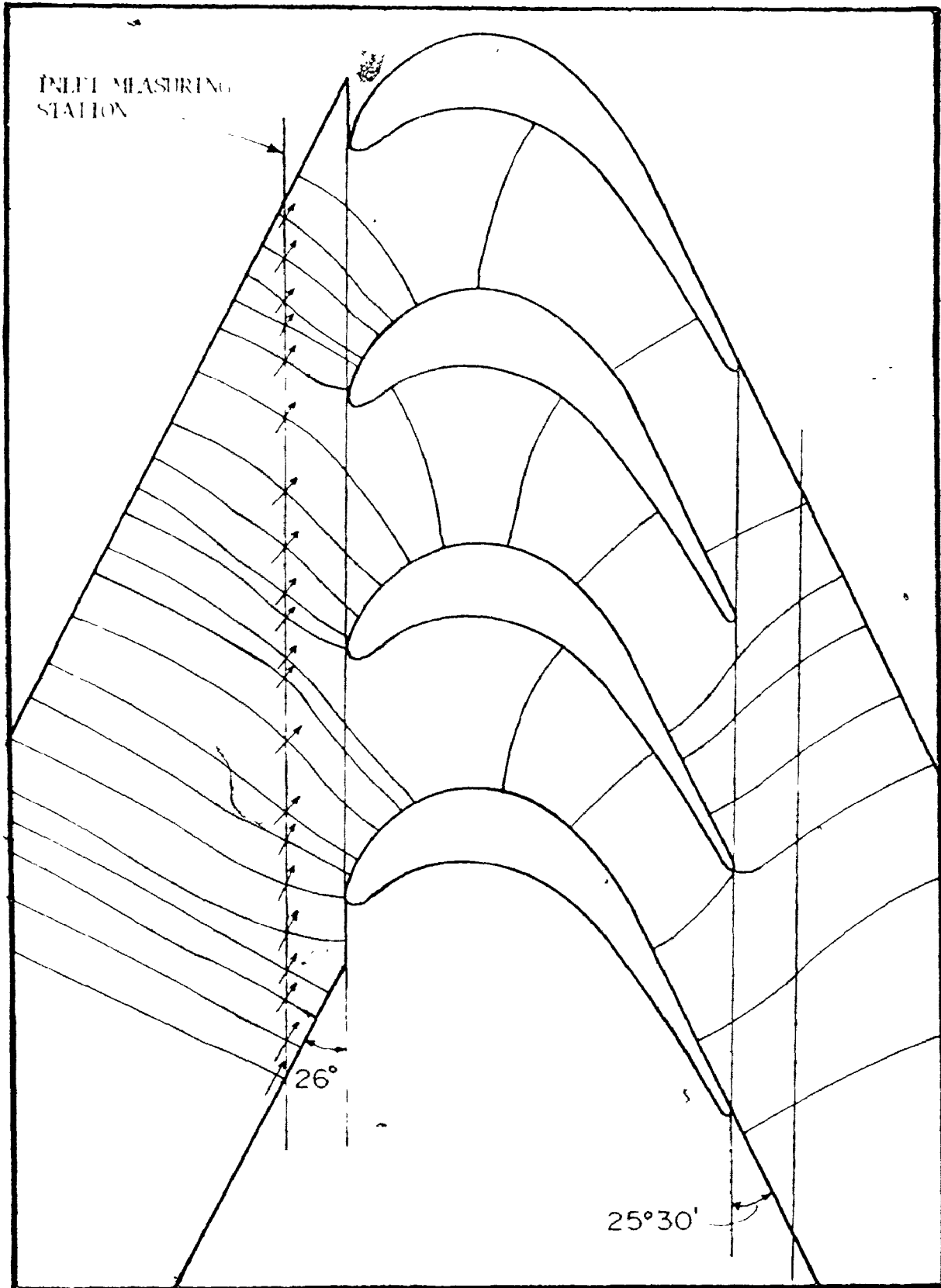
Fig. 35   Inlet Section Equipotentials at Midradius
(Obtained With a Single Source and Sink for
the Unadjusted Flow at the Inlet.
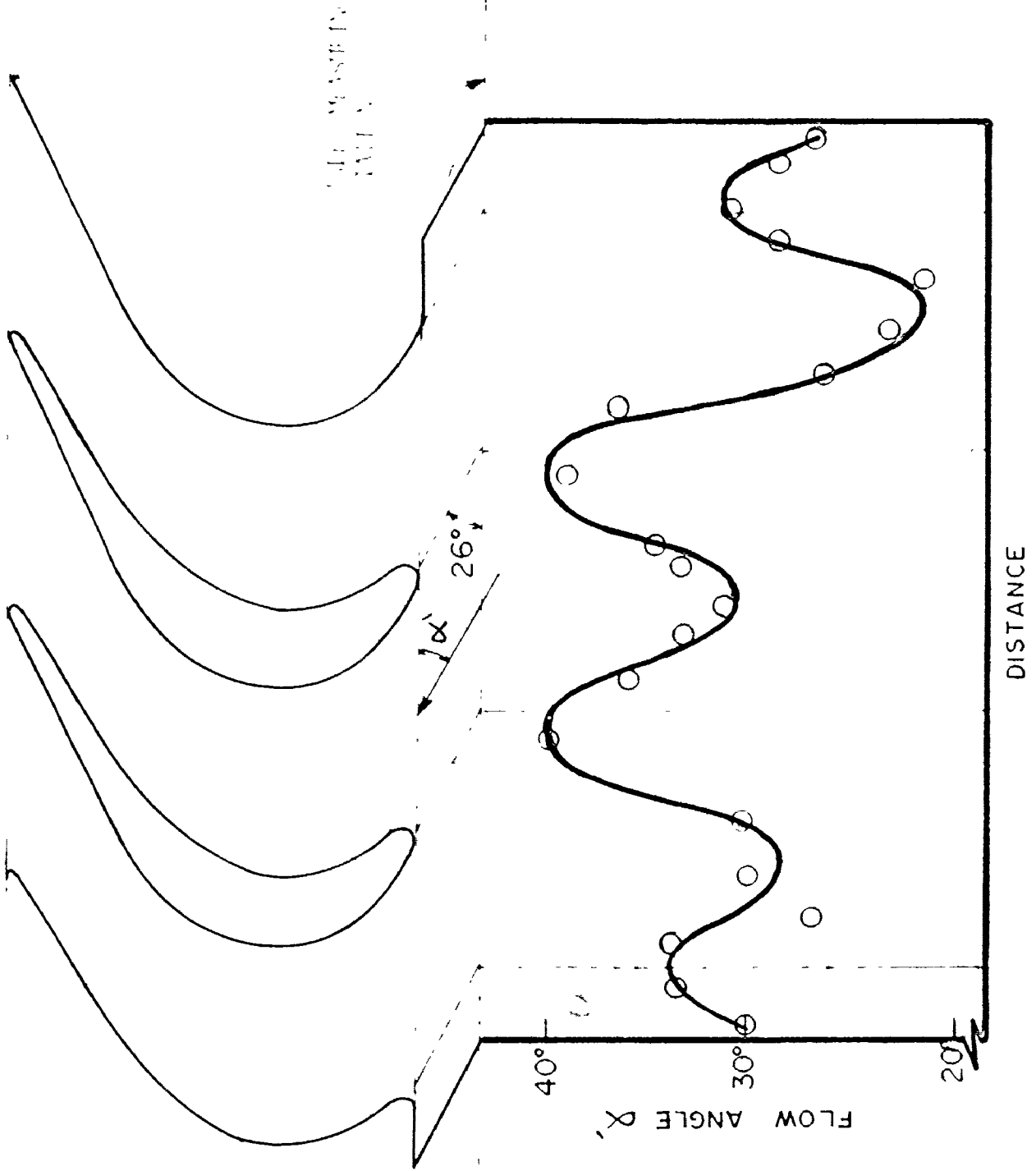
Fig. 57 Flow Angle Distribution Based on Potential Flow Solution.

FLOW ANGLE α'

DISTANCE

40°

30°

20°

26°

α
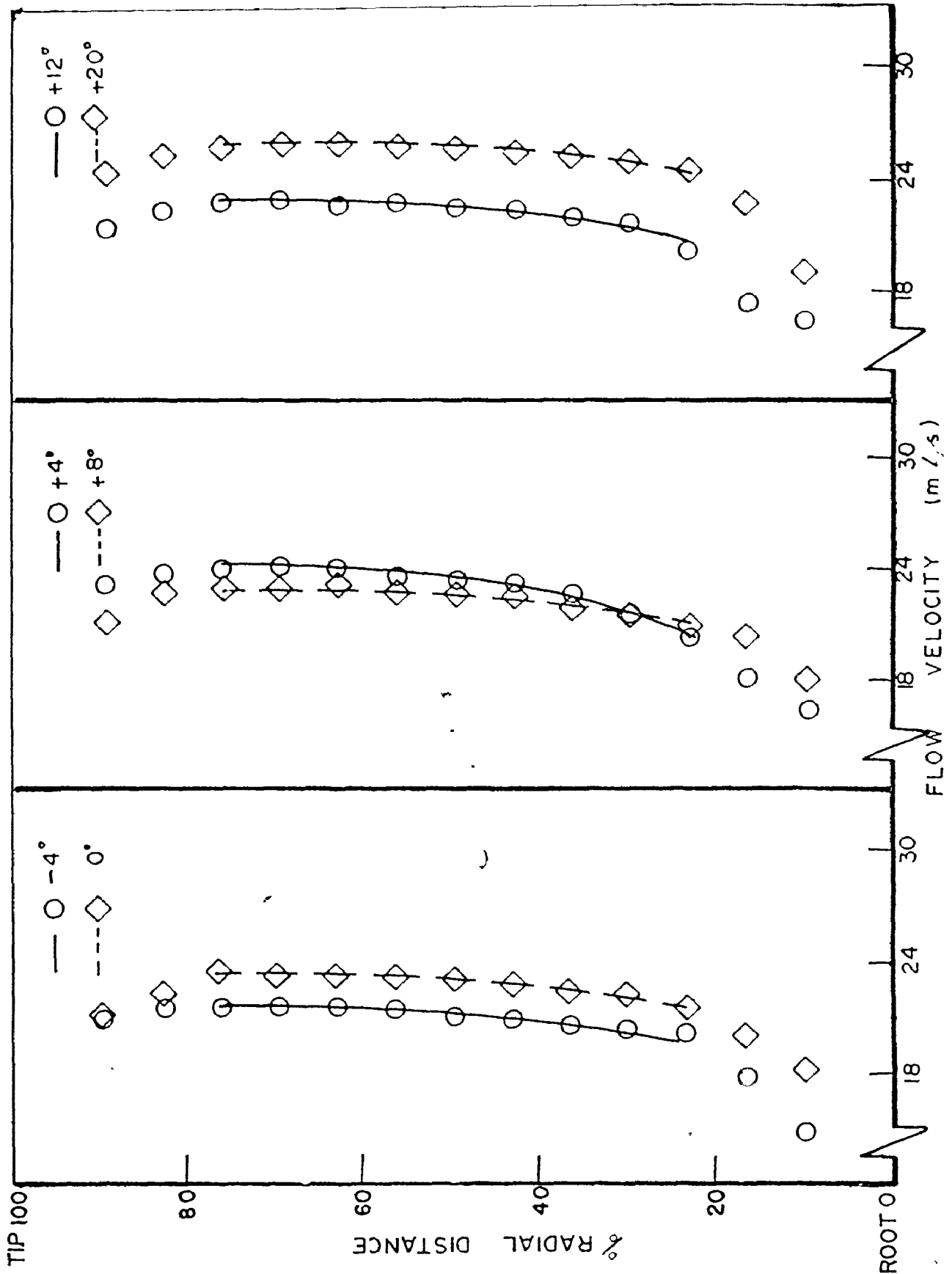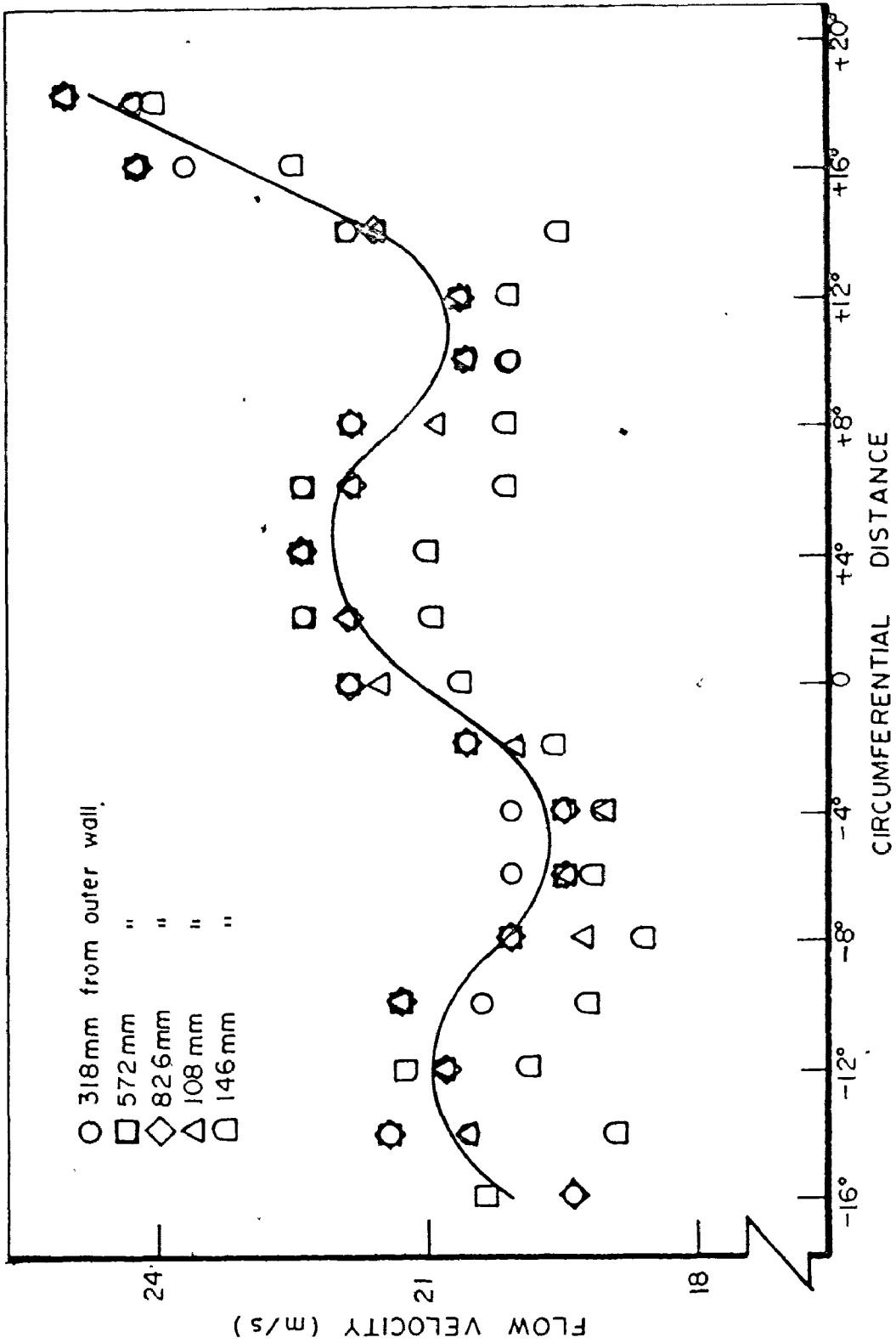
Fig. 38   Circumferential Distribution of Velocity
           at Different Radii.
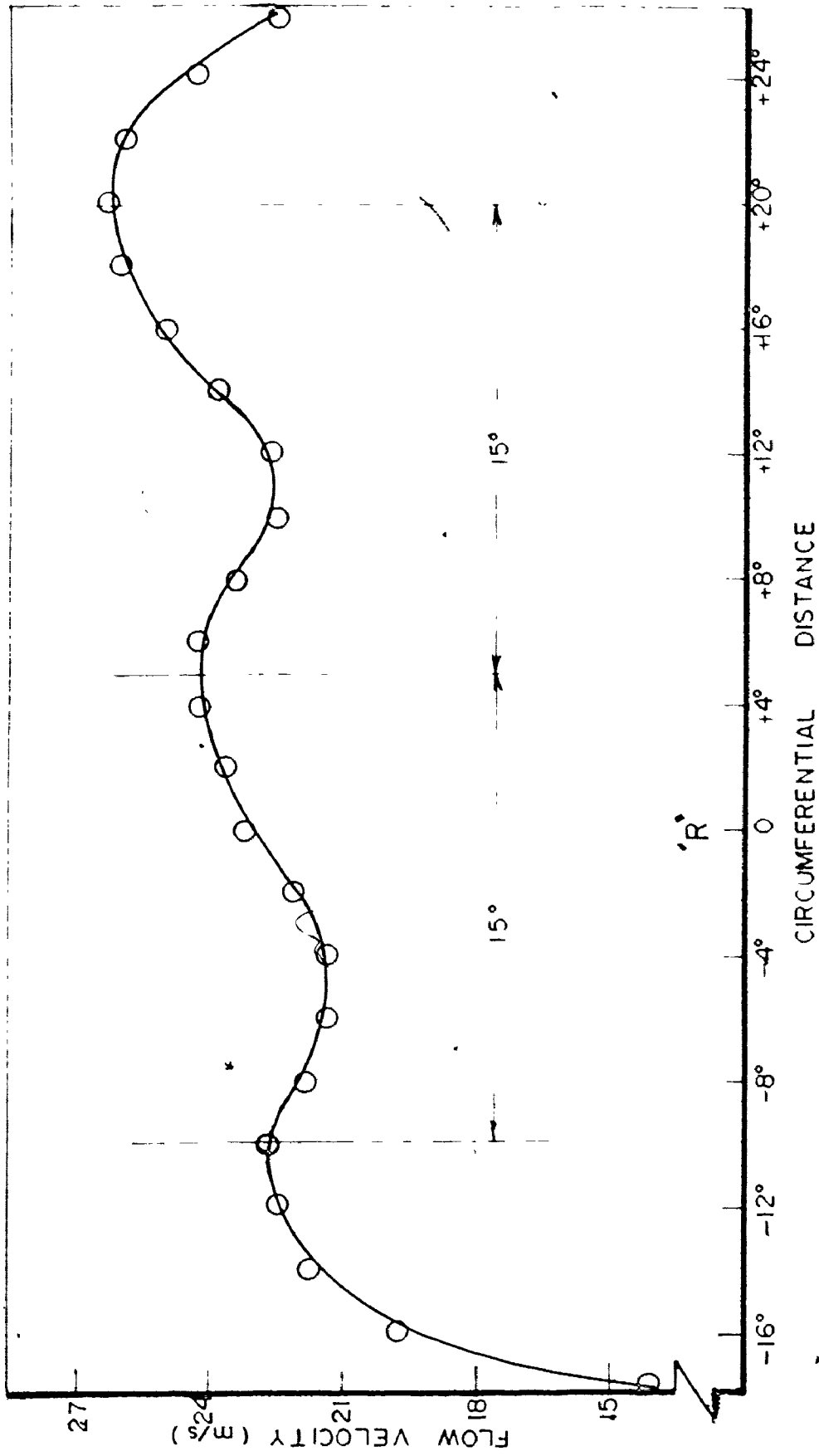
Fig. 30 Circumferential Distribution of Velocity at Midradius.

the peaks and valleys produced by the blade leading edges.

The radial and circumferential gradients in velocity were probably due to the three dimensional turning of the flow in the inlet turning cascade resulting in higher velocities at the larger radii. This corresponded to the outer wall in the radial direction, and to side wall A (Fig. 30) in the circumferential direction. The effects of the adjustments of the inlet section geometry, which were carried out to produce more uniform flow conditions at the cascade inlet, are presented in the following sections.

6.3 Circumferential Adjustment of the Velocity

The circumferential velocity gradient adjustment was carried out using a porous plate suction technique in one of the sliding side walls located at point B (see Fig. 30). These sliding side walls are shown in Fig. 83 of Appendix A, and were constructed at both points A and B so that a 4° gap could be used for either suction or blowing purposes. Experiments showed that it was not necessary to introduce a mean of flow control at point A. A variable speed Sheldon PH-1A exhauster was used to obtain the necessary pressure differential. The fan had a capacity of 525 cubic feet of air per minute against a 20.8 inch static head of water at 3500 r.p.m. absorbing 3 B.H.P. Initially 250

holes with a diameter of 2 mm were drilled on a triangular
pitch in the sliding side wall over which a plenum chamber
was constructed. A 50 mm diameter flexible hose connected
the plenum chamber to the exhauster fan. (See Fig. 6)

Several methods of flow suction were tried and the
results have been summarized in Figs. 40 to 43. Figs. 40
and 41 show the effect of suction on the yaw angle and on
the velocity at midradius. Suction was obtained using 5"
and 13.5" water differential pressure across the perforated
plate. As expected the effect of suction was to decrease
the yaw angle and the velocity gradient between the inlet
section side walls. Fig. 42 compares the effect of suction
on velocity by means of the perforated plate and a slot
opening for the same differential pressure. The slot
suction was produced by closing off the holes and sliding
the side wall to the desired slot area. It can be seen that
increasing the open area improved the circumferential
velocity distribution, and that the perforated plate suction
effect, with a hole area of 0.7×10^3 mm^2, was almost identical
to the slot suction effect with an open area of 1.9×10^3 mm^2.
Fig. 43 shows the combined effect of suction and blockage
on the velocity distribution. Inlet flow blockage was
done by means of closing off the last three inlet vane
passages located at the bellmouth entrance. It can be
seen that the combination of suction and blockage produced
almost constant peak velocities in the three test section
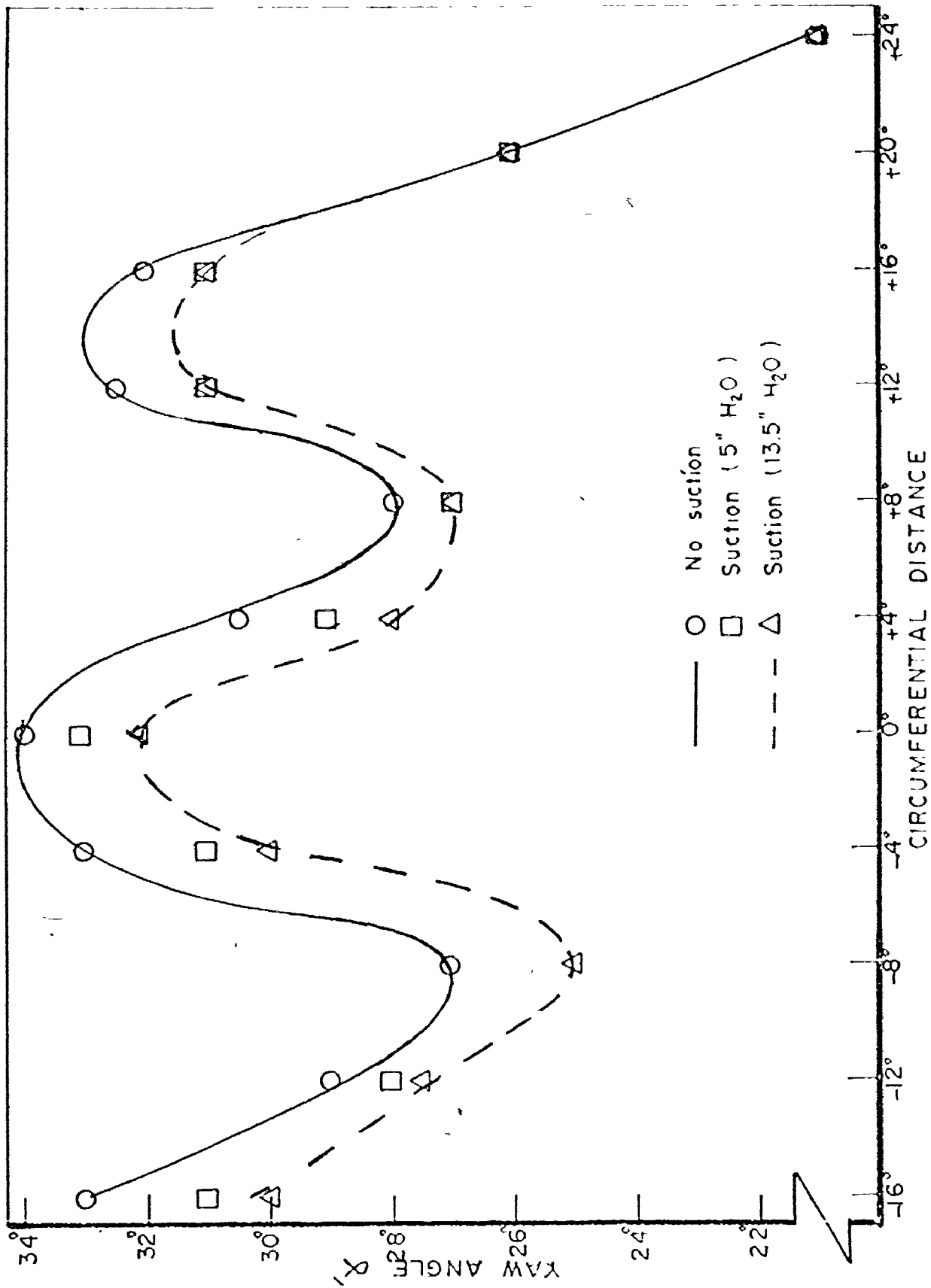
Fig. 40 Effect of Perforated Plate Suction on
         the Yaw Angle (γ) at Midradius.
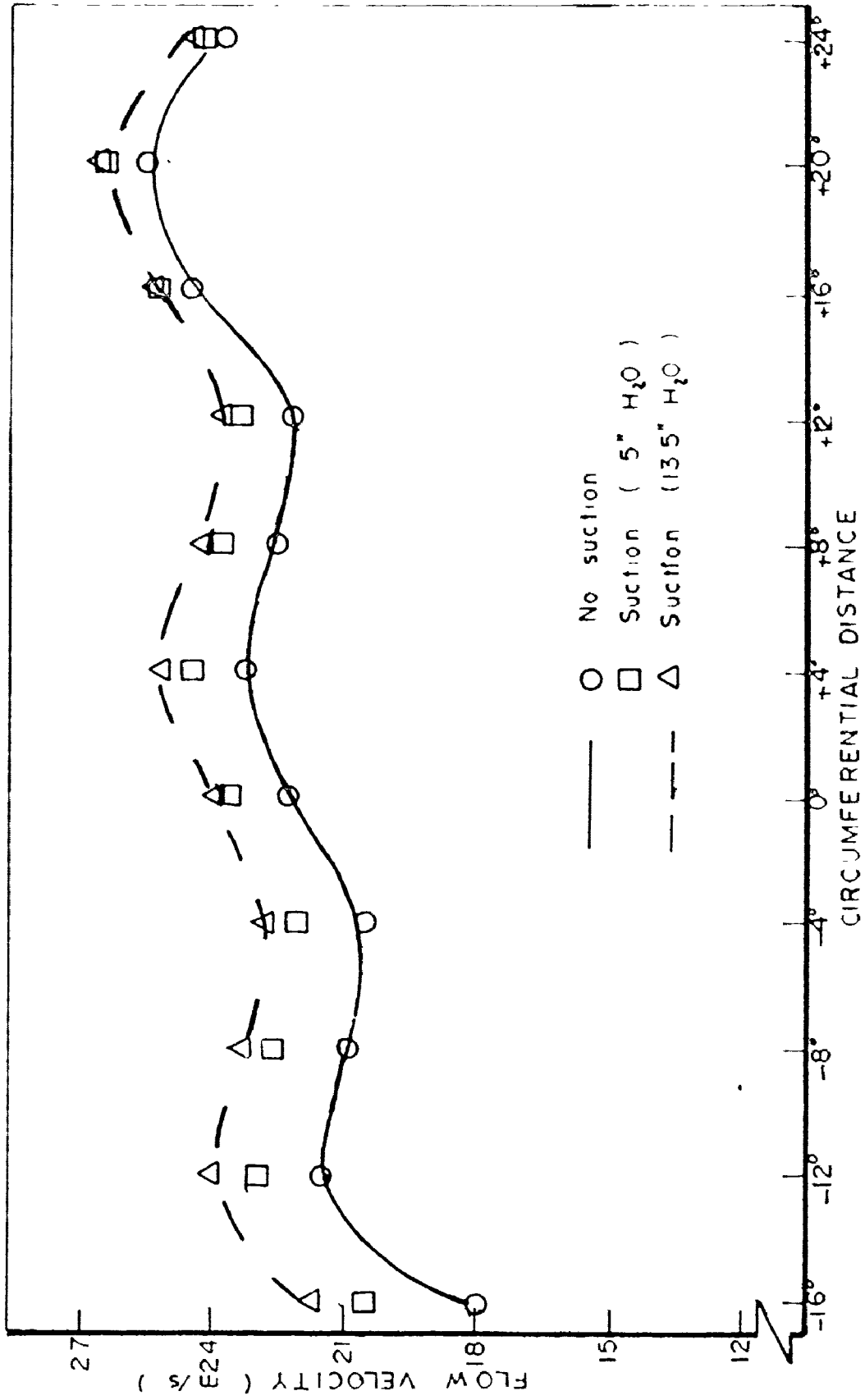
Fig. 41 Effect of Perforated Plate Suction on the
Circumferential Velocity Distribution at
½ radius
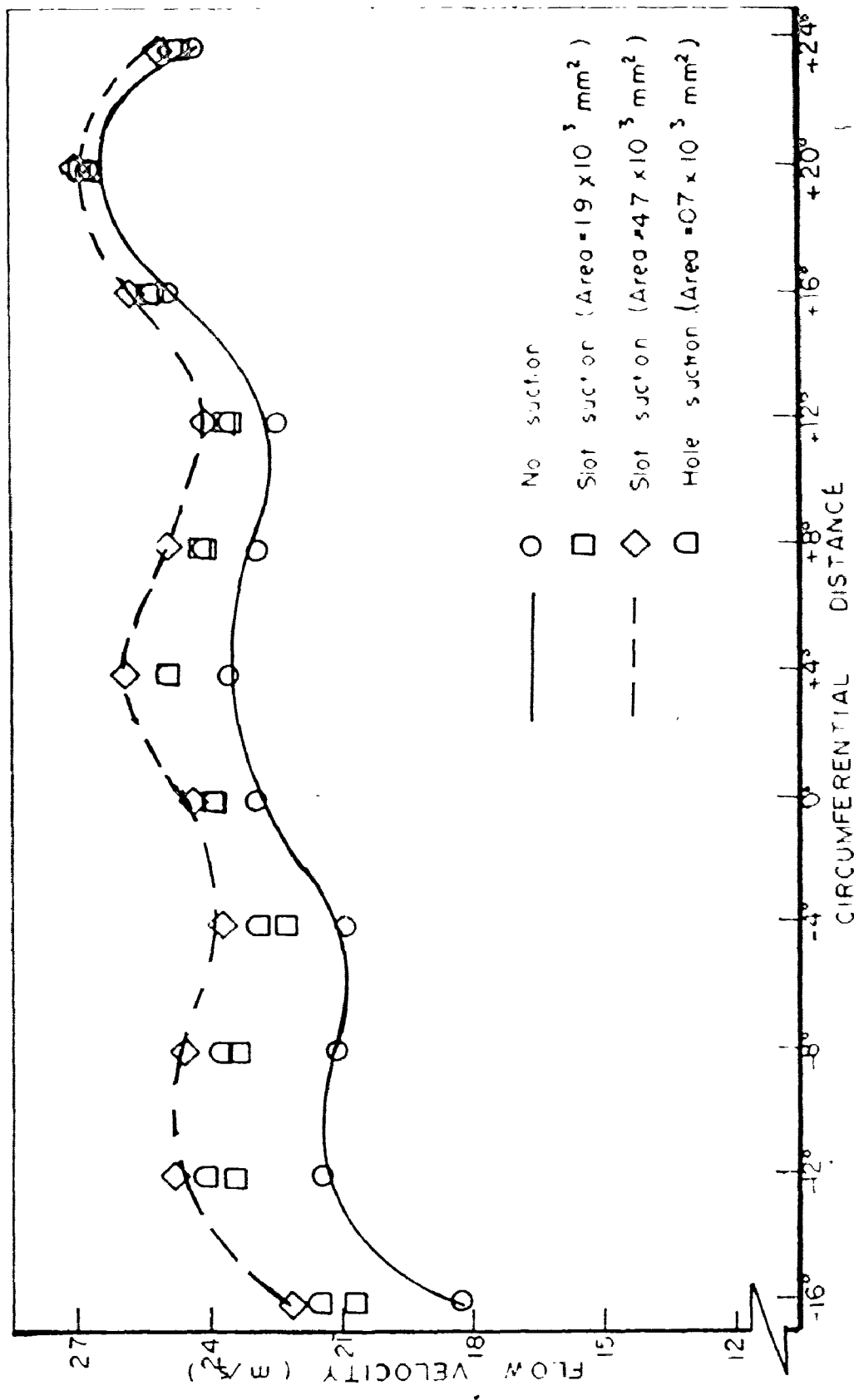
Fig. 43. A comparison of the Suction Effect on the velocity Distribution at midradius using either the slot or the perforated Plate.

Legend (as shown on chart):

- ○ No suction
- □ Slot suction (Area = 19 × 10³ mm²)
- ◇ Slot suction (Area = 47 × 10³ mm²)
- ◻ Hole suction (Area = 07 × 10³ mm²)

Axes: CIRCUMFERENTIAL DISTANCE (horizontal, from -16° to +24°); FLOW VELOCITY (m/s) (vertical, 12, 15, 18, 21, 24, 27)
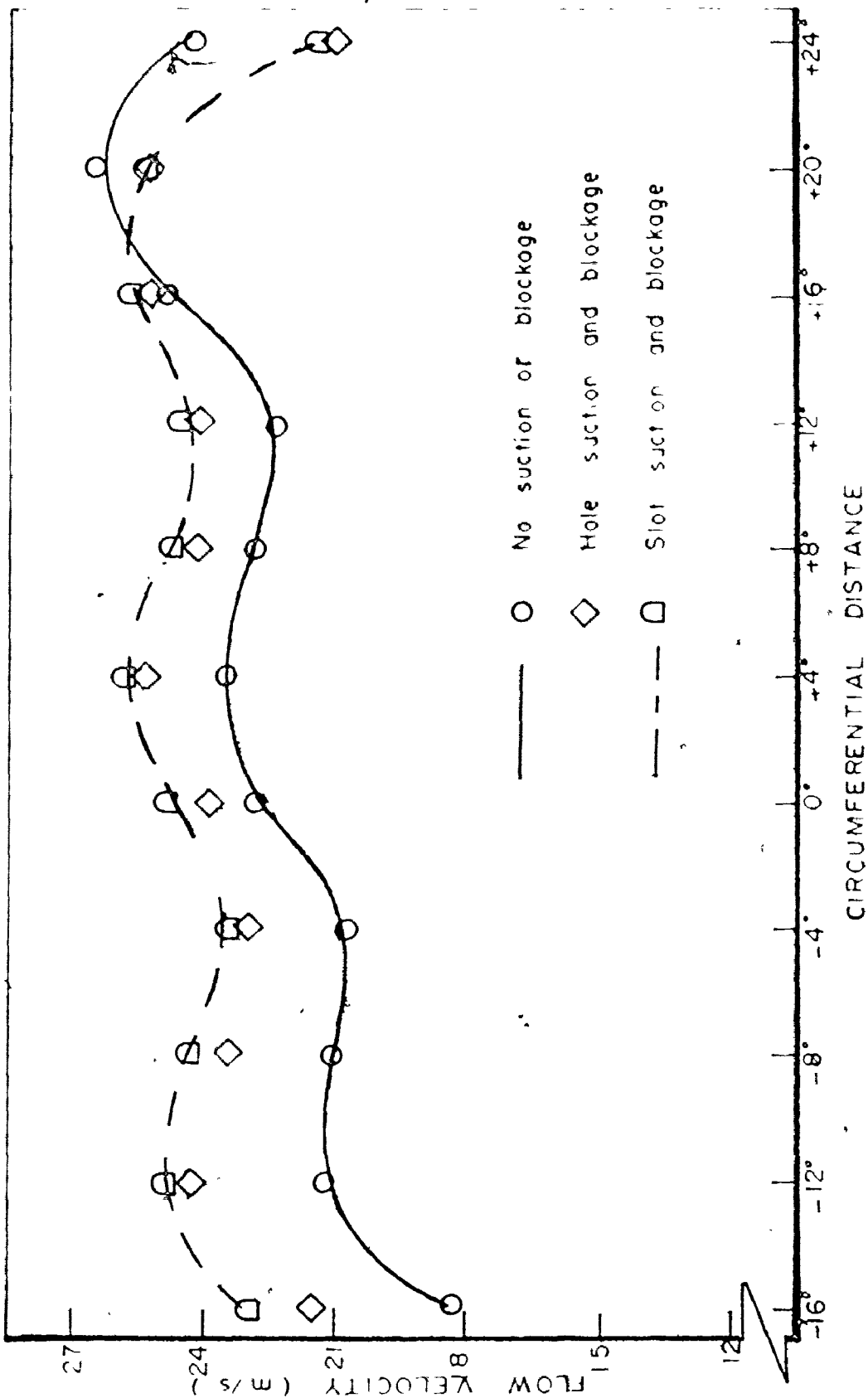
Fig. 43   The Effect of Suction and Inlet Blockage on the velocity
Distribution at Midradius.

Legend:
○   No suction or blockage
◇   Hole suction and blockage
▢   Slot suction and blockage

Axes:
FLOW VELOCITY (m/s)
CIRCUMFERENTIAL DISTANCE

blade passages. However, it should also be noted that a gradient was still present between the circumferential position of $(+12^o)$ and (-4°) which coincided with the leading edge footprints of the center blade passage.

As a result of the above tests, it was decided that the adjustment of the inlet velocity distribution would be carried out using only perforated plate suction with the hole size increased to provide an open area of 2×10^3 mm^2. This was considered to produce an effect approximately equivalent to that produced by a slot open area of 4.7×10^3 mm^2.

6.4   Radial Adjustment of the Velocity

The velocity gradient in the radial direction was adjusted by changing the curvature of the outer wall of the bellmouth entrance. This modification was in fact equivalent to blocking a part of the outer wall area without distorting the flow in the radial direction.

Fig. 44 shows the radial distribution of flow velocity and angle at different circumferential locations. Fig. 45 shows a radial traverse at 0° ('R')* for two different inlet velocities and a detailed traverse at $(+4^o)$ for both the main and boundary layer flow.

From these results it can be seen that the bellmouth modification gave a constant velocity in the main flow without affecting the flow yaw angle. The different boundary layer profiles observed on the inner and outer surfaces were

* Reference Radial Direction
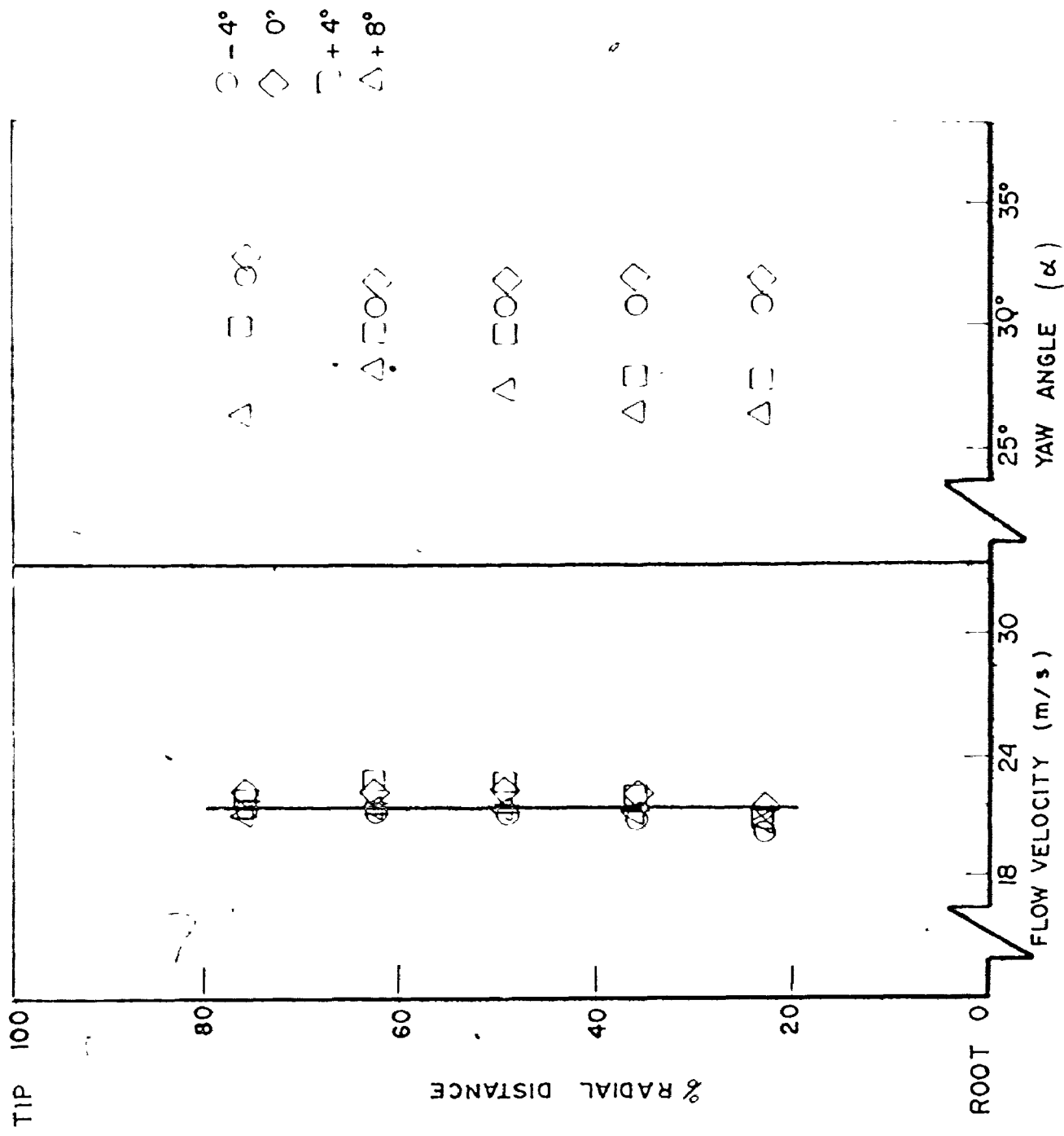
Fig. 44   Effect of the Bellmouth Modification on the Radial Velocity
Distribution and on Yaw at Inlet Flow Velocity of 21.5 m/sec.
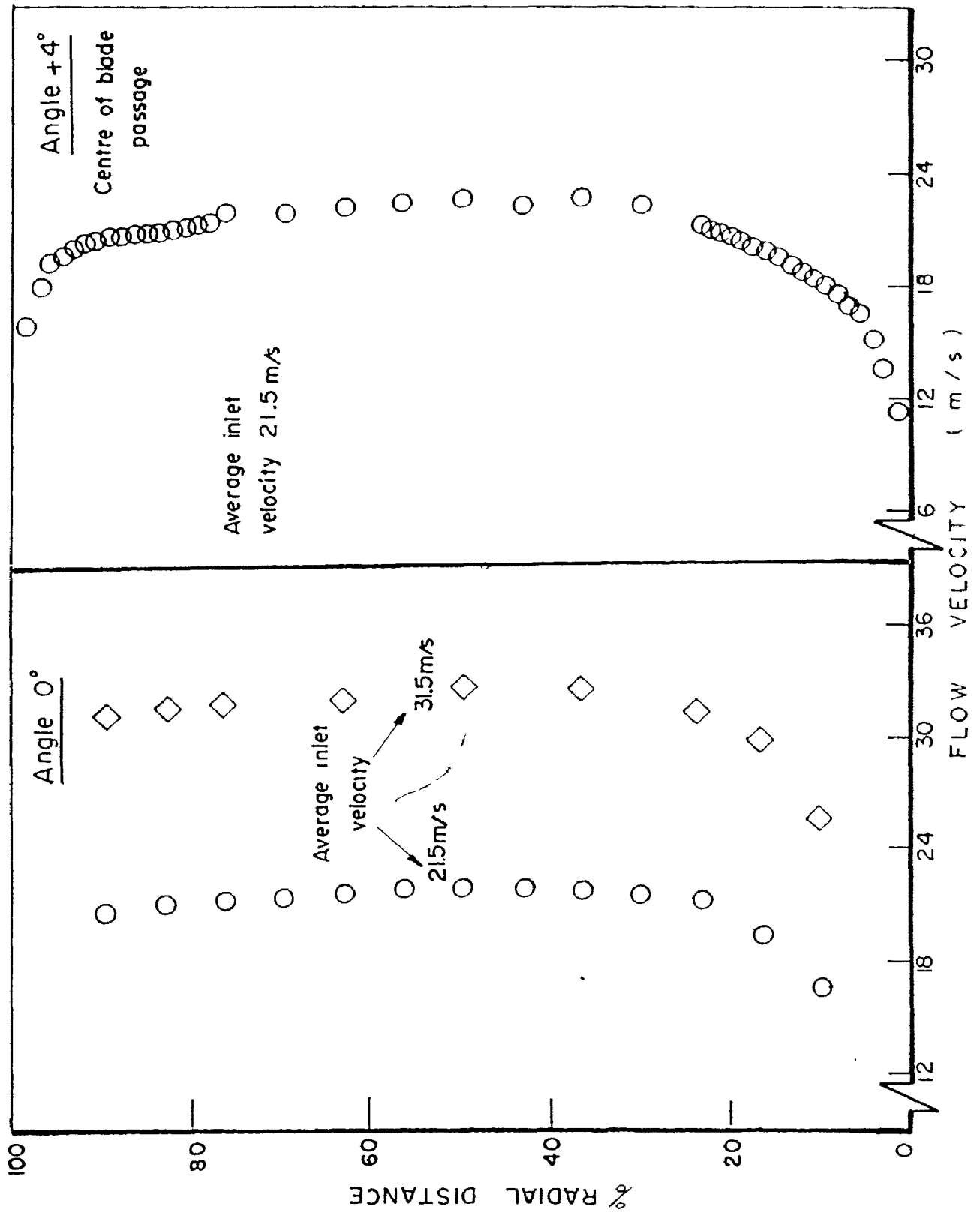
Fig. 45   The Effect of the Bellmouth Modification on
          the Radial Velocity Profile

due to the difference in the geometry of the outer and inner walls.

6.5   Final Inlet Flow Conditions

With the inlet bellmouth modified as shown in the previous section and the perforated plate hole area increased to 2×10^3 mm^2, a complete inlet flow traverse in the radial and the circumferential directions, was carried out at an average inlet velocity of 25.5 m/s.

Fig. 46 shows the final distribution of flow yaw angle at the midradius height as well as the circumferential mean velocity distribution. The mean velocity was defined as the arithmetic average velocity in the radial main flow neglecting the boundary layer on the inner and outer walls. It is clear from this figure that uniform variations of flow angle and velocity have been achieved, especially in the center blade passage within which the study was to be carried out. At the selected inlet measuring station, the effect of the leading edge for the center blade passage, was to increase the flow yaw angle from 25° at the center to 30° ahead of the leading edges (the design inlet angle being 26°). In the center blade passage the flow velocity was decelerated by 7% from the center of the passage to positions ahead of the leading edges.

Fig. 47 shows the final radial velocity profiles obtained at different circumferential positions. Figs. 48
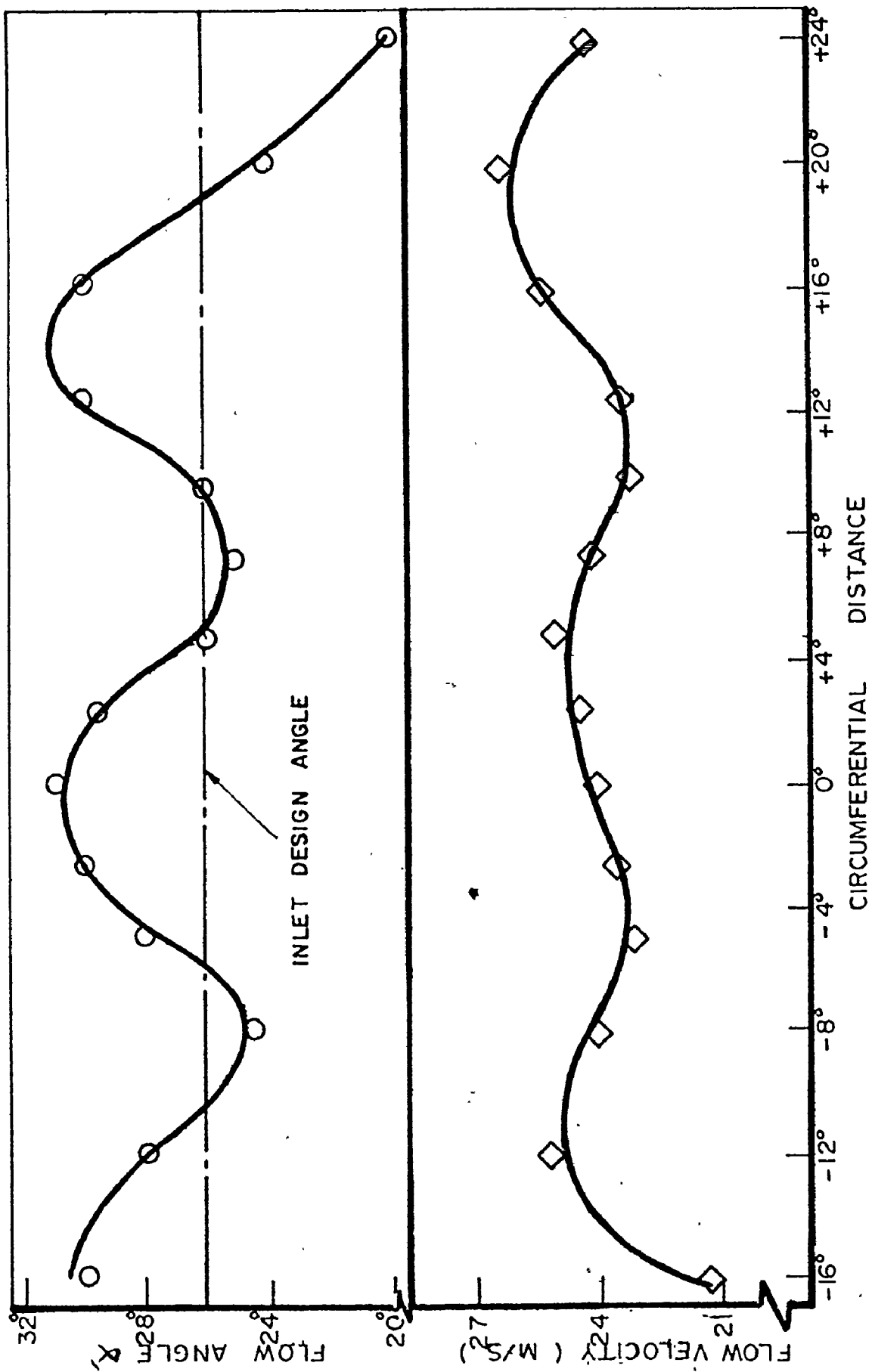
Fig. 46   Final Circumferential Distribution of Yaw Angle
and Velocity at the Midradius.
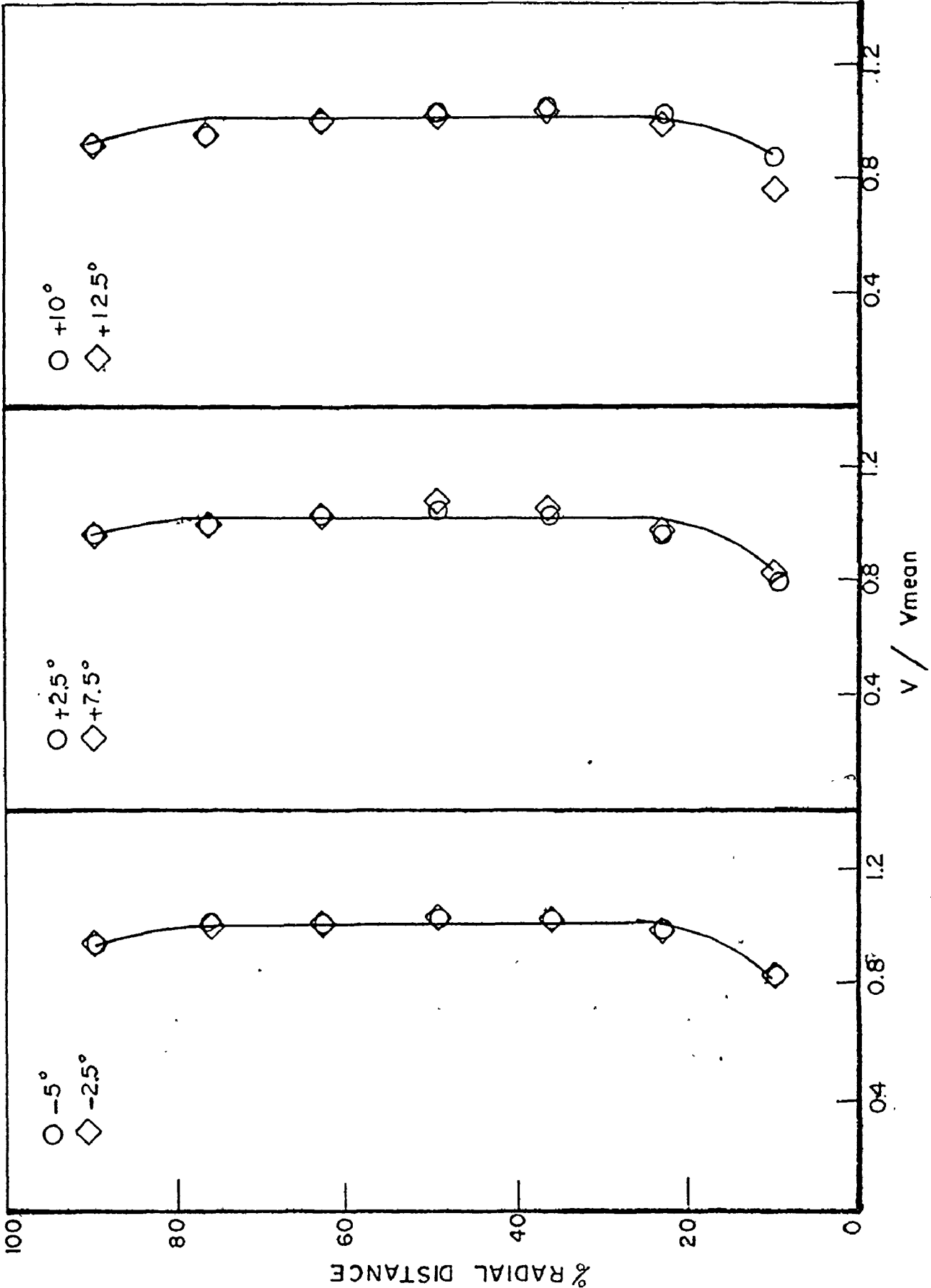
Fig. 47 Final Radial Velocity Distributions Obtained
at an inlet Mean Velocity of 25.5 m/s.

to 50 define the radial distribution of inlet flow para-
meters at three circumferential positions with respect to
the center blade passage. The angles 0° and 10° are .
essentially on the blade leading edges producing the center
passage while 5° corresponded to the center of the blade
passage. The vorticity, which has been defined as the slope
of the radial velocity profile, has been drawn in a non-
dimensional form. Reviewing the velocity profiles in
the three locations, the velocity can be seen to be constant
in the main flow and the boundary layer thinner on the outer
wall than on the inner wall. The different boundary layer
profile measured at 10° was probably due to the local
adverse pressure gradient close to the leading edge of the
blade. The yaw and pitch angles varied over a range of 2^O
from the inner to the outer wall.

The mean inlet flow parameters at position ($+5^O$)
for an average inlet velocity of 25.5 m/s are given in
Table II.

6.6   Inlet Turbulence Intensity

A significant flow parameter in all turbomachine
designs is the level of free stream turbulence. The inlet
turbulence intensity was measured at different radii and
speeds using a normal hot wire probe*. The probe was
first calibrated in the potential core of a calibration
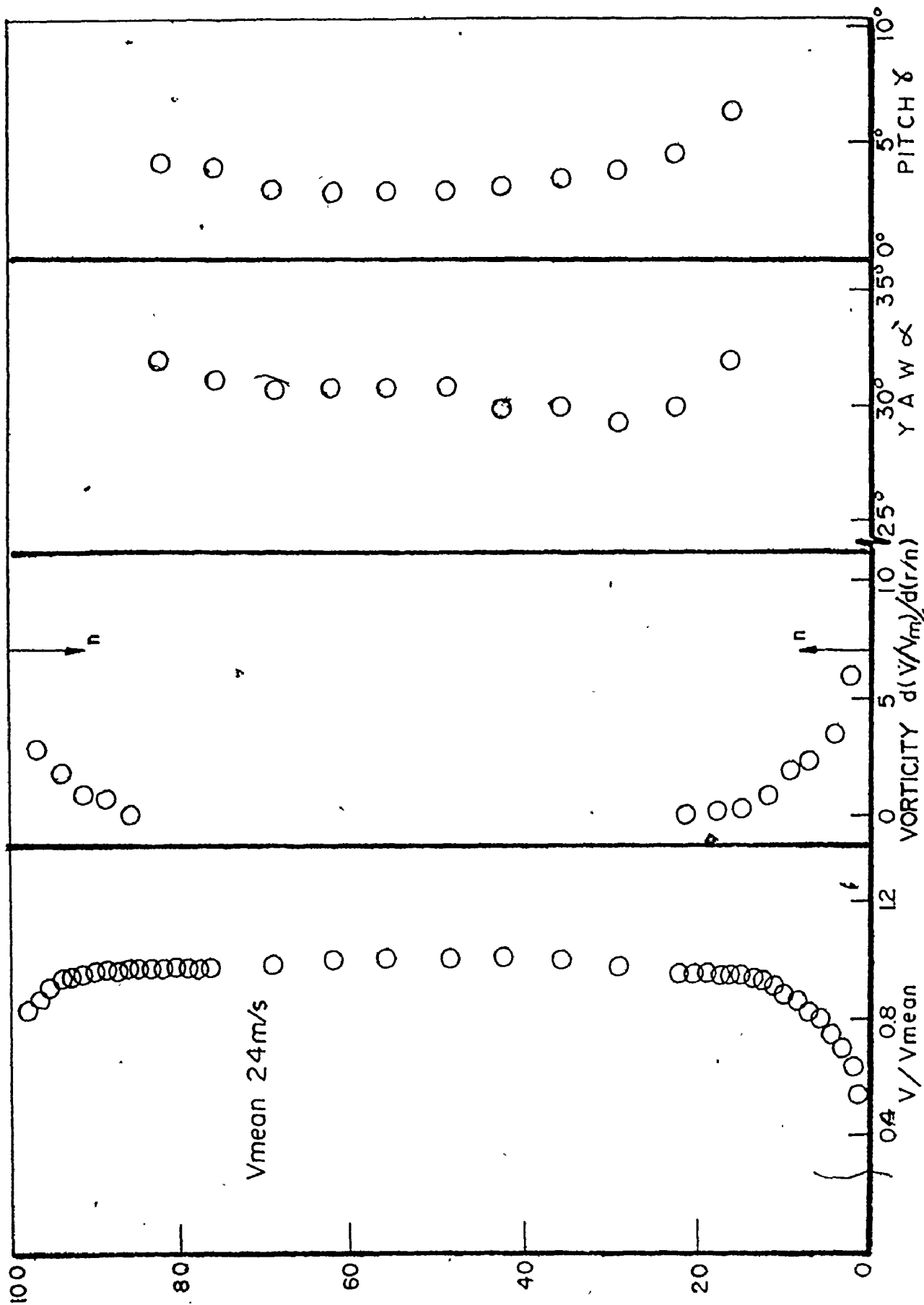
Fig. 48 Inlet Flow Parameters Obtained at a Mean Inlet Velocity of 25.5 m/s for Circumferential Position 0o.
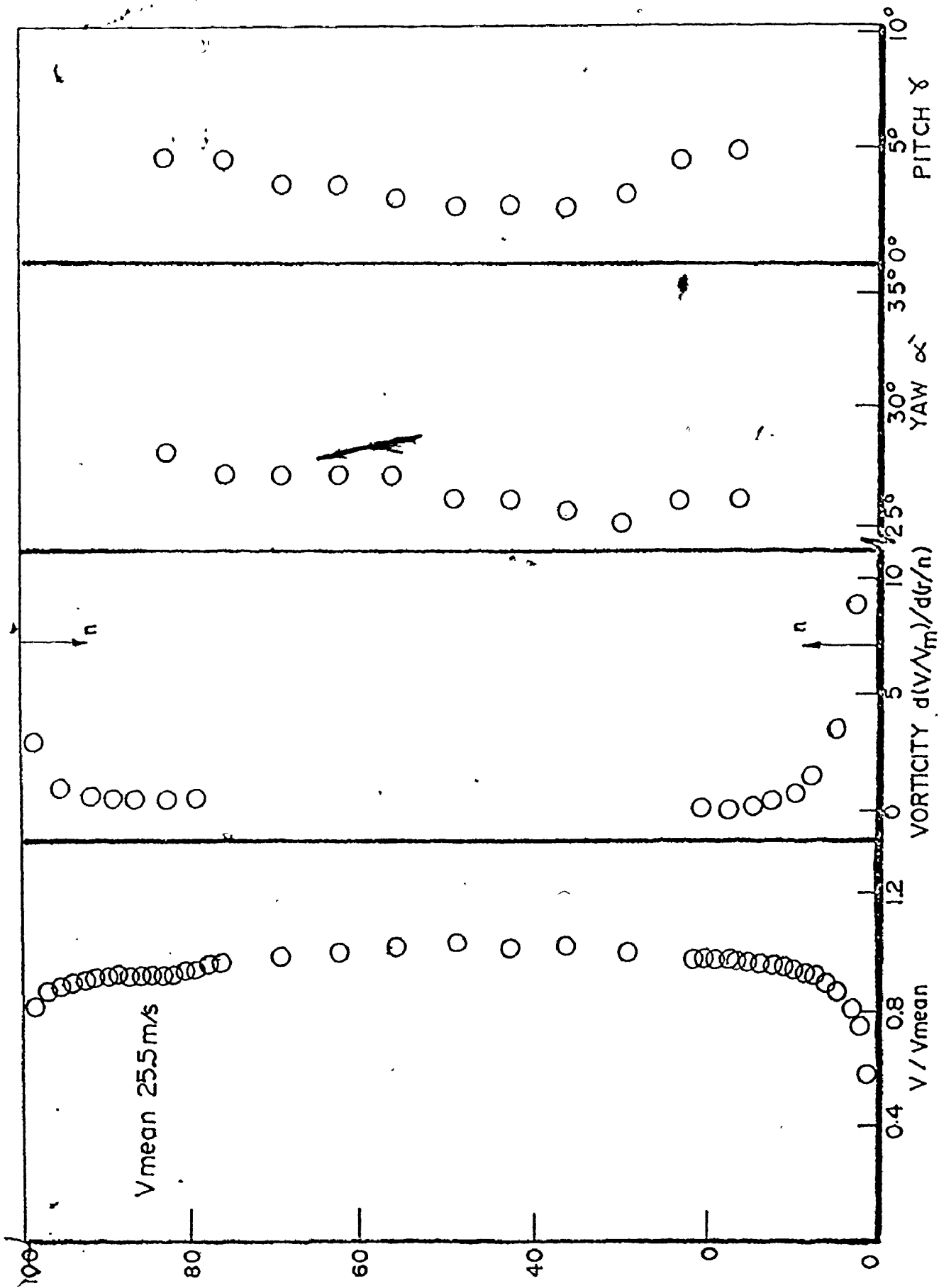
Fig. 49 Inlet Flow Parameters Obtained at a Mean Inlet
Velocity of 25.5 m/s for Circumferential. Position 5°.
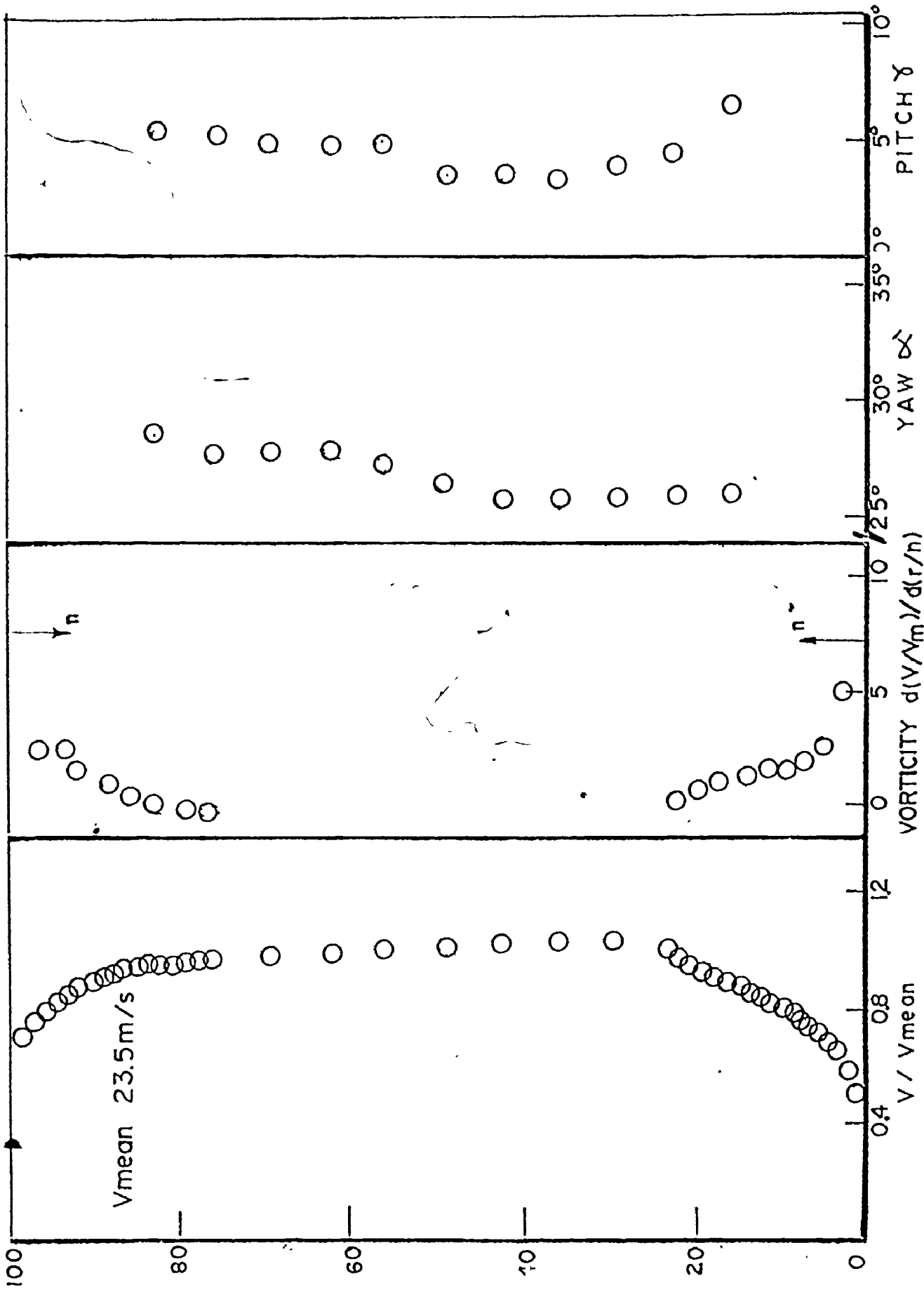
Fig. 50 Inlet Flow Parameters Obtained at a Mean Inlet.
Velocity of 25.5 m/s for Circumferential Position 10°.

Table II

Inlet Flow Parameters for a Mean Inlet Velocity of 25.5 m/s (Fan speed 700 r.p.m.)

Flow Velocity	25.5 m/s
Reynolds Number (based on blade chord)	3.29×10^5
Yaw Angle	26°
Pitch Angle	3°
Total Pressure	-0.41" water (gauge)
Static Pressure	-1.93" water (gauge)
Inner Wall Boundary Layer Thickness	25 mm
Outer Wall Boundary Layer Thickness	17 mm

Captions for Fig. 51

1. Calibration nozzle

2. Hot wire probe (Type DISA # 55P14)

3. Calibrating pitot static probe

4. Constant temperature anenometer (DISA
   Electronik, Type 55A01)

5. Digital voltmeter (Model 7050, Fairchild
   Instrumentation)

6. R.M.S. meter (Type 2409, Bruel and Kjaer)

7. Oscilloscope (Type 564 B, Tektronix)

the required speed range (20 to 60 m/s). The hot wire probe calibration curve is shown in Fig. 52. The r.m.s. turbulence level was then measured at the center of the center blade passage (circumferential position +5°) from the edge of the inner boundary layer to the edge of the outer boundary layer, at different inlet speeds. The inlet turbulence intensity is shown in Fig. 53 for three different radii. The turbulence level is plotted in the form of the percentage turbulence intensity defined as follows,

$$\text{\% turbulence} = \frac{u}{V} \times 100 = \frac{V_{r.m.s.} \times 100}{V \times \frac{dE}{dV}}$$

where $V_{r.m.s.}$ is the measured r.m.s. level, and $\frac{dE}{dV}$ is the slope of the probe calibration curve at speed V.

From Fig. 53, it can be seen that at midradius the percentage of turbulence varied from 3% to 4% and that turbulence levels were higher near the outer wall as compared to the inner wall. The percentage of turbulence levels measured in actual turbomachines are typically from 6% to 9% so that one might say that reasonable inlet turbulence levels were achieved in the annular cascade rig.

D.C. VOLTAGE (Volts)

SPEED (m/s)

DISA PROBE   Type 55P14

Sensor Resistance   4.15 Ω

Operating Resistance   6.0 Ω

E(V=0) = 3.98 Volts
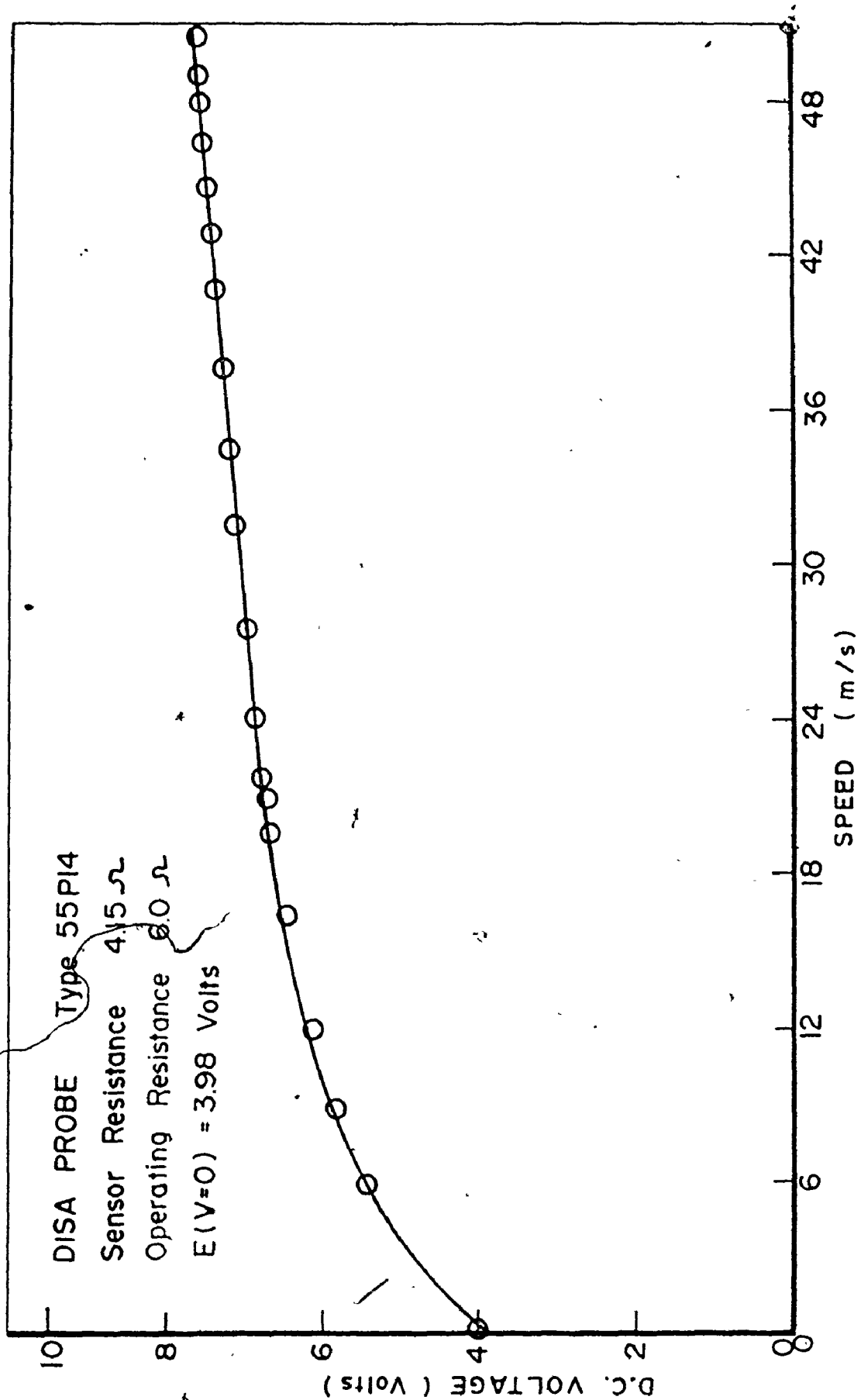
Fig. 52   Calibration Curve Obtained for the Hot Wire Probe.
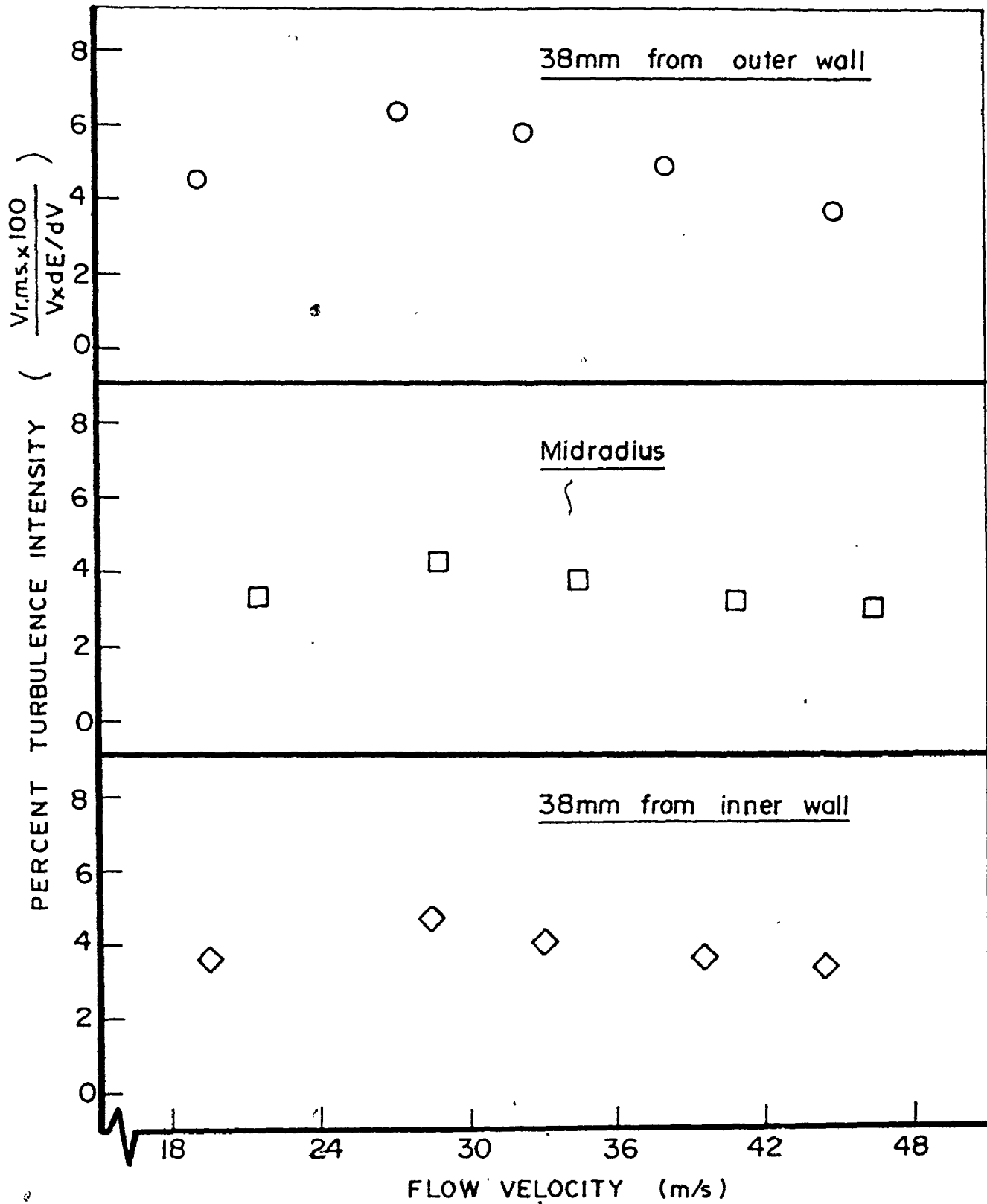
Fig. 53 Turbulence Intensity at the Cascade Inlet.

CHAPTER 7

BLADE PASSAGE PRESSURE
DISTRIBUTION STUDY

Because of the relatively large number of static measuring points available, 60 on the blade surfaces and 70 on the annular surfaces, it was possible to obtain a reasonably detailed picture of the surface pressure field within the passage. Fig. 54 defines the blade passage coordinates where the static pressures have been measured. The results presented in this chapter were obtained for an inlet R_N of 4.6 x 10^5 based on the blade chord and corresponded to a mean velocity of 35 m/s. The static pressures were expressed in terms of a static pressure coefficient defined as:

$$Cp_s = \frac{P - P_1}{\frac{1}{2}\rho V_1^2} \qquad (21)$$

where P_1 and V_1 are the mean inlet static pressure and velocity at the entrance to the center blade passage and P is the measured static pressure at a point. A value of 1.0 for Cp_s therefore corresponded to a stagnation point.

7.1 Passage Pressure Distribution

The distribution of Cp_s for the pressure and suction surfaces at 7, 27, 50, 75 and 94 percent of blade span are
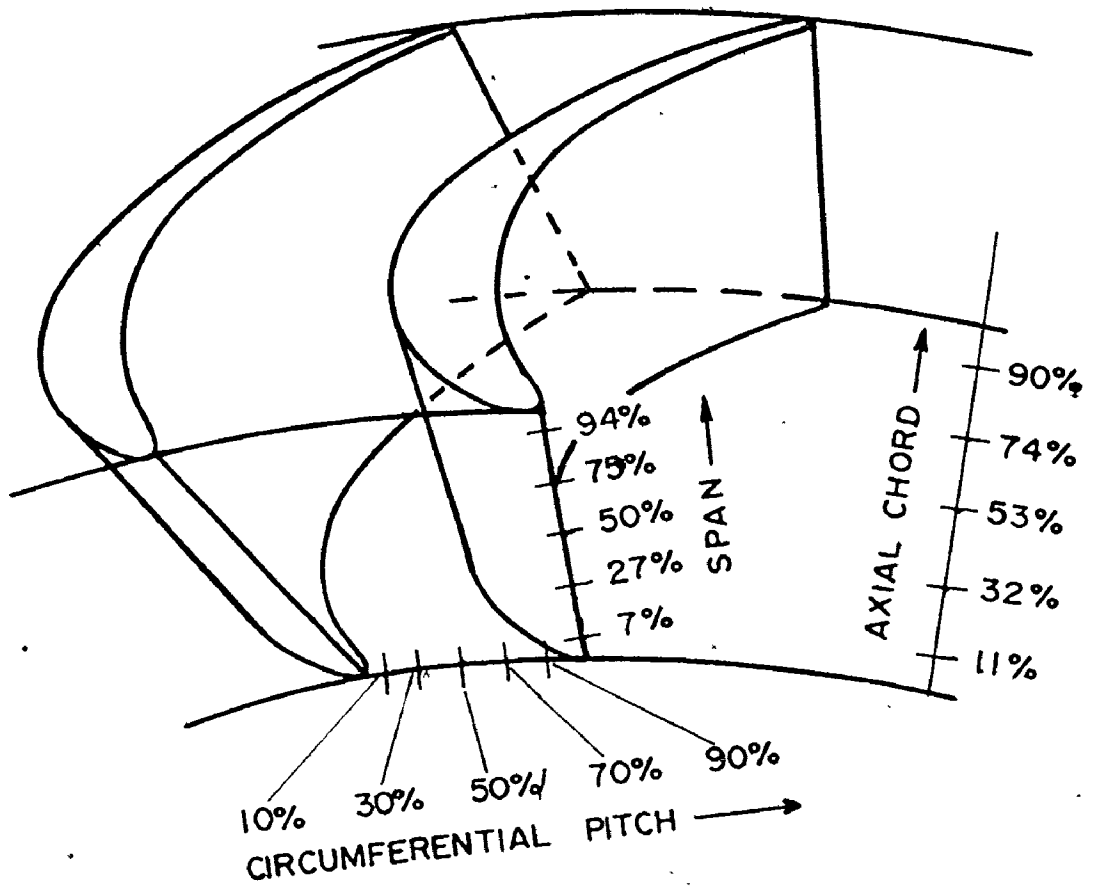
Fig. 54 Blade Passage Coordinates for
Static Pressure Measurements.

shown in Fig. 55 as a function of the percentage of axial chord. Fig. 56 shows the Cp_s distribution for the annular root and tip surfaces at 10, 30, 50, 70 and 90 percent circumferential pitch starting from the pressure surface.

Normally points on the blade pressure distribution curves have been related to passage geometry. For the pressure surface, similar profiles were obtained at all spanwise locations. The pressure slowly increased (near the root) or remained constant (near the tip) up to 30 percent chord and then decreased to the trailing edge of the blades due to passage convergence. Results of Cp_s for the annular walls near the pressure surface revealed the same distribution (Fig. 56).

On the suction surface, the pressure increased for all spanwise locations up to 30 percent of the chord, decreased to a region around the throat area which occurred at 75% of the chord and finally increased up to the trailing edge. The rise in the suction surface pressure beyond the throat was noticed at all spanwise locations as shown in Fig. 55. The same trend was evident in Fig. 56, which showed a pressure increase for circumferential pitch locations higher than 70% for the annular tip and higher than 50% for the annular root. This rise in static pressure was due to the surface curvature of the blade suction surface.
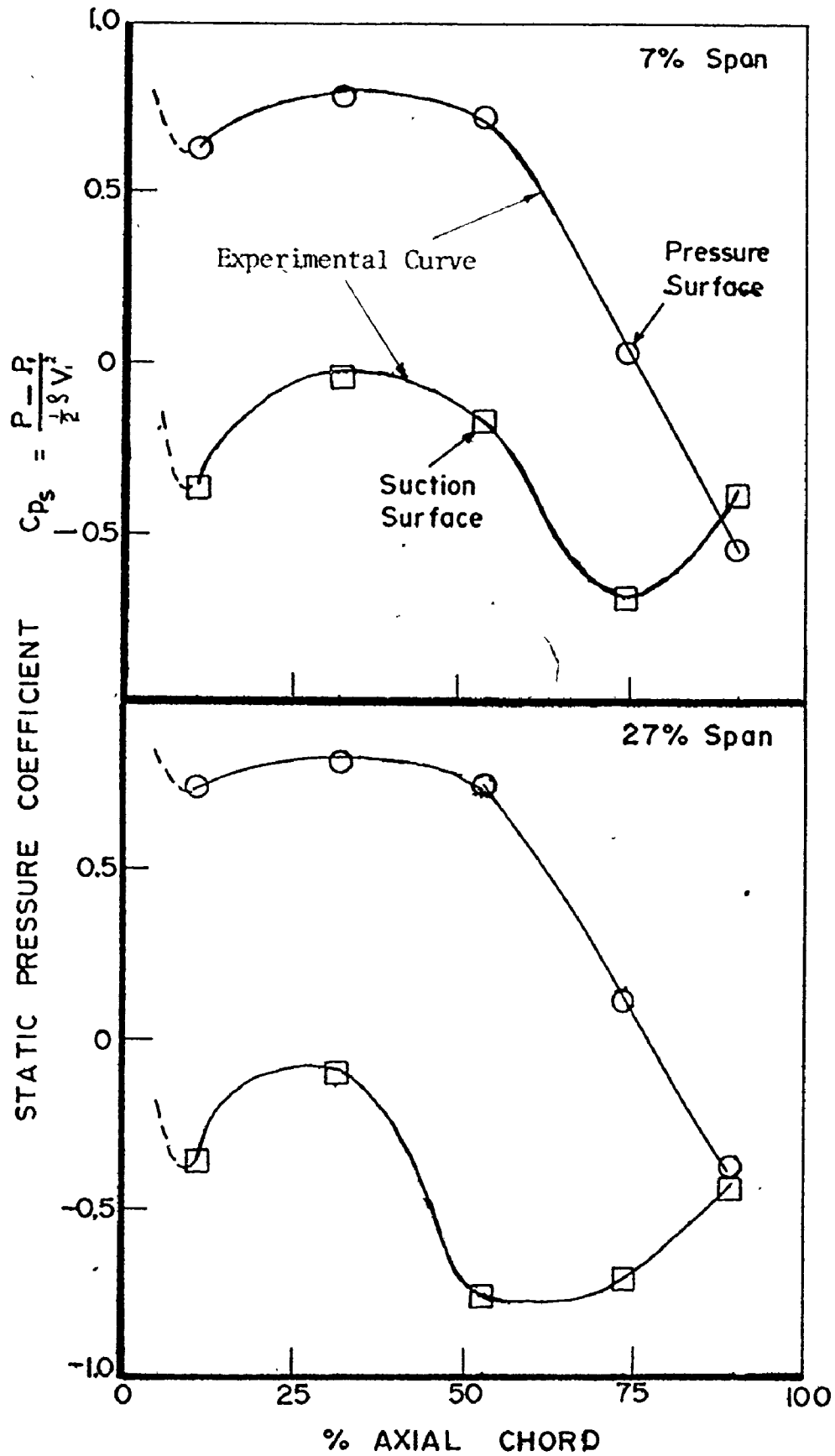
Fig. 55-a   Sur⁻   P⁻   str⁻⁻⁻
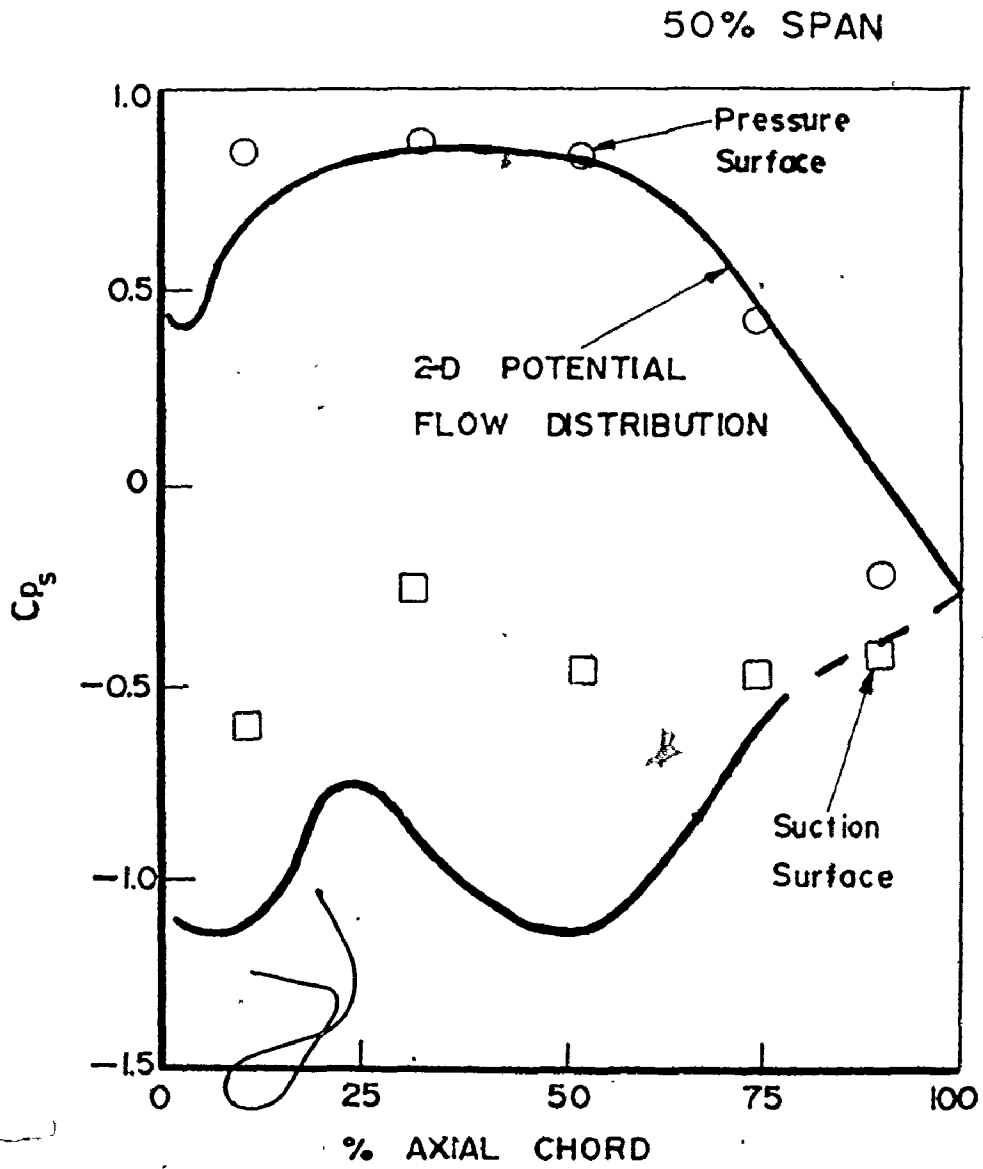
50% SPAN

Fig. 55-b   Blade Surfaces Pressure Distribution
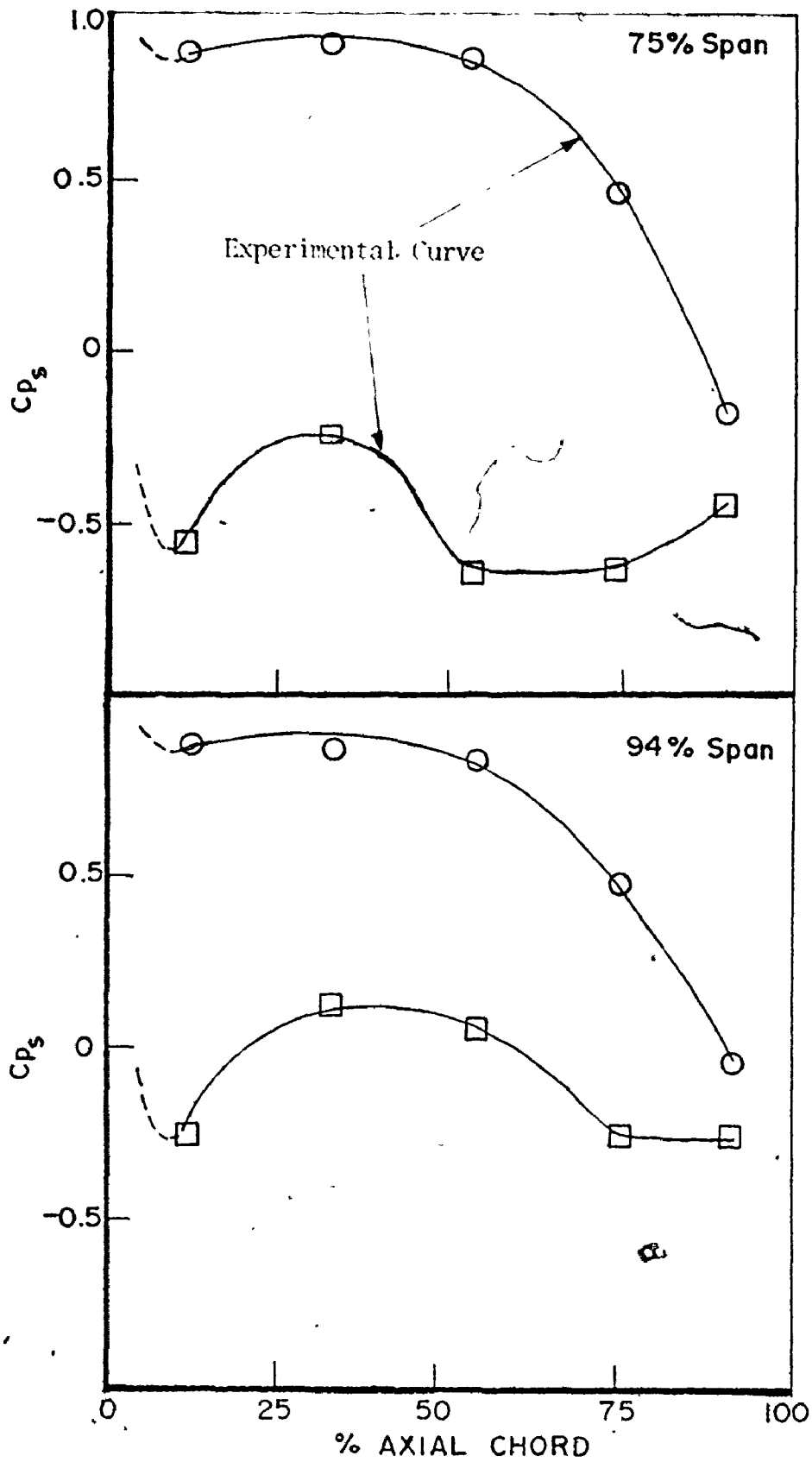
Fig. 55-c   Blade Surfaces Pressure Distribution.

ANNULAR TIP

Pressure side

Suction side

○	10%	Pitch
□	30%	"
◇	50%	"
△	70%	"
◻	90%	"

ANNULAR ROOT

Pressure side

Suction side

○	10%	Pitch
□	30%	"
◇	50%	"
△	70%	"
◻	90%	"

STATIC PRESSURE COEFFICIENT Cp

% AXIAL CHORD
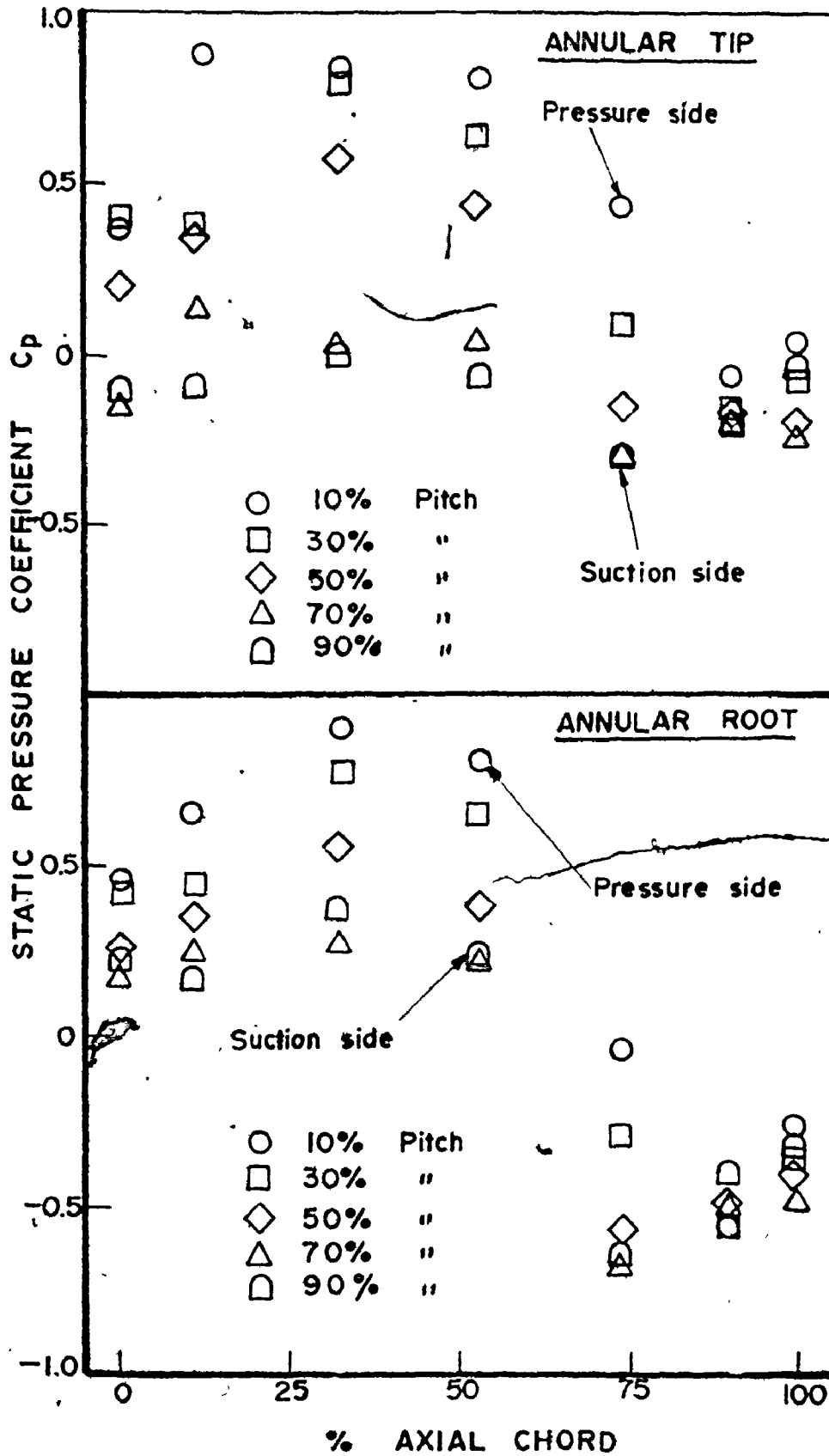
7.2 Pressure Distribution Comparison
   with Theory

The pressure distribution data at 50% span (Fig. 55-b) was compared to the results of a two-dimensional potential flow calculation using a computer program developed by Stannard [38]. On the pressure surface very good agreement can be noticed between the measured and calculated values for all axial chord locations, except near the leading edge where the location of the stagnation point was uncertain and discrepancies were to be expected. On the suction surface a considerable deviation existed between the measured and calculated values, although the shape of the distribution was similar. The deviation started to decrease at about 50% axial chord, until good agreement was found at 75% axial chord. The main reasons for this deviation were the three-dimensionality of the flow and the roll-up of the inlet boundary layer over the suction surface and then into the blade passage as will be described in Chapter 8. The area between the curves formed by the pressure distribution on the pressure and suction surfaces is proportional to the work output of the stage and the lift coefficient for the blade profile. Calculation of the areas enclosed by the pressure and suction side data showed that, as expected the blade had a lower lift coefficient than its ideal two-dimensional counterpart.

7.3   Exit Plane Static Pressure Distribution

Fig. 57 shows the circumferential variation of Cp_s across the cascade exit at the root and tip walls. From this figure it can be noticed that the minimum pressure occurred at a position of 70% circumferential pitch from the pressure surface. A distribution similar to that of Fig. 57 was obtained by Turner [33], Sjolander [34] and Langston [35].

7.4   Blade Passage Pressure Contours

The static pressure measurements made on the annular walls are also presented in Figs. 58 and 59 in terms of isobar contours of Cp_s. In order to provide for a picture of the constant static pressure areas in the blade passage, an incremental ΔCp_s of 0.2 was arbitrarily selected for the annular wall contours. From the graphical presentation it should be noted that the region of minimum pressure (Region 1) on the end wall no longer occurred at the suction surface but had moved into the channel between the two blade surfaces. This low pressure region observed at each blade end can be attributed to the vortex formation in the annular passage due to the turning of the inlet end wall boundary layer. Langston [35] reported recently the same local minimum pressure in his tests conducted on a 110° turning angle turbine cascade passage. Figs. 58 and 59 also show that the pressure gradient, which is normal
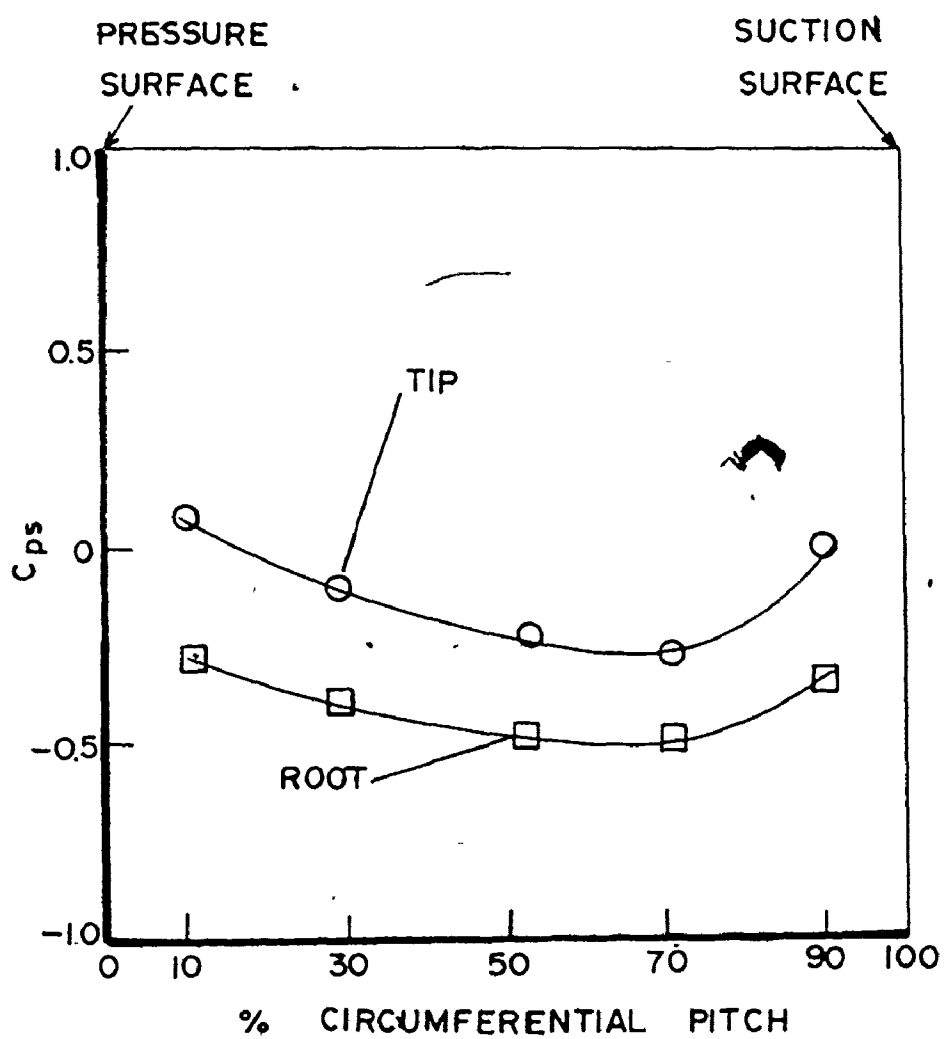
Fig. 57   Exit Plane Static Pressure Distribution.
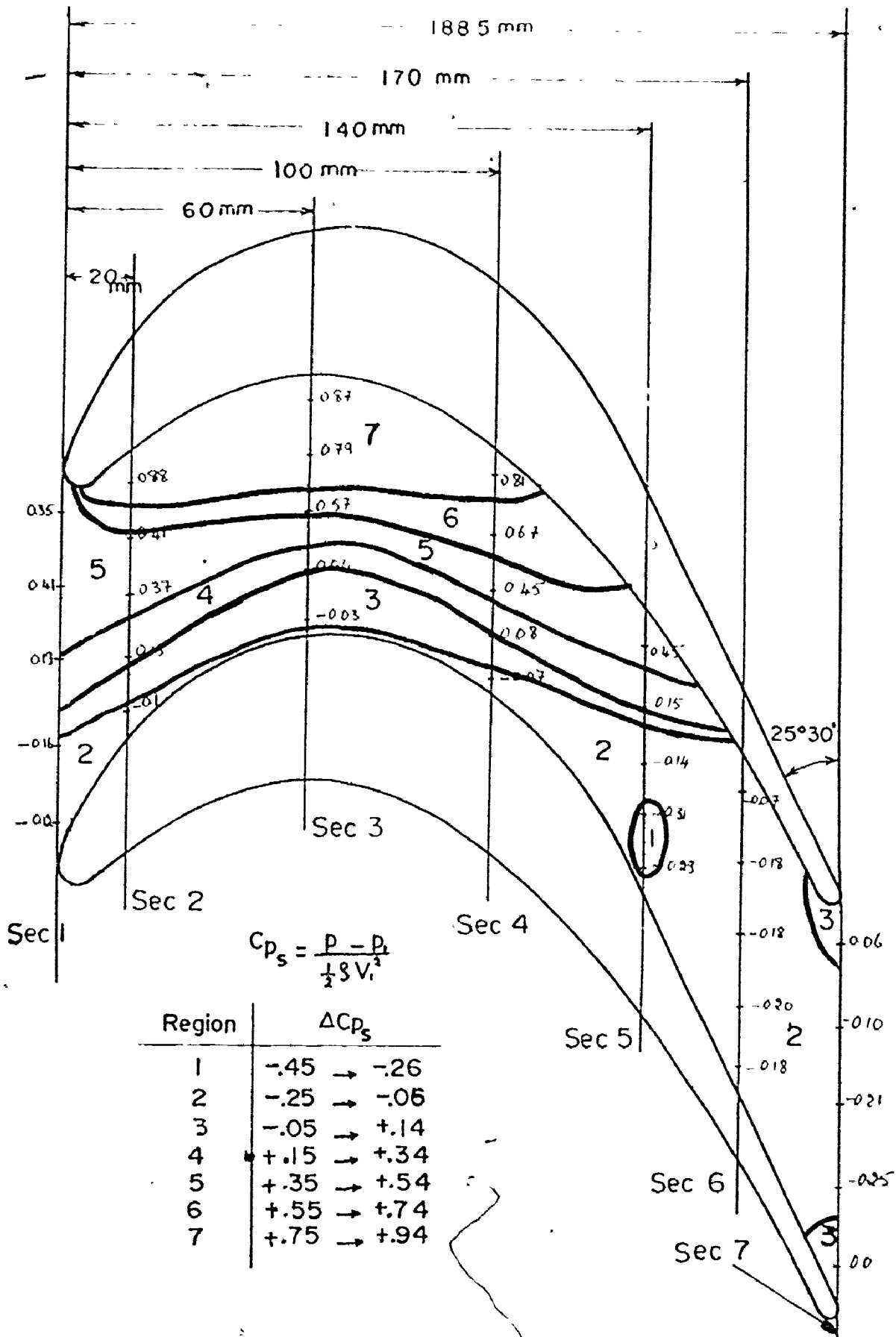
Fig. 58 Cp_s Contours for Annular Tip Walls.
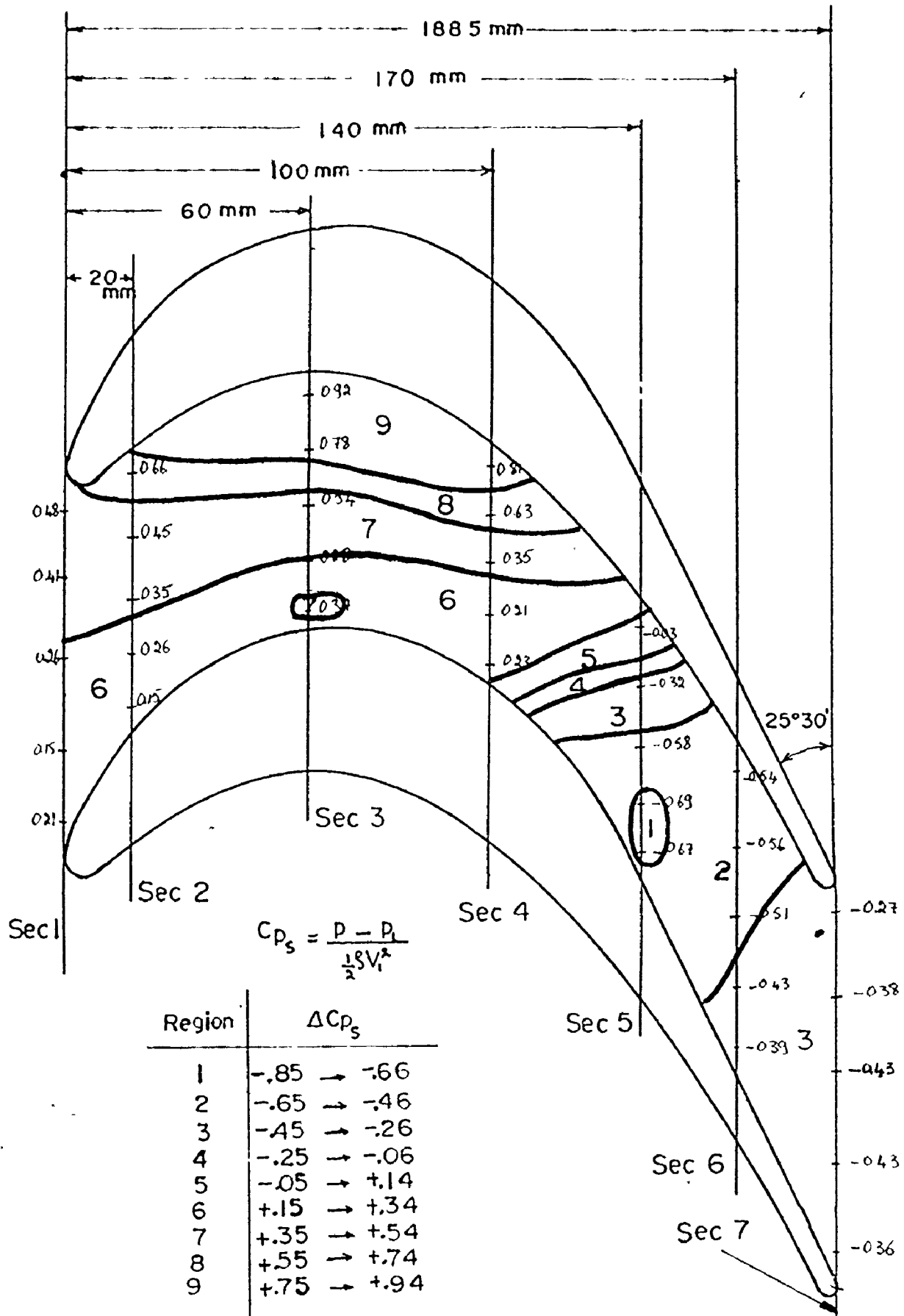
Fig. 59 Cp$_s$ Contours for Annular Root Walls.

to the constant static pressure line, was directed almost
across the passage, particularly in the downstream portion.

Fig. 60 shows the Cp_s contours for the blade suction
and pressure surfaces. Once again an incremental ΔCp_s was
selected arbitrarily in order to define the constant
static pressure areas on the blade surfaces.

The radial pressure gradient between the annular
tip and root, normally created in an annular cascade, can
be observed in all of the pressure distributions and pressure
contours presented in this chapter.
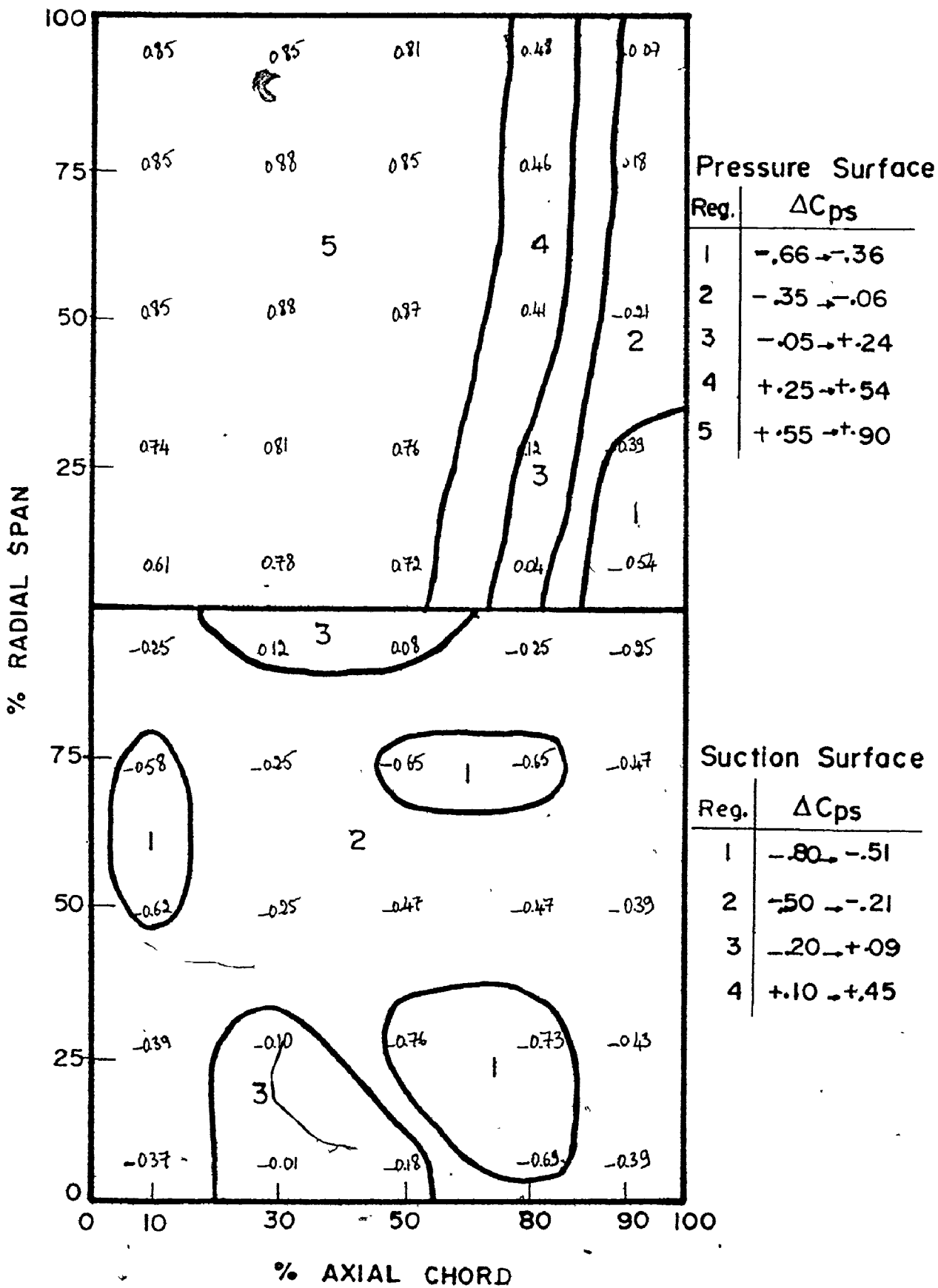
Fig. 60 Cp$_s$ Contours for Blade Surfaces.

CHAPTER 8

A STUDY OF THE EXIT PLANE
FLOW PARAMETERS

The exit plane flow parameters were determined for three
inlet conditions which covered the fan operating range.
The fan speeds were 600, 950 and 1300 r.p.m. correspond-
ing to inlet Reynolds numbers based on the blade chord,
of 3 x 10^5, 4.6 x 10^5, and 6 x 10^5, respectively. For
each test, the inlet flow conditions were determined by
means of radial traverses covering the center blade passage
and a circumferential traverse at the midchannel height.
In order to measure the secondary losses, a flow angle
and pressure survey was performed in the cascade exit
plane at approximately 200 points. The results of these
tests were processed by a digital computer and tabulated
as shown in Appendix D. This section is devoted to the
distribution of the flow parameters in the cascade exit
plane and the associated energy losses in the cascade.

8.1   Inlet Flow Conditions

In order to ensure that the center blade passage
was isolated from the remainder of the annular segment a
circumferential traverse of velocity and yaw angle was

120

performed at midradius. Fig. 61 shows the yaw angle
distribution and the velocity distribution expressed in
a non-dimensional form $V/V_{\mathbb{C}}$, where $V_{\mathbb{C}}$ was the maximum
velocity in the center blade passage. The same periodic
distribution of angles and velocities obtained in the inlet
flow study at one operating speed (Chapter 6), can be
observed to occur at all test rig operating speeds (Fig. 61).

For the purpose of verifying the constant radial
distribution of velocity, a main flow radial traverse was
carried out at three different circumferential locations
in the center blade passage (Fig. 62). Finally a complete
main flow and boundary layer radial traverse was performed
at the circumferential location "$+5^O$" in the center blade
passage. The results of these tests are shown in Figs. 63
and 64.

A summary of the inlet flow conditions to the annular
cascade at the three different speeds has been given in
Table 5 of Appendix D.

8.2 Exit Flow Traverses

The exit main flow was traversed radially and
circumferentially with the three dimensional probe, using
a radial and a circumferential increment of 0.5 inches
($\approx$ 13 mm) and 2^O respectively. A complete survey of
approximately 150 points which covered slightly more than
one passage width, was completed in about 6 hours. For
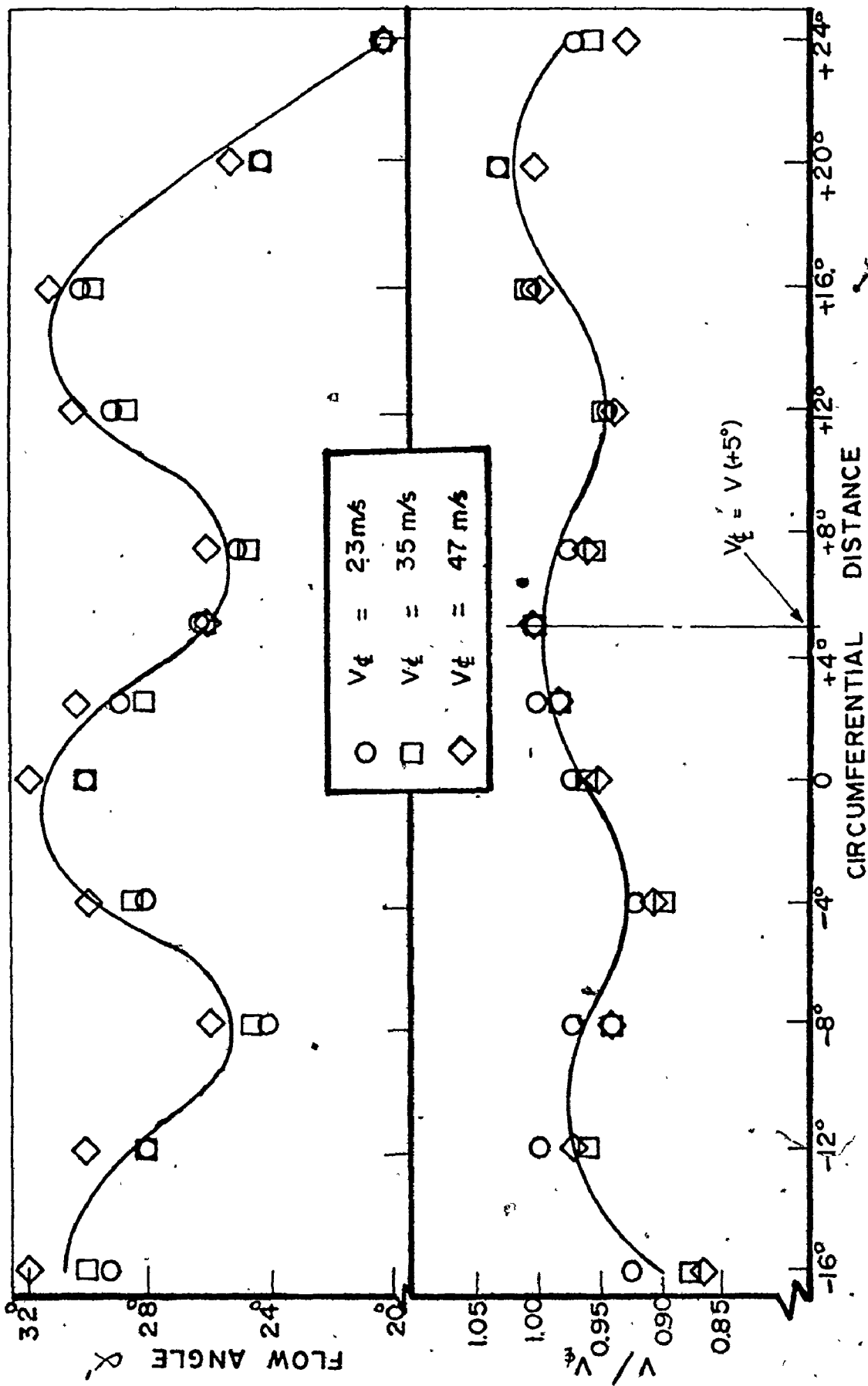
Fig. 61 The Circumferential Distribution of Yaw Angle and Velocity at Midradius at the Cascade Inlet.
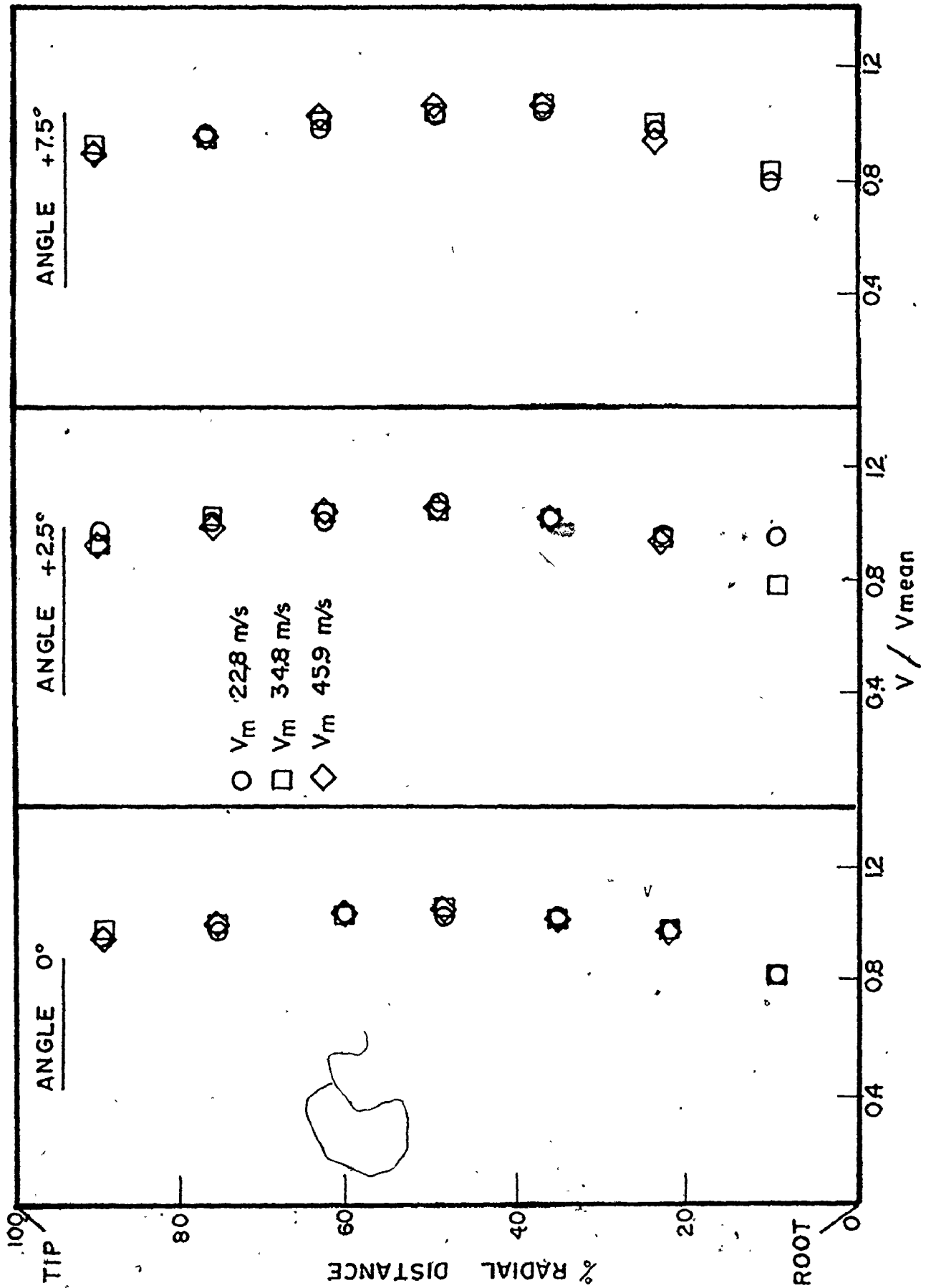
Fig. 62   Radial Distribution of Velocity in the Center Blade Passage
at the Cascade Inlet.
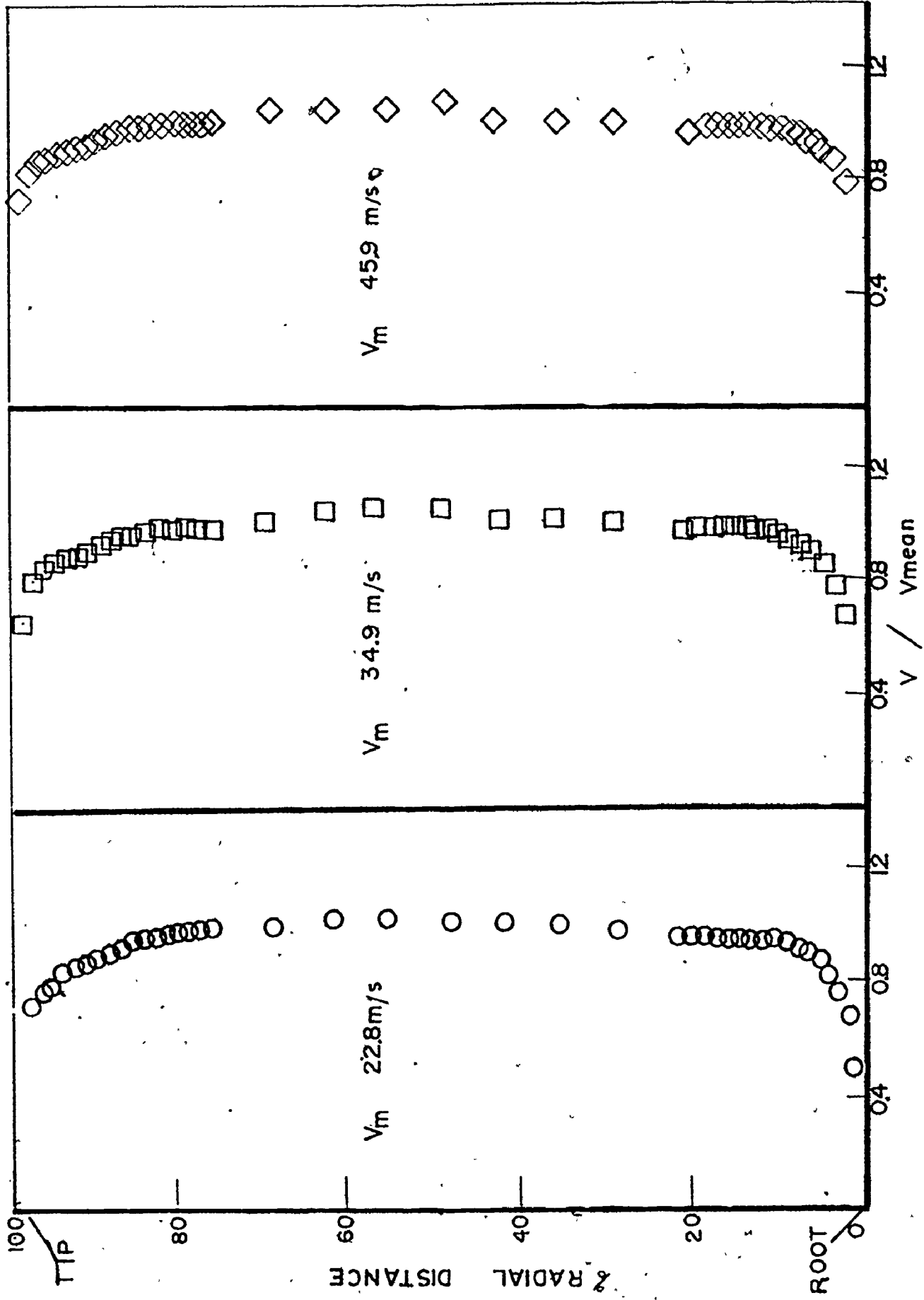
Fig. 63 Main Flow and Boundary Layer Radial Distribution of
Velocity at a Circumferential Position of +5°.
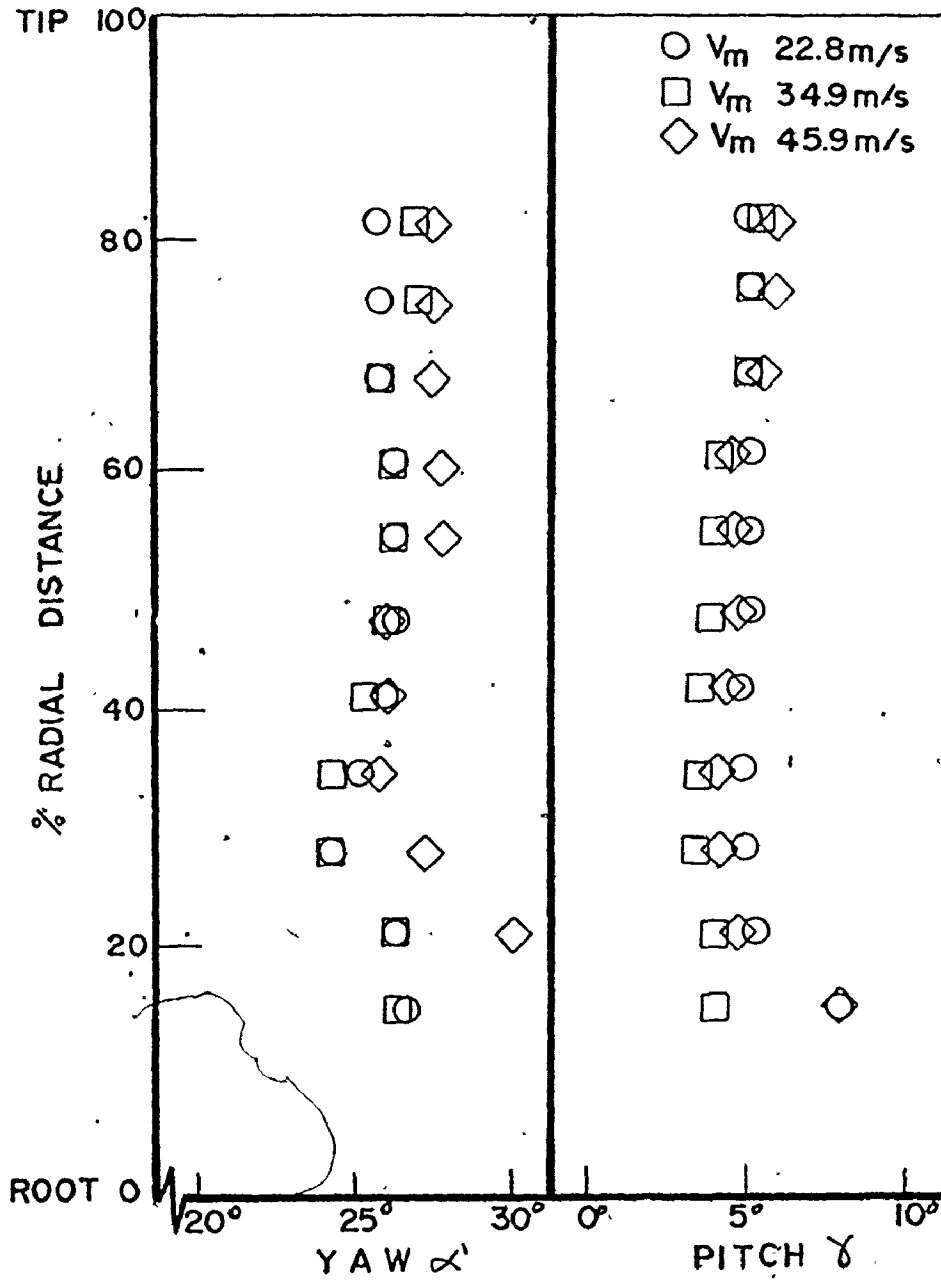
Fig. '64   The Radial Distribution of Both Yaw and
            Pitch Angle at the Circumferential Location
            +5° in the Inlet Plane.

the highest fan speed 200 points were measured to check the repeatability of the exit flow distribution in the adjacent passages. At each point, the probe was first nulled in yaw, and then the yaw angle, indicated total pressure, indicated static pressure and pitch differential pressures were measured using the micromanometers. A computer program (listed in Appendix D) was prepared to process the data. The program computed and tabulated the following local flow parameters at the cascade exit.

(a). The yaw angle (α)

(b) The pitch angle (γ). This was obtained by fitting a polynomial to the probe calibration curve as shown in Appendix D.

(c) The flow velocity (V). The correction for the pitch angle effect on dynamic head was made as described in Appendix D.

(d) The flow axial velocity $(V_a = V \cos\alpha \cos\gamma)$.

(e) The total pressure loss coefficient defined as,

$$Cp_o = \frac{P_{o1} - P_o}{\frac{1}{2} \rho V_1^2} \tag{22}$$

where P_{o1} was the inlet free stream total pressure (mean average at midradius for the center blade passage circumferential locations), $\frac{1}{2} \rho V_1^2$ the corresponding dynamic pressure and P_o the total pressure measured at a point.

(f) The static pressure coefficient defined as,

$$Cp_s = \frac{P - P_1}{\frac{1}{2}\rho V_1^2} \tag{23}$$

where P_1 was the inlet free stream static pressure
and P the static pressure at a point.

A summary of the local flow parameters, items
(a) to (f), is presented in Tables 6 to 8 in Appendix D
for the three operating speeds.

8.3   Total Pressure Loss Contours

Figs. 65 to 67 illustrate the total pressure loss
contours measured at the cascade exit for the three operating
speeds. A ΔCp_o of 0.2 was arbitrarily selected to provide
an engineering picture of the total loss distribution in
the cascade exit plane. In each of these figures, a single
high loss core (identified with the secondary vortex) was
visible at the middle of the blade passage. The evidence
provided by the contour maps made it quite clear that the
material in the vortex came from the suction surface of
the blades. This was consistent with the suggested origin
of the core as a roll-up of the inlet inner and outer wall
boundary layers over the suction surface of the blades and
finally moving into the blade passage. It is suggested
therefore that the fluid in the upstream wall boundary layer
was mostly shed from the trailing edge of the blades as a
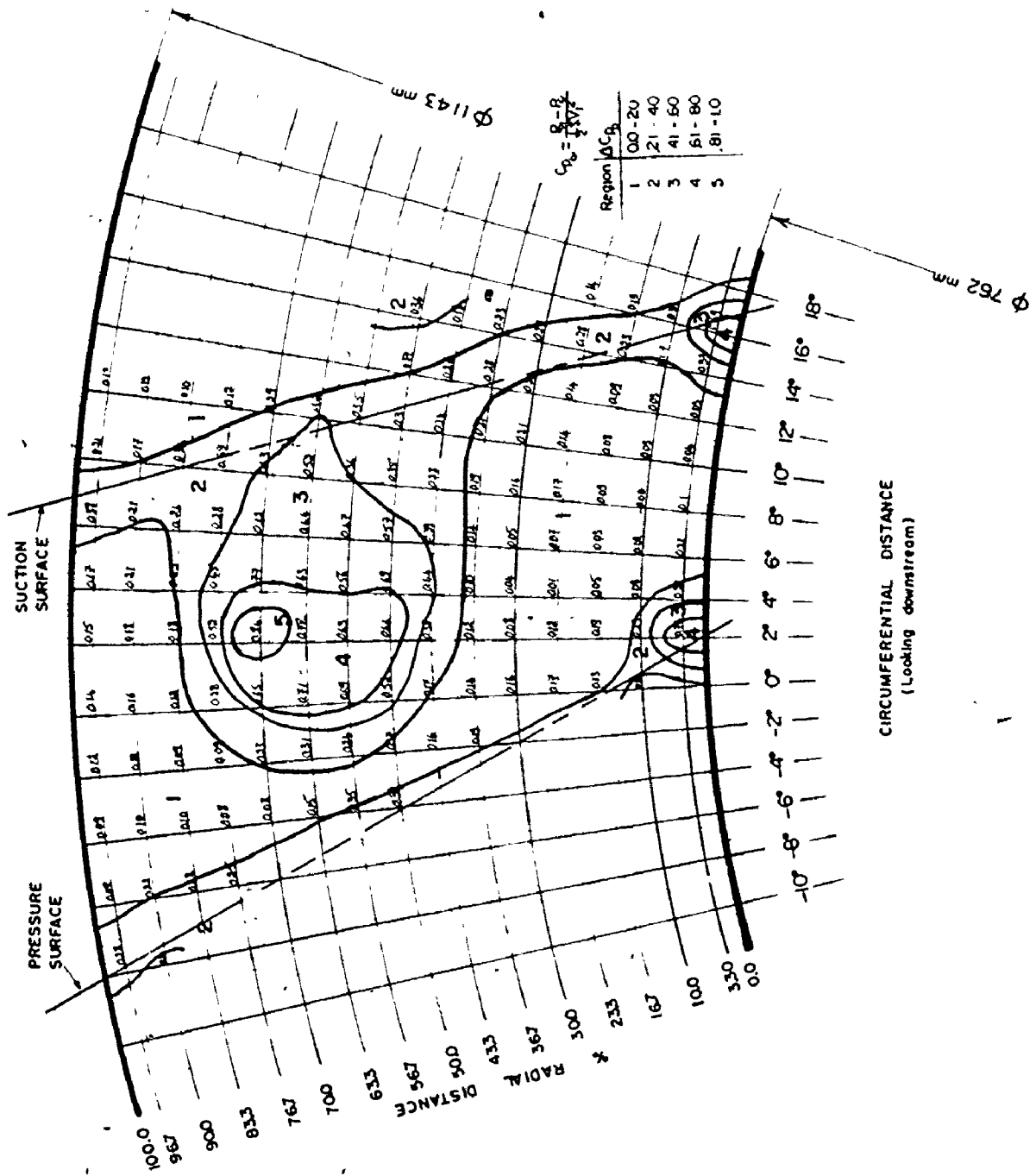
Fig. 65   Total Pressure Loss Contours at the Cascade
          Exit Plane for a R_N of 3×10^5.
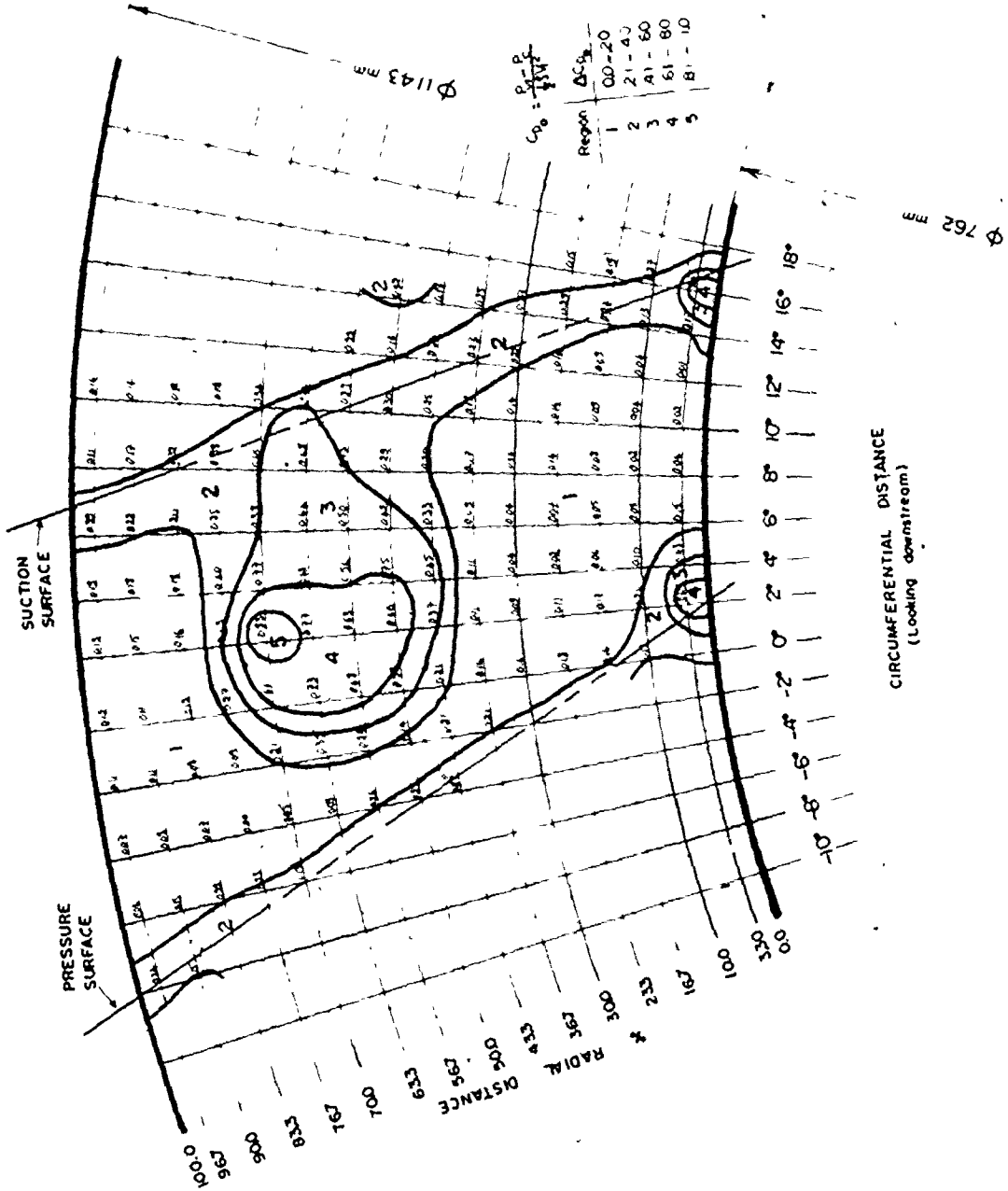
Fig. 66   Total Pressure Loss Contours at the Cascade
Exit Plane for a R_N of 4.6×10^5.
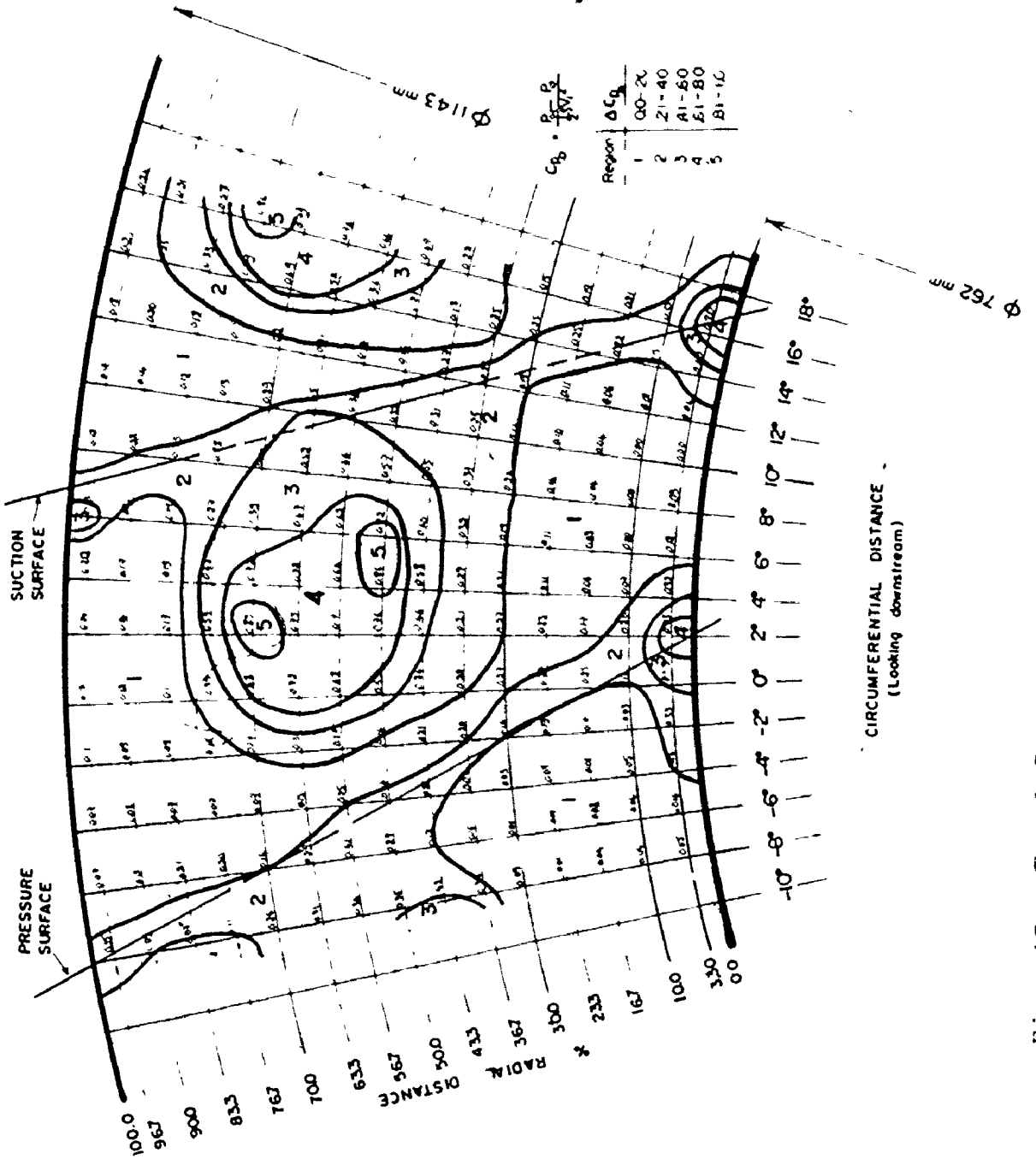
Fig. 67   Total Pressure Loss Contours at the Cascade
Exit Plane for a R_N of 6×10^5.

vortex core loss. Fig. 68 shows schematically the sequence of this vortex formation at different axial locations along the cascade.

An interesting feature of the total pressure contours was the fact that normally one expected a high loss core at each blade end corresponding to the inlet inner and outer wall boundary layers. In the present tests these areas, shown as region '5' in Fig. 67, were found at the highest test velocity to be located in the middle of the passage. For the lower inlet velocities it has been experimentally shown that the two peaks combined to give a single peak as shown in Figs. 65 and 66. In 1953 Loos [10] had speculated this behaviour for large turning angle blades, but according to the literature this fact had never been verified. Fig. 69 has been extracted from Loos's analysis and shows his expected location of the secondary vorticity pattern.

The results of three more recent tests, carried out by other researchers, were selected (starting with the lower turning angle) to verify and compare their secondary flow patterns with the present experimental results.

Sjolander [34] in his tests carried out in 1975 on an annular cascade of 50° deflection, obtained two peak losses, each near the suction surface of the blade at approximately 25% span from the end wall. Came [30] reporting on tests conducted in 1973 on a rectilinear cascade having a total deflection of 84°, found that the two

Tip

Pressure
Surface

Inlet Boundary
Layer

Suction
Surface

Root
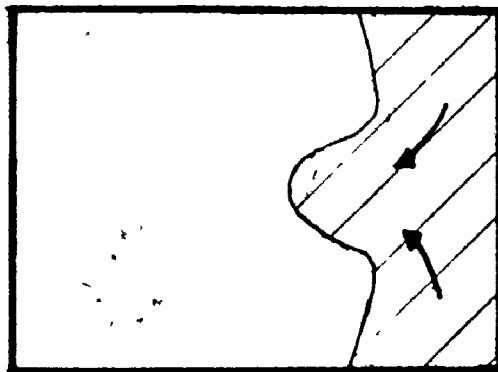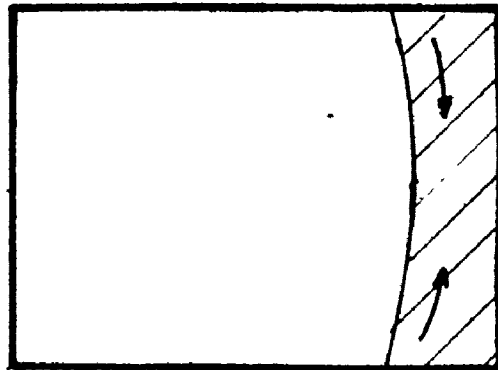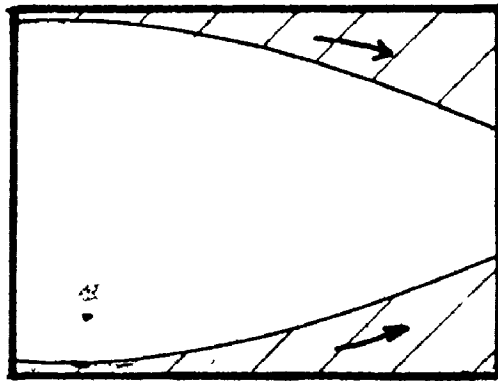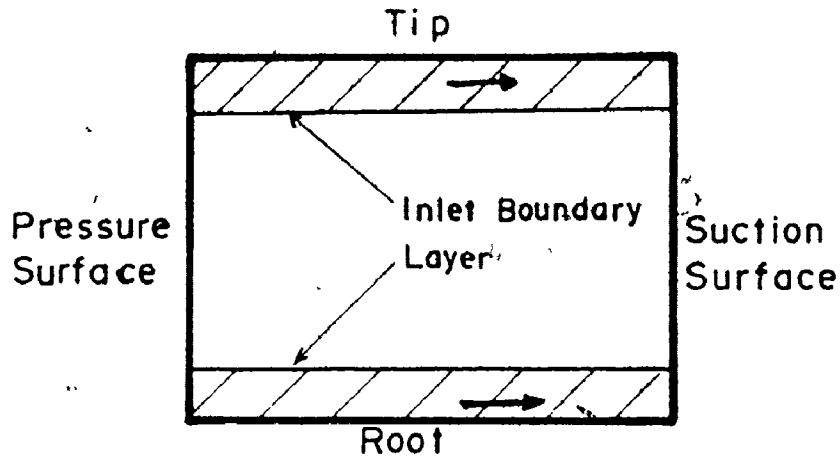
Fig. 68   A Schematic Drawing Indicating How the Inlet
Boundary Layer Moves to the Suction Surface
to Form a Vortex.

TIP WALLS

PRESSURE
SURFACE

SUCTION
SURFACE

ROOT WALLS
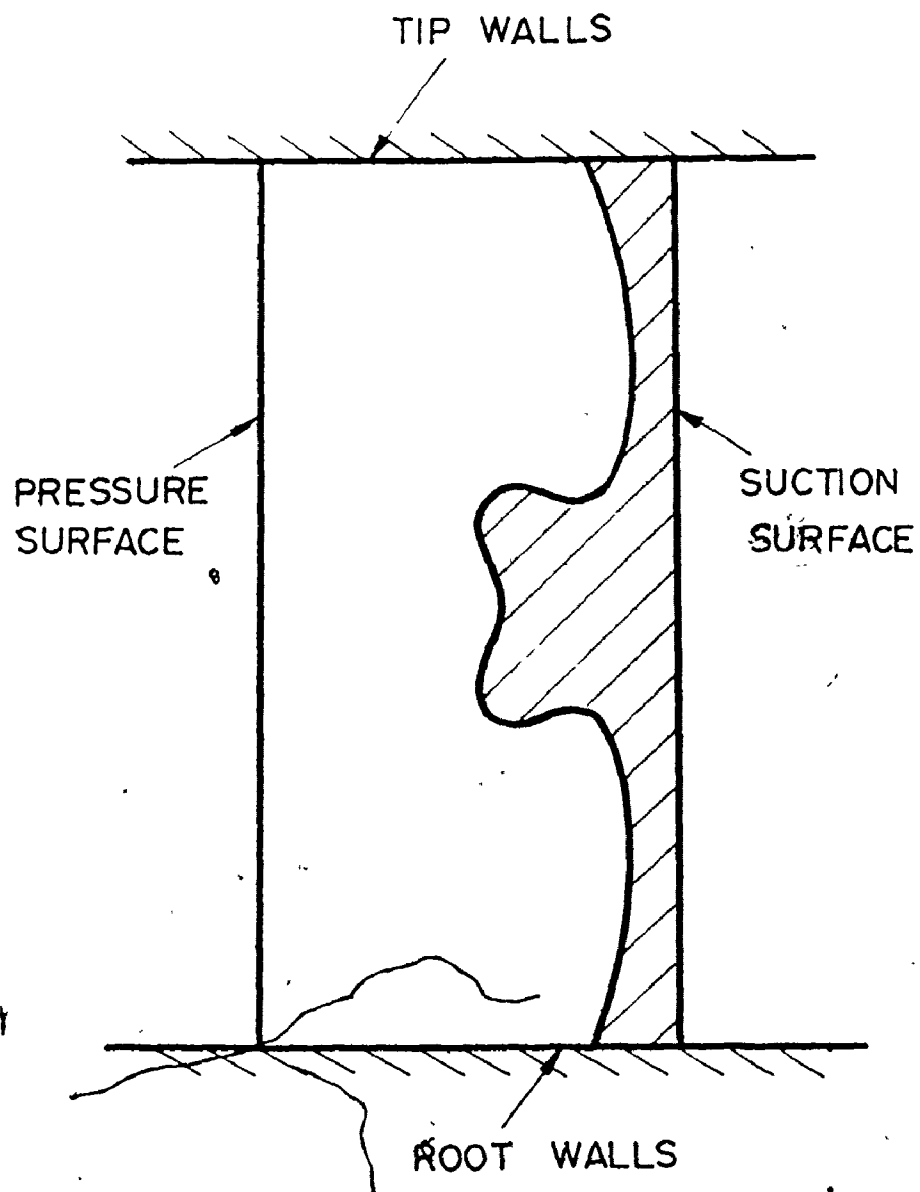
Fig. 69 The Vorticity Pattern for Very Large
Turning Angles as Suggested by Loos [10].

peaks grew in size and started to move away from the blade suction surface. In 1977 Langston [35] in tests done on a rectilinear cascade of 110° deflection obtained similar results to Came.

As a result of the work shown in the literature and the present experimental data it can be concluded that, as the blade turning angle increases the two peak losses combine to form one large single vortex core which is displaced from the suction surface into the middle of the passage. The overall annular cascade geometry is believed to have an effect on the shape and the displacement of this vortex. A third possible reason for the displacement of the vortex core into the middle of the passage could be due to the fact that the present blade passage had a lower pitch to chord ratio at the hub than at the tip. There was also the possibility that the geometry of the corner between the suction surface and the annular root contributed to the motion which forced the vortex to move upwards.

Examining Figs. 65, 66 and 67 further, a weaker high loss region was also seen at the inner wall in the region downstream of the trailing edge of the blades. At the outer wall similar regions were also apparent but with a loss magnitude smaller than that for the inner wall. These loss regions were caused by the growth of the new wall boundary layer. The reason for the difference in magnitude between the losses at the inner wall and the outer wall could

be attributed to two factors. The first factor was undoubtably the thicker boundary layer measured at the cascade exit inner wall when compared to that measured on the outer wall as shown in Fig. 70. The second factor could have been due to the spanwise pressure gradient in the annular cascade. This gradient might very well have been responsible for sweeping some of the low energy air in the inlet outer wall boundary layer down to the trailing edge resulting in larger hub than tip losses. Rohlik [31] observed this fact in his tests carried out on an annular cascade.

8.4   Exit Plane Yaw Angle Contours

Figs. 71 to 73 show the flow yaw angle contours measured at the cascade exit. For the presentation, a $\Delta\alpha$ of 10° was arbitrarily chosen in order to provide an overall impression of the flow angle characteristics in the exit plane. Normally due to the roll-up of the inlet boundary layer in the blade passage, a streamwise component of vorticity is created at each blade end. This vorticity component produces radial and tangential secondary velocities which result in overturning of the flow near the wall and underturning in the mainstream. The yaw angle contours revealed some new interesting features for the three test conditions. Due to the thicker inner wall boundary layer as shown in Fig. 70, more low energy fluid rolled over the blade suction surface and met the outer wall boundary layer
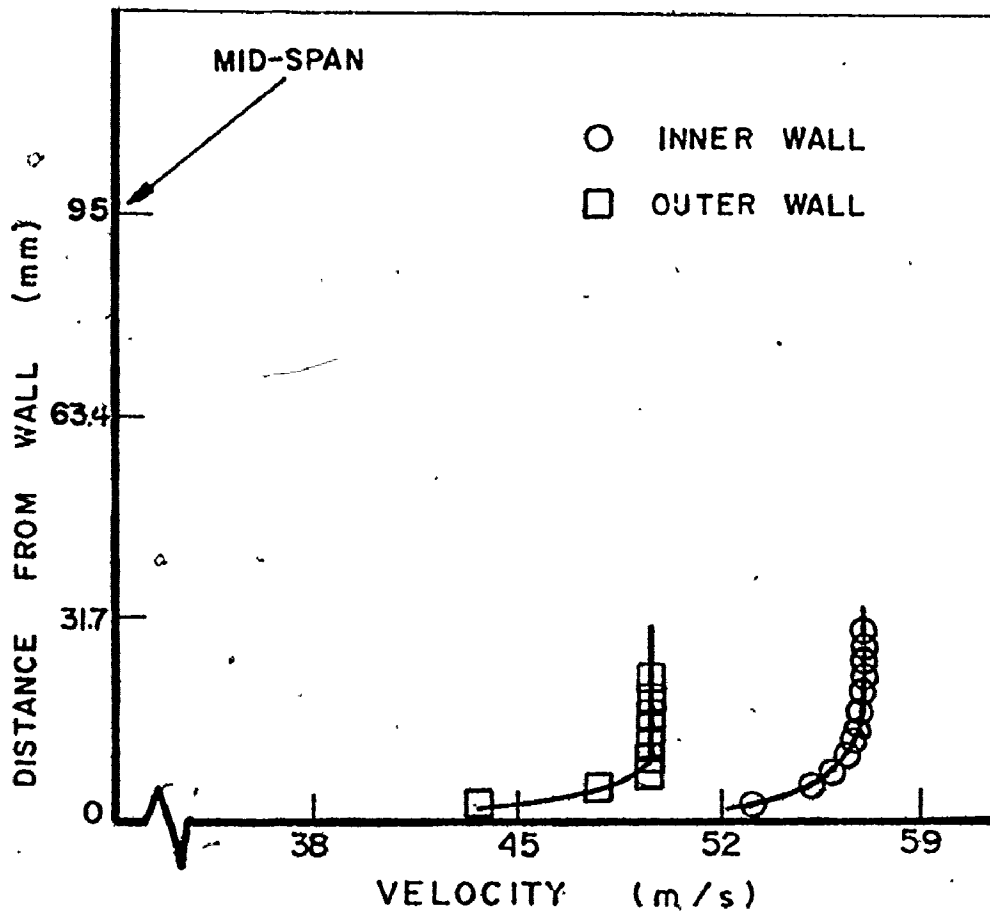
Fig. 70   Boundary Layer Profile Measured in the Plane
of the Trailing Edge at a Mean Inlet Velocity
of 45.9 m/s.
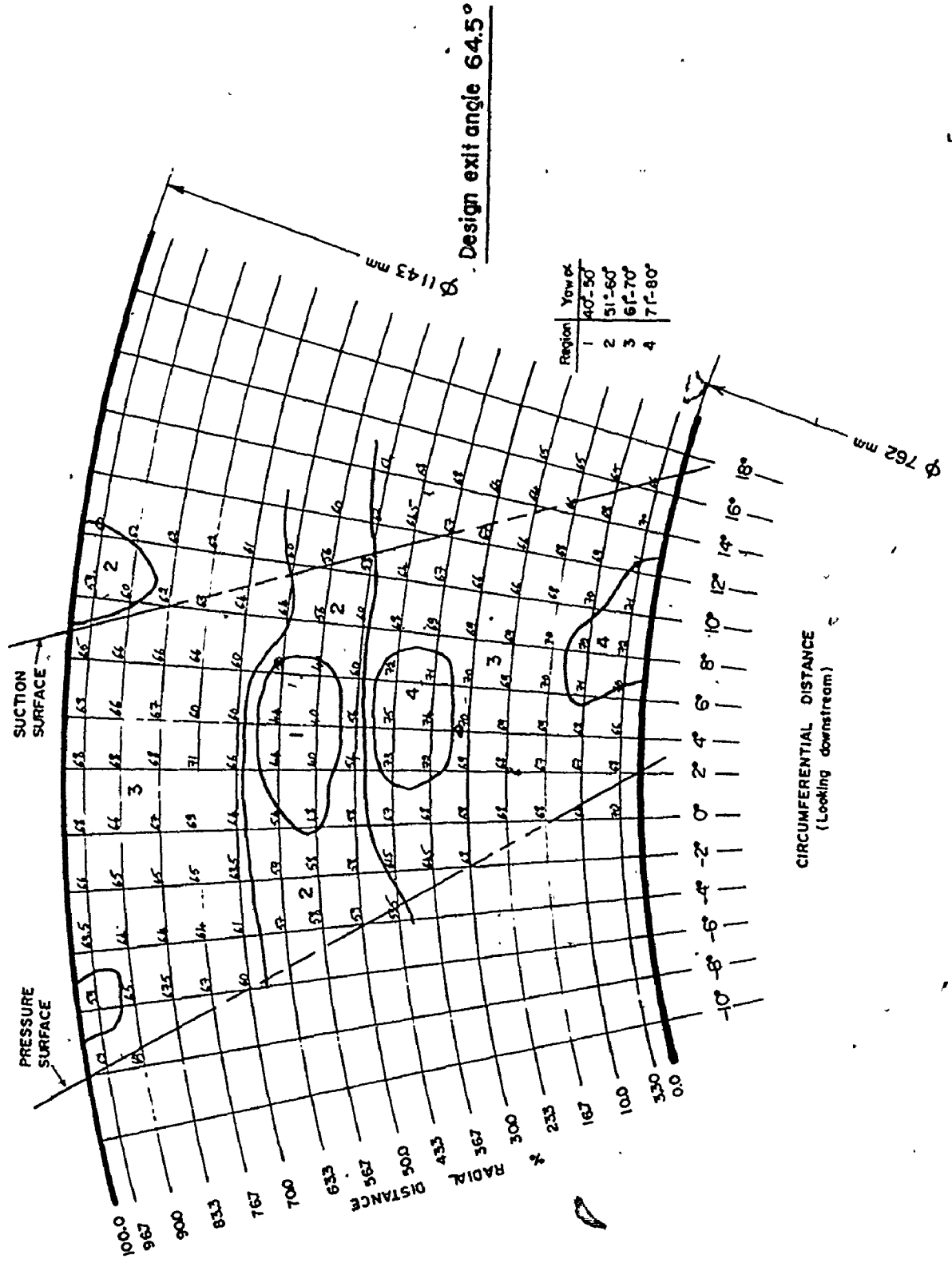
Fig. 71 Yaw Angle Contours at the Cascade Exit Plane for a P_N of 3×10^5.
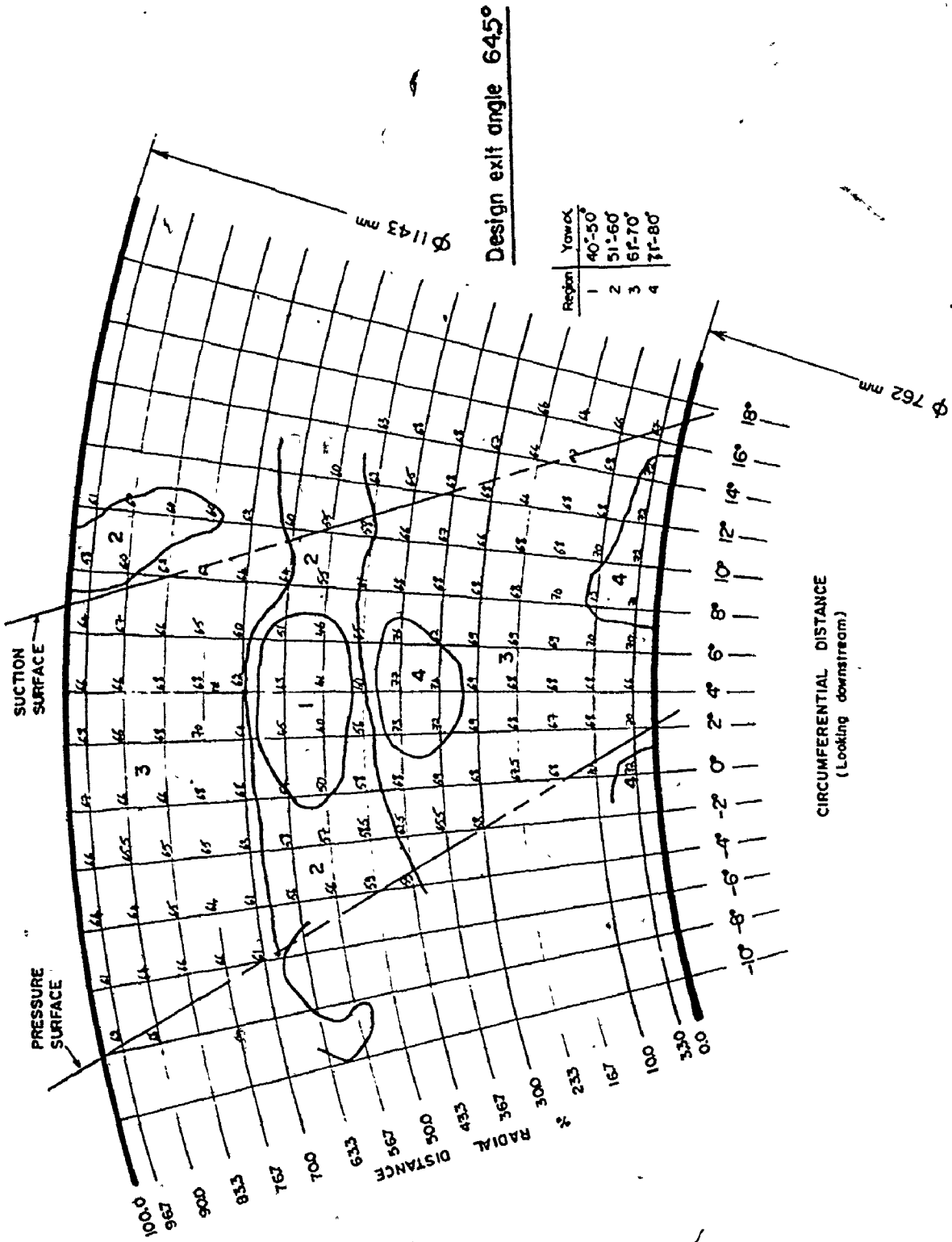
Fig. 72 Yaw Angle Contours at the Cascade Exit Plane for a R_N of 4.6×10^5.
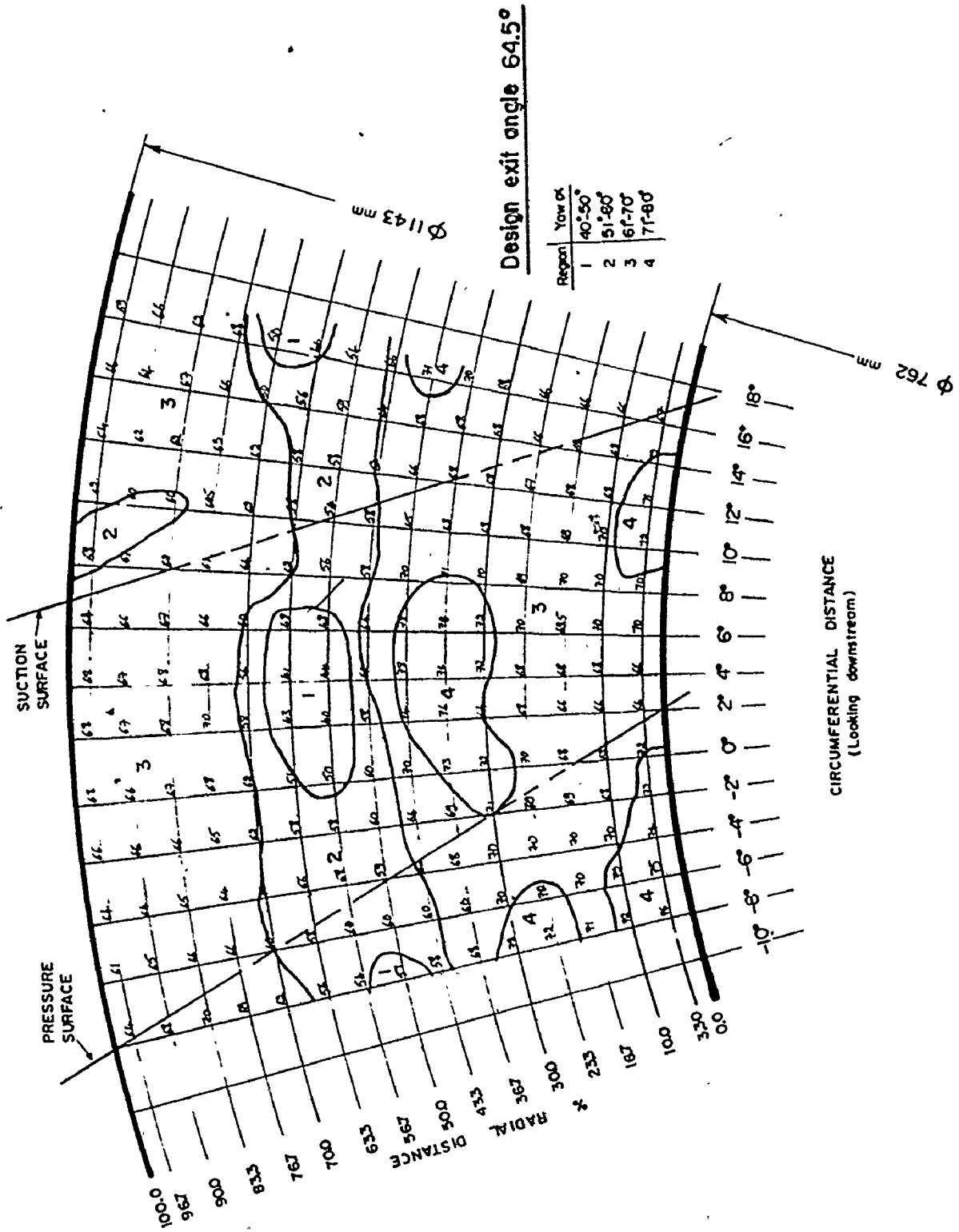
Fig. 73 Yaw Angle Contours at the Cascade Exit Plane for an R_N of 6 x 10^5.

fluid at a position above midspan (approximately 63%
radial distance). This coalescence of the boundary layer
fluids created a single strong vortex which resulted in a
large underturning (up to 24° less than the design exit
angle) at a position which was approximately 57% of the
span (Region No. 1). The vortex was also responsible for
a large overturning (up to 14° greater than the design angle)
at a position approximately 43% of the span (Region No. 4).
One also can notice the high shear experienced in this
region where the flow angle changed by 35° per inch. This
flow picture was verified later by flow visualization using
smoke injection. It is worth mentioning in this analysis,
that the flow yaw angle readings were very unstable ($\pm 5^O$)
at 50% span at the circumferential location $+2^O$, $+4^O$ and $+6^O$.
These locations coincided with the center of the passage
vortex. It was expected that the experimental measurements
made in this region, using the three dimensional probe,
were subjected to much greater errors than would be found
by taking readings in a 'normal' flow field. Areas of
lower overturning can also be seen in the yaw angle contours
near the end walls (Region 3). The presence of Region No. 4
near the hub wall only was probably due to the thicker inner
wall boundary layer. Fig. 74 is an artistic interpretation
of the overall flow picture as described by the yaw angle
contours. It can be seen that the sweeping of the boundary
layer fluid over the suction surface of the blade and then
into the passage in a certain fashion so as to create
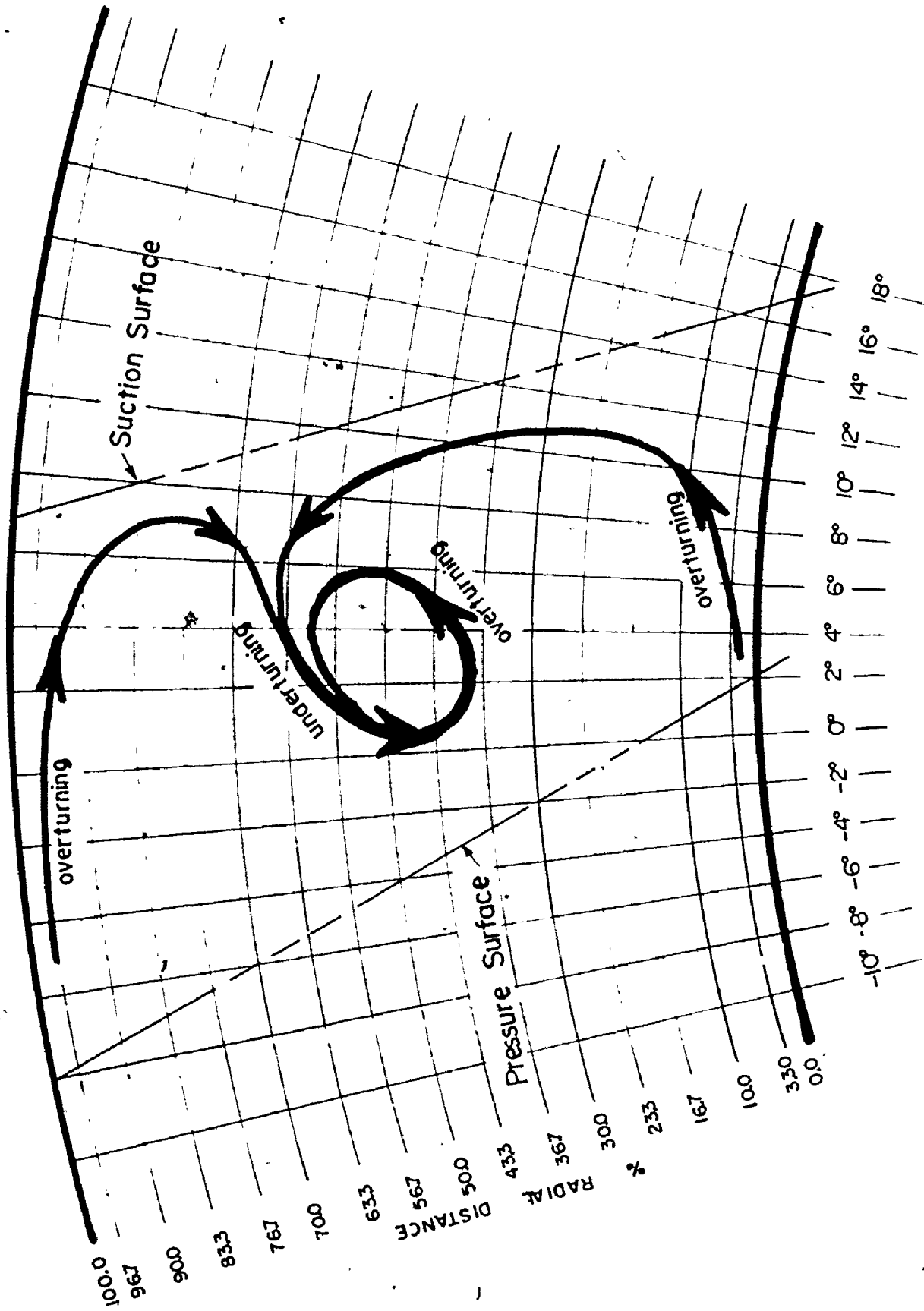
Fig. 74 Physical Interpretation of the Yaw Angle Contours in the Exit Plane.

significant overturning and underturning in·the main flow.

In conclusion,· the single passage vortex formed by the inner and outer wall boundary layer fluids resulted in significant regions of both underturning and overturning in the main stream area.

8.5   Static Pressure Contours

Fig. 75 shows the contours of static pressure coefficient Cp_s at the cascade exit. Seven regions of constant static pressure coefficient were selected with an equal interval of 0.05 to evaluate the flow field.

Normally if the flow were potential flow, lines of constant Cp_s would be straight lines, parallel to the blade surfaces and normal to the annular walls. The position of the low static pressure regions Nos. 6 and 7 confirmed the fact that the passage vortex dominated the flow in the middle of the passage. Langston [35] obtained similar isobars of static pressure at the cascade exit with the lowest pressure region displaced into the passage near the suction surface of the blades.

8.6   Spanwise Variation of Flow
Angle and Pressure Losses

Further information about the patterns of the blade passage losses and exit angles were obtained by a further analysis involving the loss coefficients and exit· flow angles. At each radial position the loss coefficients and
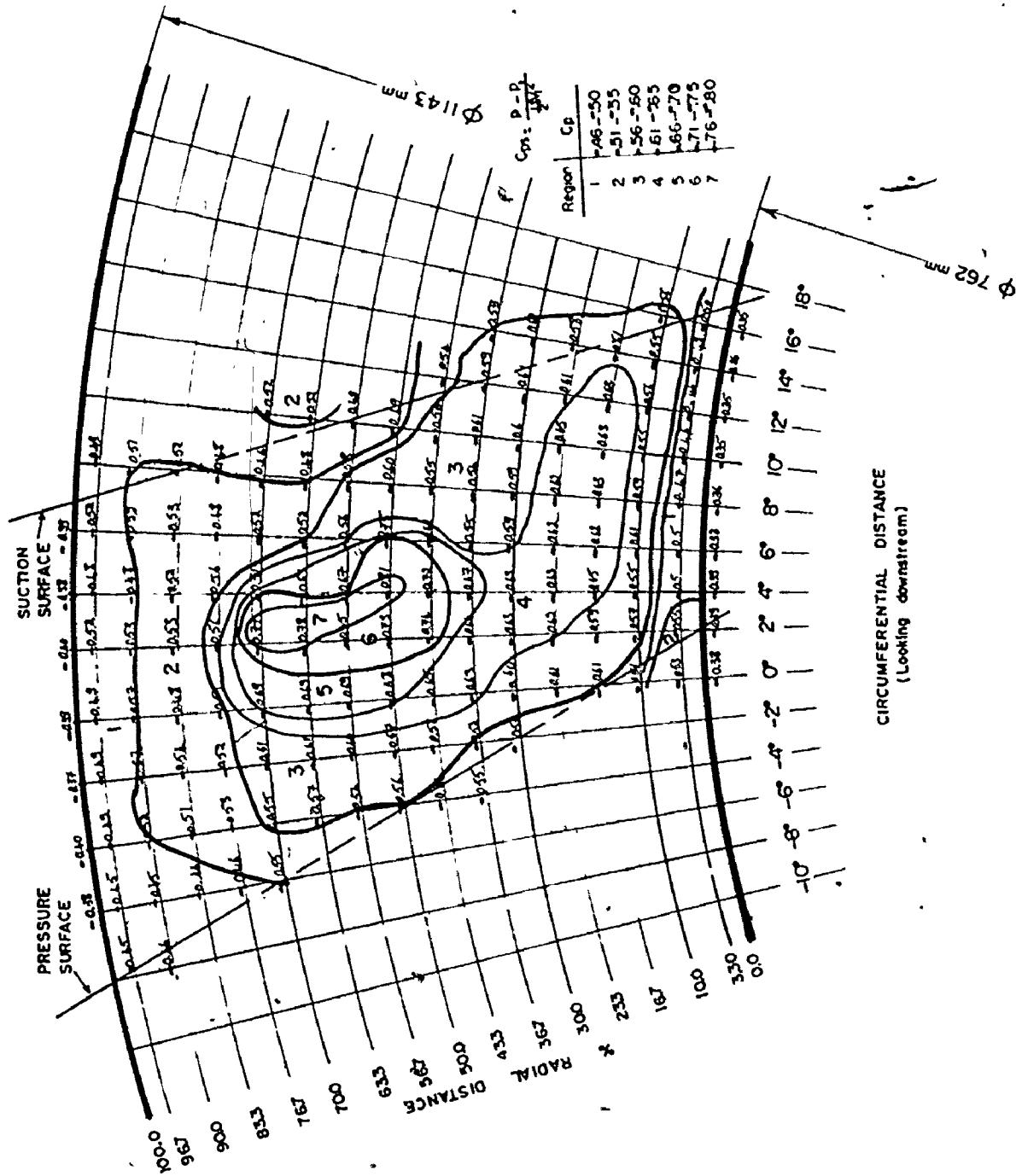
Fig. 75 Contours Showing the Static Pressure Distribution in the Exit Plane of the Cascade for a $R_N \sim 4.6 \times 10^5$.

flow angles for the different circumferential points were averaged on a mass flow basis. This was done using the data processing program listed in Appendix D. The mass average total pressure loss coefficient at each spanwise location was defined as follows:

$$Cp_{om} = \frac{\sum\limits_{o}^{S} Cp_0 (V\cos\alpha\cos\gamma)}{\sum\limits_{o}^{S} (V\cos\alpha\cos\gamma)} \qquad (24)$$

where V_a = $V\cos\alpha\cos\gamma$, and Cp_0 is defined in Section 8.2. A similar definition was used for the mass averaged yaw angle. These values together with the arithmetic means of yaw angles, losses, and velocity (both absolute and axial) are tabulated in Appendix D.

Fig. 76 shows the variation of the pitchwise mass averaged losses as a function of the radial distance. From this figure a single loss peak was visible at about 60 percent of the span corresponding to the peaks already presented in the loss contours (due to the secondary vortex). At a radial distance of about 10% and again at 90%, the pressure losses as defined by an average contour started to change direction to account for the pressure losses in the newly developed tip and root boundary layers. The pressure losses at the annular root were higher than that at the tip for a corresponding location due to the factors mentioned in Section 8.3. Came [30] obtained similar distributions,
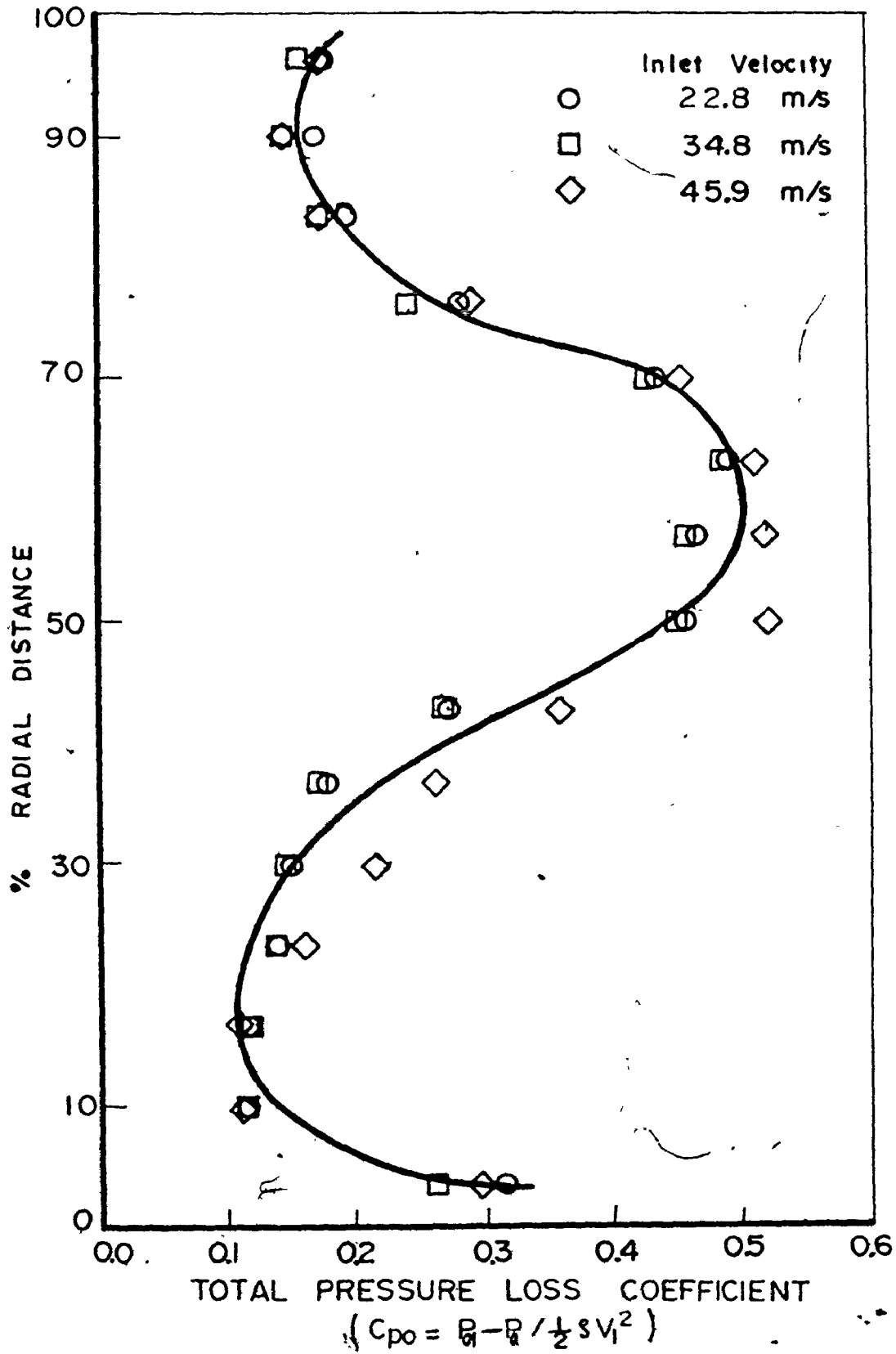
Fig. 76 Radial Variation of the Pitchwise Mass Averaged
Total Pressure Loss Coefficient.

but with two peak losses in the center of the passage outside the boundary layer regions. The area under the pressure losses curve (averaged on span) represents the overall losses in the cascade including the secondary losses, end wall boundary layer losses and the profile losses on the blade surfaces. It is of interest to note at this point that the exact extent of the profile losses is difficult to define, as both profile and secondary losses interact with each other especially in a high turning angle cascade.

Fig. 77 shows the spanwise variation of the pitch-wise mass average yaw angles. Again the overturning in the lower and upper half of the passage, and the under-turning in the center of the passage is quite apparent. The distribution as shown is in general agreement with all previous results [1, 10, 12, 14, 17, 18, 19 and 29] with the exception being that in the present high turning angle cascade the two regions of underturning have combined to form a single and much stronger region of underturning located near the center of the passage.

8.7 Comparison of the Cascade Exit Flow Angle with Existing Data

The first problem in comparing exit flow angle with other data was the choice of some single value of outlet angle change that would be useful and indicative of the measured flow pattern. The radial variation of the pitch-
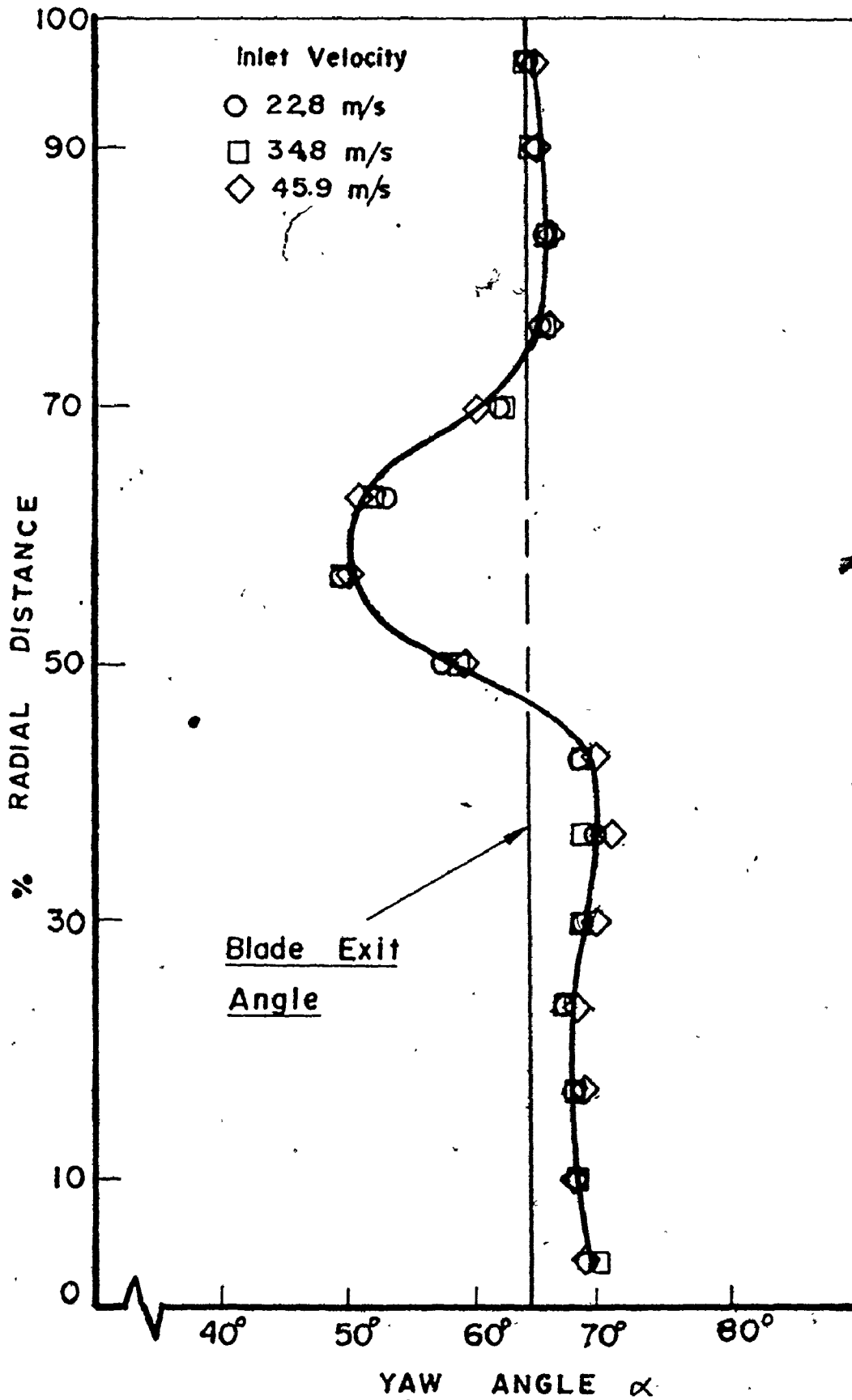
Fig. 77   Radial Variation of the Pitchwise   Mass Ave

wise (or circumferential) average values could only reflect the distribution of angles across the passage exit. On the other hand, an average value of the radial distribution would have little meaning, since due to over-turning and underturning of the flow the average value could be approximately equal to the design exit angle.

The maximum value of overturning in the spanwise direction was somewhat unreliable due to the uncertainty in measuring flow angles with the present probe in the vicinity of the wall. However, the region of underturning occupying a considerable portion of the blade passage and clearly a function of the secondary flow might well be selected to represent the exit flow angle changes. A comparison of the calculated or measured maximum flow under-turning in the radial direction is given in Table 3. The tabular values presented indicated two points. One concerned the lack of experimental results in high turning angle cascades particularly the measurement of flow angles in the exit plane. Secondly, it was apparent that the degree of underturning was in some fashion proportional to the blade turning angle.

8.8 Comparison of the Cascade Overall Loss Coefficient with Existing Correlations

In order to compare the cascade secondary loss coefficient with existing data and correlations, the overall pressure loss coefficient was calculated and tabulated in

Table 3

A Comparison of Maximum Flow Under-
turning in the Radial Direction

References	Blade Turning Angle	Maximum Underturning
Lakshminarayana [17]	20°	1.8°
Dixon [22]	64.2°	4°
Rohlik et al [31]	60°	6°
Moffatt [18]	20°	1.2°
	50°	4°
Hawthorne [19]	40°	8°
	100°	18°
Present tests	$128^\circ 30'$	11.5°

Appendix D, along with the other exit plane parameters.

The cascade loss coefficient mass-averaged in pitch and span
was defined as:

$$Y_T = \frac{\Delta P_T}{P_{o2m}-P_{2m}}$$ (25)

where

$$\Delta P_T = \frac{\sum\limits_{0}^{h}\sum\limits_{0}^{S}(V\cos\alpha\cos\gamma)\Delta P_o}{\sum\limits_{0}^{h}\sum\limits_{0}^{S}(V\cos\alpha\cos\gamma)}$$ (26)

ΔP_o = local total pressure losses = $P_{o2}-P_{o1}$

P_{o2m} = mean exit total pressure = $P_{o1}-\Delta P_T$

P_{2m} = mean exit static pressure = $P_1-\Delta P_S$ (where
ΔP_S was defined in the same manner as ΔP_T
shown above).

In order to calculate the cascade secondary losses,
one would normally calculate or estimate the passage profile
loss. As mentioned earlier in this chapter, the extent
of the profile losses could not be separated from the total
losses which were calculated unless detailed measurements
of the velocity distributions and boundary layer growth
on the blade surfaces were performed. Denton [28] in 1973
reviewed seven different profile loss correlations and
concluded that none of them predicted the losses accurately.
However it was decided for the present cascade, to compute

the profile losses by means of three different existing correlations. The correlations used gave the following values of profile losses at the maximum inlet velocity

Ainley's Correlation, 1951 [26] $Y_p = 0.11$

Baljé's Correlation, 1968 [27] $Y_p = 0.05$

Denton's Correlation, 1973 [28] $Y_p = 0.03$

An approximate value of the secondary loss coefficient was then obtained by a simple subtraction, i.e.,

$$Y_s = Y_T - Y_p \qquad (27)$$

Fig. 78 shows the variation of the secondary loss parameter with the relative upstream boundary layer displacement thickness. The blade loading factor Z in the loss parameter is defined as:

$$Z = (\frac{C_L}{S/C}) \frac{\cos^2 \alpha_2}{\cos^3 \alpha_m} \qquad (28)$$

where the lift coefficient C_L has the form:

$$C_L = 2 \frac{S}{C} (\tan\alpha_1 - \tan\alpha_2) \cos\alpha_m \qquad (29)$$

Shown in Fig. 78 are the nominal value of the secondary loss parameter used in turbine performance predictions, the Dunham [3] and Came [30] correlations and other test results reported in Ref. [30]. The total and secondary loss parameters found in the present study are also shown in Fig. 78. From this presentation it can be seen

Legend:
- ——————— Nominal value for turbine calculations (Ref. 30)
- ——————— Dunham loss correlation (Ref. 3)
- ——————— Came loss correlation (Ref. 30)
- ○ Other test results reported in Ref. 30
- ■ Y_t measured
- ◆ Y_s based on Ainley's Y_p correlation
- ▲ Y_s based on Baljé's Y_p correlation
- ⬟ Y_s based on Denton's Y_p correlation

Present tests

Y-axis: SECONDARY LOSS PARAMETER $\left(\dfrac{h}{C} \dfrac{Y_s}{Z} \dfrac{\cos \beta_1}{\cos \alpha_2}\right)$

X-axis: RELATIVE UPSTREAM BOUNDARY LAYER DISPLACEMENT THICKNESS (δ_1^*/c)

Fig. 78 A Comparison of the Annular Cascade Loss Coefficients with Existing Correlation.

that the present results agreed quite well with the available correlations. However it should be noted that most of the previous results listed in the literature measured the exit losses at some distance downstream from the trailing edge (about one chord length), thus including the mixing losses due to the trailing shed and trailing filament vortices. Came [30] measured the exit losses at different distances from the trailing edge and found a rising trend up to a distance equal to 120% of the chord. Langston [35] measured the cascade losses from the inlet section to the blades to a downstream location, 140% of the chord from the trailing edge, and found a significant rise in losses of 24% between 1.1 C and 1.4 C. If one assumed a factor of 1.24 to account for the effect of the mixing losses such as suggested by Langston[35], then the present experimental results could be plotted as shown in Fig. 79.

8.9 Blade Passage Flow Visualization

In order to obtain a qualitative description of the flow field in the blade passage, flow visualization using white smoke was conducted on the annular rig. Smoke was injected at the inlet measuring station, on the inner and outer wall boundary layer regions, to check the roll up of the boundary layer fluid on the blade suction surface. Fig. 80 shows a representative photograph of the deposits left by the smoke filament on the annular root and on the
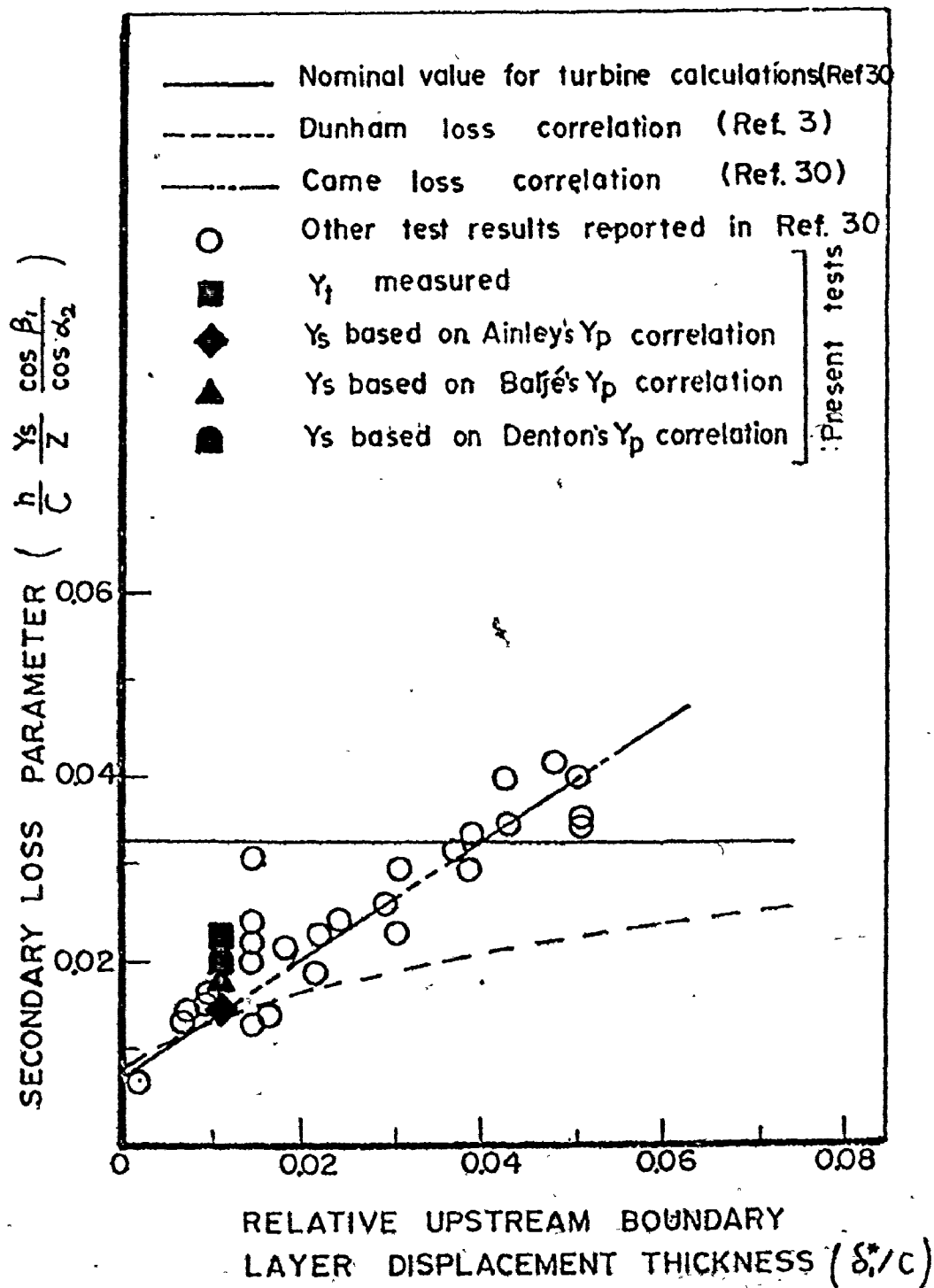
Fig. 79 A Comparison of the Annular Cascade Loss
Coefficients with Existing Correlation
After Accounting for the Mixing Losses.

blade suction surface. The smoke deposits have been out-lined by pencil to help identify the various areas. It is clear from these traces and also by direct observation of the smoke pattern that the low momentum boundary layer fluid started to overturn and roll over the blade suction surface between 15 and 30 percent of the axial chord. The passage vortex could be observed to form at about 50 percent of the axial chord, and resulted in a strong instability of the smoke filament at the exit plane of the cascade.

Roll-up of the root
boundary layer on
the suction surface

Overturning of the
annular root
boundary layer
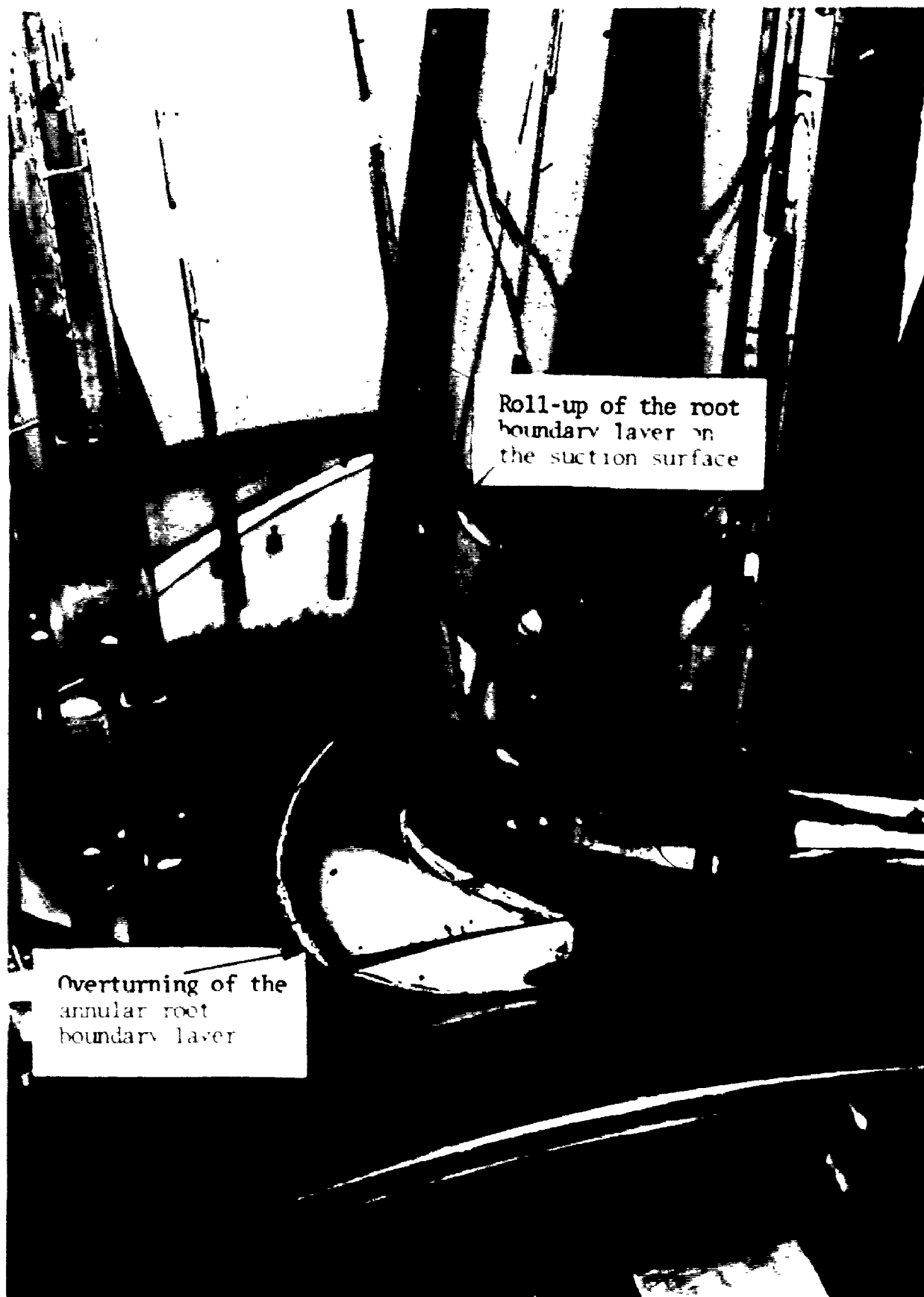
Fig. 80   Flow   Visualization Using Smoke Deposits

CHAPTER 9

CONCLUSIONS AND RECOMMENDATIONS

With the aim of carrying out an investigation of the secondary flow phenomenon in large turning angle turbine blade cascades, a special three-dimensional annular test rig was constructed and tested. Detailed cascade tests, at a Reynolds number based on the blade chord of 3×10^5 to 6×10^5, consisted of inlet and exit flow parameters traverses, blade passage pressure distributions and flow visualization.

The results, presented in the form of contours and radial distributions, were analysed and compared with existing correlations and previous investigations. The following general conclusions can be drawn:

1. The investigation of the inlet flow parameters revealed the fact that the blade leading edge disturbance was felt at the inlet measuring station in the form of cyclic variation of flow angle and velocity. This cyclic variation was in agreement with the two-dimensional potential flow solution obtained using an electric field analogue.

2. The scale of the test rig and the power supply available assured the proper Reynolds number range and provided

free stream turbulence levels compatible with those obtained in full scale machines. Sufficient flexibility was built into the rig so that the inlet flow conditions could be tailored according to the test requirements.

3. The pressure distributions obtained on the annular walls exhibited a low pressure region removed from the suction surface of the blade. This was attributed to the passage vortex resulting from the roll-up of the inlet boundary layer over the blade suction surface.

4. The pressure distributions found over the blade surfaces were compared to those obtained theoretically using a two-dimensional stream tube program developed by Stannard [38]. Good agreement was found between the experimental and theoretical pressure surface distributions. However a noticeable deviation occurred in the first 50% of the chord when one compares the results for the suction surface. This was attributed to the three-dimensionality of the flow and to the motion of the boundary layer fluid over the suction surface.

5. In the total pressure loss contours measured in the exit plane, only a single high loss core was visible and this occurred in the middle of the blade passage. The vortex formation verified for the first time the prediction made by Loos [10] in 1953 of the flow behaviour in large turning angle cascades. Other possible reasons for the coalescence of the inner and outer wall high loss

regions into a large single one were presented. These included the high blade turning angle, the general annular geometry, the thicker root boundary layer and the orientation of the blade trailing edges.

6. The exit yaw angle contours revealed regions of maximum flow underturning and overturning in the main stream. An interpretation of the formation of these regions was given. The same factors promoted the changes in the yaw angle as were present in the total pressure loss contours.

7. The cascade overall secondary loss coefficients were compared to the correlations obtained by Dunham [3] and Came [30], as well as to previous published data and good agreement was found.

8. Finally the smoke visualization study gave visual evidence of the separation of the inlet boundary layer and its roll-up on the blade suction surface.

Suggestions for Further Study

As suggestions for further study, the following recommendations are presented.

1. The effect of the inlet boundary layer thickness, on the exit flow parameters and on the cascade loss coefficient, should be investigated. The test results would have particular interest with respect to the shape and location of the vortex if one could have equal inner and outer wall boundary layer thickness.

2.   A detailed flow visualization study using the smoke technique and high speed photography could clarify some of the interpretation made in the experimental results.

3.   A more detailed study of the end wall boundary within the annular blade passage is required.

4.   The effect of a radial orientation of the blade trailing edges on the exit flow parameter contours should be studied. It should be recalled that the present test rig employs a leading edge radial orientation.

5.   In order to have an accurate prediction of the secondary loss coefficient, the profile losses should be further investigated.

6.   The effect of the location of the exit measuring station on cascade loss coefficient should be investigated in order to generalize the existing correlations.

7.   Finally a theoretical model, three-dimensional in nature, has to be developed to estimate the flow overturning and underturning in large turning angle cascades.

REFERENCES

1. Lakshminarayana, B., and Horlock, J. H., "Review: Secondary Flows and Losses in Cascades and Axial Flow Turbomachines", Int. J. Mech. Sci., 5, 287 (1963).

2. Hawthorne, W. R. and Novak, R. A., "The Aerodynamics of Turbomachinery", Annual Review of Fluid Mechanics, Vol. 1, pp. 341-366, 1969.

3. Dunham, J., "A Review of Cascade Data on Secondary Losses in Turbines", Journal of Mech. Eng. Sci., Vol. 12, No. 1, p. 48, 1970.

4. Horlock, J. H. and Lakshminarayana, B., "Secondary Flows: Theory, Experiments and Application in Turbomachinery Aerodynamics", Annual Review of Fluid Mechanics, Vol. 5, pp. 247-280, 1973.

5. Squire, H. B. and Winter, K. G., "The Secondary Flow in a Cascade of Airfoils in a Nonuniform Stream", Journal of the Aero. Sci., pp. 271-277, April 1951.

6. Hawthorne, W. R., "Secondary Circulation in Fluid Flow", Proc. R. Soc., 206 (Series A) 374, 1951.

7. Preston, J. H., "A Simple Approach to the Theory of Secondary Flows", The Aero. Quarterly, Vol. 5, Sept. 1954.

8. Hawthorne, W. R., "The Secondary Flow about Struts and Airfoils", Journal of the Aero. Sci., pp. 588-608, Sept. 1954.

9. Marris, A. W., "The Generation of Secondary Vorticity in an Incompressible Fluid", Trans. ASME, E30:525, 1963.

10. Loos, H. G., "An Analysis of Secondary Flow in the Stator of an Axial Turbomachine", Guggenheim Jet Propulsion Center, C.I.T., Tech. Rept. 3, Sept. 1953.

11. Ehrich, F. F., "Secondary Flows in Cascades of Twisted Blades", Jour. of the Aero Sci., pp. 51-60, Jan. 1955.

12. Louis, J. F., "Rotational Viscous Flow", Proc. 9th Int. Congr. Appl. Mech., 3, 306, 1956.

13. Hawthorne, W. R. "Rotational Flow Through Cascades, Part 1: The Components of Vorticity", Quart. Jour. Mech. and Appl. Math., Vol. 8, Pt. 3, 1955.

14. Hawthorne, W. R. and Armstrong, W. D., "Rotational Flow Through Cascades, Part II: The Circulation About the Cascade", Quart. Jour. Mech. and Appl. Math., Vol. 8, Pt. 3, 1955.

15. Hawthorne, W. R., "The Applicability of Secondary Flow Analysis to the Solution of Internal Flow Problems", Fluid Mechanics of Internal Flow, edited by Sovran, Elsevier Publishing Co., 1967.

16. Hawthorne, W. R., "Some Formulae for the Calculations of Secondary Flow in Cascades", A.R.C. Report No. 17, 519, March 1955.

17. Lakshminarayana, B. and Horlock, J. H., "Effect of Shear Flows on Outlet Angle in Axial Compressor Cascades. Methods of Prediction and Correlation with Experiments", Jour. of Basic Eng., March 1964, p. 191.

18. Bardon, M. F., Moffatt, W. C. and Randall, J. L., "Secondary Flow Effects on Gas Exit Angles in Rectilinear Cascades", Jour. of Eng. for Power, pp. 93-100, Jan. 1975.

19. Hawthorne, W. R. and Armstrong, W. D., "Shear Flow Through a Cascade", The Aero. Quarterly, Vol. 7, 1956.

20. Came, P. M. and Marsh, H., "Secondary Flow in Cascades: Two Simple Derivations for the Components of Vorticity", Jour. of Mech. Eng. Sci., Vol. 16, No. 6, 1974.

21. Marsh, H., "Secondary Flow in Cascades: The Effect of Axial Velocity Ratio", Jour. of Mech. Eng. Sci., Vol. 16, No. 6, 1974.

22. Dixon, S. L., "Secondary Vorticity in Axial Compressor Blades", Fluid Mechanics and Design of Turbomachines, ed. B. Lakshminarayana, Britsch, W. R. and Gearhart, W., NASA SP304, 1972.

23. Loos, H. G., "A Simple Laminar Boundary Layer with Secondary Flows", Jour. of Aero. Sci., pp. 35-40, Jan. 1955.

24. Herzig, H. Z. and Hansen, A. G., "Experimental and Analytical Investigation of Secondary Flows in Ducts", Jour. of Aero. Sci., pp. 217-231, March 1957.

25. Johnston, J. P., "On the Three-dimensional Turbulent Boundary Layer Generated by Secondary Flow", Jour. of Basic Eng., Trans. A.S.M.E., pp. 233-248. March 1960.

26. Ainley, D. G. and Mathieson, G. C. R., "An Examina-tion of the Flow and Pressure Losses in Blade Rows of Axial Flow Turbines", British ARC. R&M, 2891, March 1951.

27. Balje, O. E. and Binsley, R. L., "Axial Turbine Performance Evaluation", Jour. of Eng. Power, Trans. A.S.M.E., pp. 341-348, October 1968.

28. Denton, J. D., "A Survey and Comparison of Methods for Predicting the Profile Loss of Turbine Blades", I.Mech.Eng., Conference publication, 3, 1973, pp. 204-212.

29. Brown, R. L., "An Investigation of the Secondary Flow Phenomena in a Cascade of High Deflection Axial Flow Impulse Turbine Blades", M.Sc. Thesis, U.S. Navy Postgraduate School, Monterey, Dec. 1966.

30. Came, P. M., "Secondary Loss Measurements in a Cascade of Turbine Blades", I.Mech.Eng., Conference publication, 3, 1973, pp. 75-83.

31. Rohlik, H. E., Kofskey, M. G., Allen, H. W. and Herzig, H. Z., "Secondary Flows and Boundary Layer Accummulations in Turbine Nozzles", N.A.C.A. Rep. 1168, 1954.

32. Herzig, H. Z. and Hansen, A. G., "Visualization Studies of Secondary Flows with Applications to Turbomachines", Trans. A.S.M.E., 77, 249, 1955.

33. Turner, J. R., "An Investigation of the End Wall Boundary Layer of a Turbine Nozzle Cascade", Trans. A.S.M.E, 79, 1801, 1957.

34. Sjolander, S. A., "The Endwall Boundary Layer in an Annular Cascade of Turbine Nozzle Guide Vanes", Technical Report ME/A75-4, Carleton University, Ottawa, December 1975.

35. Langston, L. S., Nice M. L. and Hooper, R. M., "Three-Dimensional Flow Within a Turbine Cascade Passage", Jour. of Eng. Power, pp. 21-28, Jan. 1977.

36. Myachin, E. V., "A Three-Dimensional Test Rig for the Investigation of Secondary Flow in High Turning Angle Turbine Blade Cascades", Mech. Eng. Report, McMaster University, Hamilton, Ontario, Dec. 1973.

37. Malhotra, R. K., "The Two-Dimensional Development and Analysis of Blade Profiles Having Large Turning Angles", M.Eng. Thesis, Dept. of Mech. Eng., McMaster Univ., Hamilton, Ontario, 1971.

38. Stannard, J. H., "The Aerodynamic Design and Testing of High Turning Angle Turbine Blades", Ph.D. Thesis, Dept. of Mech. Eng., McMaster University, Hamilton, Ontario, 1975.

39. Bassett, R. W. and Fowler, H. S., "Improvements to a Smoke Generator for Use in Wind Tunnels", NRC of Canada Report No. 12288.

40. Dean, Robert C., "Aerodynamic Measurements", Gas Turbine Laboratory, Massachusetts Institute of Technology, 1953.

41. Private Communication with United Sensor and Control Corp., Watertown, Massachusetts.

APPENDIX A

SUPPLEMENTARY INFORMATION REGARDING
THE ANNULAR CASCADE RIG

Chapter 3 gave a description of the major components of the annular cascade rig. This Appendix is included to provide additional information on the design and construction of the rig.

The radii of the inner and outer walls (r_i and r_o) for the inlet and exit sections of the cascade were shown in Figs. 14 and 22 of Chapter 3. Figs. 81 and 82 show how these radii were calculated for a given height from the leading and trailing edge plane respectively. Figs. 83 and 84 describe the inlet and exit section flanges with the corresponding sliding segment. The sliding side walls provided in the inlet section flange for the control of the inlet flow conditions is also shown in Fig. 83. Figs. 85 and 86 show the details of the plenum chamber openings and the flexible connection used between the rig and the plenum chamber.
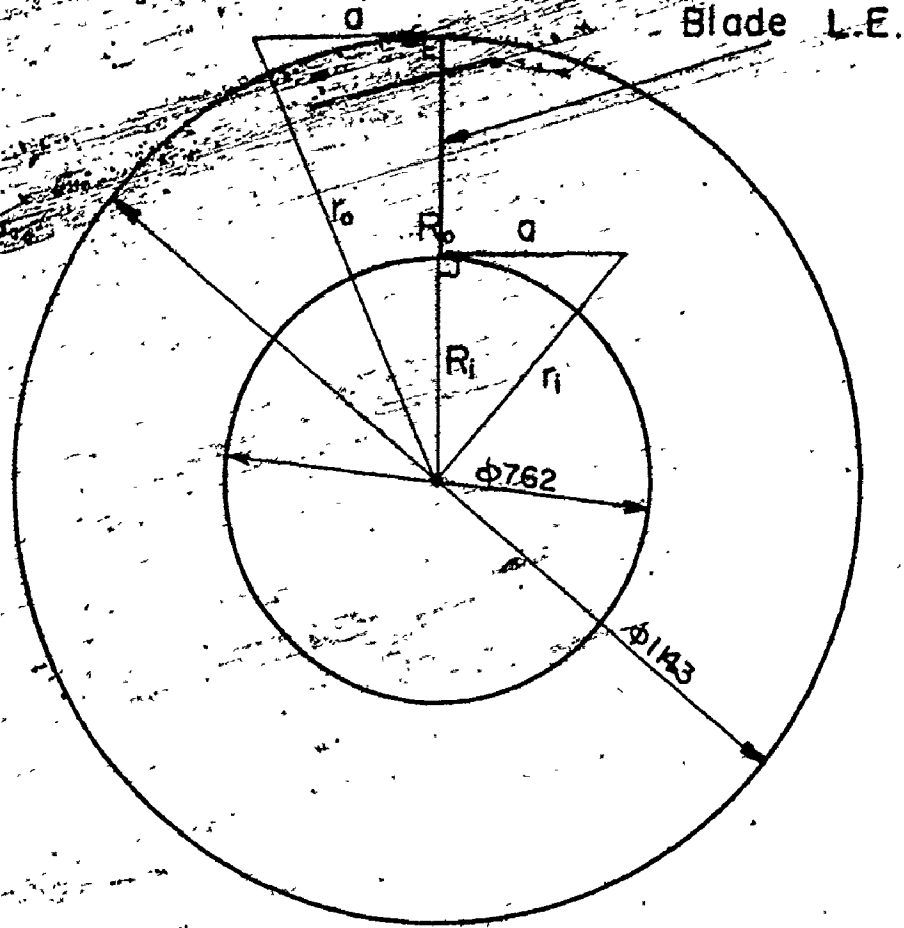
$$a = h / \tan 26°$$

$$r_{i,o} = \sqrt{a^2 + R_{i,o}^2}$$
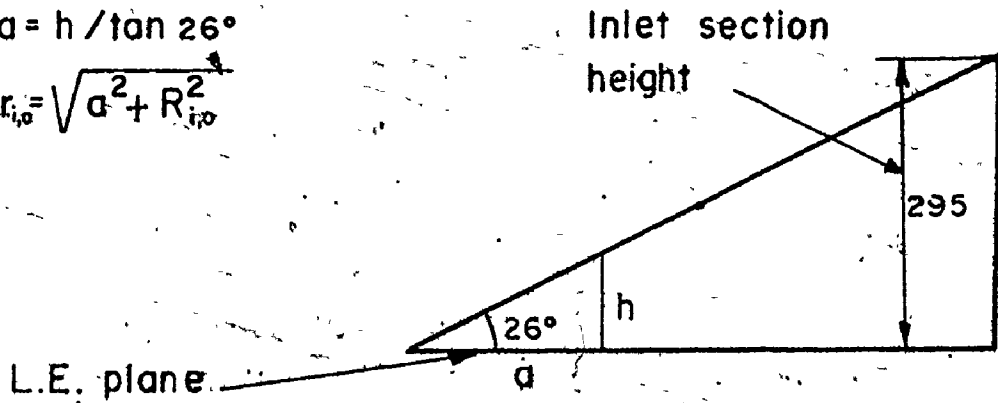
Note: All dimensions are in millimeters

Fig. 81 Radius Calculations for the Inlet Section Walls
(See Fig. 14).

Blade T.E.

$$a = h / \tan 25°30'$$
$$r_{i,o} = \sqrt{a^2 + R_{i,o}^2}$$

Exit section height

T.E. plane

25°30'

300

h

a
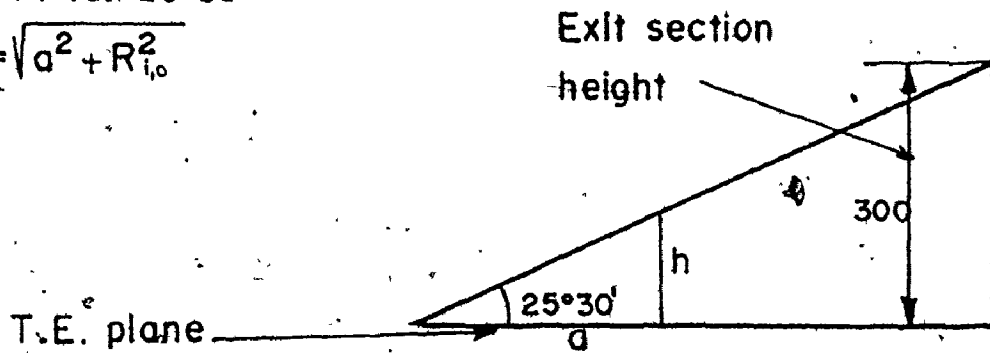
Note: All dimensions are in millimeters

Fig. 82   Radius Calculation for the Exit Section Walls
(See Fig. 22).

Sliding side
walls

ϕ795

50

Spacer

Sec AA

ϕ762

6

A'R'

53°

45°

80°

90°

ϕ750
ϕ740

1143

5°

A

A

Porous Plate for
Inlet Flow Control
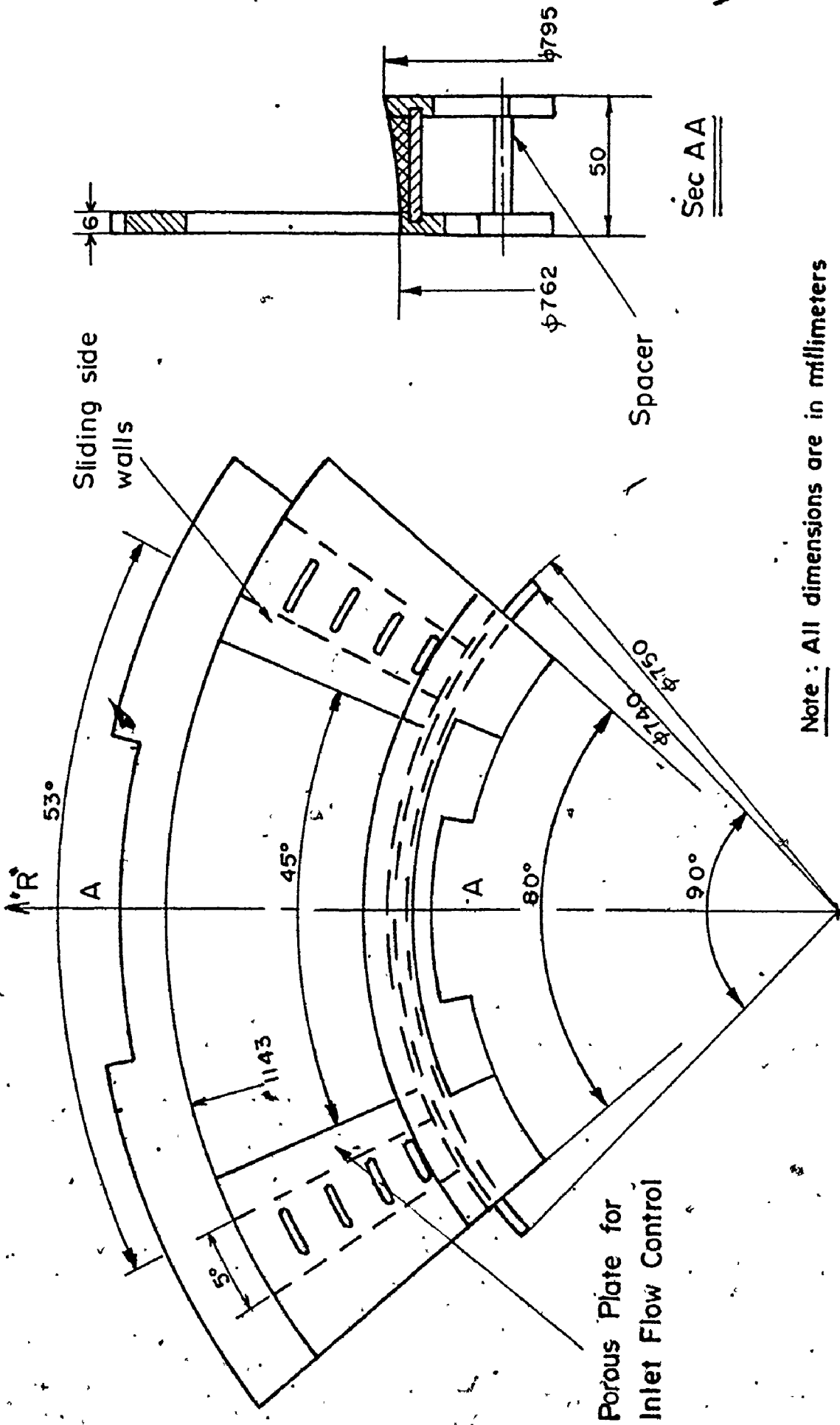
Note : All dimensions are in millimeters

Fig. 83   Inlet Section Flange.

Fig. 84 Exit Section Flange.

Note: All dimensions are
      in millimeters

Fig. 85   Plenum Chamber Openings.

19

1.6

Metal Hold-down Strips

12.7

Plenum Side

Sheet Metal

Exit Section Wall

Rubber Joint

0.8

6

Fi   Exi   nd Pl
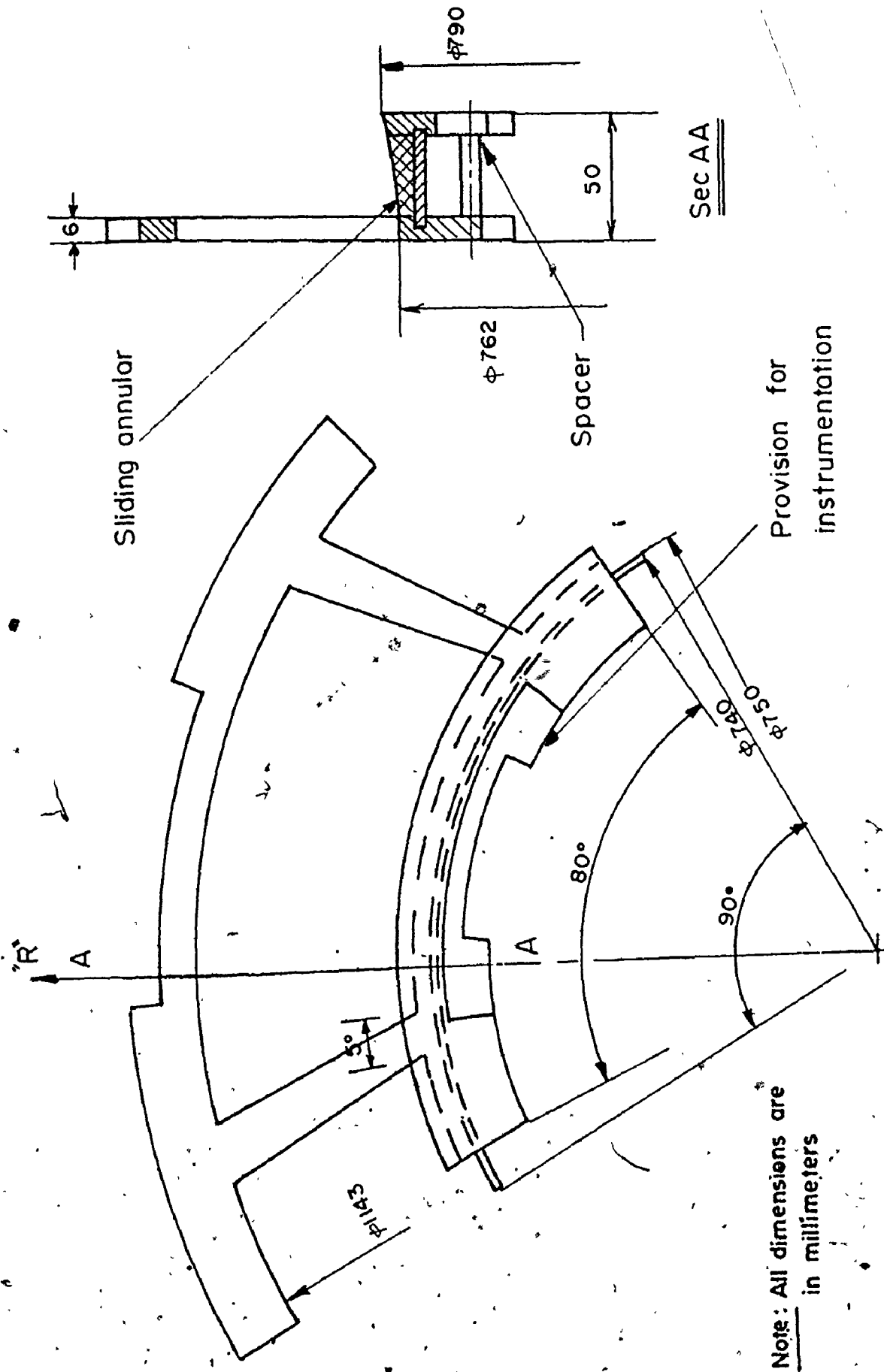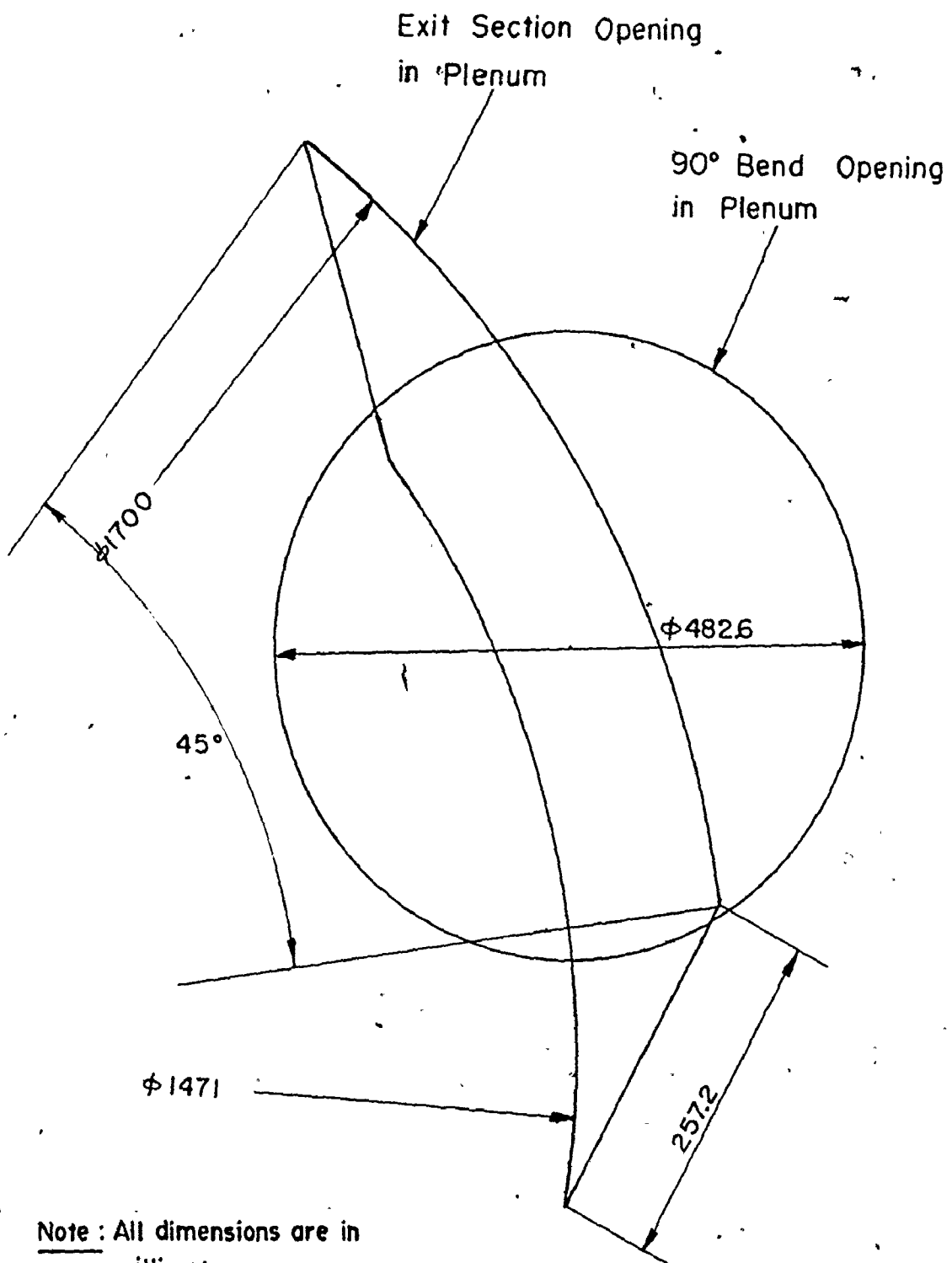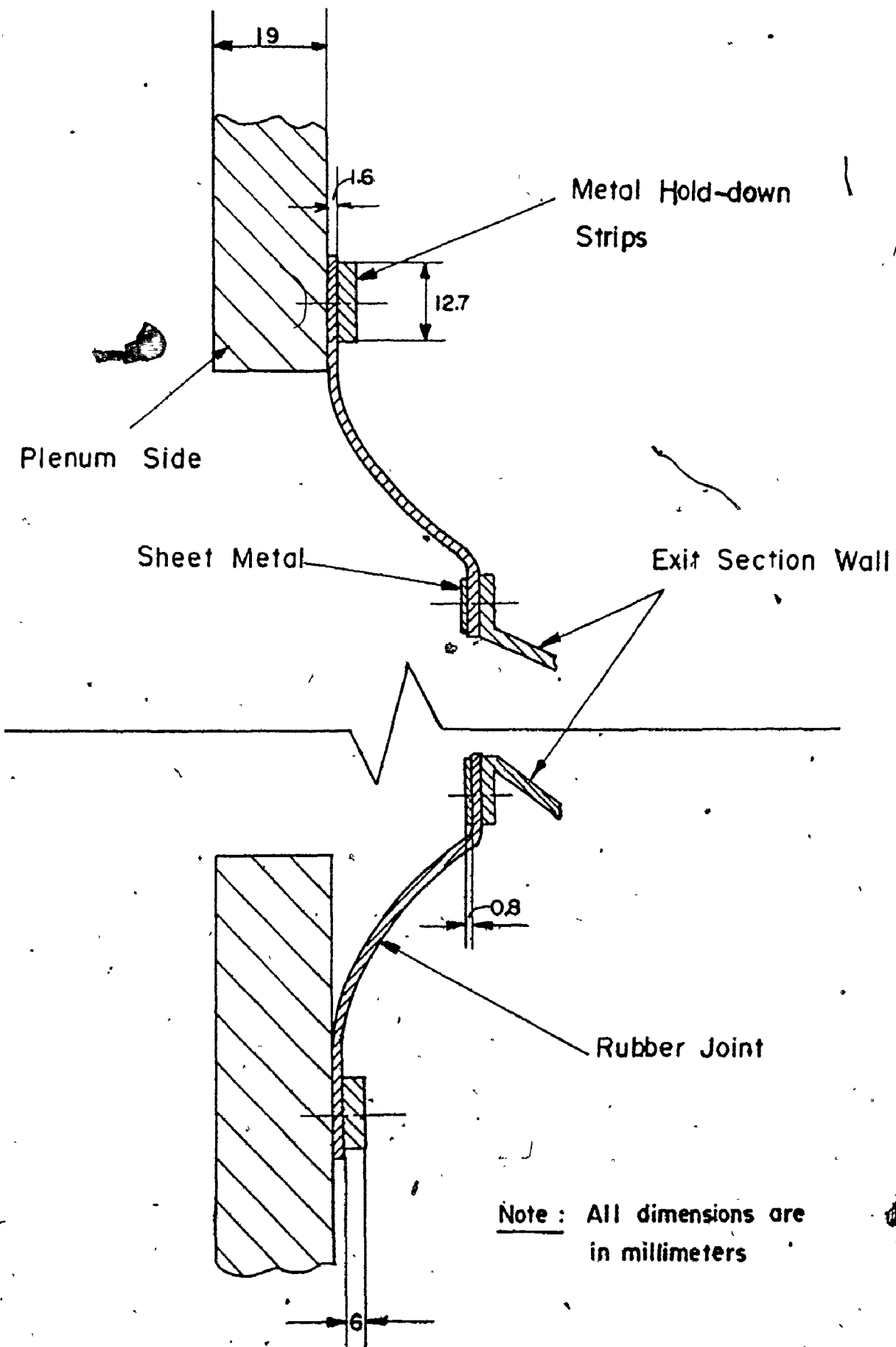
APPENDIX B

BLADE PASSAGE GEOMETRY

Due to the complexity of the blade passage geometry,
a computer program was prepared to calculate the blade
coordinates, the intersection with the annular walls and
the passage area at each axial location. The computer
notation used to describe the blade passage geometry is
given in Fig. 87.

The blade pressure and suction coordinates were first
measured at different points by means of the digitizer
available in the department. In order to define each blade
surface, a least-square polynomial fit to the data was
used and a fifth order polynomial was found to represent
each surface. The blade coordinates are given in Table 4
for 51 axial sections along the blade. The program computed
the angular positions of the intersection of the blade
surfaces with the annular walls, as well as the angular
positions at mean radius, for the different axial sections.
This was done by projecting each point on the blade surfaces
onto the leading edge plane and using the reference radial
direction, defined in Fig. 20, as the zero ordinate.
Finally, the passage cross-section area was calculated at
each station and tabulated with the previous ordinates as
shown in Table 4.
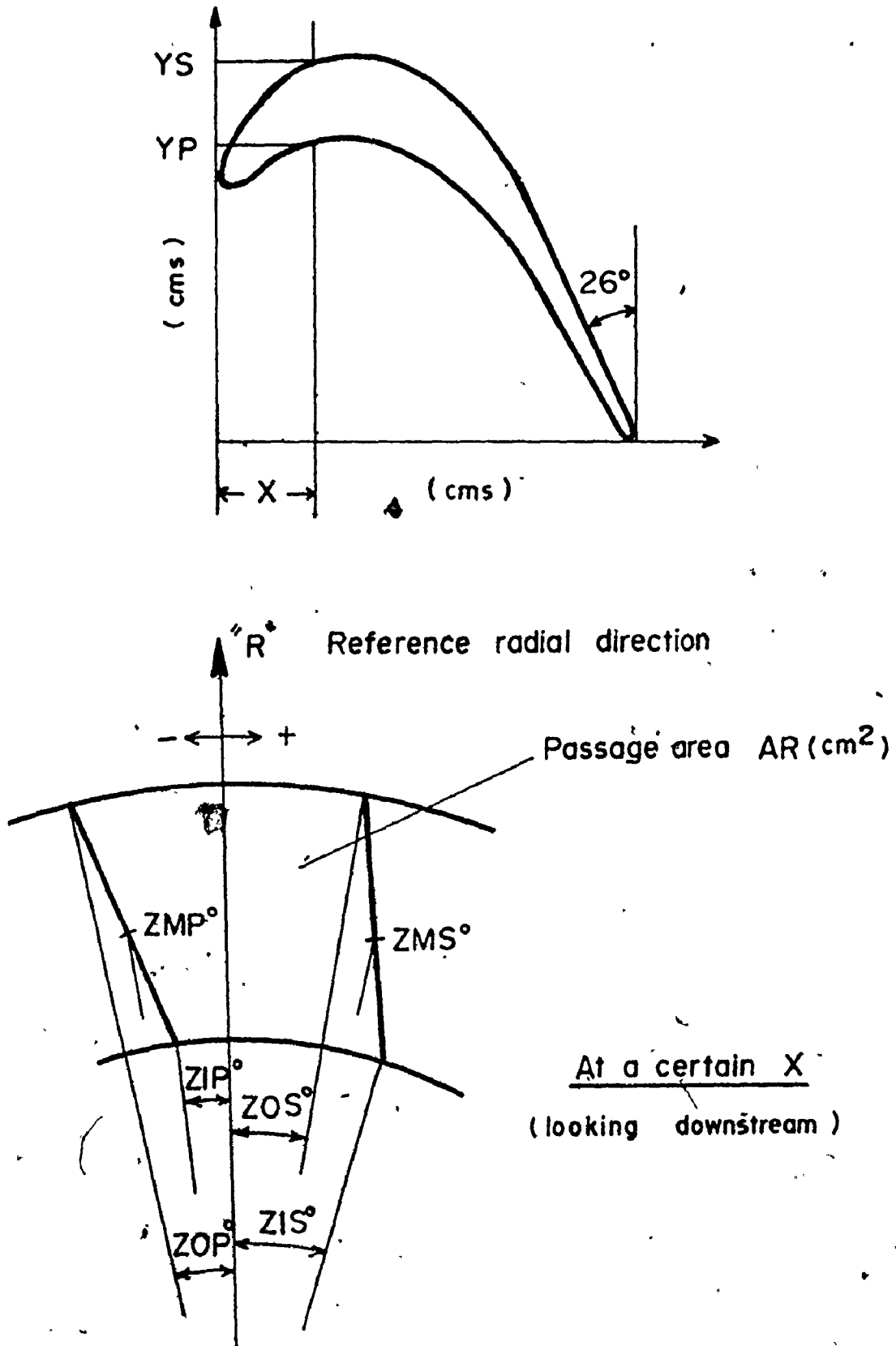
Fig. 87 Computer Notation for Passage Geometry.

	X	YP	YS	ZIP	ZIS	ZIP	ZIS	ZOP	ZCS	AZ
1		11.26	11.26	-7.50	7.50	-7.50	7.50	-7.50	7.55	237.52
2		10.72	12.23	-5.66	5.07	-6.63	6.34	-6.34	6.55	203.79
3		10.50	13.05	-6.76	4.98	-6.93	5.48	-7.52	5.62	196.57
4	1.16	11.01	13.51	-7.24	4.04	-7.29	4.73	-7.32	5.19	199.35
5		11.46	14.12	-7.65	3.22	-7.62	4.08	-7.60	4.65	185.32
6		11.44	14.55	-8.34	2.53	-7.95	3.53	-7.96	4.20	181.41
7	2.23	11.67	14.97	-8.30	1.94	-8.21	3.05	-8.09	3.82	179.43
8		12.01	15.31	-8.71	1.44	-8.47	2.65	-8.31	3.46	176.14
9		12.56	15.56	-9.05	1.02	-8.76	2.32	-7.56	3.15	174.50
10		12.40	15.81	-9.27	.66	-8.91	2.04	-8.66	2.95	175.35
11	3.77	12.66	16.00	-9.46	.37	-9.10	1.80	-8.83	2.76	172.58
12		12.74	16.16	-9.37	.13	-9.25	1.61	-8.96	2.65	172.09
13		12.85	16.26	-9.46	-.06	-9.39	1.46	-9.07	2.47	171.79
14	4.60	12.94	16.33	-10.30	-.21	-9.50	1.34	-9.17	2.37	171.62
15	5.25	13.01	16.46	-10.15	-.33	-9.58	1.25	-9.23	2.29	171.46
16		13.05	16.52	-10.17	-.41	-9.64	1.18	-9.25	2.24	171.31
17	6.03	13.17	16.55	-10.21	-.46	-9.67	1.14	-9.31	2.23	171.12
18	6.41	13.06	16.57	-11.22	-.49	-9.67	1.12	-9.31	2.19	170.86
19	5.72	13.06	16.57	-10.15	-.48	-9.65	1.12	-9.29	2.19	170.49
20	7.16	13.12	16.55	-10.12	-.45	-9.57	1.14	-9.24	2.21	170.01
21	7.54	12.95	16.51	-10.01	-.46	-9.51	1.19	-9.17	2.25	168.42
22	7.92	12.75	16.45	-9.87	-.31	-9.39	1.26	-9.08	2.30	168.72
23	8.29	12.73	16.37	-9.69	-.19	-9.25	1.36	-8.96	2.38	167.95
24	8.67	12.55	16.27	-9.47	-.03	-9.07	1.48	-8.81	2.49	167.11
25	9.05	12.41	16.14	-9.21	.16	-8.86	1.63	-8.54	2.62	166.26

Table 4   Tabular Description of the Blade Passage Geometry

26	.42	12.21	15.99	-3.95	.00	-9.62	1.82	-8.44	2.77	165.42
27	10.04	12.09	15.80	-6.56	.68	-8.35	2.05	-6.21	2.96	164.65
28	10.18	11.75	15.58	-4.18	1.02	-8.04	2.32	-7.95	3.15	164.04
29	10.66	11.49	15.32	-7.75	1.41	-7.73	2.63	-7.67	3.45	165.62
30	10.87	11.09	15.01	-7.28	1.87	-7.32	3.00	-7.35	3.75	165.43
31	11.21	13.73	14.66	-6.77	2.43	-6.91	3.42	-7.01	4.10	163.70
32	11.69	10.42	14.26	-6.21	3.01	-6.47	3.91	-6.64	4.54	164.36
33	11.96	13.13	13.80	-5.62	3.70	-6.00	4.46	-6.25	4.97	165.57
34	12.06	10.75	13.28	-4.95	4.48	-5.49	5.09	-5.82	5.43	167.42
35	12.45	9.61	12.70	-4.55	5.37	-4.94	5.79	-5.37	6.05	170.02
36	12.92	3.15	12.04	-3.75	6.36	-4.37	6.58	-4.89	6.74	173.48
37	13.10	9.66	11.33	-2.83	7.46	-3.77	7.47	-4.39	7.47	177.93
38	13.57	9.16	10.51	-2.04	8.65	-3.14	8.42	-3.86	8.27	182.47
39	14.32	7.65	9.72	-1.22	9.84	-2.40	9.57	-3.51	9.06	187.58
40	14.76	7.11	8.93	-.36	11.03	-1.79	11.32	-2.74	9.85	191.79
41	15.18	6.54	8.14	.55	12.22	-1.08	11.27	-2.15	10.64	195.64
42	15.45	5.95	7.35	1.45	13.41	-.35	12.23	-1.55	11.44	199.17
43	15.82	5.31	6.56	2.30	14.61	.40	13.13	-.92	12.23	202.42
44	16.21	4.73	5.77	3.35	15.81	1.16	14.14	-.29	13.03	205.45
45	16.69	4.13	4.98	4.33	17.01	1.94	15.16	.36	13.82	208.32
46	16.06	3.47	4.19	5.32	18.22	2.73	16.66	1.01	14.62	211.09
47	17.34	2.82	3.40	6.32	19.43	3.52	17.02	1.66	15.42	213.82
48	17.72	2.16	2.61	7.32	20.65	4.31	17.99	2.32	16.22	216.57
49	15.05	1.52	1.82	8.33	21.87	5.13	18.95	2.97	17.03	219.33
50	18.47	.87	1.03	9.34	23.10	5.93	19.93	3.63	17.83	222.11
51	18.45	.24	.24	9.34	24.34	5.93	20.90	3.64	18.64	237.52

Table 4 · Continued

APPENDIX C

THREE-DIMENSIONAL
PROBE CALIBRATION

Figure 88 shows the results of the three-dimensional probe calibration carried out at United Sensor Laboratories in August 1975 and repeated in February 1978. The probe was calibrated at midheight of a 76 mm passage, with a mean air velocity of 70 m/s. The probe was designed to read true static pressure (subject to the errors listed in Appendix E) when the holes are at least 10 probe diameters (i.e., $\sim$ 31 mm) away from the boundary they project through. The calibration of the probe will remain unaffected by changes in Reynolds number (based on probe diameter) within the range $5 \times 10^3 <$ Re $< 10^5$ [40]. For our tests the range of Reynolds number was $8.6 \times 10^3 <$ Re $< 1.7 \times 10^4$, and the calibration test Reynolds number was 2.8×10^4. It can be seen from Fig. 88 that the calibration data are in good agreement although they spanned nearly a three year period. The measurements shown in this report were made using the first calibration curve. The second calibration was carried out as a check on the accuracy of the probe.

177
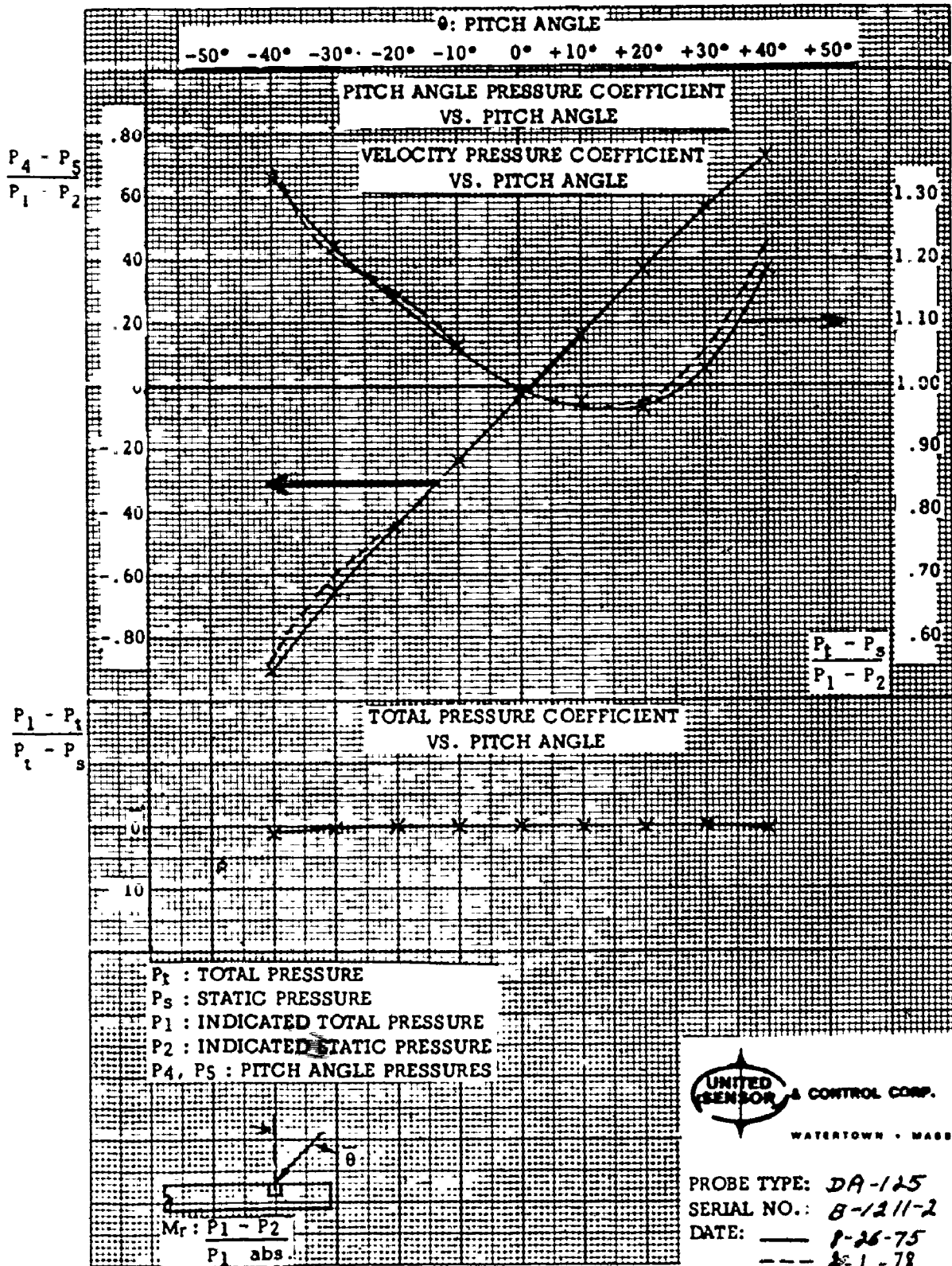
Fig. 88 Calibration Data for Type DA-125 Three-Dimensional Directional Probe.

APPENDIX D

DATA PROCESSING PROGRAM

A computer program was prepared in order to process
the data for the annular cascade rig. Program listing
and tables of inlet and exit flow parameters are given
in this Appendix.

The program started by reading the measured inlet
flow conditions, exit flow conditions and useful cascade
parameters as defined in the listing. Table 5 summarized
the inlet flow conditions at different inlet velocities.
The program then proceeded to calculate the local exit
flow parameters, which were defined in Section 8.2 and
in the listing, at the traverse points shown circled in
Fig. 89. This staggered selection in the radial direction
was made to account for the tilted orientation of the blade
trailing edge with respect to the local radial direction.
The measured and calculated values of the flow parameters in
the exit plane of the cascade are presented in Tables 6, 7
and 8. The radial variation of the circumferential
arithmetic mean and mass-averaged yaw angle and pressure loss
coefficient were then computed, followed by the calculation
of the cascade average exit flow parameters. These parameters
were also printed out as shown in Tables 9, 10 and 11 for
the different test conditions.

Table 5

Inlet Flow Conditions

Parameters	Test #1	Test #2	Test #3
Fan Speed (r.p.m.)	600	950	1300
Free stream yaw angle (Degrees)	63.5	64	64
Frae stream total pressure ("oil gauge)	-0.302	-0.623	-1.125
Free stream static pressure ("oil gauge)	-1.737	-3.873	-7.100
Mean velocity in the center blade passage (m/sec.)	22.8	34.8	45.9
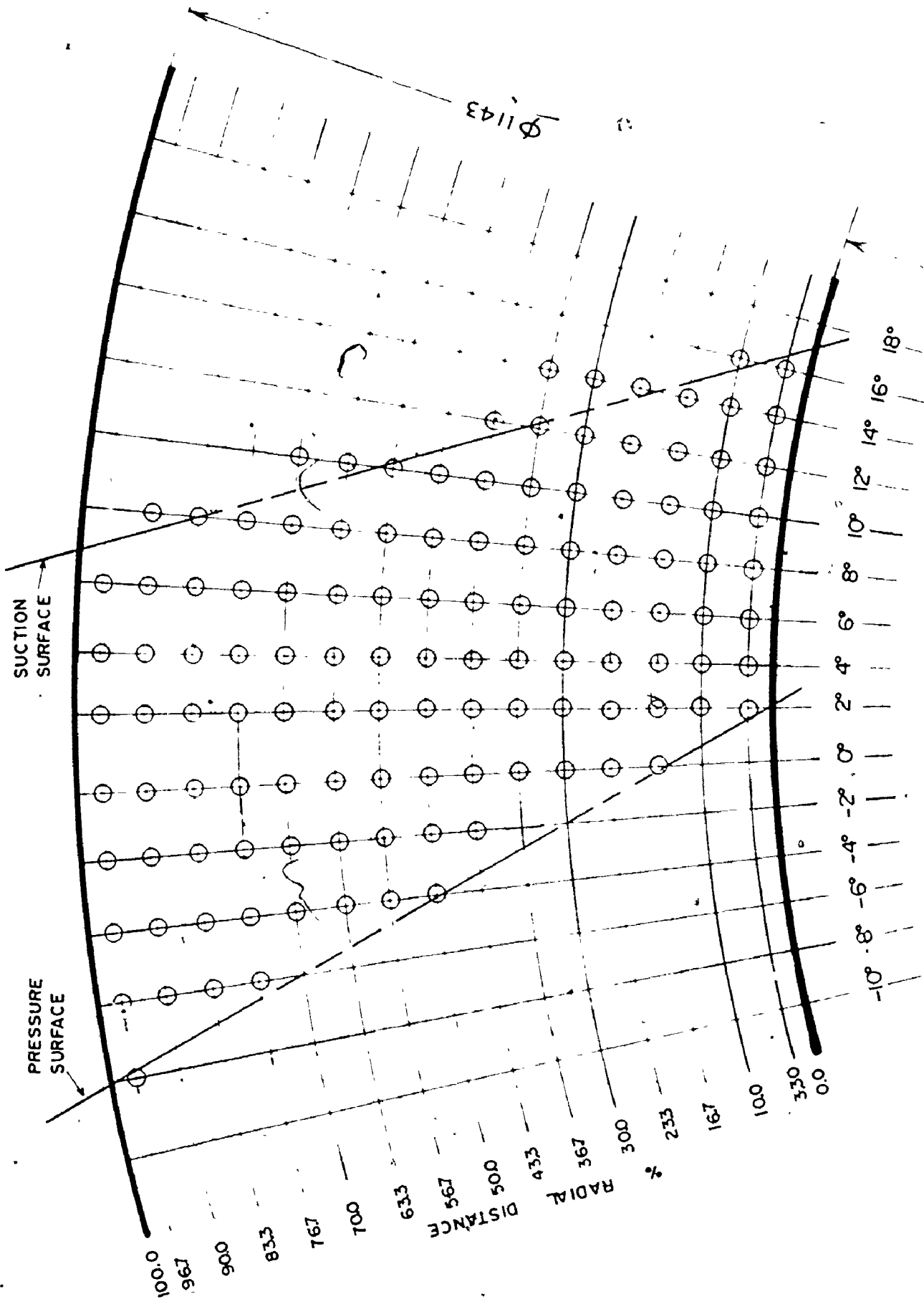
Fig. 89   Traversed Points in the Exit Plane Used
in the Data Processing Program.

```
C
C
C
C
C
C    +------------------------------------------------------------------+
C    |  DATA PROCESSING PROGRAM FOR COMPUTING THE LOCAL,RADIAL AND MEAN  |
C    |                                                                  |
C    |    EXIT FLOW PARAMETERS FOR THE ANNULAR CASCADE RIG              |
C    +------------------------------------------------------------------+
C
C    THE UNITS USED IN THE PROGRAM ARE AS FOLLOWS
C     ANGLES IN DEGREES
C     PRESSURES IN INCHES OF OIL GAUGE
C     VELOCITY IN METER PER SECOND
C     ROOM TEMPERATURE IN DEGREES RANKINE
C     ROOM PRESSURE IN INCHES OF MERCURY
C
C    IF THE NUMBER OF POINTS IN THE RADIAL AND CIRCUMFERENTIAL
C    DIRECTIONS ARE MORE THAN 15, THE COMPUTER DIMENSION HAS
C    TO BE CHANGED ACCORDINGLY
C
C    INLET FREE STEAM CONDITIONS ARE AT THE CENTRE OF THE CENTRE
C    PLATE PASSAGE
C
C    DEFINITION OF COMPUTER INPUT DATA
C    HC    HEIGHT TO CHORD RATIO
C    SC    SPACE TO CHORD RATIO
C    Y1    INLET BLADE ANGLE
C    PO1   INLET TOTAL PRESSURE
C    PS1   INLET STATIC PRESSURE
C    CD    INLET DISPLACEMENT THICKNESS PER CHORD RATIO
C    RT    ROOM TEMPERATURE
C    RP    ROOM PRESSURE
C    M     NUMBER OF POINTS IN THE RADIAL DIRECTION
C    N     NUMBER OF POINTS IN THE CIRCUMFERENTIAL DIRECTION
C    Y     EXIT YAW ANGLE
C    PO    EXIT TOTAL PRESSURE MULTIPLIED BY -1
C    PS    EXIT STATIC PRESSURE MULTIPLIED BY -1
C    P45   EXIT PITCH DIFFERENTIAL PRESSURE MULTIPLIED BY -1
C
C    DEFINITION OF COMPUTER OUTPUT PARAMETERS
C    V     ABSOLUTE VELOCITY
C    VA    AXIAL VELOCITY
C    Y     MEAN YAW ANGLE
C    YM    MASS AVERAGE YAW ANGLE
C    CPO   MEAN TOTAL PRESSURE LOSS COEFFICIENT
C    CPCM  MASS AVERAGE TOTAL PRESS E LOSS COEFFICIENT
C    YS    SECONDARY LOSS COEFFICIE    AS CALCULATED BY DUNHAM CORRELATION
C
      DIMENSION  Y(15,15),PO(15,15),PS(15,15),P45(15,15),CP(15,15),
     1P(15,15),V(15,15),VA(15,15),CPCL(15,15),CPSL(15,15),A(15),B(15),
     2C(15),AA(15),BB(15),CC(15),D(15),E(15)
C
C    READ INPUT DATA
```

```
      READ(5,1) HC,SC
1     FORMAT(2F10.4)
      READ(5,2) Y1,PC1,PS1,CC,RT,RP
2     FORMAT(6F10.4)
      READ(5,3) M,N
3     FORMAT(2I10)
      DO 20 I=1,M
      DO 10 J=1,N
      READ(5,4) Y(I,J),PC(I,J),PS(I,J),P45(I,J)
4     FORMAT(4F10.4)
      PC(I,J)=PC(I,J)
      PS(I,J)=PS(I,J)
      P45(I,J)=-P45(I,J)
10    CONTINUE
20    CONTINUE
C
      PI=3.14159/180.0
C  SS    PARAMETER USED IN DUNHAM CORRELATION
      SS=(0.0055+0.073*SQRT(CC))*HC/COS(Y1*PI)
      DP1=PC1-PS1
      YE=0.0
      DPCE=0.0
      DPSE=0.0
      DPCEM=0.0
      DPSEM=0.0
      VE=0.0
      VAE=0.0
C
      DO 30 I=1,M
      A(I) =0.0
      B(I) =0.0
      C(I)=0.0
      AA(I)=0.0
      BB(I)=0.0
      CC(I)=0.0
      D(I)=0.0
      E(I)=0.0
C
      DO 40 J=1,N
      DP(I,J)=PC(I,J)-PS(I,J)
C  CALCULATION OF PITCH ANGLE AND PRESSURE COEFFICIENT AS
C  DEFINED BY THE PROBE CALIBRATION CURVE
      P(I,J)=2.0 + 50.0*P45(I,J)/DP(I,J)
      DP(I,J)=(0.995-0.4935-2*P(I,J)+3.144E-3*P(I,J)**2
     1 +1.134E-5*P(I,J)**3)*DP(I,J)
      PS(I,J)=PC(I,J)-DP(I,J)
      V(I,J)=14.5*SQRT(RT*DP(I,J)/RP)
      VA(I,J)=V(I,J)*COS(P(I,J)*PI)*COS(Y(I,J)*PI)
      DPCL(I,J)=(PC1-PC(I,J))/DP1
      DPSL(I,J)=(PS1-PS(I,J))/DP1
      A(I)=A(I)+V(I,J)
      B(I)=B(I)+DP1*DPCL(I,J)
      C(I)=C(I)+DP1*DPSL(I,J)
      AA(I)=AA(I)+V(I,J)*VA(I,J)
      BB(I)=BB(I)+DP1*DPCL(I,J)*VA(I,J)
      CC(I)=CC(I)+DP1*DPSL(I,J)*VA(I,J)
      D(I)=D(I)+V(I,J)
```

```
      E(I)=E(I)+VA(I,J)
  40  CONTINUE
C
      AA(I)=AA(I)/E(I)
      BB(I)=BB(I)/E(I)
      CC(I)=CC(I)/E(I)
      D(I)=D(I)/FLOAT(M)
      E(I)=E(I)/FLOAT(M)
      A(I)=A(I)/FLOAT(M)
      B(I)=B(I)/FLOAT(M)
      C(I)=C(I)/FLOAT(M)
      YE=YE+A(I)
      DPCE=CPOE+B(I)
      DPSE=CPSE+C(I)
      DPCEM=CPOEM+BB(I)*E(I)
      DPSEM=CPSEM+CC(I)*E(I)
      VE=VE+D(I)
      VAE=VAE+E(I)
  70  CONTINUE
C
      CPCEM=DPCEM/VAE
      DPSEM=CPSEM/VAE
      VE=VE/FLOAT(M)
      VAE=VAE/FLOAT(M)
      YE=YE/FLOAT(M)
      DPCE=CPOE/FLOAT(M)
      DPSE=CPSE/FLOAT(M)
      PCE=FO1-CPOE
      PSE=FS1-DPSE
      PCEM=PO1-CPOEM
      DSEM=FS1-CPSEM
      CPE=CPCE/(POE-PSE)
      CPEM=CPOEM/(POEM-PSEM)
C
C  FUNHAM LOSS CORRELATION CALCULATION
      ASS=ATAN(0.5*(SIN(Y1*PI)/COS(Y1*PI)-SIN(YE*PI)/COS(YE*PI)))
      YSS=4.*SE*((SIN(Y1*PI)/COS(Y1*PI)+SIN(YE*PI)/COS(YE*PI))**2
     1    )+((COS(YE*PI))**3)/(COS(ASS))
C
      DO 150 I=1,M
      D(I)=0.305*D(I)
      E(I)=0.305*E(I)
      DO 160 J=1,M
      V(I,J)=0.305*V(I,J)
      VA(I,J)=0.305*VA(I,J)
 160  CONTINUE
 150  CONTINUE
      V=0.305*VE
      VA=0.305*VAE
C
C  WRITE LOCAL PARAMETERS
      WRITE(6,50)
 500  FORMAT(1H1,///,5X,*YAW ANGLE *,//)
      WRITE(6,50) ((V(I,J),J=1,M),I=1,M)
      WRITE(6,50)
 550  FORMAT(1H1,///,5X,*PITCH ANGLE *,//)
      WRITE(6,50) ((E(I,J),J=1,M),I=1,M)
```

```
      WRITE(6,600)
  600 FORMAT(1H1,///,55X,* VELOCITY *,//)
      WRITE(6,60) ((V(I,J),J=1,N),I=1,M)
      WRITE(6,650)
  650 FORMAT(1H1,///,55X,*AXIAL VELOCITY*,//)
      WRITE(6,60) ((VA(I,J),J=1,N),I=1,M)
      WRITE(6,700)
  700 FORMAT(1H1,///,50X,*TOTAL PRESSURE COEFFICIENT*,//)
      WRITE(6,70) ((CPOL(I,J),J=1,N),I=1,M)
      WRITE(6,750)
  750 FORMAT(1H1,///,50X,*STATIC PRESSURE COEFFICIENT*,//)
      WRITE(6,70) ((CPSL(I,J),J=1,N),I=1,M)
   60 FORMAT(31X,3F7.2/)
   70 FORMAT(34X,3F7.3/)
C WRITE RADIAL PARAMETERS
      WRITE(6,800)
  800 FORMAT(1H1,//,53X,*RADIAL PARAMETERS*,///,51X,*I*,7X,*V*,8X,*VA*,
     1 3X,*Y*,9X,*YH*,3X,*CPO*,6X,*CPS*,//)
      DO 110 I=1,M
      D(I)=B(I)/DP1
      DD(I)=BB(I)/DP1
      WRITE(6,115) I,D(I),E(I),A(I),AA(I),B(I),BB(I)
  115 FORMAT(30X,I2,FF13.3/)
  110 CONTINUE
C WRITE EXIT PARAMETERS
      WRITE(6,850) VE
  850 FORMAT(1H1,///,54X,*EXIT  PARAMETERS*,////,50X,*VELOCITY =*,F
     1 13.4//)
      WRITE(6,861) VAE
  860 FORMAT(50X,*AXIAL VELOCITY =*,F13.4//)
      WRITE(6,881) PCEH
  861 FORMAT(50X,*TOTAL PRESSURE =*,F13.4//)
      WRITE(6,882) PSEH
  862 FORMAT(50X,*STATIC PRESSURE =*,F13.4//)
      WRITE(6,870) YE
  870 FORMAT(50X,*MEAN YAW =*,F13.4//)
      WRITE(6,890) CPE
  890 FORMAT(50X,*MEAN CPO =*,F13.5//)
      WRITE(6,900) CPEH
  900 FORMAT(50X,*MASS AVERAGE CPO =*,F13.5//)
      WRITE(6,910) YSS
  910 FORMAT(50X,*YS DUNHAM =*,F13.5//)
      STOP
      END
```

YAW ANGLE (X)

3.3	64.00	66.00	7?.00	72.00	71.00	71.00	70.00	66.00
10.0	57.00	68.00	71.00	72.00	7?.00	69.00	63.00	65.00
16.7	6?.00	67.00	69.00	73.00	73.00	68.00	63.00	66.00
??	63.00	73.00	63.00	73.00	??.00	66.00	66.00	64.00
??	65.00	69.00	70.00	73.00	63.00	66.00	67.00	66.00
??	63.00	72.00	74.00	71.00	63.00	67.00	67.00	69.00
??	61.00	67.00	73.00	75.00	7?.00	68.00	64.00	64.50
??	59.00	58.00	58.00	54.00	56.00	63.00	63.00	58.00
??	58.00	54.00	43.00	40.00	43.00	46.00	56.00	56.00
??	57.00	53.00	54.00	44.00	44.00	53.00	64.00	60.00
7??	61.00	63.50	64.00	66.00	63.00	53.00	64.00	61.00
76.7	57.00	64.00	65.00	69.00	71.00	60.00	65.00	63.00
??	57.50	64.00	65.00	67.00	63.00	67.00	56.00	62.00
9.?	65.00	64.00	65.00	65.00	65.00	66.00	66.00	65.00
96?	63.00	53.00	63.50	55.00	68.00	68.00	65.00	65.00

CIRCUMFERENTIAL DISTANCE (From pressure side)

PITCH ANGLE (δ)

3.3	.15	2.00	2.00	?.00	-.13	.??	-.92	2.65
60	-?.76	.??	.00	-?.00	-?.00	-13.67	-15.50	-7.73
16.7	-15.31	-4.73	2.80	1.15	-5.11	-13.30	-22.25	-17.00
233	-3.53	-.70	?.75	-.5?	-6.07	-13.56	-20.47	-9.61
300	-?.73	-.0?	.52	-2.15	-?.15	-17.6?	-1?.11	-5.61
367	.1?	2.00	-3.60	-5.40	-12.00	-2?.71	-13.94	-.72
433	-?.??	?.??	?.?	-7.0?	-15.49	-2?.44	-2?.??	-5.7?
500	-?.??	-1.?5	-.??	.??	-?.71	-?3.1?	-?2.25	-17.4?
567	-3.43	-3.33	-9.3?	-7.45	-5.6?	-13.71	-?0.66	-5.73
633	-1?.15	-1?.3?	-2?.34	-1?.3?	-.76	4.39	-?.42	-11.33
700	-3.13	-13.25	-1?.??	-1?.??	-.??	-7.??	?.56	-13.63
767	2.3?	-?.??	-11.?5	-?.61	-5.??	-1.1?	-?.??	2.65
933	-2.22	-1?.6?	-?.??	-?.??	-5.?7	-1.51	-.75	-1.?6
900	-?.6?	-11.?3	-?.??	-?.62	-5.??	-1.4?	-1.?3	-4.??
967	.??	-7.??	-4.??	-2.??	-2.??	-1.76	-.??	-1.15

VELOCITY (V)

19.98	24.26	25.27	26.29	27.34	27.09	24.98	20.48
25.07	27.62	27.76	23.14	27.53	27.57	27.61	25.39
27.55	26.97	27.55	23.59	24.65	23.4.	27.74	26.64
25.34	27.27	27.73	27.65	25.77	27.35	27.21	25.74
27.31	24.15	26.33	27.04	27.24	25.74	26.57	25.73
27.36	27.85	24.14	27.62	26.46	26.15	25.31	25.91
26.59	27.13	25.45	25.47	25.25	25.47	25.88	25.34
26.17	26.41	23.48	23.54	23.14	25.16	24.35	24.54
24.63	25.32	25.52	22.42	23.31	23.55	24.47	23.63
26.44	25.68	21.93	22.37	23.03	22.67	21.43	23.56
27.33	26.05	22.55	20.85	21.69	24.67	22.33	25.16
24.72	26.39	27.27	25.11	23.03	23.64	25.40	23.59
24.25	27.02	27.16	26.26	25.77	25.81	25.73	24.44
24.50	26.53	26.73	26.15	25.73	25.91	26.23	26.53
23.95	26.84	27.30	26.51	26.43	26.63	26.19	24.27

AXIAL VELOCITY (V_a)

7.43	9.36	9.54	3.13	9.93	6.80	7.54	8.32
9.75	13.35	9.35	8.49	9.35	9.56	9.37	10.63
13.05	13.50	11.02	9.71	9.57	11.55	9.62	16.35
9.98	13.22	13.15	9.91	9.57	11.04	10.57	11.13
13.17	13.05	9.55	9.52	9.61	13.76	9.91	10.44
13.25	9.53	7.75	9.94	9.24	9.55	9.60	9.71
10.73	13.53	7.15	6.54	7.52	8.54	11.36	10.72
13.24	13.03	12.44	13.13	11.71	13.54	13.51	13.43
12.36	15.57	15.54	17.35	17.71	15.59	11.52	13.52
14.17	12.73	11.57	15.53	15.44	14.65	9.23	11.55
13.32	11.52	9.41	9.17	13.55	13.01	9.74	11.36
9.65	11.53	11.52	9.76	7.47	11.52	13.51	10.73
9.37	11.64	11.67	13.17	9.61	13.53	13.45	11.47
13.73	11.53	11.34	13.53	9.63	13.54	13.53	13.21
11.23	15.53	11.43	13.77	13.53	9.93	9.41	13.17

TOTAL PRESSURE COEFFICIENT (C_{P_o})

.738	.392	.208	.089	.137	.033	.333	.695
.275	.082	.016	-.001	.133	.283	.069	.365
.128	.190	.051	.030	.086	.079	.086	.229
.173	.121	.313	.068	.178	.133	.138	.277
.162	.075	.040	.051	.155	.208	.215	.238
.139	.117	.133	.138	.190	.236	.277	.225
.155	.173	.382	.441	.383	.277	.243	.263
.392	.173	.521	.643	.695	.570	.354	.302
.354	.243	.685	.633	.556	.466	.357	.354
.152	.312	.709	.733	.626	.434	.521	.417
.386	.229	.661	.835	.772	.417	.431	.295
.246	.079	.096	.277	.521	.452	.277	.392
.277	.103	.093	.124	.160	.225	.243	.337
.222	.103	.121	.162	.160	.208	.208	.173
.277	.079	.089	.131	.137	.152	.173	.375

STATIC PRESSURE COEFFICIENT (C_{P_s})

.432	.515	.427	.438	.453	.434	.521	.496
.504	.517	.439	.510	.427	.430	.523	.535
.530	.573	.545	.568	.531	.615	.554	.523
.558	.543	.546	.527	.551	.629	.552	.542
.586	.577	.562	.530	.595	.576	.573	.557
.563	.597	.615	.534	.515	.512	.523	.515
.515	.517	.616	.673	.517	.515	.512	.455
.703	.531	.573	.706	.713	.534	.532	.451
.509	.525	.653	.532	.527	.524	.536	.420
.466	.571	.619	.713	.635	.432	.396	.476
.477	.524	.642	.665	.547	.576	.383	.508
.414	.469	.515	.471	.733	.515	.509	.454
.412	.497	.521	.446	.544	.437	.235	.470
.557	.446	.539	.471	.647	.459	.525	.515
.373	.454	.452	.445	.473	.423	.432	.453

YAW ANGLE (α)

% RADIAL DISTANCE								
3.30	70.00	66.00	70.00	72.00	72.00	72.00	72.00	67.00
10.0	66.00	68.00	73.00	72.00	70.00	66.00	69.00	66.00
16.7	68.00	67.00	58.00	69.00	70.00	68.00	67.00	57.00
23.3	67.50	68.00	68.00	69.00	65.00	69.00	66.00	54.00
30.0	65.00	69.00	63.00	63.00	63.00	66.00	65.00	67.00
36.7	69.00	72.00	74.00	62.00	63.00	67.00	63.00	68.00
43.3	62.50	68.00	73.00	77.00	75.00	63.00	66.00	65.00
50.0	59.00	53.50	53.00	55.00	63.00	65.00	61.00	58.00
56.7	56.00	57.00	50.00	40.00	41.00	46.00	55.00	55.00
63.3	56.00	58.00	54.00	45.00	43.00	51.00	64.00	60.00
70.0	61.00	63.00	66.00	64.00	62.00	60.00	64.00	62.00
76.7	66.00	64.00	65.00	63.00	70.00	63.00	65.00	62.00
83.3	66.00	65.00	65.00	66.00	65.00	68.00	66.00	62.00
90.0	64.00	64.00	65.00	66.00	65.00	66.00	67.00	60.00
96.7	62.00	61.00	64.00	65.00	57.00	58.00	65.00	64.00

CIRCUMFERENTIAL DISTANCE (From pressure side)

PITCH ANGLE (γ)

% RADIAL DISTANCE								
3.30	.12	2.00	2.00	.12	-1.50	-1.63	.13	2.00
10.0	-4.13	.52	1.03	-2.64	-6.54	-11.17	-12.23	-5.52
16.7	-10.22	-3.25	2.00	.23	-4.57	-11.40	-15.63	-11.83
23.3	-3.11	-1.05	1.20	-1.74	-7.41	-14.62	-19.63	-9.23
30.0	-5.54	-.25	-1.14	-3.24	-3.75	-13.13	-15.68	-5.39
36.7	-.04	.50	-2.74	-7.18	-11.75	-13.62	-1.70	-.05
43.3	-.07	2.73	.00	-.41	-15.00	-13.57	-19.33	-4.19
50.0	-9.11	-1.35	.25	2.42	-3.55	-2.05	-30.01	-16.15
56.7	-7.15	-3.00	-3.53	-5.36	-5.73	-16.75	-35.35	-9.54
63.3	-5.29	-13.13	-22.54	-12.25	-.01	.59	-12.14	-16.54
70.0	-6.16	-13.87	-16.03	-13.07	4.65	3.00	3.34	-12.71
76.7	-.23	-7.55	-3.35	-5.13	-4.42	3.65	7.17	4.42
83.3	-3.05	-3.33	-3.03	-7.41	-4.05	-.55	3.42	-2.46
90.0	-5.15	-3.61	-7.51	-5.00	-4.53	-1.00	.83	-5.43
96.7	1.50	-4.67	-4.65	-2.54	-2.17	-2.06	-2.82	-.35

CIRCUMFERENTIAL DISTANCE (From pressure side)

VELOCITY (V)

33.12	36.17	42.55	41.73	41.73	42.67	33.92	32.17
40.27	42.13	43.61	43.75	42.64	43.07	41.62	39.63
42.07	41.65	43.96	43.63	43.33	43.23	43.34	40.76
41.72	42.93	44.55	43.45	42.44	42.96	42.03	39.66
41.31	43.22	44.07	43.19	41.72	41.92	41.13	40.49
42.62	43.16	43.57	42.16	43.94	41.49	33.98	40.34
40.87	41.93	43.65	39.27	43.63	40.43	33.96	39.66
37.65	41.78	37.55	36.02	36.63	37.12	39.87	35.12
39.57	40.76	34.99	35.21	36.66	35.93	33.05	36.32
42.40	39.23	34.22	35.15	34.62	36.31	34.97	36.17
42.77	41.23	36.35	33.79	33.73	37.32	35.09	37.97
38.80	43.14	41.74	33.82	35.65	37.59	35.62	36.43
53.94	41.30	42.14	40.66	40.87	40.23	40.25	38.24
39.77	41.77	42.22	42.13	41.10	39.79	40.79	40.39
38.42	41.16	41.61	41.16	43.93	41.16	33.64	37.13

AXIAL VELOCITY (V_a)

11.29	14.73	13.66	12.39	12.91	12.39	12.34	12.55
15.35	15.73	14.38	13.51	14.54	15.63	15.24	16.05
15.51	16.25	16.46	15.66	14.73	15.66	15.56	15.53
15.31	16.10	16.61	15.55	15.75	15.54	16.10	17.16
15.63	15.43	15.73	15.45	15.45	15.21	14.83	15.75
15.77	13.34	12.63	13.66	15.62	15.36	14.72	15.11
18.77	15.66	11.94	6.77	9.66	1.62	15.33	16.71
17.16	21.73	13.63	23.12	17.63	14.24	15.74	19.43
21.42	21.13	22.16	26.35	27.13	23.96	25.71	21.57
23.46	23.24	13.63	24.29	26.32	22.65	14.96	17.73
26.53	18.43	14.15	14.43	15.61	13.43	15.36	17.33
15.76	18.75	17.33	14.33	12.53	14.36	16.19	17.34
15.32	17.46	17.53	16.41	15.27	15.67	15.34	17.93
17.36	15.35	17.36	17.15	16.67	16.1	13.94	20.37
16.37	13.53	15.66	16.72	15.45	15.46	16.13	16.36

TOTAL PRESSURE COEFFICIENT (Cp_0)

.554	.427	.147	.039	.021	.011	.173	.654
.239	.098	.033	.024	.042	.641	.125	.273
.159	.171	.051	.047	.285	.093	.096	.242
.178	.138	.318	.055	.138	.139	.159	.285
.162	.333	.036	.058	.161	.150	.224	.273
.141	.105	.111	.093	.168	.198	.281	.251
.205	.258	.373	.454	.351	.234	.254	.244
.393	.144	.522	.662	.747	.616	.296	.301
.258	.239	.635	.631	.554	.504	.325	.285
.093	.347	.731	.771	.624	.442	.478	.450
.054	.238	.608	.833	.773	.378	.454	.341
.225	.331	.094	.270	.454	.401	.251	.387
.216	.373	.085	.116	.162	.187	.202	.313
.147	.035	.105	.116	.147	.137	.224	.173
.239	.352	.073	.107	.119	.131	.193	.385

STATIC PRESSURE COEFFICIENT (Cp_s)

.549	.503	.496	.466	.454	.464	.431	.504
.572	.554	.638	.575	.543	.563	.547	.563
.511	.595	.647	.614	.633	.625	.631	.555
.506	.624	.631	.614	.616	.650	.609	.575
.503	.626	.633	.539	.569	.633	.612	.616
.531	.638	.659	.573	.544	.611	.592	.587
.72	.643	.742	.713	.684	.548	.551	.534
.558	.571	.673	.727	.612	.747	.642	.495
.543	.503	.690	.649	.673	.563	.577	.493
.562	.61.	.593	.735	.607	.534	.431	.524
.556	.6.7	.633	.772	.707	.521	.465	.524
.460	.529	.724	.607	.557	.560	.475	.474
.460	.537	.643	.474	.535	.515	.552	.513
.145	.527	.568	.572	.533	.4.6	.539	.512
.451	.462	.494	.437	.434	.521	.433	.521

YAW ANGLE (α)

% RADIAL DISTANCE								
3.30	66.00	65.00	70.00	71.00	72.00	71.00	72.00	67.00
10.0	66.00	63.00	70.00	70.00	71.00	68.00	60.00	66.00
16.7	58.00	65.00	68.00	69.50	70.00	69.00	63.00	68.00
23.3	70.00	63.00	65.00	70.00	63.00	58.00	67.00	66.00
30.0	72.00	64.00	72.00	72.00	70.00	65.00	65.00	68.00
36.7	73.00	76.00	76.00	78.00	71.00	68.00	63.00	68.00
43.3	64.00	70.00	74.00	78.00	73.00	70.00	65.00	65.00
50.0	59.00	60.00	60.00	58.00	62.00	64.00	55.00	58.00
56.7	58.00	59.00	53.00	40.00	44.00	48.00	55.00	54.00
63.3	56.00	58.00	51.00	45.00	41.00	48.00	62.00	58.00
70.0	50.00	62.00	52.00	58.00	56.00	60.00	64.00	62.00
76.7	66.00	64.00	65.00	68.00	70.00	68.00	65.00	61.00
83.3	66.00	65.00	66.00	57.00	66.00	65.00	67.00	62.00
90.0	65.00	64.00	66.00	66.00	67.00	67.00	66.00	61.00
96.7	64.00	61.00	64.00	65.00	65.00	68.00	68.00	64.00

CIRCUMFERENTIAL DISTANCE (From pressure side)

PITCH ANGLE (γ)

% RADIAL DISTANCE								
3.30	-1.41	-.39	1.28	1.52	.29	.65	4.56	3.30
10.0	-4.53	.35	-.15	-3.22	-6.34	-9.55	-3.11	-4.69
16.7	-12.72	-2.56	2.00	.19	-3.93	-9.23	-13.79	-9.43
23.3	-12.52	-1.42	3.84	1.37	-4.77	-11.39	-15.72	-6.82
30.0	-5.41	-1.19	2.65	.83	-5.63	-13.51	-14.95	-7.36
36.7	-1.51	1.32	-.41	-4.37	-6.36	-17.35	-12.17	-3.69
43.3	-.56	3.41	1.62	-5.76	-16.61	-23.73	-13.73	-8.11
50.0	-9.67	-.12	.74	-.27	-13.12	-22.13	-30.12	-17.39
56.7	-6.35	-6.63	-7.59	-5.69	-12.22	-14.55	-33.27	-10.04
63.3	-8.59	-12.25	-19.33	-16.02	-6.35	-4.56	-16.33	-8.91
70.0	-6.72	-12.33	-20.56	-16.27	1.12	3.69	1.50	-16.14
76.7	-.32	-3.39	-13.22	-13.39	-6.72	4.54	7.44	-.54
83.3	-2.32	-9.12	-3.12	-7.09	-4.23	-.15	5.44	-3.39
90.0	-4.27	-5.67	-7.00	-5.67	-4.41	-.??	2.71	-6.21
96.7	-.11	-4.63	-4.01	-7.24	-3.65	-3.72	-4.53	-5.19

VELOCITY (V)

43.11	52.33	54.77	56.43	56.37	56.22	43.57	40.55
53.30	57.95	53.14	50.04	59.29	58.17	55.68	51.63
55.85	56.05	59.44	63.09	53.41	53.85	53.79	55.76
54.55	56.63	53.80	53.65	57.46	53.55	53.27	55.44
55.02	55.56	57.42	57.02	55.63	57.36	55.35	53.96
55.36	56.26	56.23	52.91	51.96	54.37	54.60	54.11
54.71	55.14	53.27	51.06	49.70	48.55	52.00	53.12
52.59	55.46	51.73	49.01	45.62	45.73	49.52	51.97
53.03	53.66	46.79	41.43	47.63	47.30	50.51	51.65
55.99	53.73	46.53	46.38	46.43	48.60	46.59	49.83
57.36	54.31	48.33	46.00	46.53	45.54	45.61	52.49
53.34	57.45	56.54	51.17	48.31	50.16	52.15	49.85
52.95	56.59	55.58	55.83	55.13	55.15	54.58	51.33
54.36	56.74	56.10	56.77	55.54	55.12	54.89	53.63
50.34	55.10	56.05	56.23	56.32	55.71	54.34	49.91

AXIAL VELOCITY (V_a)

17.45	21.29	18.73	19.30	17.42	18.30	15.27	15.82
21.55	21.71	20.23	20.50	20.15	21.49	20.60	20.95
20.41	22.73	22.25	21.05	20.27	21.17	21.39	20.63
18.23	21.21	22.05	20.05	20.52	21.47	21.92	22.23
16.93	34.35	17.72	17.62	13.96	20.26	20.39	20.55
16.33	13.61	13.60	10.97	16.51	13.65	19.99	20.23
23.35	13.65	14.58	10.55	10.70	15.50	21.50	21.39
26.70	27.74	25.39	25.97	21.17	13.57	22.70	26.26
27.73	23.25	23.73	35.25	33.75	29.51	25.62	30.31
30.36	27.56	27.71	32.31	34.57	32.55	20.97	26.03
23.45	24.11	21.15	20.47	25.21	24.04	20.43	24.26
21.57	24.33	23.51	10.65	16.51	18.74	21.05	24.17
21.52	23.61	23.72	21.65	20.60	23.67	21.33	24.07
23.16	24.53	22.55	22.33	21.73	21.55	22.30	25.47
22.29	26.62	24.53	22.36	21.15	20.35	20.50	21.73

TOTAL PRESSURE COEFFICIENT (Cp_0)

.724	.322	.119	.032	.302	.038	.397	.313
.255	.071	.098	-.064	-.304	.016	.146	.322
.253	.172	.036	.033	.338	.037	.059	.217
.272	.234	.109	.105	.131	.106	.105	.247
.268	.268	.213	.137	.236	.161	.180	.255
.224	.213	.268	.322	.372	.247	.247	.249
.205	.238	.456	.532	.598	.527	.314	.271
.339	.138	.531	.762	.355	.316	.573	.320
.255	.264	.582	.707	.640	.523	.464	.356
.146	.305	.724	.749	.715	.473	.523	.448
.369	.272	.682	.849	.724	.397	.464	.297
.201	.071	.121	.309	.590	.431	.272	.381
.213	.071	.086	.110	.172	.133	.197	.331
.130	.079	.098	.121	.142	.167	.205	.213
.256	.071	.071	.105	.126	.138	.201	.443

STATIC PRESSURE COEFFICIENT (Cp_s)

.517	.531	.508	.507	.474	.502	.536	.563
.601	.627	.629	.656	.624	.504	.533	.560
.698	.627	.672	.705	.672	.636	.660	.657
.652	.722	.721	.642	.558	.691	.573	.671
.570	.534	.741	.703	.673	.635	.551	.604
.570	.579	.732	.619	.623	.647	.623	.615
.592	.647	.773	.730	.637	.610	.635	.573
.520	.564	.725	.674	.553	.705	.709	.571
.559	.537	.695	.732	.633	.647	.647	.601
.599	.545	.729	.706	.717	.576	.533	.593
.504	.535	.756	.830	.727	.493	.471	.574
.504	.600	.502	.602	.671	.647	.532	.532
.517	.555	.574	.554	.565	.593	.570	.554
.523	.571	.554	.614	.592	.574	.601	.554
.449	.477	.529	.572	.596	.575	.534	.602

		V	VA	Y	YM	CPO	CPCM
% R A D I A L D I S T A N C E	3.30	24.46	3.53	69.23	69.21	.314	.307
	10.0	27.09	9.66	63.79	63.67	.164	.139
	16.7	27.75	1..02	63.25	63.21	.110	.111
	23.3	27.24	10.23	57.57	57.33	.133	.139
	30.0	27.21	9.96	58.12	63.03	.143	.151
	36.7	26.93	9.25	68.56	69.32	.175	.177
	43.3	25.76	9.34	63.13	67.21	.293	.273
	50.0	24.16	12.35	57.57	57.73	.455	.456
	56.7	23.80	14.55	50.25	49.23	.456	.476
	63.3	23.35	13.27	54.06	52.91	.434	.439
	70.0	23.82	10.81	62.43	62.13	.293	.283
	76.7	24.97	10.22	65.62	65.21	.193	.196
	83.3	25.90	10.49	65.81	65.67	.172	.171
	90.0	26.05	10.93	65.06	64.82	.175	.171
	96.7	25.93	10.94	64.93	64.63		

AVERAGE EXIT FLOW PARAMETERS

VELOCITY = 25.52

AXIAL VELOCITY = 10.71

TOTAL PRESSURE = -.63

STATIC PRESSURE = -2.43

MEAN YAW = 64.35

MEAN CPO = .2111

MASS AVERAGE CPO = .221.

YG ... YAW = .1021

Table 9   Distribution of the Parameters in the Radial
the Av...   Flow P

		V	VA	Y	YH	CFO	CPOM
% R A D I A L D I S T A N C E	3.30	33.42	12.94	70.12	70.05	.266	.263
	10.0	42.14	15.12	63.75	63.65	.103	.111
	16.7	42.75	15.73	65.12	65.13	.119	.118
	23.3	42.44	16.38	67.31	67.27	.135	.137
	30.0	42.20	15.57	65.00	67.98	.145	.145
	36.7	41.79	15.05	63.53	63.06	.169	.168
	43.3	40.43	17.83	59.43	63.27	.285	.267
	50.0	38.00	18.63	59.43	59.17	.463	.451
	56.7	37.53	23.10	50.03	49.32	.435	.447
	63.3	35.63	20.93	53.87	52.31	.492	.493
	70.0	37.29	15.81	62.75	62.57	.455	.428
	76.7	39.96	15.76	66.63	65.74	.260	.246
	83.3	40.39	16.48	65.75	65.65	.170	.170
	90.0	40.39	17.33	64.81	64.67	.143	.147
	96.7	40.15	17.37	64.75	64.53	.164	.161

AVERAGE EXIT FLOW PARAMETERS

VELOCITY = 40.31

AXIAL VELOCITY = 16.73

TOTAL PRESSURE = -1.47

STATIC PRESSURE = -.74

MEAN YAW = 64.53

MEAN CPO = .1925

MASS AVERAGE CPO = .2002

YS DUMMY = .1664

Table 10   Distribution of the Parameters in the
Ra

		V	VA	Y	YM	CPO	CPOM
	3.30	51.27	17.39	69.25	69.16	.305	.293
	10.0	56.98	20.93	63.25	63.21	.101	.133
%	16.7	53.15	21.24	63.31	63.23	.105	.105
	23.3	57.52	20.96	63.25	63.13	.164	.152
R	30.0	56.14	19.61	63.25	63.35	.222	.223
A	36.7	54.61	16.39	72.25	71.53	.263	.265
D	43.3	52.17	16.97	70.62	69.16	.353	.359
I	50.0	51.11	24.31	59.67	59.63	.542	.519
A	56.7	49.86	29.99	51.60	50.33	.493	.512
L	63.3	49.31	29.24	52.12	51.23	.510	.516
D	70.0	50.34	24.03	60.53	60.37	.469	.457
I	76.7	52.33	21.14	66.00	65.63	.313	.295
S	83.3	54.77	22.01	66.12	66.03	.171	.172
T	90.0	55.52	23.11	65.25	65.14	.145	.145
A	96.7	54.38	22.55	65.37	65.13	.175	.172

AVERAGE EXIT FLOW PARAMETERS

VELOCITY = 53.52

AXIAL VELOCITY = 22.03

TOTAL PRESSURE = -2.91

STATIC PRESSURE = -10.54

MEAN YAW = 64.32

MEAN CPO = .2133

MASS AVERAGE CPO = .2253

YS DURHAM = .1531

Table 11 Distribution of the Parameters in the

APPENDIX E

ERROR ANALYSIS

In order to assess the uncertainty in the measurement and the computation of the flow parameters, Test #2 was selected to calculate typical absolute errors.

Table 12 summarizes the effect of the different errors on each measured flow parameter. The total absolute error in measuring each flow parameter was then calculated using the equation:

$$E = \sqrt{E_1^2 + E_2^2 + \ldots E_n^2} \qquad (30)$$

where

E = total error in the measurement

$E_1, E_2, \ldots E_n$ = individual errors.

Table 13 shows the error in the calculated flow parameters. The following equation was used to compute this error:

$$E_R = [(\frac{\partial R}{\partial X_1}E_1)^2 + (\frac{\partial R}{\partial X_2}E_2)^2 + \ldots \ldots + (\frac{\partial R}{\partial X_n}E_n)^2]^{1/2} \qquad (31)$$

where

R = result computed

E_R = uncertainty in result R

X_n = n^{th} variable

E_n = uncertainty in the nth variable.

From Table 13 it can be seen that the percentage error was less than $\pm$ 1% for the velocity, and $\pm$ 3 to 5% for the static and total pressure coefficients.

Table 12

Estimated Error in the Measured Flow Parameters

Error Component / Flow Parameter	Due to Yaw Angle Effect ("H$_2$O)	Due to Turbulence Effect ("H$_2$O)	Due to Wall Effect ("H$_2$O)	Due to Meniscus Effect ("H$_2$O)	Due to Scale Reading	Total Error
...al Pressure	$\pm$0.013 [41]	+0.005 [10]	-	$\pm$0.025	$\pm$0.0008 "H$_2$O	$\pm$0.028 "H$_2$O
...v Static Pressure	$\pm$0.0008	+0.005 [10]	+2.75x10^{-4} [41]	$\pm$0.025	$\pm$0.0008 "H$_2$O	$\pm$0.028 "H$_2$O
...l Static Pressure	-	+0.005 [40]	-0.013 [40]	$\pm$0.025	$\pm$0.025 "H$_2$O	$\pm$0.028 "H$_2$O
...ch Pressure or P$_S$	$\pm$0.0008	+0.005 [40]	+2.75x10^{-4} [41]	$\pm$0.025	$\pm$0.0008 "H$_2$O	$\pm$0.028 "H$_2$O
Angle	-	-	-	-	$\pm$0.2°	$\pm$0.2°
...metric Pressure	-	-	-	-	$\pm$0.01 "Hg	$\pm$0.14 "H$_2$O
...oom Temperature	-	-	-	-	-	$\pm$5°F

Table 13

Estimated Error in the Calculated Flow Parameters

Flow Parameter	Definition of Flow Parameter	Error
Pitch Differential Pressure	$(P_4 - P_5)$	± 0.047 "H_2O
Dynamic Head	$(P_o - P)$	± 0.059 "H_2O
Pitch Angle	$2 + 50(P_4 - P_5)/(P_o - P)$	$\pm 0.87^o$
Velocity	$4.78\sqrt{\dfrac{\text{Room Temp.}}{\text{Room Press.}} \times (P_o - P)}$	± 0.3 m/sec.
Static Pressure Coefficient	$\dfrac{P_1 - P}{\frac{1}{2}\rho V_1^2}$	± 0.018
Total Pressure Coefficient	$\dfrac{P_{o1} - P_o}{\frac{1}{2}\rho V_1^2}$	± 0.015

APPENDIX F

METRIC CONVERSION FACTORS

The author apologizes for the fact that the thesis contains mixed symbols and units including SI metric and Imperial. The Imperial units have been used to describe the power sources and the pressure measurements including mano-meters, traversing mechanisms, etc. The test apparatus on the other hand has been designed using metric scales. A series of conversion factors taken from the National Standard of Canada Metric Practice Guide (CAN3-Z234.1-76) are shown below to facilitate conversion where necessary.

Units used in Thesis	Equivalent in SI Units
inch	25.4 mm
inch water (20°C)	248.641 Pa
inch oil (20°C)	205.375 Pa
inch mercury (20°C)	3.374 k Pa
p.s.i.	6.895 k Pa
c.f.m.	0.472 dm^3/s
r.p.m.	0.0167 rev/s
B.H.P.	746 W